Spectroscopic Excitation and Quenching Processes in Rare-Earth-Ion-Doped Al_2O_3 and their Impact on Amplifier and Laser Performance

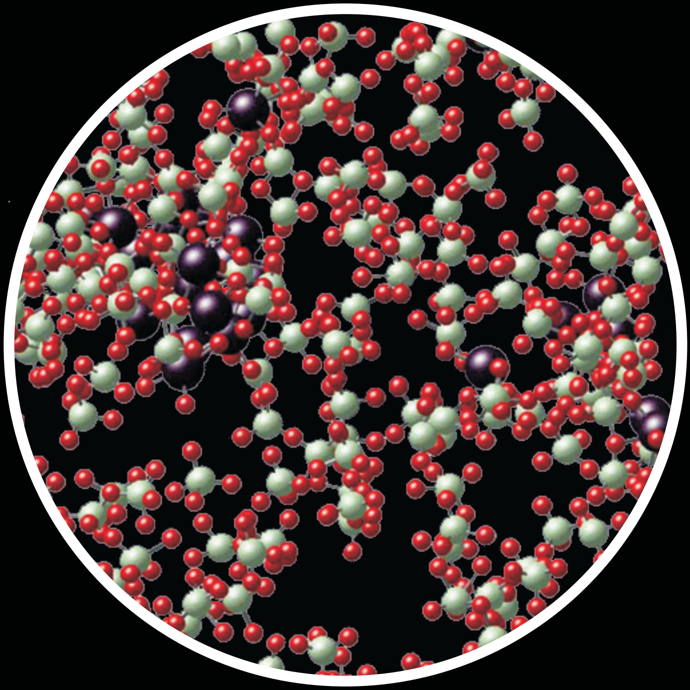

Laura Agazzi
2012

Spectroscopic Excitation and Quenching Processes in Rare-Earth-Ion-Doped Al_2O_3 and their Impact on Amplifier and Laser Performance

Laura Agazzi

Graduation committee:

Chairman and Secretary:	
Prof. Dr. Ir. A. J. Mouthaan	University of Twente
Promoter:	
Prof. Dr. M. Pollnau	University of Twente
Assistant Promoter:	
Dr. K. Wörhoff	University of Twente
Members:	
Prof. Dr. J. C. T. Eijkel	University of Twente
Prof. Dr. W. L. Vos	University of Twente
Prof. Dr. P. Dorenbos	Delft University of Technology
Dr. A. Toncelli	University of Pisa

The research described in this thesis was carried out at the Integrated Optical MicroSystems (IOMS) Group, Faculty of Electrical Engineering, Mathematics and Computer Science, MESA+ Institute for Nanotechnology, University of Twente, P.O. Box 217, 7500 AE Enschede, The Netherlands.

This work was financially supported by the Smartmix Memphis programme of the Dutch Ministry of Economic Affairs.

Cover design:

Front: Microscopic world: snapshot of a rare-earth-ion-doped glass structure. Dark spheres are rare-earth ions, red spheres are oxygen and light grey spheres are aluminum. Adapted with permission from A. Monteil *et al.*, “Clustering of rare-earth in glasses, aluminum effect: experiments and modeling,” J. Non-Cryst. Solids **348**, 44-50 (2004).

Reverse: Macroscopic world: illustration of advanced integrated photonic circuit with amplification of existing signal light and additional signal light generated by miniature active rare-earth-ion-doped waveguide amplifiers and lasers (red sections). The operation of the macroscopic waveguide devices is intricately linked to the microscopic glass structure.

ISBN: 978-90-365-3423-9

Printed by Wöhrmann Print Service, The Netherlands

Copyright © 2012 by Laura Agazzi, Enschede, The Netherlands

Spectroscopic Excitation and Quenching Processes in Rare-Earth-Ion-Doped Al_2O_3 and their Impact on Amplifier and Laser Performance

DISSERTATION

to obtain
the degree of doctor at the University of Twente,
on the authority of the rector magnificus,
prof. dr. H. Brinksma,
on account of the decision of the graduation committee,
to be publicly defended
on Thursday the 20th of September 2012 at 12:45

by

Laura Agazzi
born on the 20th of December 1983
in Vimercate, Italy

This dissertation is approved by:
the promoter: Prof. Dr. M. Pollnau
the assistant promoter: Dr. K. Wörhoff

Contents

List of Symbols and Abbreviations

Constants

c	Speed of light
e	Elementary charge
h	Planck's constant
k_B	Boltzmann's constant

Parameters

α	Host-dependent parameter in Eqs. (2.33) and (2.36)
α_{abs}	Loss coefficient due to the ion absorption
α_{bck}	Material-dependent loss
α_{Total}	Total loss in a waveguide
$\beta(J \rightarrow J')$	Radiative branching ratio between states J and J'
γ	Donor-acceptor energy-transfer coefficient
Γ	Confinement factor of the light inside the waveguide
γ_{ro}	Damping constant
ΔE	Energy gap
θ	Phase
λ	Wavelength
$\bar{\lambda}$	Mean wavelength
λ_L	Laser wavelength
λ_P	Pump wavelength
λ_S	Luminescence/signal wavelength
λ_{ZL}	Peak absorption wavelength
$\hat{\mu}_A$	Acceptor dipole moment
$\hat{\mu}_D$	Donor dipole moment
ν	Frequency
$\tilde{\nu}$	Wavenumber
ρ	Radiation density [$\mathrm{J \cdot s/cm^3}$]
σ_{abs}	Absorption cross-section
σ_{em}	Emission cross-section
σ_{ESA}	Excited-state-absorption cross-section
$\sigma_{ij/ji}$	Absorption/emission cross-sections between Stark levels i and j belonging to different manifolds
σ_{GSA}	Ground-state-absorption cross-section
σ_{SE}	Stimulated emission cross-section
τ	Various luminescence lifetimes
τ_0	Migration time
τ_{1q}	Decay time of quenched ions
τ_c	Cavity lifetime

τ_D	Intrinsic decay of a donor’s excitation
$\tau_{D,rad}$	Radiative lifetime of a donor in absence of energy transfer
τ_{rad}	Radiative lifetime
τ_w	Effective lifetime
ϕ	Phonon density
φ_P	Pump photon flux
ψ_P	Pump-power distribution
ψ_S	Probe-power distribution
ω_L	Laser eigenfrequency
ω_{ro}	Relaxation-oscillation frequency
$\Omega_{\tilde{t}}$ ($\tilde{t} = 2, 4, 6$)	Judd-Ofelt parameters
A	Total radiative decay-rate constant
A'	Amplitude
A_{10}	Einstein coefficient of spontaneous emission
$A(J \rightarrow J')$	Radiative decay-rate constants between states J and J'
$A_{non\text{-}rad}$	Decay-rate constant of multiphonon relaxation from level J to level J–1
A_r	Active area
B_{01}	Einstein coefficient of absorption
B_{10}	Einstein coefficient of stimulated emission
C	Host-dependent parameter in Eqs. (2.33) and (2.36)
C^*	Arbitrary constant
C_{DA}	Microparameter for donor-acceptor energy transfer
C_{DD}	Microparameter for donor-donor energy transfer
E_i	Energy of the level i
E_{ZL}	Zero-phonon-line energy
f	Probability that an excited donor did not transfer its energy to an acceptor
F	Nonlinear quenching rate
f_a	Fraction of active ions
f_D	Probability of finding an excited donor
f_q	Fraction of quenched ions
f_q^*	Fraction of quenched ions among all ions in the excited state
g	Small-signal gain coefficient
g_{abs}	Spectral line shape distributions of absorption
g_{em}	Spectral line shape distributions of emission
g_i	Degeneracy of the level i
$\hat{H}_{dip-dip}$	Dipole-dipole interaction Hamiltonian
I	Various intensities
J	Total angular momentum quantum number
k	Donor-acceptor energy-transfer coefficient
ℓ	Path length of laser light inside a resonator
L	Total orbital angular momentum quantum number
L_{rt}	Loss per roundtrip
m	Multipolarity of an energy-transfer process
m_{DA}	Multipolarity of donor-acceptor interaction

m_{DD}	Multipolarity of donor-donor interaction
n/n_{medium}	Refractive index (n_{medium} in Chapter 4)
n	Number of ions (only in Chapter 4)
$n(T)$	Bose-Einstein occupation number
$N_{1,cw}$	Population density in the upper laser level during steady-state laser operation
N_A	Acceptor concentration
N_c	Critical transfer concentration
N_d	Total dopant concentration
N_D	Donor concentration
N_e	Total excitation density summed over the population densities of the substantially populated excited states
N_e^{eff}	Integral of N_e averaged over the waveguide volume and probe-beam distribution
N_i	Population density of the level i
N_i^{eff}	Integral of N_i averaged over the waveguide volume and probe-beam distribution
$N_{ia/q}$	Population density of the level i for active/quenched ions
p	Number of phonons necessary to bridge an energy gap
P	Probability of donor-acceptor energy transfer
P_P	Pump power
$P_P(0)$	Launched pump power
$P_P(L)$	Transmitted pump power
Q	Critical quenching concentration
r	Distance
R	Distance between two ions
R_{DA}	Förster radius for donor-acceptor energy transfer
R_{DD}	Förster radius for donor-donor energy transfer
R_k	Distance between a donor and an acceptor k
R_{out}	Reflectivity
R_P	Pump rate
$R_{Pa/q}$	Pump rate for active/quenched ions
$R_{P,thr}$	Threshold pump rate
S	Total spin quantum number
S_{calc}	Electric dipole line strength
S_{enh}	Signal enhancement
S_{meas}	Measured line strength
t	Time
t_{exp}	Asymptotic decay time
T	Temperature
$U^{(\tilde{t})}$ ($\tilde{t} = 2, 4, 6$)	Doubly reduced matrix elements
$\overline{W}$	Ensemble-averaged migration-assisted energy-transfer rate
W_{DA}	Probability per unit time for donor-acceptor interaction
W_{DD}	Probability per unit time for donor-donor interaction
W_{ETU}	Various macroscopic energy-transfer upconversion coefficients
Z_i	Energy-partition function of the manifold i

Abbreviations

CR	Cross relaxation
CW	Continuous wave
DFB	Distributed feedback
ESA	Excited-state absorption
ETU	Energy-transfer upconversion
EXAFS	X-ray absorption fine structure
GSA	Ground-state absorption
ICP	Inductively-coupled plasma
IOMS	Integrated Optical MicroSystems
J-O	Judd-Ofelt
NMR	Nuclear-magnetic resonance
PECVD	Plasma-enhanced chemical-vapor deposition
RBS	Rutherford Backscattering Spectroscopy
RIE	Reactive ion etching
ROI	Region of interest
SE	Stimulated emission
SOA	Semiconductor optical amplifier
SOI	Silicon-on-insulator
TE	Transverse Electric
TREM	Total Rare-Earth Metal
WDM	Wavelength-division multiplexing

Abstract

This thesis presents in-depth spectroscopic investigations of the optical properties of $Al_2O_3:Er^{3+}$ and $Al_2O_3:Yb^{3+}$, materials employed for the realization of integrated optical devices such as waveguide amplifiers and lasers. The aim is to provide important spectroscopic parameters for the design and optimization of such devices. Nevertheless, some of the spectroscopic investigations presented in this thesis have a fundamental importance as well.

$Al_2O_3:Er^{3+}$ and $Al_2O_3:Yb^{3+}$ films are deposited on thermally oxidized silicon wafers using reactive co-sputtering, and reactive ion etch is applied to realize low-loss waveguide structures in the films. Monolithic integration of $Al_2O_3:Er^{3+}$ gain structures with passive silicon-on-insulator (SOI) waveguides is demonstrated. A signal enhancement of 7.2 dB at 1533 nm is shown in an $Al_2O_3:Er^{3+}$-Si-$Al_2O_3:Er^{3+}$ structure. To our knowledge, this is the first time that monolithic integration of active rare-earth-ion-doped waveguides with passive SOI waveguides is achieved and signal enhancement is measured, which in the future will allow us to make use of potential Er-doped gain devices in passive Si photonic circuits. Basic optical and spectroscopic properties, including propagation losses, absorption and emission cross-sections, and lifetimes are determined.

The ion-ion process of energy-transfer upconversion (ETU) is investigated in $Al_2O_3:Er^{3+}$. Generally this process, in combination with energy migration, can be detrimental for the amplifier or laser performance of a number of rare-earth-ion-doped compounds by depleting the population of the long-lived upper state of the corresponding luminescence transition, thereby diminishing the available optical gain. The most important energy-transfer models found in the literature from the last sixty years – Burshteîn's and Zubenko's microscopic treatments of ETU, as well as Grant's macroscopic rate-equation approach – are put to the test when applied to analyze photoluminescence decay measurements under quasi-CW excitation performed on $Al_2O_3:Er^{3+}$. Zubenko's model provides the best agreement.

A fast quenching process induced by, e.g., active ion pairs and clusters, undesired impurities, or host material defects such as voids, that is not revealed by any particular signature in the luminescence decay curves because of negligible emission by the quenched ions under quasi-CW excitation, is verified by pump-absorption experiments. Such fast quenching process is investigated in both $Al_2O_3:Er^{3+}$ and $Al_2O_3:Yb^{3+}$, and results are compared. A new model that takes the fast quenching into account is presented, which can be helpful in predicting and optimizing the performance of rare-earth-ion-doped devices.

The impact of quenching on $Al_2O_3:Er^{3+}$ amplifiers and on $Al_2O_3:Yb^{3+}$ distributed-feedback lasers is discussed. In the former, it is observed that the fast quenching strongly degrades the amplifier performance already at low concentrations. In the latter, the focus is on the measurement of the laser relaxation-oscillation frequency as a function of pump rate, usually performed in order to determine parameters of the laser medium or cavity. It is shown that the fast quenching of a

fraction of dopants affects the relaxation oscillations, resulting in incorrect values for the parameter deduced from this measurement. In the equations describing the relaxation oscillations, the lifetime of the upper laser level is replaced by an effective lifetime that takes the quenching into account.

Finally, the higher energy levels of $Al_2O_3:Er^{3+}$ are also investigated. A Judd-Ofelt analysis is performed, excited-state-absorption measurements are presented, and the presence of the ETU process, $(^4I_{13/2}, {}^4I_{11/2}) \rightarrow (^4I_{15/2}, {}^4F_{9/2})$ or alternatively $(^4I_{13/2}, {}^4I_{11/2}) \rightarrow (^4F_{9/2}, {}^4I_{15/2})$ is proved.

Samenvatting

In dit proefschrift worden diepgaande spectroscopische onderzoeken naar de optische eigenschappen van $Al_2O_3:Er^{3+}$ en $Al_2O_3:Yb^{3+}$ gepresenteerd. Deze materialen worden gebruikt voor het realiseren van geïntegreerde optische componenten zoals golfgeleiderversterkers en lasers. Het doel is om belangrijke spectroscopische parameters voor het ontwerp en de optimalisatie van zulke componenten te geven. Daarnaast hebben enkele van de onderzoeken die hier worden gepresenteerd ook fundamentele relevantie.

Dunne films van $Al_2O_3:Er^{3+}$ en $Al_2O_3:Yb^{3+}$ worden gesputterd op thermisch geoxideerde silicium-wafers door middel van *reactive co-sputtering*. Daarna worden verliesarme golfgeleiderstructuren in deze films geëtst middels *reactive ion etching*. Monolithische integratie van op $Al_2O_3:Er^{3+}$ gebaseerde versterkingsstructuren met passieve golfgeleiders op basis van *silicon-on-insulator*-technologie (SOI) wordt gedemonstreerd. Een signaalverbetering van 7,2 dB op 1533 nm wordt aangetoond in een $Al_2O_3:Er^{3+}$-Si- $Al_2O_3:Er^{3+}$-structuur. Voor zover ons bekend, is dit de eerste keer dat monolithische integratie van actieve golfgeleiders die met zeldame aardemetaal-ionen zijn gedoteerd, en passieve SOI-golfgeleiders, is bereikt, en dat hierbij signaalverbetering is gemeten. In de toekomst zal dit ons in staat stellen om met erbium gedoteerde versterkingsstructuren daadwerkelijk te gebruiken in passieve optische schakelingen op basis van silicium. Belangrijke optische en spectroscopische eigenschappen, waaronder propagatieverliezen, absorptie- en emissie-apertuur, en levensduur zijn vastgesteld.

Energy-transfer upconversion (ETU), een interactieprocess tussen twee ionen, is onderzocht in $Al_2O_3:Er^{3+}$. In het algemeen is dit proces, in combinatie met energiemigratie, schadelijk voor de prestaties van versterkers of lasers op basis van een aantal materialen die met zeldzame aardmetaal-ionen zijn gedoteerd. Dit komt door uitputting van de populatie van de aangeslagen toestand met lange levensduur, waardoor de beschikbare optisch versterking afneemt. De belangrijkste energie-overdracht-modellen die in de literatuur van de afgelopen zestig jaar zijn gevonden – Burshteîn's en Zubenko's microscopische behandeling van ETU, als ook Grant's macroscopische aanpak op basis van *rate-equations* worden beproefd door ze toe te passen op de analyse van fotoluminescentie-vervalmetingen onder quasi-continue excitatie van $Al_2O_3:Er^{3+}$. Het model van Zubenko komt het beste overeen met de metingen.

Een snel *quenching*-proces dat wordt veroorzaakt door bijvoorbeeld actieve ion-paren en clusters, ongewenste onzuiverheden, of defecten in het basismateriaal, kan niet worden aangetoond door metingen van luminescentie-vervalcurves, doordat de emissie door de gequenchte ionen onder quasi-continue excitatie verwaarloosbaar is. Middels pomp-absorptie-metingen wordt dit proces wel aangetoond. Zulke processen zijn onderzocht in zowel $Al_2O_3:Er^{3+}$ als $Al_2O_3:Yb^{3+}$, en de resultaten hiervan zijn met elkaar vergeleken. Een nieuw model waarin snelle quenching wordt meegenomen, wordt gepresenteerd. Dit model kan helpen bij het voorspellen en optimaliseren van de prestaties van met zeldame aardmetaal-ionen gedoteerde componenten.

De invloed van *quenching* op het gedrag van versterkers op basis van $Al_2O_3:Er^{3+}$ en van lasers op basis van gedistribueerde terugkoppeling in $Al_2O_3:Yb^{3+}$ wordt besproken. In de eerste wordt gezien dat *quenching* de prestaties van de versterker al bij lage doteringconcentraties verslechtert. Bij de tweede ging de aandacht vooral uit naar het meten van de relaxatie-oscillatiefrequentie als functie van de *pump rate*. Deze methode wordt vaak toegepast om parameters van het medium of van de resonatorholte te bepalen. Er wordt aangetoond dat *quenching* van een deel van de doteringen invloed heeft op de relaxatie-oscillatie, wat leidt tot onjuiste waarden voor de parameters die met deze methode worden bepaald. Dit wordt opgelost door in de vergelijkingen die de relaxatie-oscillatie beschrijven de levensduur van het hoogste laser-niveau te vervangen door een effectieve levensduur waarin het effect van *quenching* wordt verdisconteerd.

Ten slotte worden de hoogste energieniveau's van $Al_2O_3:Er^{3+}$ onderzocht. Een *Judd-Ofelt*-analyse is uitgevoerd, metingen aan de absorptie van de aangeslagen toestand worden gepresenteerd, en de aanwezigheid van het ETU-process $({}^4I_{13/2}, {}^4I_{11/2}) \rightarrow ({}^4I_{15/2}, {}^4F_{9/2})$ dan wel $({}^4I_{13/2}, {}^4I_{11/2}) \rightarrow ({}^4F_{9/2}, {}^4I_{15/2})$ wordt bewezen.

Chapter 1

Introduction and Outline

1.1 From Optical Fibers to Integrated Optics

During the past few decades, optical fibers have revolutionized the communication field thanks to their unprecedented potential for high-capacity and high-speed data transmission, providing affordable connectivity between people in different parts of the world. Optical fiber-based systems are now widely used for telephony, but also for high-speed internet, and cable TV. In general such systems contain several optical components, such as amplifiers, lasers, modulators, multiplexers, splitters, and detectors, connected by optical fibers. A significant reduction in system size and cost can be achieved by the development of integrated optics to replace some of the discrete components used in fiber optical communication [1].

In analogy to the earlier investigations and developments of electronic integration, developments of integrated optics are now being intensively investigated, in which several optical functions are performed by miniaturized optical devices on a single substrate [2,3]. An extremely large amount of data can travel in a very small space, making integrated optics very attractive. Besides telecommunications [4], applications for integrated optics include, for example, on-chip optical interconnects for high-speed computing [5], in addition to sensors, imaging devices, and laser sources [6-8].

In integrated optical circuits, light is confined and routed to different optical components through optical waveguides. One of the candidates for integrated optical circuits is silicon, because of the already well-developed processing infrastructure, the possibility of very high integration density (due to its relatively high refractive index), and the capability of monolithic integration of optical and electronic circuits. Within the last decade silicon-on-insulator (SOI) technology has rapidly developed into a well-established photonics platform [9] to create a wide range of passive devices to guide and direct light. Although integrated modulation schemes [10] and light detection [11] have been addressed, active devices that emit or amplify light have as yet not been achieved on silicon due to the indirect bandgap of this material.

Light generation on silicon chips can be achieved by integration of III-V semiconductor layers or rare-earth-ion-doped dielectric thin films. Both approaches yield their specific advantages and drawbacks [11]. For III-V/Si integration, direct epitaxial growth of III-V compounds on Si substrates would be the most desirable approach, but this typically introduces defects due to the large lattice mismatch.

Therefore integration schemes such as die-to-wafer bonding [12,13] are required, which however are complex and costly. Instead the second approach can allow for direct wafer-scale deposition onto silicon substrates [14]. On the other hand, electrical pumping of III-V semiconductors provides a clear advantage over optical pumping of rare-earth ions. Thus far, electrically pumped rare-earth-ion-doped dielectrics in a slotted Si-waveguide configuration have been proposed [15], but an experimental verification is still missing. In addition, III-V semiconductor optical amplifiers (SOAs) deliver a gain per unit length of a few hundred dB/cm [16], while their dielectric counterparts typically provide only a few dB/cm [14,16], although recently a gain of 935 dB/cm was demonstrated in a rare-earth-ion-doped double tungstate [17].

Nevertheless, for specific applications rare-earth-ion-doped dielectrics are superior to III-V semiconductors. For instance, in an erbium-doped waveguide amplifier on a Si wafer operating at around 1550 nm, amplification at bit rates up to 170 Gbit/s was demonstrated without noise penalty or patterning effects [18]. And there is the prospect for higher bit rates, as in erbium-doped fibers high-speed amplification of an optical time division multiplexed and polarization multiplexed signal has reached 1.28 Tbit/s [19]. In contrast, when operating SOAs in a saturated or quasi-saturated gain regime, eye closure occurs, because their carrier lifetime of typically 100 ps causes transient gain suppression and recovery depending on bit rate and sequence [20]. Rare-earth-ion-doped amplifiers instead, with their long excited-state lifetimes of several ms are practically insensitive to the bit rate and sequence. Furthermore, laser linewidths of free-running single-longitudinal-mode distributed-feedback (DFB) lasers as narrow as 1.7 kHz have been demonstrated in rare-earth-ion-doped materials [21,22], while the typical linewidth of commercially available III-V DFB lasers ranges from 1 to 10 MHz [23,24]. Last but not least, operation of SOAs is more strongly influenced by temperature than their dielectric counterparts [16]. With increasing temperature the gain spectrum shifts significantly in wavelength. In III-V lasers, temperature shifts can result in mode hopping. With rare-earth-ion-doped dielectrics instead, temperature stabilization can often be avoided altogether.

At the Integrated Optical MicroSystems (IOMS) group of the University of Twente, where the research presented in this thesis was performed, a number of rare-earth-ion-doped dielectric materials are used to realize active devices integrated on a single chip. Figure 1.1 shows an example of an advanced on-chip optical circuit that includes DFB waveguide laser sources and high-speed erbium doped amplifiers. This thesis deals specifically with the spectroscopy of the dielectric material amorphous aluminum oxide (Al_2O_3), doped with erbium (Er^{3+}) and ytterbium (Yb^{3+}) ions. The spectroscopic study is an important aspect for the optimization of the fabrication process and generates essential input for the design of active waveguide devices for amplification and lasing.

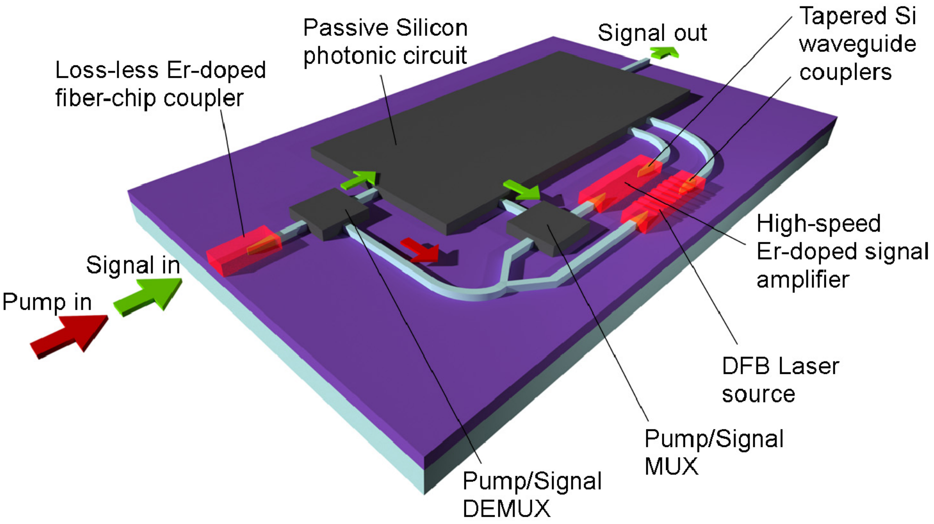

Fig. 1.1. Illustration of an advanced on-chip optical circuit with amplification of existing signal light and additional signal light generated by miniature erbium-doped distributed feedback (DFB) waveguide lasers.

1.2 Integrated Active Devices in Rare-Earth-Ion-Doped Al_2O_3

Many materials can be used as hosts for rare-earth ions, and Al_2O_3 is one of them. This material can be easily deposited on different substrates by reactive co-sputtering, thus enabling its integration with other photonic devices. As-deposited planar waveguides and dry-etched channel waveguides with losses as low as 0.1 dB/cm and 0.2 dB/cm, respectively, are reliably fabricated [14,25]. Furthermore, the refractive index of Al_2O_3 (n = 1.65 at λ = 1.55 µm) is high compared to other typical non-crystalline dielectric hosts, such as silica (n = 1.45) or phosphate glass (n = 1.55), meaning that smaller devices can be realized compared to these other glass materials. Its broad transparency spectrum and high rare-earth-ion solubility make Al_2O_3 an excellent host for active ions [26].

Among all the rare-earth-ions (whose optical properties are summarized in Chapter 2), the IOMS group has decided to focus, in the recent years, on the incorporation of erbium, ytterbium, and neodymium in Al_2O_3 for the realization of integrated active devices operating at the typical emission wavelengths of such ions. This thesis focuses on erbium and ytterbium. Er^{3+} is of particular interest because it provides emission around 1550 nm, a very important wavelength for telecommunication applications. Yb^{3+} is characterized by a strong luminescence peak around 980 nm and broadband emission at around 1020 nm. Neodymium-doped Al_2O_3 was investigated for integrated optical active applications at around 880, 1060, and 1330 nm, the latter being a standard wavelength for telecommunications as well, and this work was performed by J. Yang and reported in her PhD thesis [27].

Here are summarized the main results achieved by IOMS on erbium- and ytterbium-doped Al_2O_3 in the past few years. In erbium-doped Al_2O_3, for Er^{3+} concentrations of 1-2 × 10^{20} cm^{-3}, amplification with peak net gain of 2.0 dB/cm at λ = 1533 nm and a gain bandwidth of 80 nm (λ = 1500-1580 nm) was achieved [28], resulting in the realization of a range of on-chip integrated active devices, such as a high-speed amplifier operated at 170 GBit/s [18], a zero-loss optical power splitter [29], and a wavelength-selective ring laser operating almost across the entire telecom C-band [30]. An ultra-narrow linewidth (1.7 kHz) was achieved in DFB lasers [22], which makes them enabling elements for applications such as optical coherent communications (telecommunications) and optical clock generation, just to mention a few. In addition, an ytterbium-doped Al_2O_3 dual-wavelength DFB laser was fabricated and photonic generation of microwave signals was demonstrated [31].

1.3 Context of this Thesis

The development and optimization of the devices listed above was a multi-step process, consisting of several phases. First of all, reliable fabrication methods – film growth, developed by K. Wörhoff, and channel waveguide etching, developed by J. D. B. Bradley – had to be established. Secondly, optical waveguides and basic integrated waveguide components for bending, coupling, and splitting light on a chip were designed and tested. Afterward, the fabrication methods were applied to realize $Al_2O_3:Er^{3+}$ optical amplifiers with different Er^{3+}-doping concentrations and to investigate the maximum possible gain in $Al_2O_3:Er^{3+}$ waveguides. Only then, the integrated devices [18,29,30] based on $Al_2O_3:Er^{3+}$ could be designed and realized. This work was presented in the PhD thesis of J. D. B. Bradley [32]. The task of developing ultra-narrow linewidth DFB lasers in $Al_2O_3:Er^{3+}$ and $Al_2O_3:Yb^{3+}$ was fulfilled by E. H. Bernhardi, whose PhD research is expected to be concluded in 2012. However, the realization and optimization of such new and promising integrated active devices could not be achieved without the in-depth spectroscopic investigation of the optical properties of $Al_2O_3:Er^{3+}$ and $Al_2O_3:Yb^{3+}$, which are the subject of this thesis. A number of spectroscopic parameters, including propagation losses, absorption and emission cross-sections, lifetimes had to be determined in order to properly understand, model, and optimize the different device performances. For compact (≈ cm) on-chip devices, relatively large dopant concentrations are normally required to obtain a total gain value comparable to longer (≈ m) fiber devices. However, as the dopant concentration increases, ion-ion energy-transfer processes between the dopant ions become increasingly important. These processes may lead to increased or decreased population of particular energy levels and thus are important for the amplifier or laser performance. For this reason the development of any practical device requires a very detailed knowledge of the population dynamics within the energy levels of the rare earth ions and of the relevant ion-ion energy-transfer processes. Therefore, the dominant energy-transfer processes have been identified and analyzed. Also the spectroscopy of the upper energy levels in $Al_2O_3:Er^{3+}$ has been investigated and the mechanisms of excited-state absorption (ESA) and energy-transfer upconversion (ETU), that potentially influence the gain, have been clarified.

Some of the spectroscopic investigations presented in this thesis have a fundamental importance as well. For example, a number of models developed to understand the physical nature of energy-transfer mechanisms are put to the test in this thesis, and their limits are discussed. It is found that even the best model breaks down in the presence of a second, spectroscopically distinct class of ions, established in rare-earth-ion-doped Al_2O_3 by a fast quenching process that arises owing to, e.g., fast static ETU in ion pairs and clusters or the presence of impurities or defects within the host material and affects only a fraction of the ions. Such fast quenching process is included in a new, extended model, and we extract the fraction of quenched ions and quantify its effect on the $Al_2O_3:Er^{3+}$ and $Al_2O_3:Yb^{3+}$ device performances. With appropriate adjustments our approach can be generally applied to other rare-earth ions and optical materials as well to provide a new level of understanding of their behavior.

1.4 Outline of this Thesis

After the brief introduction of Chapter 1, in Chapter 2 a background theory of the interaction of light and matter in active media based on Einstein's treatment is presented. The main processes and parameters for optical devices in erbium- and ytterbium-doped systems, including the absorption and emission cross-sections, lifetime, energy migration and ETU are discussed.

In Chapter 3 the fabrication techniques to realize Er^{3+}- and Yb^{3+}-doped Al_2O_3 waveguides are presented. Moreover we report monolithic integration of active $Al_2O_3:Er^{3+}$ waveguides with passive silicon-on-insulator waveguides. This Chapter also describes the experimental arrangements used for the spectroscopic measurements. Optical loss, luminescence spectrum, and luminescence lifetime are investigated and discussed. The results for $Al_2O_3:Yb^{3+}$ are presented, whereas the results for $Al_2O_3:Er^{3+}$, already reported in [32], are briefly recalled.

In Chapter 4 the most important energy-transfer models found in the literature from the last sixty years are summarized and they are put to the test when applied to analyze photoluminescence decay measurements under quasi-CW excitation performed on $Al_2O_3:Er^{3+}$.

In Chapter 5 a fast quenching process induced by, e.g., active ion pairs and clusters, undesired impurities, or host material defects such as voids, that is not revealed by any particular signature in the luminescence decay curves because of negligible emission by the quenched ions under quasi-CW excitation, is verified by pump-absorption experiments. Such fast quenching process is investigated in both $Al_2O_3:Er^{3+}$ and $Al_2O_3:Yb^{3+}$, and results are compared. A new model that takes the fast quenching into account is presented and the effects of such process on $Al_2O_3:Er^{3+}$ amplifiers and on $Al_2O_3:Yb^{3+}$ DFB lasers are discussed.

In Chapter 6 the higher energy levels of $Al_2O_3:Er^{3+}$ are also investigated. A Judd-Ofelt (J-O) analysis is performed, ESA measurements are presented, and the presence of an additional ETU mechanism only marginally reported before in the literature is finally proved.

In Chapter 7 the main results and conclusions based on the work presented in this thesis are summarized.

Chapter 2

Optical Processes in Rare-Earth Ions

In this Chapter, the basic theory necessary for physical understanding of the relevant phenomena occurring in rare-earth-ion-doped materials is presented. First, in Section 2.1 a brief review of Einstein's treatment is presented, describing the interaction of light and matter in active media. The derivation follows the textbooks by Koechner [33] and Siegman [34]. Absorption, emission, and gain are discussed, and the Judd-Ofelt theory is introduced. In Section 2.2 the optical properties of rare-earth ions in solid-state hosts are addressed, together with lifetimes and energy-transfer processes between ions. To conclude, we focus on erbium and ytterbium ions in their trivalent oxidation state, and discuss the energy transitions in erbium- and ytterbium-doped Al_2O_3.

2.1 Interaction between Light and Atomic Systems in Active Media

2.1.1 Einstein Coefficients

Electrons in atomic systems such as atoms, ions and molecules can exist only in discrete energy states. A transition from one energy state to another in Einstein's treatment is associated with either the emission or absorption of a photon. The frequency v of the absorbed or emitted radiation is given by Bohr's frequency relation

$$E_1 - E_0 = h\nu\,, \tag{2.1}$$

where E_1 and E_0 are two discrete energy levels of the atomic system and h is Planck's constant.

By combining Planck's law and Boltzmann statistics, Einstein could formulate the concept of stimulated emission. When electromagnetic radiation in an isothermal enclosure, or cavity, is in thermal equilibrium at temperature T, the distribution of blackbody radiation density is given by Planck's law

$$\rho(\nu) = \frac{8\pi n^3 h\nu^3}{c^3}\frac{1}{e^{h\nu/k_B T} - 1}\,, \tag{2.2}$$

where $\rho(v)$ is the radiation density per unit frequency [J·s/cm^3], k_B is Boltzmann's constant, c is the velocity of light in vacuum and n is the refractive index of the medium. When a large collection of similar atoms is in thermal equilibrium, the relative populations of any two energy levels E_1 and E_0 (as in Fig. 2.1) are related by the Boltzmann ratio

$$\frac{N_1}{N_0} = \frac{g_1}{g_0} \exp\left[-\left(E_1 - E_0\right)/k_B T\right], \tag{2.3}$$

where N_0 and N_1 are the number of atoms per unit volume in each of the two states and g_0, g_1 are the degeneracies of level 0 and 1, respectively.

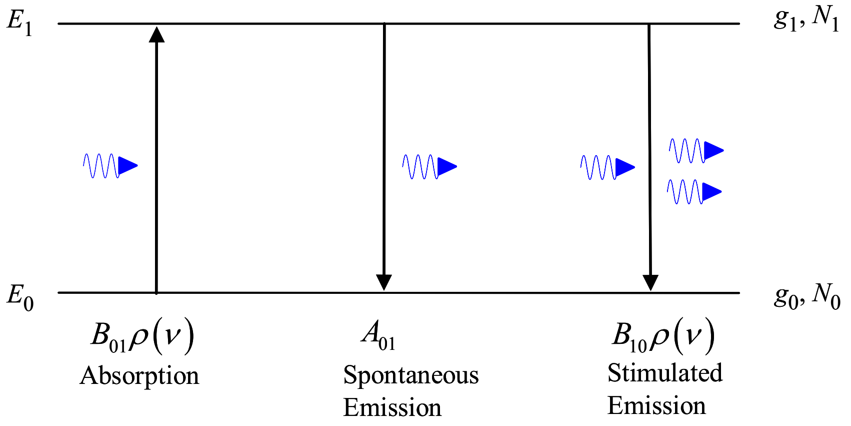

Fig. 2.1. Absorption, spontaneous emission and stimulated emission in a two-level system.

In Einstein's treatment, a phenomenological description of the interaction of light with matter is given for the absorption and emission of radiation of a two-level system, as illustrated in Fig. 2.1. We can identify three types of interaction between electromagnetic radiation and the two-level system:

Absorption. If electromagnetic radiation of frequency ν passes through an atomic system with energy gap $h\nu$, then the population of the lower level will be depleted proportional to both the radiation density $\rho(\nu)$ and the lower level population N_0,

$$\left.\frac{dN_0}{dt}\right|_{abs} = -B_{01}\rho(\nu)N_0 \, , \tag{2.4}$$

where B_{01} is a constant with dimensions cm^3/(J·s^2).

Spontaneous emission. After an atom has been excited to the upper level by absorption, the population of that level decays spontaneously to the lower level at a rate proportional to N_1,

$$\left.\frac{dN_1}{dt}\right|_{\substack{spont\\em}} = -A_{10}N_1 \, , \tag{2.5}$$

where A_{10} is a rate constant with dimensions s^{-1}. There is no phase relationship between the individual emission processes from the collection of atoms; the photons emitted are incoherent. Equation (2.5) has the solution

$$N_1(t) = N_1(0)\exp(-t/\tau_{rad}), \tag{2.6}$$

where $\tau_{rad} = A_{10}^{-1}$ is the radiative lifetime for spontaneous emission from level 1 to level 0.

Stimulated emission. Emission also takes place under stimulation by electromagnetic radiation of frequency ν and the upper level population N_1 decreases according to

$$\left.\frac{dN_1}{dt}\right|_{\substack{stim\\em}} = -B_{10}\rho(\nu)N_1, \tag{2.7}$$

where B_{10} is a constant with dimensions $cm^3/(J{\cdot}s^2)$. The phase of the stimulated emission is the same as that of the stimulating external radiation. The photon emitted to the radiation field by the stimulated emission is coherent with it. This process contributes to the amplification of the light in an active medium.

If the total number of atoms remains constant and the system is in thermal equilibrium a steady state situation arises where the transition rate from ground state to first excited state equals the transition rate from first excited state to ground state

$$B_{01}\rho(\nu)N_0 = A_{10}N_1 + B_{10}\rho(\nu)N_1. \tag{2.8}$$

Using the Boltzmann distribution for describing the N_1/N_0 ratio in thermal equilibrium, one obtains

$$\rho(\nu) = \frac{A_{10}/B_{10}}{(g_0/g_1)(B_{01}/B_{10})e^{h\nu/k_BT} - 1}, \tag{2.9}$$

and comparing this expression with the blackbody radiation law (2.2) gives the Einstein relations

$$g_0B_{01} = g_1B_{10}, \tag{2.10}$$

$$A_{10} = \frac{8\pi n^3 h\nu^3}{c^3}B_{10}. \tag{2.11}$$

2.1.2 Absorption, Emission and Gain

As monochromatic light traverses an amplifying medium of a finite length, a fraction of it may get either absorbed by the atoms of the medium, or may induce light emission by forcing atoms in the excited state to decay to a lower energy state. Consider a thin slab of the amplifying medium of thickness *dz*, illuminated by photons with intensity *I*, then the change in intensity per unit length for small signal amplification satisfies a Lambert-Beer law-like relation [34]

$$dI = g(\nu) I\left(\nu, z\right) dz \,, \tag{2.12}$$

where $g(\nu)$ is the small-signal gain coefficient (cm^{-1}), defined to contain both emission amplification and absorption losses. Here spontaneous emission is ignored.

The photons added to the signal per unit time per unit volume can be written with the help of Eqs. 2.4 and 2.7 as

$$\frac{dN_1}{dt} = \left[B_{10} g_{em}\left(\nu\right) N_1 - B_{01} g_{abs}\left(\nu\right) N_0 \right] \cdot \frac{I\left(\nu, z\right)}{c/n} \,, \tag{2.13}$$

where $g_{em}(\nu)$ and $g_{abs}(\nu)$ are the spectral line shape distributions of emission and absorption, respectively, which are used to describe the atomic transitions. The radiation density ρ in this case is expressed in terms of the light intensity as *I/(c/n)*. The net intensity increase in the thin slab is

$$dI = \frac{dN_1}{dt} \cdot h\nu \cdot dz = \left[B_{10} g_{em}\left(\nu\right) N_1 - B_{01} g_{abs}\left(\nu\right) N_0 \right] \cdot \frac{I\left(\nu, z\right)}{c/n} \cdot h\nu \cdot dz \,. \tag{2.14}$$

Equating (2.12) and (2.14) gives the relation

$$g(\nu) = \left[B_{10} g_{em}\left(\nu\right) N_1 - B_{01} g_{abs}\left(\nu\right) N_0 \right] \cdot \frac{h\nu}{c/n} \,. \tag{2.15}$$

We write the stimulated $\sigma_{em}(\nu)$ emission and $\sigma_{abs}(\nu)$ absorption cross-sections of the transition as

$$\sigma_{em}\left(\nu\right) = B_{10} g_{em}\left(\nu\right) \cdot \frac{h\nu}{c/n} \,, \tag{2.16}$$

$$\sigma_{abs}\left(\nu\right) = B_{01} g_{abs}\left(\nu\right) \cdot \frac{h\nu}{c/n} \,. \tag{2.17}$$

Therefore the small-signal gain coefficient $g(\nu)$ can be expressed in terms of the two cross-sections as

$$g(\nu) = \sigma_{em}\left(\nu\right) N_1 - \sigma_{abs}\left(\nu\right) N_0 \,. \tag{2.18}$$

Amplification of light occurs when the term containing stimulated emission overcomes the one containing absorption, resulting in a positive net gain. The gain is determined by the two cross-sections and the populations of the two levels. To design optical amplifiers and lasers, good knowledge of these parameters is required.

The absorption cross-section σ_{abs} can be derived from absorption measurements (see Chapter 3). The emission cross-section σ_{em} can be derived from the measured emission spectrum using the Füchtbauer-Ladenburg theory, which will be discussed in the following section. Finally, absorption and emission cross-section can be derived from each other using the McCumber theory, which will be discussed in Section 2.1.4.

2.1.3 Füchtbauer-Ladenburg Theory

The Füchtbauer-Ladenburg equation [35-37] relates the emission cross-section σ_{em} with the radiative lifetime τ_{rad}, and can be derived from the Einstein relation (Eq. 2.11). The Füchtbauer-Ladenburg equation can be written (either in ν- or λ-scale) as follows:

$$\frac{1}{\tau_{rad}} = \frac{8\pi n^2}{c^2} \int \nu^2 \sigma_{em}(\nu) d\nu = 8\pi n^2 c \int \frac{\sigma_{em}(\lambda)}{\lambda^4} d\lambda \,, \tag{2.19}$$

Under the assumption of a not too large emission bandwidth, the mean wavelength $\bar{\lambda}$ of the considered transition can be used instead of λ

$$\frac{1}{\tau_{rad}} = \frac{8\pi n^2 c}{\bar{\lambda}^4} \int \sigma_{em}(\lambda) d\lambda \,. \tag{2.20}$$

Using the fact that the fluorescence intensity $I(\lambda)$ is proportional to the emission cross-section (within a narrow frequency interval), Eq. 2.19 can be written in the form [38]

$$\sigma_{em}(\lambda) = \frac{\bar{\lambda}^4}{8\pi n^2 c \tau_{rad}} \frac{I(\lambda)}{\int I(\lambda) d\lambda} \,. \tag{2.21}$$

Using this equation, the emission cross-section between an upper level and a lower level can be directly calculated from the measured emission spectrum.

2.1.4 McCumber Theory

The theory of McCumber provides simple relations that uniquely relate absorption and emission cross-sections [39]. These relations are obtained in the context of narrow energy widths of the individual Stark levels, and take into account the thermal distribution of the population, which assumes that the time for the populations of the ground and excited state to reach thermal equilibrium is short compared to the radiative lifetime of the excited level [40]. Figure 2.2 schematically represents the Stark splitting, where $\sigma_{ij}(\nu)$ and $\sigma_{ji}(\nu)$ are the absorption and emission cross-section of the transition, respectively, between two individual Stark levels with energy E_{0i} and E_{1j} belonging to the lower and upper manifold, respectively.

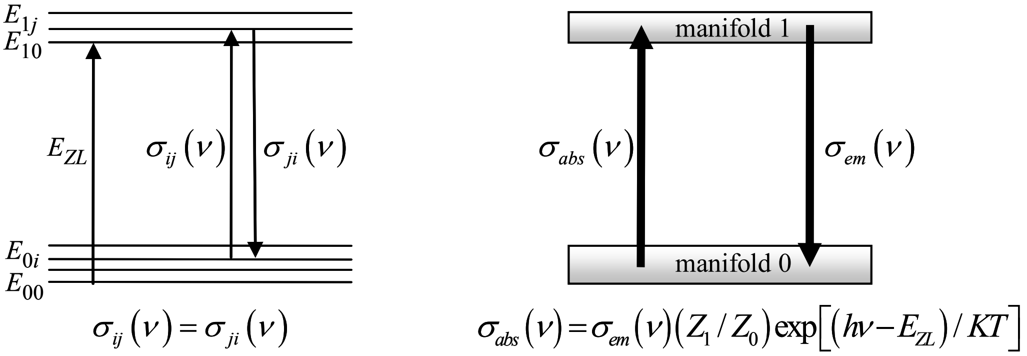

Fig. 2.2. Representation of optical transitions between two Stark manifolds in a rare-earth doped system.

By using the equality $\sigma_{ji}(\nu) = \sigma_{ij}(\nu)$, known as detailed balance or microscopic reciprocity, the McCumber equation can be derived,

$$\sigma_{abs}(\nu) = \sigma_{em}(\nu)\frac{Z_1}{Z_0}\exp\left(\frac{h\nu - E_{ZL}}{k_{\mathrm{B}}T}\right), \tag{2.22}$$

$$\sigma_{abs}(\lambda) = \sigma_{em}(\lambda)\frac{Z_1}{Z_0}\exp\left[hc\left(\frac{1}{\lambda}-\frac{1}{\lambda_{ZL}}\right)/k_{\mathrm{B}}T\right], \tag{2.23}$$

where Z_0 and Z_1 are the energy-partition functions based on the Stark splitting and thermal distribution of the population of the ground and excited states,

$$Z_0 = \sum_i \exp\left[-\left(E_{0i} - E_{00}\right)/k_{\mathrm{B}}T\right], \tag{2.24}$$

$$Z_1 = \sum_j \exp\left[-\left(E_{1j} - E_{10}\right)/k_{\mathrm{B}}T\right]. \tag{2.25}$$

The wavelength λ_{ZL} corresponds to the peak absorption wavelength and is related to the transition energy between the two lowest Stark levels, which is referred to as the zero-phonon-line energy

$$E_{ZL} = E_{10} - E_{00} = hc/\lambda_{ZL}. \tag{2.26}$$

If the Stark levels and the zero-line energy are known, the emission cross-section can be determined from the measured absorption cross-section, or vice versa.

2.1.5 Judd-Ofelt Theory

The Judd-Ofelt theory [41,42], based on the absorption spectrum of a rare-earth-ion-doped material, is a successful model for the calculation and characterization of the optical transitions occurring in the rare-earth-ion-doped material itself.

In the Judd-Ofelt theory, the electric dipole line strength S_{calc} [cm^2] of the transition between the initial state J characterized by the quantum numbers (S, L, J) (explained in Sect. 2.2.1) and the final state J' given by the quantum numbers (S', L', J') can be written as [35]

$$S_{calc}(J \to J') = \sum_{\tilde{t}=2,4,6} \Omega_{\tilde{t}} \left| \left\langle (S,L)J \left\| U^{(\tilde{t})} \right\| (S',L')J' \right\rangle \right|^2 = \Omega_2 \left[U^{(2)} \right]^2 + \Omega_4 \left[U^{(4)} \right]^2 + \Omega_6 \left[U^{(6)} \right]^2 , \tag{2.27}$$

where $\Omega_{\tilde{t}}$ ($\tilde{t} = 2, 4, 6$) [cm^2] are the Judd-Ofelt parameters, characteristic of the ion-host interaction, and $U^{(\tilde{t})}$ ($\tilde{t} = 2, 4, 6$) are the doubly reduced matrix elements which depend only on the rare-earth ion because they are calculated with eigenfunctions of the free ion. Since they are independent of the host, the values can be obtained from the literature [43,44]. In the standard Judd-Ofelt technique, the three Judd-Ofelt parameters Ω_2, Ω_4 and Ω_6 are determined by measuring the absorption line strengths for a number of ground-state transitions.

The measured line strength S_{meas} [cm^2] of the chosen bands can be determined using the following expression:

$$S_{meas}(J \to J') = \frac{3ch(2J+1)}{8\pi^3 \bar{\lambda} e^2} \left[\frac{9n}{\left(n^2+2\right)^2} \right] \int_{manifold} \sigma_{abs}(\lambda) \mathrm{d}\lambda , \tag{2.28}$$

where e is the elementary charge, J is the angular momentum of the initial state, and n is the wavelength-dependent refractive index which is determined from Sellmeier's dispersion equation.

A least-squares fit of S_{meas} to S_{calc} is used to obtain the values of the three Judd-Ofelt parameters $\Omega_{\tilde{t}}$ ($\tilde{t} = 2, 4, 6$), which can now be applied to Eq. (2.27) to calculate the line strengths corresponding to the transition from the upper manifold states to their corresponding lower-lying manifold states. With these line strengths, we can calculate the radiative decay-rate constants $A(J \to J')$ of electric dipole transitions between an excited state J and lower-lying manifolds J', the total radiative decay-rate constant A and radiative lifetime τ_{rad} of each excited state J and the radiative branching ratios $\beta(J \to J')$,

$$A(J \to J') = \frac{64\pi^4 e^2}{3h(2J+1)\lambda^3} \frac{n\left(n^2+2\right)^2}{9} S_{calc}(J \to J') , \tag{2.29}$$

$$\frac{1}{\tau_{rad}(J)} = A(J) = \sum_{J'} A(J \to J') , \tag{2.30}$$

$$\beta(J \rightarrow J') = \frac{A(J \rightarrow J')}{\sum_{J'} A(J \rightarrow J')} = A(J \rightarrow J')\tau_{rad} \, . \qquad (2.31)$$

In Chapter 6, the Judd-Ofelt theory will be applied to study $Al_2O_3:Er^{3+}$.

2.2 Optical Properties of the Rare-Earth Ions

2.2.1 Electronic Structure

The rare-earth ions of interest are the lanthanides, a group of fourteen elements from atomic number 57 (lanthanum) to 71 (lutetium), placed in the sixth period of the periodic table and characterized by filling of the $4f$ shell. The neutral atoms have a ground state configuration of a xenon core ($1s^2$ $2s^2 2p^6$ $3s^2 3p^6 3d^{10}$ $4s^2 4p^6 4d^{10}$ $5s^2 5p^6$) with two outer electrons ($6s^2$) and a number of $4f$ electrons.[a] Their most common oxidation state is +3, having lost their $6s$ electrons and one electron from the $4f$ shell,[b] leaving the ions La^{3+} through Lu^{3+} with electronic configuration of the form [Xe] $4f^N$, with N varying from 0 to 14.

The optical properties of the rare-earth ions in the visible and near-infrared spectral region are determined by the $4f$ electrons, which are well shielded from the environment by the outer $5s$ and $5p$ electrons. As a consequence, the interaction between the $4f$ electrons and the surrounding medium is very weak, both with the crystal field of the host and with the lattice phonons. This results in a narrow spread of the Stark-level structure (compared to transition-metal ions, for example, which involve $3d$ electrons that are only shielded by two outer $4s$ electrons), spectra that do not present large variations from host to host, and low non-radiative decay rates of the excited states.

The energy levels for a given electronic configuration can be determined and labeled using the quantum numbers L, S and J, where L is the total orbital angular momentum, S is the total spin and J is the total angular momentum. In the Russell-Saunders coupling scheme the values of L and S are obtained by combining, respectively, the l and s values of all electrons, and J is calculated as L+S. The different J states have separations usually on the order of 10^3 cm^{-1}. Only the electrons in the $4f$ shell contribute to the calculation, as all the other shells are filled, hence their L and S values are zero in this case. This also means that all optical transitions take place within the $4f$ shell, but in principle they are forbidden due to the parity selection rule of the electric dipole transitions. Nevertheless these transitions, although characterized by low probabilities, are observed due to mixing of the $4f^N$ states with empty higher-lying states of opposite parity $4f^{N-1}5d$ induced by the crystal field [45]. These transitions are called "weakly allowed". Whereas typical upper-state decay times are on the order of a few nanoseconds in the case of allowed transitions for spontaneous emission, weakly allowed transitions can have upper-state decay times typically between microseconds and milliseconds. Such long-lived levels are called metastable states. The crystal field, besides causing the parity mixing, also causes a splitting of the energy levels due to the Stark effect, typically on the order of 10^2 cm^{-1}.

---

[a] Lanthanum, cerium, gadolinium and lutetium have a $5d$ electron in place of a $4f$ electron.

[b] Lanthanum, cerium, gadolinium and lutetium lose the $5d$ electron instead of the $4f$ electron .

By convention the energy levels are labeled using the Russell-Saunders notation ($^{2S+1}L_J$). Here $2S+1$ is the spin multiplicity, i.e. the possible orientations of the spin S and the maximum number of different possible states of J for a given (L, S) combination.

2.2.2 Lifetime

The luminescence lifetime of a given energy level is the time constant describing the decay of ions from that level, which is exponential in the absence of energy-transfer processes. It is also defined as the time needed for an ensemble of ions excited in a certain energy level to decrease to the fraction 1/e ≈ 0.37 of its original number. It is inversely proportional to the probability per unit time of the decay of an ion from that level, and the inverse of the luminescent lifetime can be written as a sum of inverse lifetimes which characterize the different decay paths. These can be divided into radiative and non-radiative decay. Radiative decay results in the spontaneous emission of a photon, while in non-radiative decay the energy is transferred to phonons, i.e., vibrations of the host material. The following equation relates the various contributions to the luminescence lifetime:

$$\frac{1}{\tau(J)} = A(J) + A_{non-rad}(J \rightarrow J-1), \tag{2.32}$$

where τ is the luminescence lifetime of level J and $A_{non\text{-}rad}$ is the decay-rate constant of multiphonon relaxation from level J to level J–1, related to the energy gap ΔE between one energy level and the next lower level by the equation [45,46]

$$A_{non-rad} = C\left[n(T)+1\right]^{p} \mathrm{e}^{-\alpha\Delta E}, \tag{2.33}$$

where C and α are host-dependent parameters, p is the number of phonons necessary to bridge the energy gap, and $n(T)$ is the Bose-Einstein occupation number for the effective phonon mode at the temperature T

$$n(T) = \frac{1}{\exp\left(h\tilde{\nu}c / k_{\mathrm{B}}T\right)-1}. \tag{2.34}$$

$h\tilde{\nu}c$ is the phonon energy described in wavenumbers $\tilde{\nu}$, which is usually on the order of 10^3 cm^{-1} in glass materials. Given $p = \Delta E/(h\tilde{\nu}c)$, Eq. (2.33) can be rewritten as

$$A_{non-rad} = C\exp\left[\left(\frac{\ln\left(n(T)+1\right)}{h\tilde{\nu}c} - \alpha\right)\Delta E\right]. \tag{2.35}$$

Since $\ln\left(n(T)+1\right)/\left(h\tilde{\nu}c\right)$ (≈10^{-5} cm) << α (≈10^{-3} cm) [45], we finally obtain

$$A_{non-rad} = C\,e^{-\alpha\Delta E} . \qquad (2.36)$$

2.2.3 Energy Transfer Between Ions

Transitions between energy levels due to absorption, spontaneous and stimulated emission, and non-radiative decay, which were described above, are single-ion processes. As the dopant concentration increases and the ions get spatially closer one to another, energy-transfer processes between neighboring ions may occur. These processes are believed to occur mainly due to an electric dipole-dipole interaction and are thus proportional to R^{-6}, where R is the distance between two ions. Moreover, they can be either resonant or non-resonant (involving the creation or destruction of phonons). Two types of energy-transfer processes are considered in this thesis, which are depicted in Fig. 2.3:

Energy migration. The energy is transferred from an excited ion (donor) to a neighboring ion initially in its ground state. The first ion relaxes to the ground state and the second is excited. This is called a donor-donor transfer, because the newly excited ion can act as a donor ion for a subsequent energy-transfer process. This process can eventually result in loss of excitation through energy dissipation at an impurity (such as an OH^- group). Moreover, it can enhance the probability of occurrence of the following process:

Energy-transfer upconversion (ETU). The energy is transferred from an excited ion (donor) to a neighboring ion which is also excited. The first ion relaxes to the ground state and the second is excited to an even higher state. This is called donor-acceptor transfer.

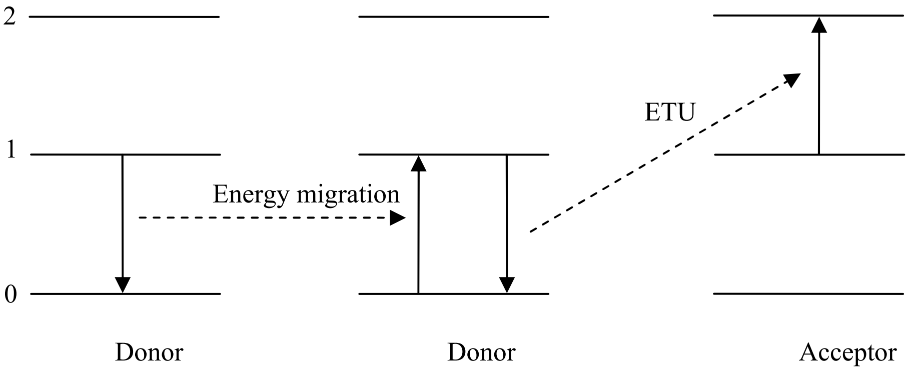

Fig. 2.3. Schematic of energy migration and ETU between individual ions in a simple three-level system.

2.2.4 The Er^{3+} System

Er^{3+} has an electronic configuration [Xe] $4f^{11}$ which is split by electronic and spin-orbit interactions into a number of multiplet energy levels. Figure 2.4 shows a schematic representation of the lower-lying energy levels of Er^{3+}, starting from the $^4I_{15/2}$ ground state and continuing up to the $^4F_{3/2}$ level. Only those levels relevant for the work described in this thesis are shown in the figure, however additional higher energy levels of the 4*f* shell exist. Also displayed in the figure are the luminescence lifetimes (either directly measured or estimated, see the next Chapters), the wavelength corresponding to the ground-state transition and the approximate energy in cm^{-1} relative to the ground state for each level. The Stark splitting of the multiplets is not represented in Fig. 2.4 for simplicity. It appears that Er^{3+} is a quite complicated system, with numerous energy levels within its 4*f* subshell and ground-state absorption (GSA), excited-state absorption (ESA), as well as various radiative and non-radiative relaxation processes occurring among them. The specific energy-level structure of Er^{3+} with several almost equidistant crystal-field manifolds gives also rise to a number of ETU and cross relaxation (CR) processes.

As an example, the processes and transitions involved in the operation of Er^{3+}-doped waveguide amplifiers designed for wavelengths around 1.53 μm (which will be considered in Chapter 5 of this thesis) are now illustrated. The amplifiers operate based on stimulated emission (SE) of ≈ 1530 nm signal light on the $^4I_{13/2} \rightarrow {}^4I_{15/2}$ transition. The metastable $^4I_{13/2}$ level has a long lifetime of several ms, as opposed to the higher-energy levels, with lifetimes ranging from a few to tens of μs due to their non-radiative decay rates of 10^4 s^{-1} or faster (derived in Chapter 6). Thus, pumping into one of the higher-energy levels yields a fast non-radiative transition to the metastable $^4I_{13/2}$ level, of which the energy gap to the ground state is too large to allow fast non-radiative relaxation. Pump light at a wavelength of 976 nm can be used, giving an efficient indirect pumping of the $^4I_{13/2}$ level via a three-level pumping scheme. This in represented in Fig. 2.4 by the ground-state absorption GSA$_2$ of pump light on the $^4I_{15/2} \rightarrow {}^4I_{11/2}$ transition, followed by rapid non-radiative decay to the $^4I_{13/2}$ level. 976 nm pump light is also absorbed by the excited-state absorption ESA$_2$ occurring from the $^4I_{11/2}$ level to the $^4F_{7/2}$ level. It is also common to pump directly into the $^4I_{13/2}$ level at a wavelength of 1480 nm, as illustrated by GSA$_1$ in the figure. SE of 976 nm and 1480 nm pump light also occurs from the $^4I_{11/2}$ and $^4I_{13/2}$ levels, respectively, but is not shown in the figure. The energy-transfer upconversion process ETU$_1$ involves energy transfer between two ions in the $^4I_{13/2}$ level resulting in de-excitation of one ion to the ground state and promotion of the other to the $^4I_{9/2}$ state. This process decreases the number of ions in the $^4I_{13/2}$ state available for stimulated emission and can have a significant impact on the performance of Er^{3+}-doped amplifiers. More details of the relevant studies will be discussed in the following Chapters. Spontaneous emission on the $^4I_{13/2} \rightarrow {}^4I_{15/2}$ transition releases non-coherent photons in a broad spectrum around the signal wavelength. When such light is amplified in an optical amplifier, it is referred to as amplified spontaneous emission and it adds noise to the amplified signal.

The remaining processes in Fig. 2.4 (GSA$_3$, ESA$_3$, ESA$_4$, ETU$_2$, ETU$_{3a/b}$, CR$_1$, and the remaining multiphonon- and luminescence-decay transitions) will be treated in Chapter 6.

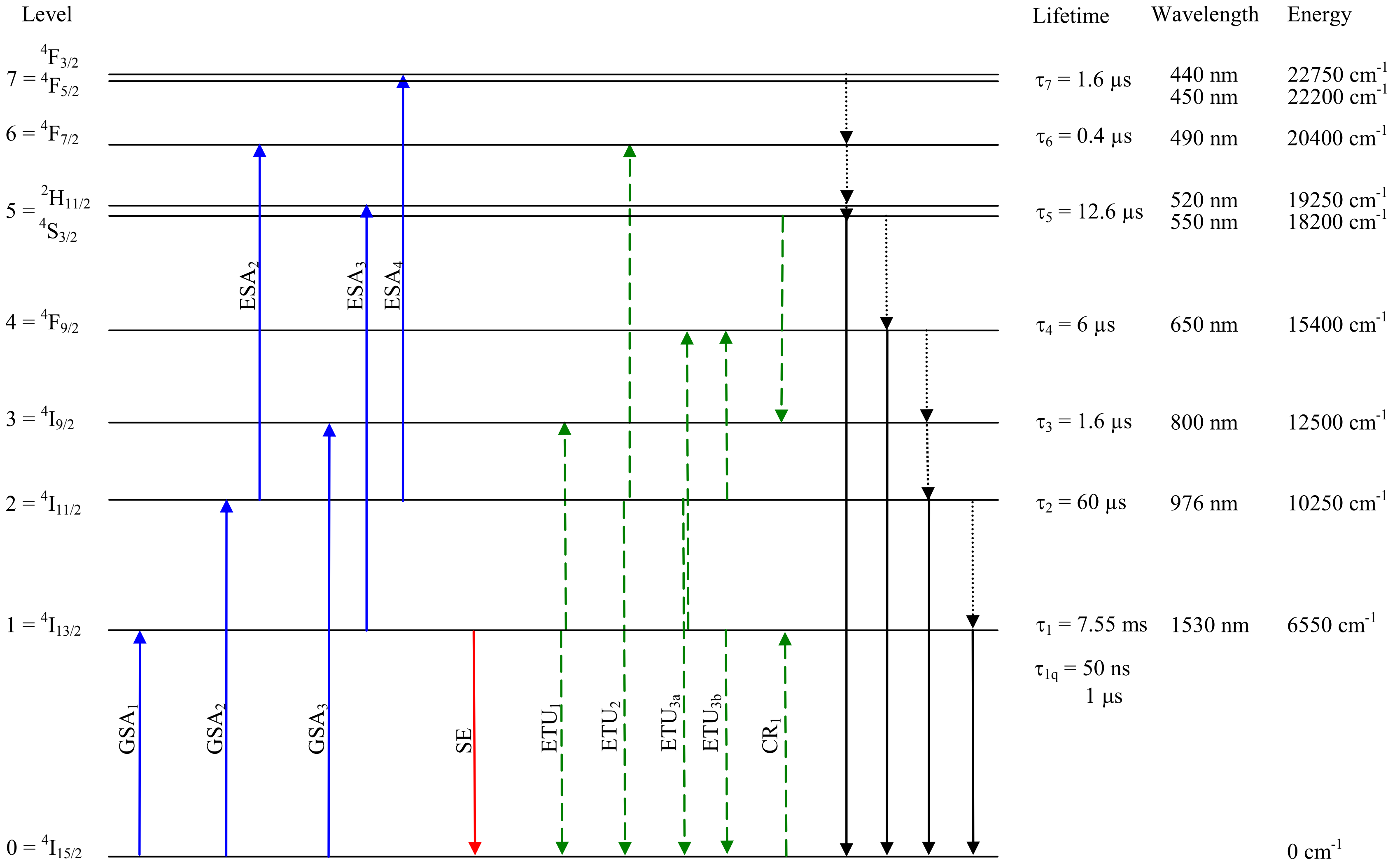

Fig. 2.4. Partial energy-level diagram of Er^{3+}, indicating the GSA, ESA, SE, ETU, CR, multiphonon-relaxation, and luminescence-decay processes relevant to this work, together with the measured or estimated luminescence lifetimes of the considered levels (see next Chapters). The SE indicated in the diagram is relative to the amplification around 1.53 µm of the Er^{3+} amplifiers considered later on in this thesis. The energy in cm^{-1} relative to the ground state and the wavelength corresponding to a photon of this energy are also indicated. Only the energies and the wavelengths of the $^4F_{7/2}$, $^4F_{5/2}$, and $^4F_{3/2}$ levels are unknown, therefore they have been taken from [47,48].

2.2.5 The Yb^{3+} System

Compared to the other rare-earth ions, Yb^{3+} has a very simple $4f$ energy-level structure. Yb^{3+} has a ground electronic configuration [Xe] $4f^{13}$, which can be considered as a "one-hole" configuration, resulting in a two-level system with the upper-energy level manifold labeled $^2F_{5/2}$ and the lower energy level labeled $^2F_{7/2}$, see Fig. 2.5. Since there are only two levels, there should not be parasitic upconversion processes. Nevertheless, a type of upconversion mechanism, namely cooperative upconversion, has been observed in a number of Yb^{3+}-doped materials [49-51]. This phenomenon corresponds to the simultaneous de-excitation of two excited ytterbium ions, so close to each other that they form a dimeric system, resulting in the emission of a single photon that contains the combined energies of both ions. However the emission probability of such process is rather low and we have not observed the typical cooperative upconversion spectrum [49] in Al_2O_3:Yb^{3+}, therefore this process will not be considered in the remainder of this work.

The energy gap between the $^2F_{5/2}$ and $^2F_{7/2}$ manifolds is approximately 10^4 cm^{-1} and the Stark splitting of the two manifolds is on the order of 10^2 cm^{-1}. The exact phonon energy of amorphous Al_2O_3 is unknown, however the highest phonon energy in crystalline Al_2O_3 (sapphire) is 870 cm^{-1} for transverse optical phonons [52] and assuming a similar energy for amorphous Al_2O_3, it follows that more than 11 phonons would be required to span the gap. Using Eq. (2.36) and the values $C = 4.09 \times 10^7$ s^{-1}, and $\alpha = 2.32 \times 10^{-3}$ cm (which will be derived in Chapter 6), this results in a non-radiative decay rate of 1.92×10^{-3} s^{-1}, which is so small that multi-phonon non-radiative decay from the excited state can be neglected. The luminescence lifetime of the excited state in Al_2O_3 was determined from lifetime measurements and resulted in 740 μs (see Chapter 5).

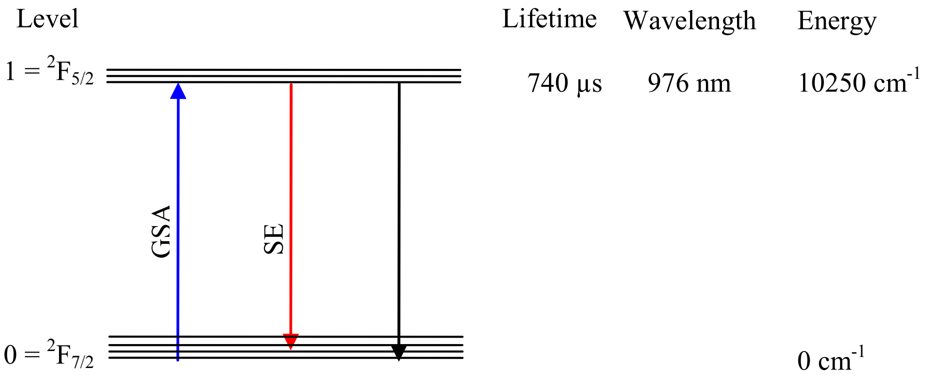

Fig. 2.5. Schematic of the energy levels of Yb^{3+} (with an indication of the Stark splitting), indicating GSA, SE, and luminescence-decay. The zero-phonon-line energy (in cm^{-1}) and the corresponding wavelength are also indicated.

In Chapter 5 of this thesis, an Yb^{3+}-doped laser designed for operation at ≈ 1020 nm is considered. Therefore, the transitions relevant to such laser are shown in Fig. 2.5. Pump light at the zero-phonon-line wavelength of 976 nm was used in order to populate the $^2F_{5/2}$ level. The first transition shown in the figure is that of GSA of pump light on the

$^2F_{7/2} \rightarrow {}^2F_{5/2}$ transition. The second transition shows stimulated emission of ≈ 1020 nm signal light from the $^2F_{5/2}$ level to the high-energy part of the $^2F_{7/2}$ manifold, from where the excitation will undergo fast thermal relaxation to a lower Stark level in the same manifold. Finally the spontaneous emission process on the $^2F_{5/2} \rightarrow {}^2F_{7/2}$ transition is shown.

2.3 Summary

In this Chapter, the theoretical background of interaction between light and atomic systems in active media relevant for this thesis has been presented. The optical properties of the rare-earth ions have been presented with a focus on erbium and ytterbium. The main processes and parameters necessary for the understanding of the following Chapters, such as absorption and stimulated emission, their cross-sections, spontaneous emission and its lifetime, energy migration and ETU, have been introduced.

Chapter 3

Fabrication and Optical Characterization

Erbium- and ytterbium-doped amplifiers and lasers are of interest for a wide range of applications at the ions' specific emission wavelengths and have been intensively studied over the last decades. Erbium-doped fiber amplifiers have been crucial for the development of optical communication technology, due to the wide-band emission from the Er^{3+} $^4I_{13/2} \rightarrow {}^4I_{15/2}$ transition around 1.55 μm, where the optical fibers have a low-loss and low-dispersion window [16]. Ytterbium-doped fibers have so far been used mostly for laser applications at wavelengths around 1 μm ($^2F_{5/2} \rightarrow {}^2F_{7/2}$ transition) [53-55], although their ability to provide amplification over the very broad wavelength range from ≈ 975 to ≈ 1200 nm is expected to generate increasing interest in the near future. Apart from their broad gain bandwidth, Yb^{3+}-doped fiber amplifiers can offer high output power and excellent power conversion efficiency. Possible applications include power amplifiers, small-signal amplifiers in sensing applications and free-space laser communications [56]. In recent years significant efforts have been undertaken to develop erbium- and ytterbium-doped waveguide amplifiers and lasers to enhance or generate light at the ions' specific emission wavelengths on a robust, low-cost, miniature chip [57-63].

Amorphous aluminum oxide (Al_2O_3) is an excellent host material for the realization of rare-earth-ion-doped waveguide devices. Of particular interest are the high solubility of rare-earth-ions like erbium and ytterbium in the Al_2O_3 matrix and the relatively high refractive index of the material compared to other typical non-crystalline dielectric hosts ($n \approx 1.65$ at $\lambda = 1.55$ μm), which allows for the fabrication of compact integrated optical devices and enables the realization of small waveguide cross sections. An additional attractive feature of Al_2O_3 is the possibility of reliable and reproducible deposition (with high optical quality) on thermally oxidized silicon, which allows for active-passive integration with existing silicon-compatible waveguide technology.

In the first section of this chapter, the fabrication of $Al_2O_3{:}Er^{3+}$ and $Al_2O_3{:}Yb^{3+}$ waveguides is discussed. Planar waveguide fabrication is based on thin film deposition by reactive co-sputtering. Channel waveguides are defined by standard lithography followed by reactive ion etching (RIE). In addition active $Al_2O_3{:}Er^{3+}$ structures have been monolithically integrated with passive silicon-on-insulator waveguides and a signal enhancement at 1533 nm was measured.

In section 3.2 the characterization techniques to determine relevant optical and spectroscopic properties of $Al_2O_3{:}Er^{3+}$ and $Al_2O_3{:}Yb^{3+}$ are presented. First two different methods for the investigation of optical propagation loss in the waveguides – moving prism and top-view technique – are described and compared. In combination with photoluminescence measurements, the optical propagation loss measurements have been used to determine the $Al_2O_3:Yb^{3+}$ absorption and emission cross-sections. Finally, the experimental setup for luminescence-decay measurements, one of the key elements of this thesis, is presented.

3.1 Er^{3+}- and Yb^{3+}-doped Al_2O_3 Waveguide Fabrication

3.1.1 Film Deposition

The deposition of rare-earth-ion-doped Al_2O_3 thin films by reactive co-sputtering has been previously developed and optimized in the IOMS group [14,32]. Here we summarize the $Al_2O_3:Er^{3+}$ and $Al_2O_3:Yb^{3+}$ deposition process.

Figure 3.1 depicts the schematic layout of the AJA ATC 1500 sputtering system, which is equipped with a load-lock and three sputtering guns. The sample, which can be up to 100-mm size, is fixed in a bottom-up sputtering configuration on a substrate holder which can be rotated and heated up to a maximum temperature of 800ºC. The deposition chamber can be pumped to a background pressure of 10^{-7} mTorr by a Turbo pump. The three sputtering guns, each connected to an Argon (Ar) gas line, are designed for 2-inch sputtering targets and can be driven individually by RF or DC power supplies, having a maximum range of 500 W. Metallic sputtering targets, with purity of 5N (99.999%) for Al and 3.5 N (99.95%) for Er and Yb, were fixed into the three guns. This configuration allows for fairly accurate control of the layer composition and dopant concentration. Through an additional gas inlet oxygen (O_2) can be introduced to the chamber. The oxygen flow can be adjusted by a mass flow controller.

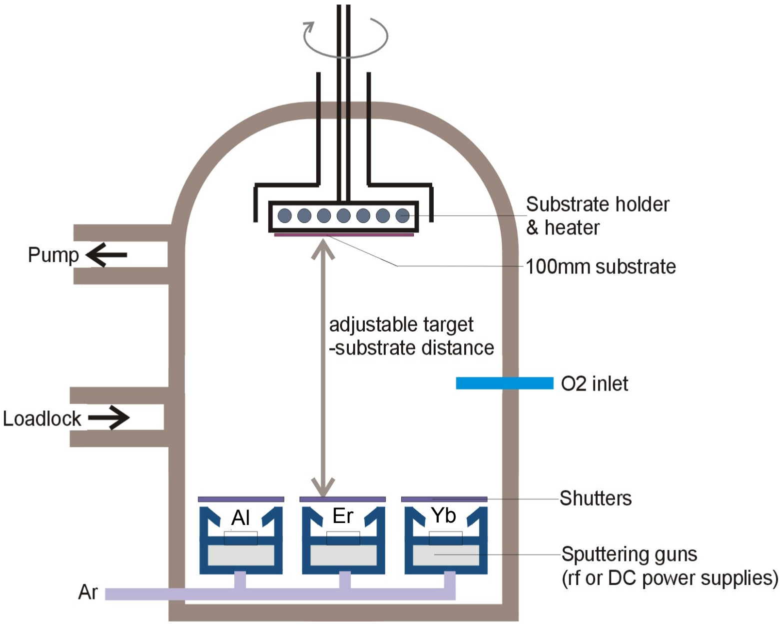

Fig. 3.1. Schematic illustration of the reactive co-sputtering system applied for the rare-earth-ion-doped Al_2O_3 film growth.

Based on the optical loss performance of as-deposited planar waveguides RF sputtering was chosen and the process parameters were optimized [14]. The substrate holder was heated at a temperature of 650ºC. The Ar gas flow was 30 sccm and 5% oxygen was added to the process in order to ensure an optimum oxidation of the grown film. The sputtering power applied to the Al target was held constant at 200 W, while the power on the rare-earth targets can be varied in order to adjust the dopant concentration. The deposition rate for the samples used in this thesis was typically 4-5 nm/min, and the deposition time was typically 3-4 hours, resulting in layer thicknesses of up to 1 µm. For all samples the deposition was carried out on 100-mm silicon substrates covered with 8-µm thick amorphous silicon dioxide (SiO_2). Low propagation losses of 0.1 dB/cm were measured in as-deposited, undoped planar waveguides.

For the deposition of the Er^{3+}- and Yb^{3+}-doped films the sputtering powers on both targets were varied between 6-25 W and 16-33 W, respectively. The dopant concentration was determined by Rutherford Backscattering Spectroscopy (RBS). For the Er^{3+}-doped films an RBS setup at the University of Utrecht was used, while the Yb^{3+}-doped layer were investigated with RBS at ETH Zurich.

Figure 3.2(a) shows the resulting Er^{3+} concentration versus sputtering power applied to the Er target. The concentration ranges from 0.27 to 4.22 × 10^{20} cm^{-3}. In Figure 3.2(b) the measured Yb^{3+} concentration versus sputtering power applied to the Yb target is given. This concentration ranges from 1.33 to 6.55 × 10^{20} cm^{-3}. The uniformity of the dopant concentration throughout the layer was measured for one sample, having an Er^{3+} concentration of 1.17 × 10^{20} cm^{-3}, and it was found to be ± 0.05 × 10^{20} cm^{-3}.

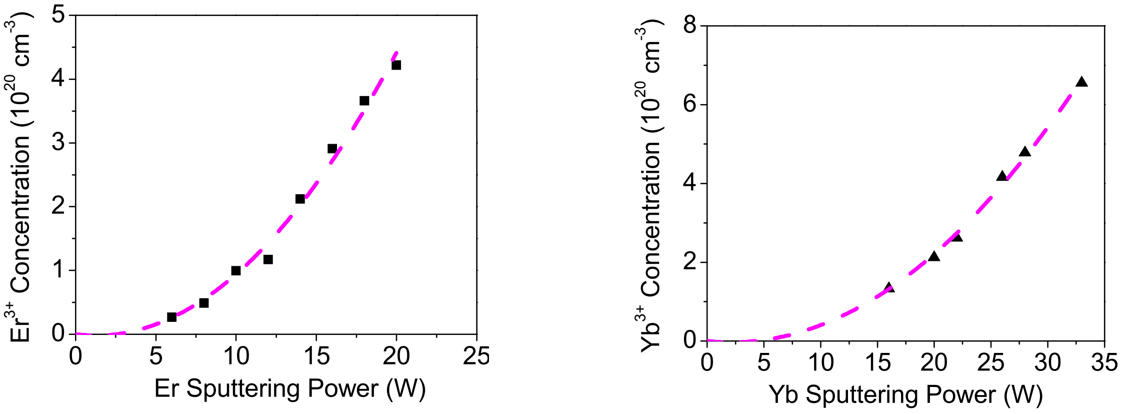

(a) (b)

Fig. 3.2. (a) Er^{3+} and (b) Yb^{3+} concentration vs. Er and Yb sputtering power, respectively. The dotted lines are qualitative parabolic fits.

3.1.2 Waveguide Structuring

The patterning of Al_2O_3 thin films has been studied in detail during previous research at IOMS applying an Oxford Plasmalab 100 inductively-coupled plasma (ICP) reactive ion etch system [25,32]. The process optimization focused on the realization of high-quality channel waveguides (i.e., low propagation loss) and aimed for enabling the use of standard resist lithography. The etch recipe optimization resulted in a BCl_3:HBr flow ratio of 5:2, an ICP power of 1750 W, RF electrode power of 25 W, a chamber pressure of 12 mTorr, and a total gas flow of 35 sccm. The etch rate for the amorphous Al_2O_3

films was 60 nm/min with a selectivity to the resist mask of 0.76. This performance allows for an etch depth up to 500 nm, while enabling a resolution (feature size) down to 1 µm. The realization of channel waveguides with smooth, steep sidewalls and low roughness was demonstrated. Low additional propagation losses (≈ 0.1 dB/cm at 1523 nm) were measured in single-mode Al_2O_3 channel waveguides [25].

A typical process flow for the fabrication of either erbium- or ytterbium-doped Al_2O_3 channel waveguides is depicted in Figure 3.3. On top of the Al_2O_3 layer deposited onto the thermally oxidized silicon substrate [Fig. 3.3(a)] a 1-µm thick resist film is spin-coated [Fig. 3.3(b)] and patterned using standard lithography [Fig. 3.3(c)]. In the next step the waveguide pattern is etched into the Al_2O_3 [Fig. 3.3(d)] followed by removal of the residual resist [Fig 3.3(e)]. A cross-sectional view of a fabricated Al_2O_3 channel waveguide is given in the SEM picture in Fig. 3.4 (a). The deposition of a SiO_2 top cladding (e.g. by a PECVD process) is optional [Fig. 3.3(f)]. An SEM cross-section of a cladded waveguide is shown in Fig. 3.4(b).

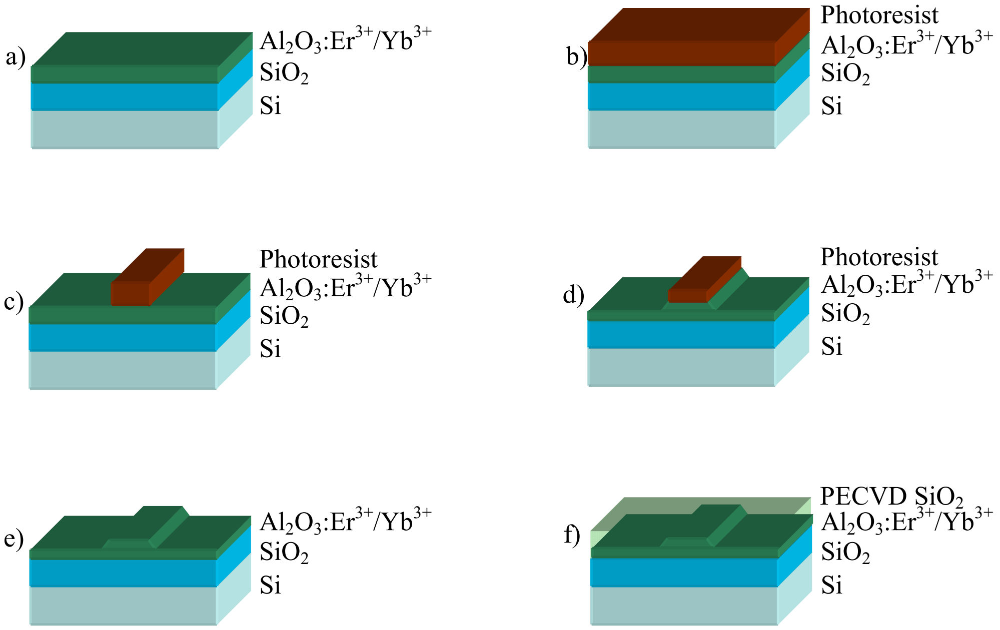

Fig. 3.3. Fabrication process of $Al_2O_3:Er^{3+}/Yb^{3+}$ channel waveguides. (a) Reactive co-sputtering of an $Al_2O_3:Er^{3+}/Yb^{3+}$ film on a thermally oxidized Si substrate; (b) spin-coating of photoresist; (c) photoresist patterning by standard lithography; (d) etching in Oxford Plasmalab ICP RIE; (e) resulting channel waveguide after removal of the photoresist; (f) after deposition of a SiO_2 PECVD top-cladding.

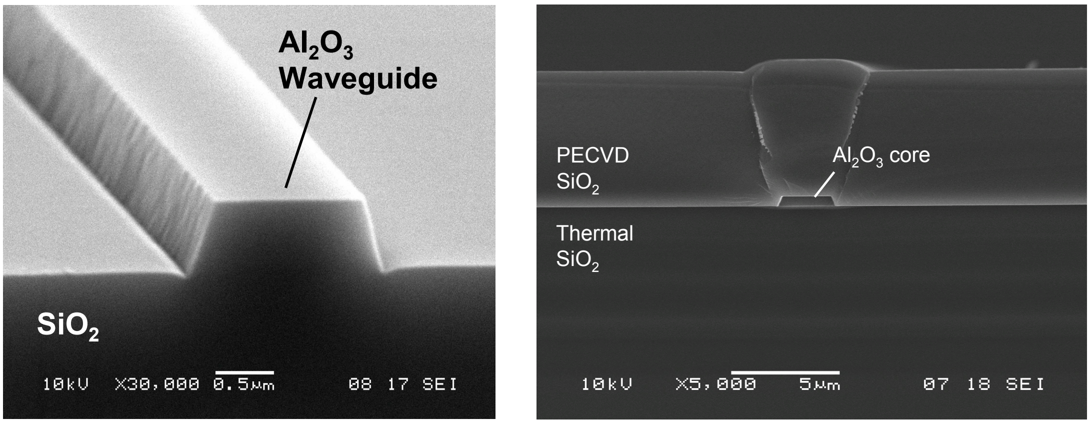

(a) (b)

Fig. 3.4. (a) SEM image of an uncladded Al_2O_3 channel waveguide and (b) SEM cross-section image of an Al_2O_3 waveguide with PECVD SiO_2 top-cladding.

3.1.3 Integration of Al_2O_3:Er^{3+} with Silicon Waveguides

Silicon is the ideal material to realize photonic integrated circuits, thanks to its high refractive index and the possibility of using the highly developed CMOS processing infrastructure for device fabrication [9]. However, efficient light emission and amplification directly from silicon remains a bottleneck. For applications in the telecommunication field, emission at 1.55 µm is desirable. In addition to the excellent propertied discussed in the introduction of this chapter, Al_2O_3:Er^{3+} shows a wide emission spectrum around 1533 nm, with 2 dB/cm peak gain at this wavelength and 80 nm gain bandwidth [28]. Therefore, in collaboration with the Photonics Research Group from Ghent University, we have integrated Al_2O_3:Er^{3+} waveguide amplifiers with SOI passive waveguides [64].

Silicon-on-insulator (SOI) rib waveguides with a cross section of 450 nm × 220 nm were defined by deep UV lithography. A 1-µm-thick Al_2O_3:Er^{3+} layer was grown directly on top by the reactive co-sputtering process described in Sect. 3.1.1 and 2.0-µm-wide ridge waveguides were defined by reactive ion etching (Sect. 3.1.2) to a depth of 270 nm. The Er^{3+} concentration was approximately 2.7×10^{20} cm^{-3}. In order to achieve highly efficient coupling the Si waveguides were horizontally tapered down to 100 nm over a length of 400 µm to adiabatically transform the silicon waveguide mode to that of the Al_2O_3:Er^{3+} waveguide. The chip was then diced to expose the end facets. A schematic of the whole structure is shown in Fig. 3.5, the process flow is illustrated in Fig. 3.6, and a SEM picture in presented in Fig. 3.7.

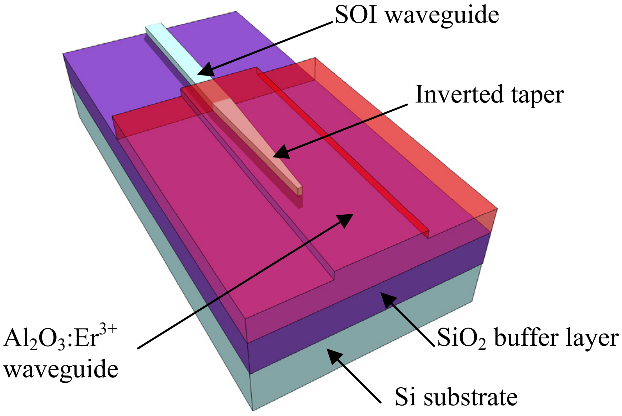

Fig. 3.5. Schematic of the adiabatically inverted taper structure for efficient light coupling.

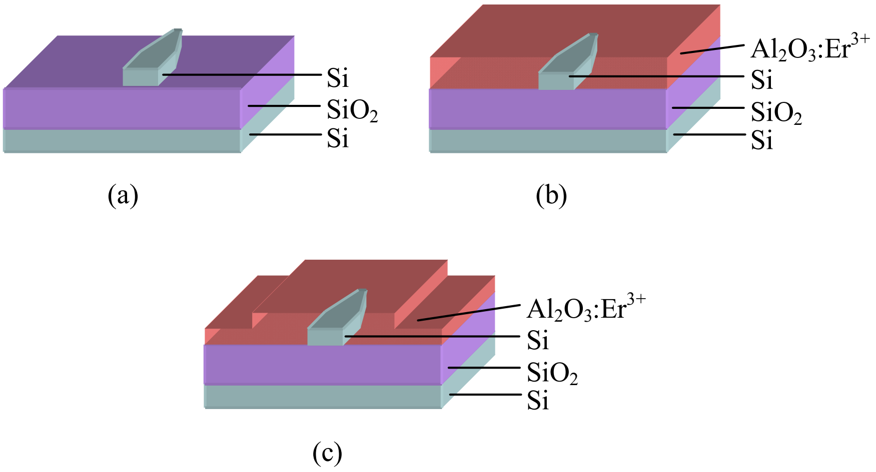

Fig. 3.6. Process flow for integration of $Al_2O_3:Er^{3+}$and Si waveguides (top view and cross-sectional view). (a) SOI waveguide; (b) deposition of the $Al_2O_3:Er^{3+}$ layer; (c) structuring of the $Al_2O_3:Er^{3+}$ layer.

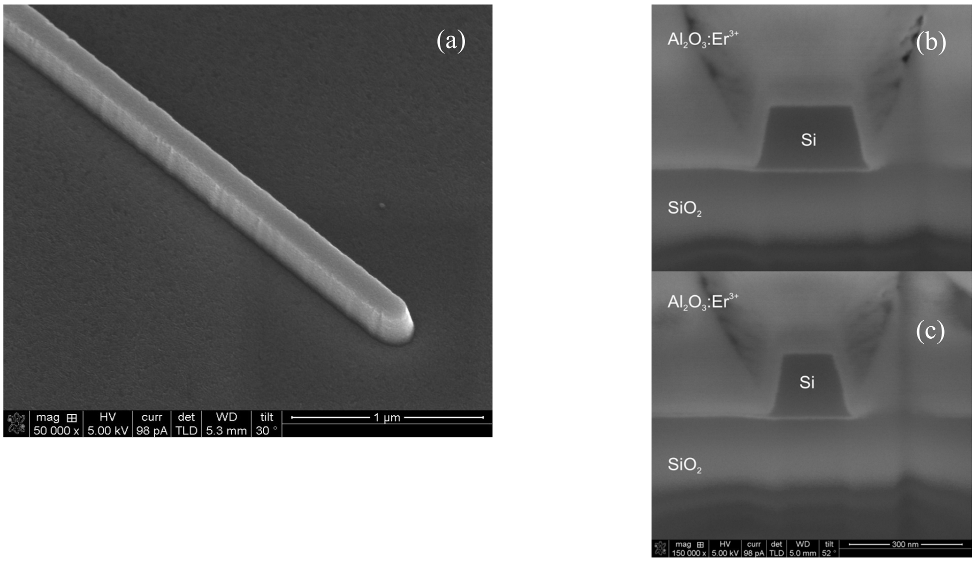

Fig. 3.7. (a) Scanning electron microscope (SEM) picture of an inversely tapered Si waveguide end before deposition of $Al_2O_3:Er^{3+}$; (b and c) SEM cross-sectional pictures of the tapered Si waveguide with decreasing horizontal size, covered by the $Al_2O_3:Er^{3+}$ overlay.

Losses in the Si-$Al_2O_3:Er^{3+}$ couplers were measured by comparing the transmission of 1533-nm light in $Al_2O_3:Er^{3+}$ waveguides both with and without Si-taper couplers, resulting in a value of 2.5 dB per coupler. Simulations indicate that this loss can be reduced to 0.5 dB.

Signal enhancement is defined as the ratio of transmitted signal light with and without the pump light and gives information about amplification at the output of an optical device. Signal enhancement measurements were performed in an $Al_2O_3:Er^{3+}$-Si-$Al_2O_3:Er^{3+}$ structure, by launching simultaneously 1480-nm pump light from a laser diode and modulated signal light from a tunable laser source operated at different wavelengths relevant for the C-band into the channel waveguides using a 1.48/1.55-µm WDM fiber coupler. The output signal light was separated from the residual pump light by a second WDM coupler and acquired by a detector and lock-in amplifier. The two $Al_2O_3:Er^{3+}$ sections had a total length of 9.5 mm, while the Si waveguide was 4 mm long, including the tapers. The signal enhancement S_{enh} was calculated from the equation

$$S_{enh} = 10\log_{10}\left[I_p / I_u\right], \tag{3.1}$$

where I_p and I_u are the transmitted signal intensities in the pumped and unpumped case, respectively. A signal enhancement > 0 indicates that the signal light at the output is amplified when the pump is switched on. In Fig. 3.8(a) the signal enhancement in the $Al_2O_3:Er^{3+}$-Si-$Al_2O_3:Er^{3+}$ structure is shown as a function of launched pump power for 1-µW signals at wavelengths of 1525 nm and 1565 nm, corresponding to the edges of the C-band, and 1533 nm, the gain peak of $Al_2O_3:Er^{3+}$. An enhancement of 7.2 dB was measured for the peak wavelength of 1533 nm at a launched pump power of 53 mW. In [64] it has been demonstrated that this performance is comparable to the results obtained with traditional $Al_2O_3:Er^{3+}$ amplifier devices, indicating that internal net gain can be achieved in these integrated structures. The signal enhancement measurement for different 1533-nm signal powers is shown in Fig. 3.8(b). The small-signal-gain regime is evident for the lower signal power values, whereas saturation effects start to show up when signals of 100 µW are launched.

To our knowledge, this is the first time that monolithic integration of rare-earth-ion-doped waveguides with SOI waveguides is achieved and signal enhancement is measured. This fundamental result will allow us to make use of potential Er-doped gain devices, e.g. high-speed amplifiers and arrays of narrow-linewidth DFB lasers, in passive Si photonic circuits for the realization of complex optical functionalities.

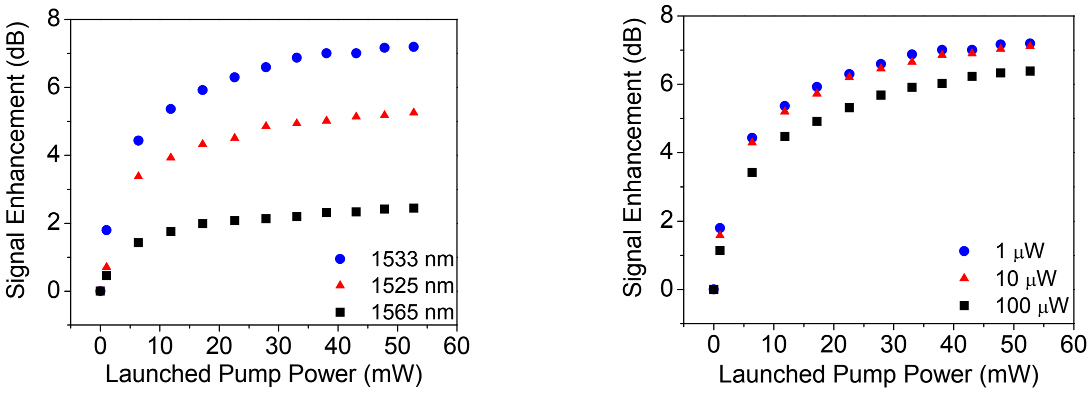

(a) (b)

Fig. 3.8. Signal enhancement in a 13.5-mm-long $Al_2O_3:Er^{3+}$-Si-$Al_2O_3:Er^{3+}$ structure as a function of launched pump power (a) for three different C-band wavelengths and (b) for varying signal input power at the peak wavelength of 1533 nm.

3.2 Measurement Techniques and Results

3.2.1 Summary of the Samples used in the Spectroscopic Investigations of this Thesis

The $Al_2O_3:Er^{3+}$ and $Al_2O_3:Yb^{3+}$ samples used in the spectroscopic investigations presented in this thesis consist of uncladded, shallow-etched waveguides with thickness of ≈ 1 µm, see Fig. 3.3(e). The width of such channels ranged from 1.5 to 4 µm; the etch depths were measured using a Dektak profilometer and resulted in 43 to 99 nm in $Al_2O_3:Er^{3+}$ and 43 to 53 nm in $Al_2O_3:Yb^{3+}$. The shallow etch depth minimized the etching-induced scattering losses and the overall design allowed for single-mode propagation at wavelengths ≥ 800 nm (which comprises the operational Er^{3+} and Yb^{3+} wavelengths relevant for this thesis), and ensured strong confinement of the propagating optical signals within the active $Al_2O_3:Er^{3+}/Yb^{3+}$ core (85-98%, depending on the wavelength).

End facets were prepared by cleaving the samples. The fabricated $Al_2O_3:Er^{3+}$ and $Al_2O_3:Yb^{3+}$ samples are summarized in Table 3.1. For $Al_2O_3:Er^{3+}$ two sets of samples were obtained, one characterized by “Length A”, used for instance for loss measurements and for the gain experiments reported in [28,32], the other characterized by a shorter “Length B” used for pump-absorption measurements which will be presented in Chapter 5. Both sets are listed in Table 3.1(a). For $Al_2O_3:Yb^{3+}$ only one set was used.

Table 3.1. Fabricated (a) $Al_2O_3:Er^{3+}$ and (b) $Al_2O_3:Yb^{3+}$ samples used in this thesis.

(a)

Er^{3+} Concentration [10^{20} cm^{-3}]	**Thickness [nm]**	**Etch Depth [nm]**	**Length A [cm]**	**Length B [cm]**
0.27	1204	82	6.4	-
0.49	1301	99	5.9	-
1.00	916	50	4.0	-
1.17	1093	69	5.4	0.9
2.12	928	53	1.8	1.0
2.91	1071	88	1.3	0.9
3.66	894	43	1.0	1.0
4.22	976	64	1.0	-

(b)

Yb^{3+} Concentration [10^{20} cm^{-3}]	**Thickness [nm]**	**Etch Depth [nm]**	**Length [cm]**
1.33	1044	53	0.5
2.12	1010	55	0.4
2.62	1010	52	0.4
4.16	1009	47	0.5
4.78	1009	45	0.4
6.55	989	43	0.4

3.2.2 Loss Measurements

In the field of integrated optics, the fabrication of low-loss waveguiding structures is of great importance for the realization of efficient integrated optical devices, either active or passive. This section focuses on the measurement methods related to optical loss characterization in waveguides.

With reference to Sect. 2.1.2, at very low excitation densities N_1 is negligible and N_0 is approximately equal to the total ion concentration N_d. Eqs. (2.12) and (2.18) can therefore be rewritten (in λ-scale) as

$$dI = -\alpha_{abs}(\lambda) I(\lambda, z)\, dz\,, \tag{3.2}$$

$$\alpha_{abs}(\lambda) = \Gamma(\lambda)\sigma_{abs}(\lambda)N_0 \approx \Gamma(\lambda)\sigma_{abs}(\lambda)N_d\,, \tag{3.3}$$

where α_{abs} is the loss due to the ion absorption (which in our case may be written as $\alpha_{Er}(\lambda)$ or $\alpha_{Yb}(\lambda)$ to describe the absorption due to Er^{3+} or Yb^{3+} ions, respectively) and $\Gamma(\lambda)$, the confinement factor of the light inside the waveguide, is also taken into account. The total loss in a waveguide α_{Total} should actually also include the background losses α_{bck}, due to the material-dependent loss and scattering due to interface roughness of the waveguide

$$\alpha_{Total}(\lambda) = \alpha_{bck}(\lambda) + \alpha_{abs}(\lambda). \tag{3.4}$$

Optical measurements are required to determine each of these contributions to the total propagation loss of optical waveguides.

In our group, optical losses of Al_2O_3:Er^{3+} waveguides samples at the fixed wavelengths of 633, 976, 1320 and 1533 nm have been investigated with a moving-prism method [65,66] on planar waveguides –obtained by keeping one half of each Al_2O_3:Er^{3+} layer unpatterened before etching – and have been reported in [28,32]. The experimental setup is depicted in Fig. 3.9. In brief, an in-coupling prism is placed above the planar waveguide, separated from it by a small air gap. Incident light is totally reflected at the base of the prism, and the waves in the prism and in the waveguide are coupled through their evanescence fields in the gap, under certain orientation conditions of the incident beam. Light is coupled out using a second prism after propagating over a distance *l* through the waveguide. The propagation distance *l* in the planar waveguide is varied by fixing the position of the in-coupling prism while moving the out-coupling prism in discrete steps, from smaller to larger distance. By a least-squares fit of a set of measured transmitted light intensities at a certain wavelength with the Lambert-Beer law which results from solving the above equations the single-wavelength loss of a planar waveguide can be determined.

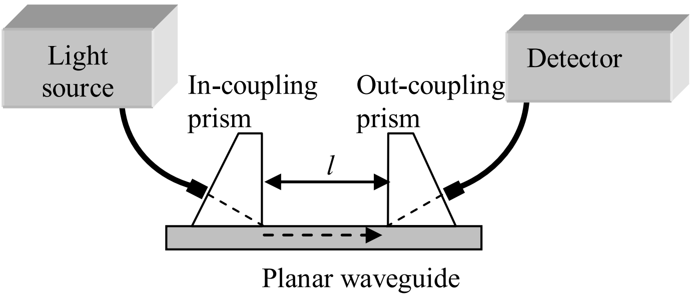

Fig. 3.9. Prism coupling setup used for propagation loss measurements in planar waveguides.

For example, the moving-prism method was applied to investigate the optical losses as a function of substrate temperature during the deposition process to study the quality of the amorphous Al_2O_3:Er^{3+} layer [14]. This work was performed during the optimization of the Al_2O_3 deposition procedure developed by K. Wörhoff. Figure 3.10 displays the optical propagation losses versus deposition temperature in an Al_2O_3 layer with an Er^{3+} concentration of $\approx 2 \times 10^{20}$ cm^{-3} at the wavelengths of 633 nm and 1320 nm, which are both outside the Er^{3+} absorption bands. While the optical losses at 1320 nm are low at all deposition temperatures, those at 633 nm decrease significantly with increasing temperature. At 650ºC deposition temperature, chosen for fabricating the eight samples investigated here, optical propagation losses of 0.3 ± 0.1 dB/cm and 0.2 ± 0.1 dB/cm were measured at 633 nm and 1320 nm, respectively. The higher the temperature during layer deposition, the higher the surface mobility of the particles that constitute the layer, which leads to fewer clusters and voids in the layer structure, hence lower losses. Further increase of the deposition temperature leads to a change in the material properties, probably due to the onset of crystallization. This investigation will be recalled in Sect. 5.1.1 of Chapter 5.

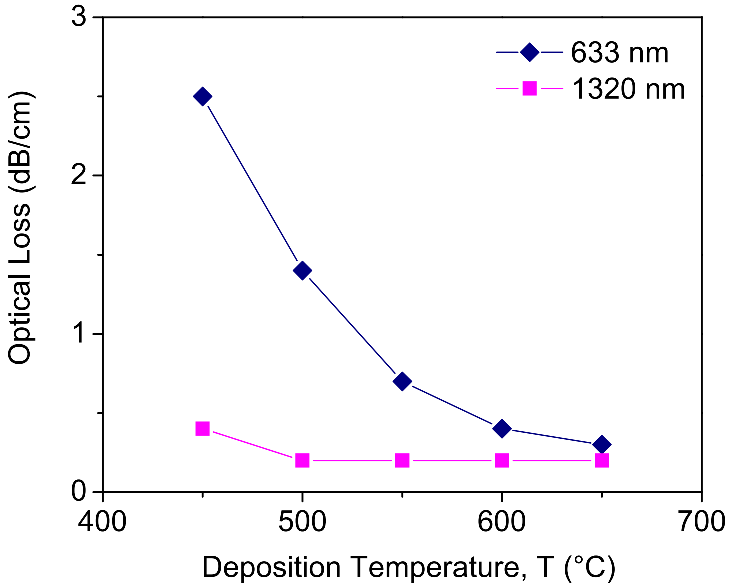

Fig. 3.10. Optical losses of $Al_2O_3:Er^{3+}$ waveguides at wavelengths of 633 nm and 1320 nm as a function of deposition temperature [14].

However, the moving-prism method can be time consuming, since the movement of the out-coupling prism and the processing of the recorded intensities is done manually. An additional challenge is to keep the in- and out-coupling efficiencies constant and reproducible at each out-coupling length since minor coupling variations largely influence the measurement accuracy.

To overcome these issues, we have implemented a top-view technique, where the drop of light intensity along the length of the waveguide is captured by a CCD camera placed on top of the waveguide. We have chosen to investigate this technique with light at the fixed wavelength of 1533 nm.

The experimental setup is depicted in Fig. 3.11. The output from a light source is coupled into a channel waveguide and the streak of light along the waveguide is recorded by a CCD camera (Moticam 2003). The advantage of this contactless method is that there is no need to move an out-coupling prism along the thin film interface, since the change in light intensity along the propagation path can be captured at once. Figure 3.12(a) shows a typical infrared picture of the streak of light (the colors are inverted in order to better highlight the streak). In this example, TE-polarized light at 1533 nm was coupled from the left-hand side into a 4-cm-long $Al_2O_3:Er^{3+}$ channel waveguide having an Er concentration of 1.00×10^{20} cm^{-3}. Scattering of light at the incoupling end-facet disturbed the image acquisition, therefore a piece of cardboard was placed on top to block it and the first cm of the light streak was discarded during image analysis. The decay of light along the propagation direction is evident. The thin vertical line at the right side is the scattering from the right-hand end-facet.

In this example, a wavelength (1533 nm) belonging to the Er^{3+} $^4I_{15/2} \rightarrow {}^4I_{13/2}$ absorption band was chosen. Therefore the excitation light coupled into the waveguide layer is not only scattered, but also absorbed while propagating through the waveguide. Besides the scattered light, also generated fluorescence light is detected; however it was assumed that such fluorescence is proportional to the light intensity distribution in the film, which is valid as long as low excitation intensities are used.

After image acquisition, an image analysis was performed to determine the loss of the waveguide, using the software Maskaligner and Curveloss [67]. In Maskaligner the waveguide is selected and the proper scaling factor is applied, whereas in Curveloss a region of interest (ROI) around the waveguide is chosen, where the analysis will be performed. After subtracting the background intensity relative to the area outside the ROI, the decrease of intensity profile in the ROI can be analyzed in order to calculate the losses, see the dots in Fig. 3.12(b). Here the solid line is the least-mean-squares fit to a decreasing exponential, the slope of which yields the power loss coefficient. In this example the propagation loss of the TE mode at 1533 nm is $\alpha_{Total} = 2.32 \pm 0.04$ dB/cm. The propagation loss measured with the prism-coupling setup was $\alpha_{Total} = 2.27 \pm 0.05$ dB/cm.

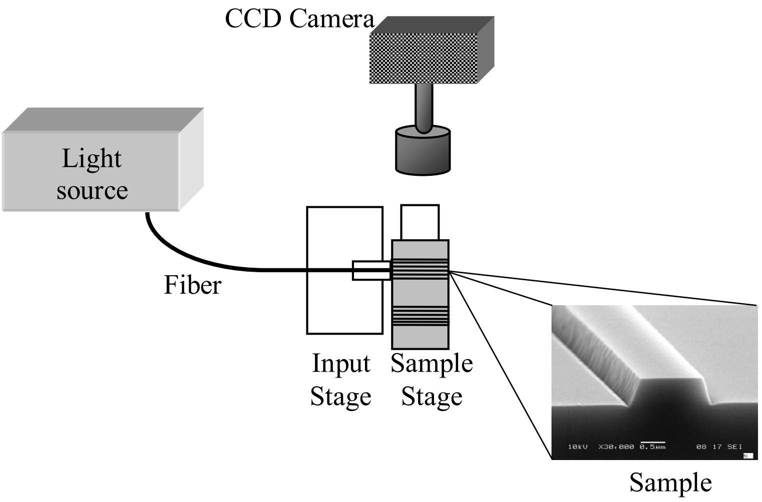

Fig. 3.11. Setup used for propagation streak-of-luminescence loss measurements in channel waveguides.

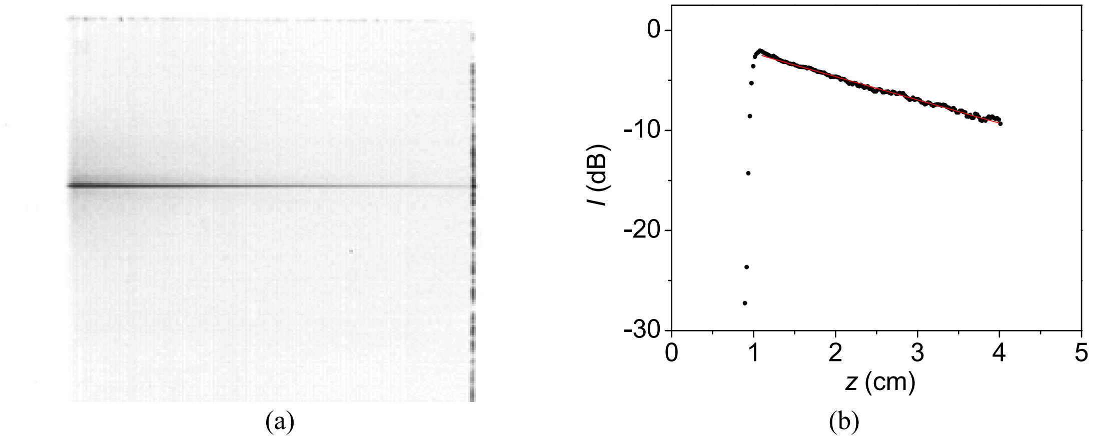

(a) (b)

Fig. 3.12. (a) Infrared picture (inverted colors) of the luminescence streak along a 4-cm-long $Al_2O_3:Er^{3+}$ waveguide with an Er concentration of 1.00×10^{20} cm^{-3}. (b) Streak-of-luminescence intensity as a function of propagation length (dots: measured points, red line: exponential fit).

In general the results agree within the experimental accuracy with the measurements performed by means of the moving-prism method on planar waveguides at 1533 nm and reported in [32]. Although the moving-prism loss measurements were performed on planar waveguides and the top-view loss measurements on channel waveguides, the two sets of measurements are comparable because the shallow etch depth (43 to 99 nm) selected for the channel waveguides investigated here ensured negligible additional scattering losses. The top-view method, once validated against the moving-prism method, is very simple and rapid; the only requirement is to have relatively long samples in order to observe a significant decrease in the scattered intensity of low-loss waveguides.

As mentioned above, the optical losses in $Al_2O_3:Er^{3+}$ have already been reported in [28,32], and the results will not be repeated here. Instead, here we report the optical losses in $Al_2O_3:Yb^{3+}$. The top-view method with a diode laser was used to measure the total propagation losses at 976 nm. They increase with Yb^{3+} concentration due to absorption at the $^2F_{7/2} \rightarrow {}^2F_{5/2}$ transition. The total propagation loss as a function of Yb^{3+} concentration is shown in Fig. 3.13.

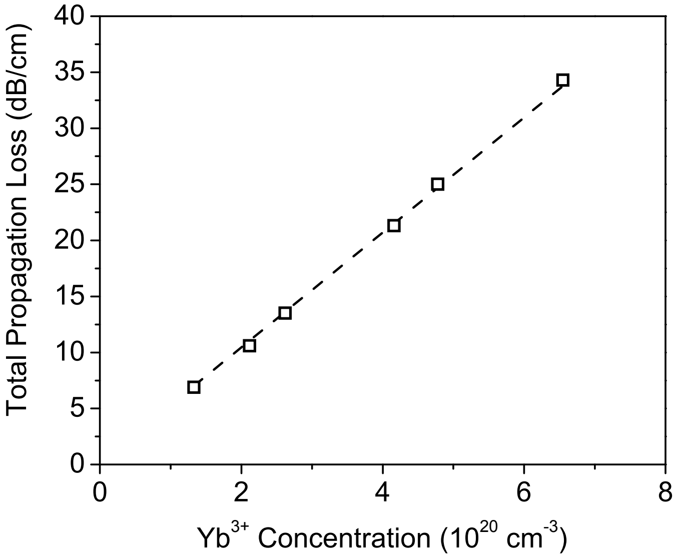

Fig. 3.13. Total propagation loss α_{Total} at 976 nm as a function of Yb^{3+} concentration. The dashed line represents the calculated propagation loss at 976 nm using the absorption cross-sections determined from this data set and the average background loss and average confinement factor in the six samples.

Using the measured total propagation losses, the wavelength-dependent Yb^{3+} ground-state-absorption (GSA) cross-section $\sigma_{GSA}(\lambda)$ in cm^2 could be calculated using the equation

$$\sigma_{GSA}(\lambda) = \frac{\alpha_{Yb}(\lambda)}{10 \cdot \log(e)\Gamma(\lambda)N_0}, \tag{3.5}$$

where $\alpha_{Yb}(\lambda)$ is the Yb^{3+} absorption coefficient in dB/cm, $\Gamma(\lambda)$ is the calculated confinement factor of the light within the active $Al_2O_3:Yb^{3+}$ channel waveguide (equal to 0.935), and N_0 is the ground-state population density in cm^{-3}. The numerical factor

10·log(e) ≈ 4.34 simply allows to convert from dB to linear scale. $\alpha_{Yb}(\lambda)$ was found by subtracting the background propagation loss, $\alpha_{bck}(\lambda)$, from the measured total propagation loss, $\alpha_{Total}(\lambda)$. For the background propagation loss at 976 nm the same values as measured in Al_2O_3:Er^{3+} (≈ 0.25 dB/cm) were used [28] and N_0 was approximated as being equal to the total dopant concentration in the layer, N_d (valid at low excitation densities). Based on the cross-sections calculated at each concentration, an average absorption cross-section of $(12.70 \pm 0.20) \times 10^{-21}$ cm^2 was determined at 976 nm.

Now that the cross-section is known, the Yb^{3+}-related absorption $\alpha_{Yb}(\lambda)$ and the total propagation losses $\alpha_{Total}(\lambda)$ can be calculated for a given waveguide geometry (with a corresponding confinement factor), Yb^{3+} concentration and background propagation loss. The line shown in Fig. 3.13 was obtained using the absorption cross-section determined above and the average confinement factor and background propagation losses of the Al_2O_3:Yb^{3+} waveguides in this investigation.

3.2.3 Photoluminescence Measurements

Photoluminescence measurements are used to investigate the luminescence properties of the active ions in a host material. Figure 3.14 illustrates the photoluminescence measurement in a channel waveguide. Photoluminescence spectra of Er^{3+} and Yb^{3+} in Al_2O_3 were investigated by exciting the active-ion-doped waveguides using a diode laser at 976 nm and a Ti:Sapphire laser at 940 nm, respectively. The luminescence light was collected from the top of the waveguides by a liquid-core fiber (3.5.mm diameter), and luminescence peaks were detected by a spectrometer (iHR550, Horiba, Jobin Yvon).

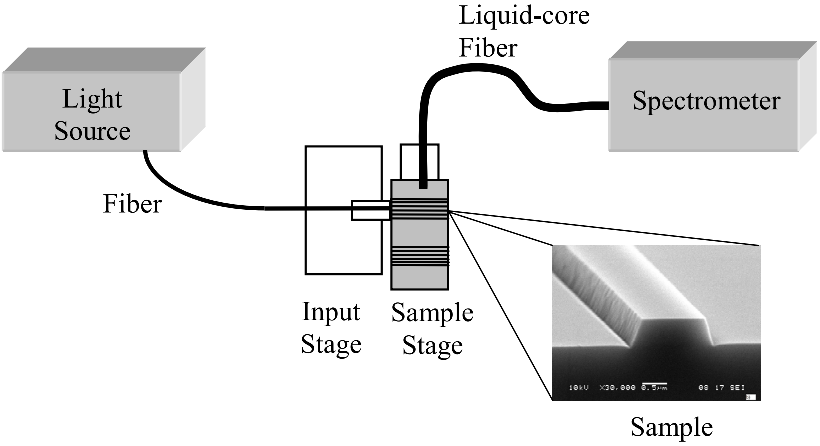

Fig. 3.14. Schematic picture of a photoluminescence measurement setup in a channel waveguide.

The photoluminescence spectra of Al_2O_3:Er^{3+} and Al_2O_3:Yb^{3+} could then be used to evaluate the absorption and emission cross-sections using a combination of McCumber and Füchtbauer-Ladenburg theories. The $^4I_{15/2} \leftrightarrow {}^4I_{13/2}$ absorption and emission cross-sections in Al_2O_3:Er^{3+} have been presented in [28], but the final results are reported here as well, see Fig. 3.15, as they will be recalled in the next Chapters.

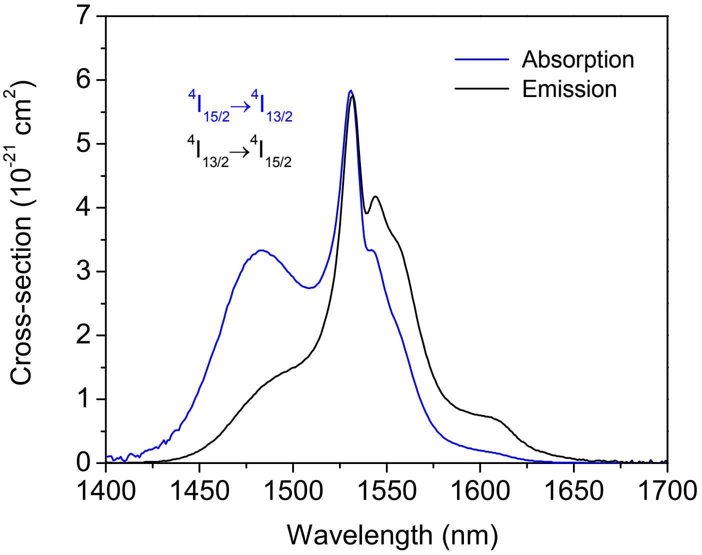

Fig. 3.15. $^4I_{15/2} \leftrightarrow ^4I_{13/2}$ absorption and emission cross-sections of $Al_2O_3:Er^{3+}$, taken from [28].

To evaluate the $Al_2O_3:Yb^{3+}$ cross-sections, a similar procedure as the one described in [32] for $Al_2O_3:Er^{3+}$ was used. The emission cross-section was determined by scaling the photoluminescence spectrum to the measured absorption cross-section value around the peak at 976 nm. This requires that the ratio Z_1/Z_0 of the energy-partition functions presented in the McCumber theory (Sect. 2.1.4) is equal to 1, which is valid in Yb^{3+}-doped glasses within a few percent [56]. Afterward the absorption cross-section spectrum between 850-1100 nm was calculated with the McCumber theory and Eq. (2.23).

The obtained absorption and emission cross-sections are displayed in Fig. 3.16. They are similar to those reported previously in $Al_2O_3:Yb^{3+}$ waveguides fabricated with a different technique [68], in terms of shape and peak cross-section values.

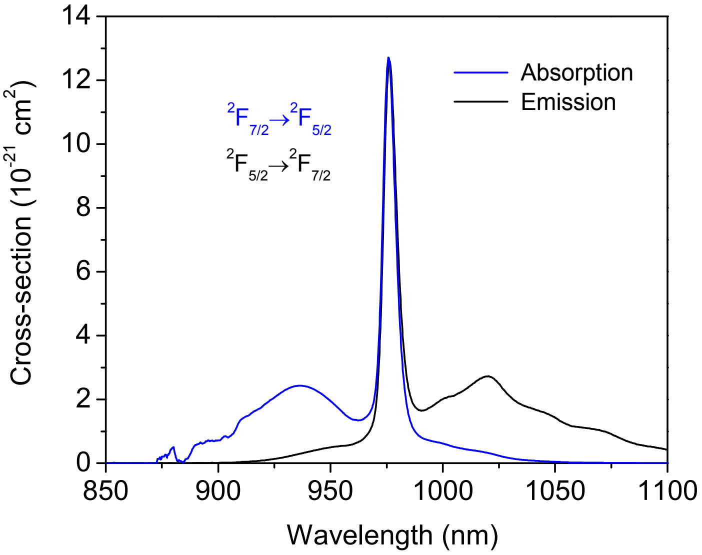

Fig. 3.16. $^2F_{7/2} \leftrightarrow ^2F_{5/2}$ absorption and emission cross-sections of $Al_2O_3:Yb^{3+}$.

3.2.4 Luminescence-Decay Measurements

The experimental setup applied for the decay measurements under quasi-CW excitation from the Er^{3+} $^4I_{13/2}$, $^4I_{11/2}$, and $^4S_{3/2}$ levels and from the Yb^{3+} $^2F_{5/2}$ level is shown in Fig. 3.17. For the luminescence-decay measurements the channel waveguides are excited with pump light from diode lasers (for measurements from the Er^{3+} $^4I_{13/2}$ and $^4S_{3/2}$ levels and from the Yb^{3+} $^2F_{5/2}$ level) and a Ti:Sapphire (for measurements from the Er^{3+} $^4I_{11/2}$ level), the diode lasers modulated by an external square-pulse generator and the Ti:Sapphire by a chopper, both with 50% duty cycle and a cutoff time varying between 6 μs and less than 1 μs (depending on the repetition rate). The chopper and external square-pulse generator were set at a repetition rate which in all the measurements allowed firstly, the population densities of all the excited states relevant for the luminescence analysis to reach a steady-state regime before the pump was switched off (at $t = 0$) and, secondly, the excitation in these states to relax completely before the pump was switched on again. The modulated pump light was coupled into the waveguides with an optical fiber and the luminescence was collected with a high-numerical-aperture liquid-core fiber mounted normal to the sample surface. The fiber was placed at the beginning of the waveguides where the pump absorption and, accordingly, the excitation is the highest in order to diminish the influence of lifetime elongation owing to reabsorption of luminescence by ions remaining in the ground state. The luminescence was discriminated by a 125-mm monochromator and detected by an InGaAs photodiode (for luminescence at 1480, 976, and 1025 nm from the Er^{3+} $^4I_{13/2}$ and $^4I_{11/2}$ levels, and from the Yb^{3+} $^2F_{5/2}$ level, respectively) or a photomultiplier (for luminescence at 550 nm from the Er^{3+} $^4S_{3/2}$ level). The resulting signal was amplified, acquired with a digital oscilloscope and averaged over 4096 shots.

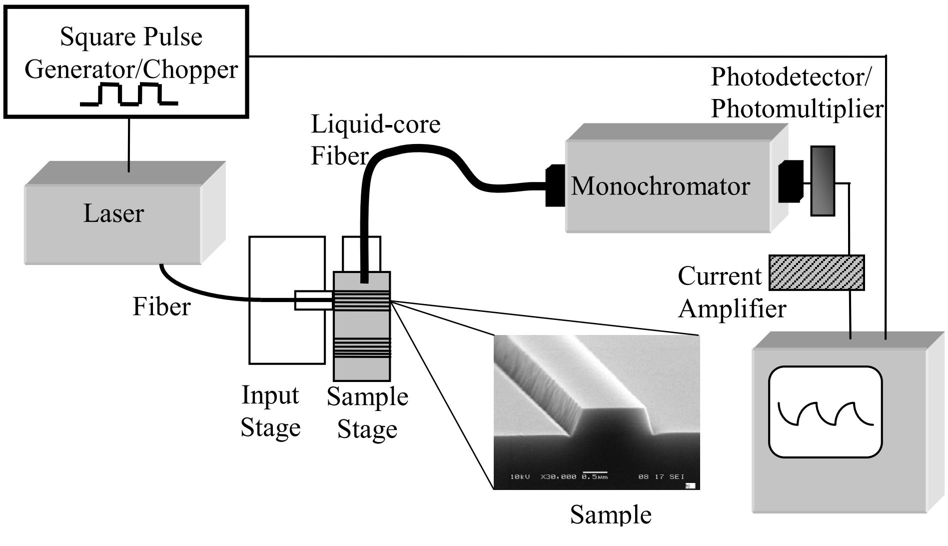

Fig. 3.17. Schematic of a setup for measuring the luminescence lifetime in channel waveguides.

The Er^{3+} $^4I_{13/2}$ level was directly excited at a wavelength of 1480 nm, at a repetition rate of 13 Hz. The luminescence decay on the Er^{3+} $^4I_{13/2} \rightarrow {}^4I_{15/2}$ transition at 1533 nm was measured.

Luminescence-decay measurements from the Er^{3+} $^4I_{11/2}$ level were performed by pumping into the $^4I_{9/2}$ level at a wavelength of 800 nm, with a repetition rate of 17 Hz. With reference to Fig. 2.4, the excitation rapidly decays via multiphonon relaxation to the $^4I_{11/2}$ level, from which luminescence on the $^4I_{11/2} \rightarrow {}^4I_{15/2}$ transition at 976 nm is observed. Pumping at 800 nm instead of directly into the $^4I_{11/2}$ level allows one to better discriminate the luminescence signal from residual pump light.

Luminescence-decay measurements from the Er^{3+} $^4S_{3/2}$ level were performed by pumping into the $^4I_{11/2}$ level at a wavelength of 976 nm, with a repetition rate of ≈ 3 kHz. The ESA_2 and ETU_2 processes shown in Fig. 2.4 populate the $^4F_{7/2}$ level, the excited ions rapidly decay via multiphonon relaxation to the $^4S_{3/2}$ level, from which luminescence on the $^4S_{3/2} \rightarrow {}^4I_{15/2}$ transition at 550 nm is observed.

The Yb^{3+} $^2F_{5/2}$ level was pumped with 976 nm wavelength, at a repetition rate of 77 Hz. For Yb^{3+} the $^2F_{5/2} \rightarrow {}^2F_{7/2}$ luminescence decay at 1025 nm was measured.

A complete discussion concerning luminescence decay in $Al_2O_3:Er^{3+}$ and $Al_2O_3:Yb^{3+}$ will follow in Chapters 4, 5, and 6. In Fig. 3.18 we just show, as an example, a typical luminescence decay curve of Yb^{3+} measured in an $Al_2O_3:Yb^{3+}$ sample with an Yb^{3+} concentration of 1.33×10^{20} cm^{-3}, yielding a lifetime of 708 ± 18 μs (the R^2 of the exponential fit is 0.9996, close to the ideal value of 1).

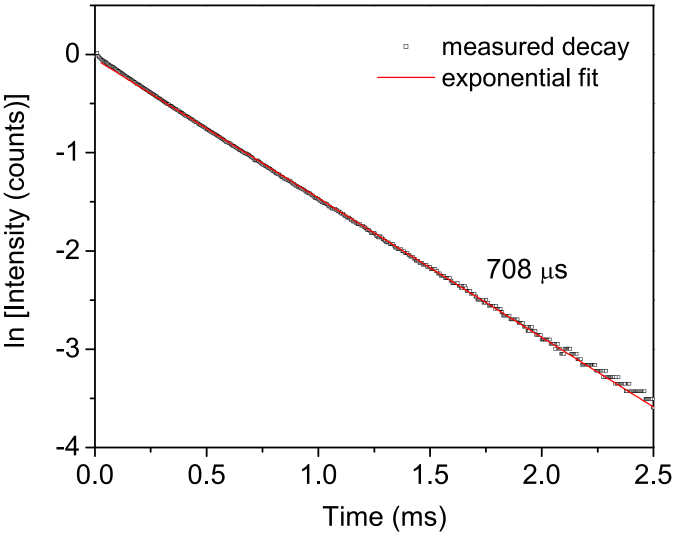

Figure 3.18. Normalized luminescence decay of Yb^{3+} measured at 1025 nm in $Al_2O_3:Yb^{3+}$ with an Yb^{3+} concentration of 1.33×10^{20} cm^{-3}, yielding a lifetime of 708 ± 18 μs ($R^2 = 0.9996$).

3.3 Summary

Er^{3+}- and Yb^{3+}-doped planar and channel waveguides have been fabricated in Al_2O_3. Thin films have been deposited on thermally oxidized silicon wafers by reactive co-sputtering and channel waveguides have been patterned by RIE. In addition, monolithic integration of active $Al_2O_3:Er^{3+}$ structures with passive silicon-on-insulator waveguides has been demonstrated.

An overview has been given on the experimental setups that have been used to determine relevant optical and spectroscopic properties of $Al_2O_3:Er^{3+}$ and $Al_2O_3:Yb^{3+}$. Losses in $Al_2O_3:Yb^{3+}$ have been investigated, and the absorption and emission cross-sections of this material have been determined.

Chapter 4

Energy-Transfer Upconversion

Energy-transfer upconversion (ETU), often assisted by energy migration (both described in Chapter 2), has a significant impact on the amplifier or laser performance of a number of rare-earth-ion-doped compounds by depleting the population of the long-lived upper state of the corresponding luminescence transition, thereby diminishing the available optical gain [69-78]. ETU can also be exploited to deplete the lower laser level [79-82] or generate upconversion luminescence and lasing [83-87]. Different models of macroscopic or microscopic nature have been developed to understand the underlying physical mechanisms and predict practical device performance. While the macroscopic rate-equation treatment introduced by Grant [88] is often believed to provide erroneous results because of an incorrect treatment of the specific influence of energy migration on ETU, the microscopic models developed by Burshteîn [89], Zusman [90], and Zubenko *et al.* [91], the latter combining the previous works by Zusman and Burshteîn with that by Grant, explicitly take this effect into account. Nevertheless, even these models may be considered imperfect, because they treat all ions equally, thereby neglecting the locally different active environment of individual ions.

In this Chapter, all the above-mentioned models are put to the test. In Section 4.1, we summarize the most important energy-transfer models found in the literature from the last sixty years and adapt Zubenko's microscopic [91] as well as Grant's macroscopic [88] treatment to the case of $Al_2O_3:Er^{3+}$. We focus on the first excited level $^4I_{13/2}$ of Er^{3+} and use amorphous $Al_2O_3:Er^{3+}$ as the example, but with appropriate adjustments our approach can be generally applied to other rare-earth ions and optical materials as well. Then we show in Section 4.2 that results calculated from Zubenko's analytical equation provide good accuracy when interpreting decay curves of luminescence from the Er^{3+} $^4I_{13/2}$ level measured under quasi-CW excitation. When applying a commonly accepted misinterpretation of Bernoulli's equation, also Grant's model provides reasonably good fits and especially provides values of the macroscopic ETU parameter that are very similar to the values derived from Zubenko's comprehensive model, whereas previous donor-acceptor models fail to reproduce the experimental results.

4.1 Theoretical Descriptions of Energy-Transfer Upconversion

4.1.1 Förster's and Dexter's Theory of Ion-Ion Interaction

Förster [92] described the energy transfer from a set of donor atoms to a set of acceptor atoms (donor-acceptor interaction) via electric dipole-dipole interaction. The interaction rate W_{DA} is proportional to the absolute square of the dipole-dipole interaction Hamiltonian, $\hat{H}_{dip-dip}$,

$$\hat{H}_{dip-dip} = \frac{1}{4\pi\varepsilon_0}\left[\hat{\mu}_D \cdot \hat{\mu}_A - 3(\hat{\mu}_D \cdot \hat{r})(\hat{\mu}_A \cdot \hat{r})\right]\frac{1}{R^3}, \tag{4.1a}$$

$$W_{DA} \propto \left|\hat{H}_{dip-dip}\right|^2, \tag{4.1b}$$

where R is the distance between the dipoles, $\hat{r}$ is the unit vector, $\hat{\mu}_D$ is the donor dipole moment, and $\hat{\mu}_A$ is the acceptor dipole moment (Fig. 4.1). Generally, the donor and acceptor atom are of different species, however there is also a possibility for a donor atom to transfer its energy to an atom of the same species, i.e., donor-donor interactions. Dexter's theory [93] of sensitized luminescence in solids expanded Förster's treatment to multipole-multipole interaction (and also exchange interaction) between individual ions. The probability per unit time for multipole-multipole interaction is [93-95]

$$W_{DD/DA} = \frac{1}{\tau_{D,rad}}\left(\frac{R_{DD/DA}}{R}\right)^m = \frac{C_{DD/DA}}{R^m}, \tag{4.2}$$

where $\tau_{D,rad}$ is the radiative lifetime of the donor in absence of this process, $R_{DD/DA}$ is the Förster radius for donor-donor or donor-acceptor energy transfer, defined as the distance at which the rate of energy transfer by dipole-dipole coupling equals the luminescence decay rate, $C_{DD/DA}$ are the donor-donor and donor-acceptor microparameters with dimensions cm^6/s, and the exponent m denotes the multipolarity of the process. Dipole-dipole interaction, as exclusively considered in this work, is represented by $m = 6$. The Förster radius and microparameters can be calculated through the cross-section overlap function [94]

$$C_{DD/DA} = \frac{R^6_{DD/DA}}{\tau_{D,rad}} = \frac{6c}{(2\pi)^4 (n_{medium})^2}\int \sigma^D_{em}(\lambda)\sigma^{D/A}_{GSA/ESA}(\lambda)d\lambda, \tag{4.3}$$

where n_{medium} is the refractive index of the medium and σ_{ESA} is the excited-state-absorption cross-section. The processes of energy migration and ETU, which were depicted in Chapter 2, Fig. 2.3, are described by transition probabilities equal to W_{DD} and W_{DA}, respectively.

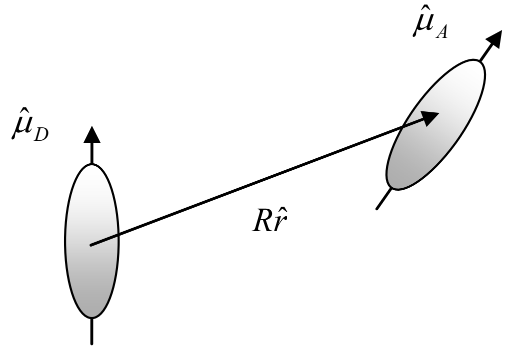

Fig. 4.1. Schematic of dipole-dipole interaction.

4.1.2 Donor-Acceptor Models by Inokuti-Hirayama, Burshteîn, and Zusman

In 1965, Inokuti and Hirayama presented a treatment of the relationship between transfer rate and luminescence decay [96] that has been used in its original form or adapted by many authors. One of the assumptions of their treatment is that only donor-acceptor energy transfer occurs, whereas donor-donor transfer is negligible. The probability $f_D(t)$ of finding a donor, which can transfer energy to n acceptors k at distances R_k within a finite volume around the donor, in the excited state at time t is [96]

$$f_D(t) = \exp(-t/\tau_D)\prod_{k=1}^{n}\exp[-tW_{DA}(R_k)]. \tag{4.4}$$

Here $f_D(t)$ decreases with time due to both, intrinsic decay of the excitation in a time τ_D and the donor-acceptor energy transfer. The intensity of donor luminescence decay is proportional to the average of $f_D(t)$ over an infinitely large number of donors. Assuming a random spatial distribution of acceptors around a donor, the decay of luminescence intensity I can be expressed as

$$I(t) = I(0)\exp\left[-\frac{t}{\tau_D} - \Gamma\left(1-\frac{3}{m}\right)\frac{N_A}{N_c}\left(\frac{t}{\tau_D}\right)^{3/m}\right], \tag{4.5}$$

where τ_D is the intrinsic lifetime of the donor, Γ is the gamma function, N_A is the acceptor concentration, and N_c is a critical transfer concentration. The luminescence decay has a static nature, because the excitation vanishes within the donor-acceptors unit in which it arises, without further migrations over other donors. For $m = 6$ one obtains $N_c = 3/\left(4\pi R_{DA}^3\right)$, and the above expression becomes

$$I(t) = I(0)\exp\left(-\frac{t}{\tau_D} - \gamma\sqrt{t}\right), \tag{4.6a}$$

$$\gamma = \frac{4}{3}\pi^{3/2}N_A\sqrt{C_{DA}}\ . \tag{4.6b}$$

According to Ref. [97] this treatment is valid only for very diluted systems and is not applicable to transfer mechanisms between rare-earth ions, because the high ion concentrations usually employed invalidate the assumption of negligible donor-donor interaction. In addition, the Inokuti-Hirayama theory considers a continuous distribution of acceptor sites around the donors, therefore it was argued in Ref. [98] that it cannot generally be applied to energy-transfer processes in doped materials, because the discrete nature of the host lattice must be taken into account for the short-ranged interactions in question.

Burshteîn [89] and Zusman [90] expanded the Inokuti-Hirayama model by considering also donor-donor interactions. In the hopping regime of donor-donor interaction, which has been proposed to be applicable to rare-earth ions [89], the excitation can enter a sphere surrounding the acceptor, which is given by the Förster radius R_{DA}, in a single discrete step. At the edge of the sphere, a donor excitation has an equal probability to be quenched by the acceptor or to migrate out of the sphere. The hopping regime is realized when

$$C_{DA}/C_{DD} << N_D^{(m_{DD}-m_{DA})/3} . \tag{4.7}$$

where N_D is the donor concentration. For dipole-dipole interactions, i.e., the multipolarities of donor-donor and donor-acceptor interaction are $m_{DD} = m_{DA} = 6$, the condition becomes $C_{DA} / C_{DD} << 1$. According to Burshteîn [89], when a donor is excited at $t = 0$, the probability $f_D(t)$ that it remains in the excited state decreases with time, likewise Eq. (4.4), because of the intrinsic decay of the excitation in a time τ_D and the impurity quenching in which excitation is transferred from the donor to an acceptor, leading to the equation

$$f_D(t) = \exp(-t/\tau_D)P(t) . \tag{4.8}$$

Here $P(t)$ is a complicated multi-step process containing the acceptor and donor concentrations N_A and N_D as parameters, whose rate is determined by the migration of excitations over donors. $P(t)$ satisfies the equation

$$\frac{dP}{dt} = -k(t)N_A P , \tag{4.9}$$

with $k(t)N_A$ being the instantaneous rate of quenching. Evaluation of Eq. (4.9) in the hopping regime leads to the following expression for the luminescence decay:

$$I(t) = I(0)\exp\left(-\frac{t}{\tau_D} - \gamma\sqrt{t}\right)\exp\left(-\overline{W}t\right), \tag{4.10a}$$

$$\overline{W} = \pi\left(\frac{2\pi}{3}\right)^{5/2}\sqrt{C_{DA}C_{DD}}N_D N_A , \tag{4.10b}$$

where $\overline{W}$ is an ensemble-averaged migration-assisted energy-transfer rate. Equation (4.10a) is the product of Inokuti-Hirayama's static equation (4.6a) and an energy-migration-dependent exponential term.

Zusman [90] described the temporal evolution of donor excitation by first considering the balance of excitation probability for one donor and then averaging the result over the ensemble of donors. The probability *f(r,t)* that an excited donor placed at the origin in space did not transfer its energy during time *t* to an acceptor at distance *r* is given by

$$\frac{\partial f(r,t)}{\partial t} = -W_{DA}(r) f(r,t) - \frac{1}{\tau_0} f(r,t) + \frac{1}{\tau_0}, \tag{4.11a}$$

$$\Rightarrow f(r,t) = \exp\left[-\left(W_{DA}(r) + \frac{1}{\tau_0}\right)t\right] + \frac{1}{W_{DA}(r)\tau_0 + 1}\left\{1 - \exp\left[-\left(W_{DA}(r) + \frac{1}{\tau_0}\right)t\right]\right\}, \tag{4.11b}$$

where τ_0 is defined as the most probable migration time. The nonlinear quenching rate *F*(*t*) is calculated as [90]

$$\begin{aligned} F(t) &= \int_0^{\infty} W_{DA}(r) f(r,t) 4\pi r^2 dr \\ &= \frac{2\pi^2}{3}\sqrt{\frac{C_{DA}}{\tau_0}}\left[\sqrt{\frac{\tau_0}{\pi t}}\exp\left(-\frac{t}{\tau_0}\right) + \operatorname{erf}\left(\sqrt{\frac{t}{\tau_0}}\right)\right], \end{aligned} \tag{4.12}$$

and the luminescence decay is expressed as [90]

$$I(t) = I(0)\exp\left[-\frac{t}{\tau_D} - N_A \int F(t) dt\right], \tag{4.13}$$

which is fairly close to Burshteîn's Eq. (4.10a), with minor corrections at $t \ll \tau_0$ and $t \gg \tau_0$. According to Zusman [90] there is a simple connection between the most probable migration time τ_0 and the donor concentration N_D:

$$\frac{1}{\tau_0} = C_{DD} {N_D}^2. \tag{4.14}$$

Grant argued [88] that the concentration ranges, levels of excitation, and relative magnitudes of transfer times encountered in rare-earth-ion-doped crystals render the model proposed by Inokuti-Hirayama (hence also Burshteîn's and Zusman's models) inappropriate in this context. The non-linear nature of ETU is an experimentally manifested feature that is precluded at the outset in the previously described models. In fact, the donor-acceptor models of Inokuti-Hirayama, Burshteîn, and Zusman can only deal with a donor and acceptors of different species and can treat only linear quenching processes, such as energy transfer to impurities in the ground state. Although Burshteîn's model can treat, e.g., the case of self-quenching in Nd^{3+} systems, in which both, donor and acceptor are Nd^{3+} ions [89], this process represents an energy transfer from an excited ion to an ion in the ground state and is, therefore, linear as long as ground-state bleaching is negligible. Instead, ETU is an interaction between two excited ions, which is non-linear. Grant showed that Förster's starting equations (and, consequently, Inokuty-Hirayama's model) can be derived by linearizing Eq. (15) in his non-linear treatment [88], which is achieved by neglecting the intra-species interactions. Burshteîn adds migration to Inokuti-Hirayama's linear model by means of yet a linear equation (Eq. 3.1 in Ref. [89]), which is valid only "when the number of excitations is so small that the encounters between them can be neglected". Thus, also Burshteîn's model is linear and cannot be applied to non-linear ETU.

4.1.3 Rate-Equation Model by Grant

Grant's model allows one to describe the non-linear nature of ETU. It assumes an infinitely fast energy-migration rate, leading to a "sea" of excitations in the metastable excited state, which are smeared out over the excitation volume. Starting from first principles, Grant derived a non-linear rate equation in which the effect of ETU can be expressed by a term $W_{ETU} N_1^2$, where W_{ETU} is the time-independent, averaged transition probability (the macroscopic ETU coefficient, with dimensions cm^3/s), N_1 is the time-dependent population density of the excited state in which the ETU process originates [88], and the exponent of 2 reflects the two-ion character of the ETU interaction, see Fig. 2.3 in Chapter 2. This approach leads to the following rate equation and form for the temporal dynamics of the excited-state population density $N_1(t)$, respectively [99]:

$$\frac{dN_1(t)}{dt} = -\frac{N_1(t)}{\tau_D} - 2W_{ETU} N_1^2(t) \tag{4.15a}$$

$$\Rightarrow N_1(t) = \frac{N_1(0)\exp(-t/\tau_D)}{1 + 2W_{ETU}\, N_1(0)\tau_D\left[1 - \exp(-t/\tau_D)\right]}, \tag{4.15b}$$

where $N_1(0)$ is the initial excitation density and τ_D is the intrinsic lifetime, which includes luminescence decay as well as multiphonon relaxation. Equation (4.15b) is known as Bernoulli's equation.

Since it assumes an infinitely fast energy-migration rate, Grant's rate-equation approach fails to describe effects arising from the finite time of energy migration among donors.

4.1.4 Zubenko's Model

The model presented in the work of Zubenko *et al.* [91] combines the approaches by Zusman and Grant in a single model, thus considering simultaneously the finite energy-migration rate (via τ_0) in Zusman's equations and the non-linearity present in Grant's model. Zubenko makes the *ad hoc* assumption that the temporal dynamics of the excited-state population density $N_1(t)$ can be described by replacing the time-independent ETU coefficient W_{ETU} in Grant's rate equation (Eq. 4.15a) by Zusman's nonlinear quenching rate $F(t)$ presented in Eq. (4.12), leading to the rate equation

$$\frac{dN_1(t)}{dt} = -\frac{N_1(t)}{\tau_D} - F(t)N_1^2(t), \tag{4.16}$$

whose solution is [91]

$$N_1(t) = \frac{N_1(0)\exp(-t/\tau_D)}{1 + N_1(0)\dfrac{2\pi^2}{3}\sqrt{\dfrac{C_{DA}}{\tau_0}}\,\tau_D\left[\sqrt{1+\dfrac{\tau_0}{\tau_D}}\,\mathrm{erf}\left(\sqrt{t\left(\dfrac{1}{\tau_0}+\dfrac{1}{\tau_D}\right)}\right) - \exp(-t/\tau_D)\,\mathrm{erf}\left(\sqrt{\dfrac{t}{\tau_0}}\right)\right]}. \tag{4.17}$$

The mathematical derivation of Eq. (4.17), including all relevant steps and intermediate equations in provided in Appendix A. For $\tau_0^{-1} \to \infty$ (infinitely fast migration), resulting in erf(∞) → 1, Eq. (4.17) reduces to Bernoulli's Eq. (4.15b), with [91]

$$W_{ETU} = \frac{\pi^2}{3}\sqrt{\frac{C_{DA}}{\tau_0}}. \tag{4.18}$$

The same result, namely $F(t) = 2W_{ETU}$, is derived by solving Zusman's Eqs. (4.11) and (4.12) in the steady-state regime, i.e., $\partial f(r,t)/\partial t = 0$.

4.1.5 Adaptation of Zubenko's Model

We need to adapt the result of Eq. (4.17) to our specific case, the investigation of de-excitation from the first excited level $^4I_{13/2}$ of Er^{3+} in Al_2O_3, from now on indicated with the subscript "1" in the nonlinear quenching rate *F*(*t*) (and also in the macroscopic ETU coefficient W_{ETU}).

Figure 4.2 displays a partial energy-level scheme of Er^{3+} with the relevant transitions when pumping directly into the first excited level $^4I_{13/2}$. We assume that the excitation which reaches higher excited states quickly relaxes back to the first excited state, e.g. by multiphonon relaxation. This assumption is justified for $Al_2O_3:Er^{3+}$ because of the rather high phonon energies of 870 cm^{-1} that was assumed in Sect 2.2.5 based on the results in crystalline Al_2O_3 (sapphire) [52]. As a result, the whole system can be modeled in a three-level scheme, like the one shown in Fig. 2.3 in Chapter 2. The population densities of the two excited states are N_1 and N_2, and the lifetime of the first excited state τ_1 is long compared to that of the second excited state τ_2. After ions are pumped by GSA into the first excited state, migration processes ($^4I_{13/2}$, $^4I_{15/2}$) → ($^4I_{15/2}$, $^4I_{13/2}$) and ETU processes ($^4I_{13/2}$, $^4I_{13/2}$) → ($^4I_{15/2}$, $^4I_{9/2}$) occur. ETU from higher-lying excited states is not considered in Zubenko's model. With these assumptions, we can describe the population dynamics of the excited levels after termination of the pump excitation by the rate-equation system

$$\frac{dN_2(t)}{dt} = \frac{F_1(t)}{2}N_1^2(t) - \frac{N_2(t)}{\tau_2}, \tag{4.19a}$$

$$\frac{dN_1(t)}{dt} = -\frac{N_1(t)}{\tau_1} - F_1(t)N_1^2(t) + \frac{N_2(t)}{\tau_2}. \tag{4.19b}$$

Since Zubenko's model treats all ions equally – which might be considered as its major deficiency – it is irrelevant whether the excitation density at $t = 0$, when the pump is switched off, is achieved via a short laser pulse or established via continuous-wave excitation. Experimentally, these two excitation schemes will normally lead to different populations at $t = 0$ because of the different active environments of individual active ions if distributed non-uniformly in the host material, i.e., statistically or even including clustering.

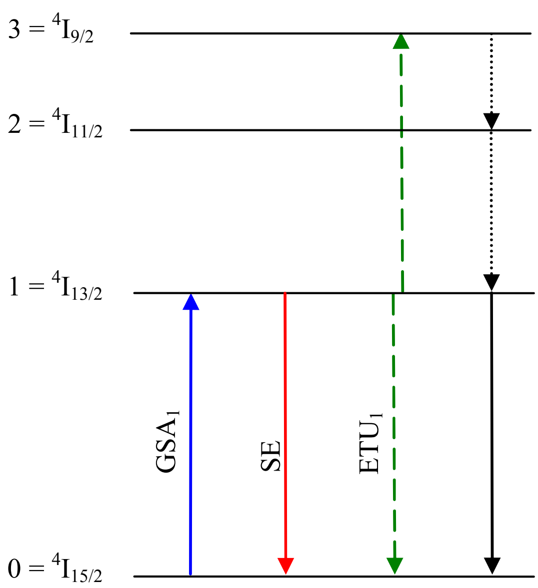

Fig. 4.2. Partial energy-level diagram of Er^{3+}, indicating direct pumping of the ${}^4I_{13/2}$ level by GSA, stimulated emission at the pump wavelength, ETU from the ${}^4I_{13/2}$ level, multiphonon relaxations from the ${}^4I_{9/2}$ and ${}^4I_{11/2}$ levels, and luminescence decay from the ${}^4I_{13/2}$ level.

Since $\tau_2 << \tau_1$, the excitation of the second excited state responds to changes of the population density of the first excited state quasi instantaneously, i.e., $dN_2(t)/dt \approx 0$ at time scales relevant to changes of the population density of the first excited state, and thus

$$N_2(t) = \tau_2 \frac{F_1(t)}{2} N_1^2(t) \tag{4.20a}$$

$$\frac{dN_1(t)}{dt} = -\frac{N_1(t)}{\tau_1} - \frac{F_1(t)}{2} N_1^2(t). \tag{4.20b}$$

The solution of Eq. (4.20b) is

$$N_1(t)=\frac{N_1(0)\exp(-t/\tau_1)}{1+N_1(0)\frac{\pi^2}{3}\sqrt{\frac{C_{DA}}{\tau_0}}\,\tau_1\left[\sqrt{1+\frac{\tau_0}{\tau_1}}\,\mathrm{erf}\left(\sqrt{t\left(\frac{1}{\tau_0}+\frac{1}{\tau_1}\right)}\right)-\exp(-t/\tau_1)\,\mathrm{erf}\left(\sqrt{\frac{t}{\tau_0}}\right)\right]}. \tag{4.21}$$

It appears that the only difference between Eqs. (4.17) and (4.21) is a factor of 2 in the second part of the denominator, which accounts for the fact that the upconverted ion quickly relaxes back to the metastable state, resulting in only one excitation in the metastable state being lost by each ETU process. The same correction holds for the macroscopic model and Bernoulli's Eq. (4.15b):

$$N_1(t)=\frac{N_1(0)\exp(-t/\tau_1)}{1+W_{ETU1}N_1(0)\tau_1\left[1-\exp(-t/\tau_1)\right]}. \tag{4.22}$$

4.2 Applying the Different Models to Luminescence Decay Curves

In this Section we present luminescence decay curves measured in Al_2O_3:Er^{3+} channel waveguide samples with different dopant concentrations and at different pump powers. We apply the different approaches described in the previous section and show that the model proposed by Burshteîn fails to reproduce the pump-power as well as concentration dependence of the decay curves. The model proposed by Grant, resulting in Bernoulli's equation, fails to reproduce the concentration dependence, but provides fairly good results when misinterpreting the intrinsic decay time as a free parameter. Finally, Zubenko's model, which combines the two different approaches, allows us to fit all decay curves properly.

4.2.1 Luminescence Decay Measurements in Al_2O_3:Er^{3+}

The eight Al_2O_3:Er^{3+} channel waveguide samples with Er^{3+} concentrations ranging from 0.27 to 4.22 × 10^{20} cm^{-3}, listed in Table 3.1(a) in Chapter 3, were investigated.

Regarding luminescence decay measurements, details of the experimental setup have already been described in Sect. 3.2.4 in Chapter 3. A comparison of measured luminescence decay curves for different pump powers is shown in Fig. 4.3, in this example for an Er^{3+} concentration of 3.66 × 10^{20} cm^{-3}, whereas a comparison for different dopant concentrations, for the same launched pump power of 30 mW, is displayed in Fig. 4.4. The analysis of the luminescence decay curves is addressed later on. The curves exhibit two distinct temporal components: a fast non-exponential behavior induced by ETU during the initial temporal part of the decay, which becomes increasingly non-exponential (a signature of the non-linear nature of ETU) with increasing pump power and Er^{3+} concentration, followed by an approximately exponential tail characterized by an asymptotic decay time $t_{\exp}$, whose value is determined by applying a linear fit to the final portion of the graph. The value of $t_{\exp}$ is independent of the applied pump power, but decreases from 7.55 ms down to 6 ms (± 0.15 ms) when the Er^{3+} concentration increases from 0.27 to 3.66 × 10^{20} cm^{-3} [squares in Fig. 4.5(a)], a qualitative behavior that is well documented in the literature [100]. Although eight samples were investigated, for clarity the results of only five of them are presented in Fig. 4.4 and, hence, also in Fig. 4.5.

An empirical law was proposed, relating $t_{\exp}$ to the Er^{3+} concentration N_d [100]:

$$t_{\exp} = \frac{\tau_1}{1+\left(N_d / Q\right)^p}, \tag{4.23}$$

where τ_1 is the intrinsic lifetime, Q is a critical quenching concentration, and the exponent p is experimentally often found equal or similar to 2 [100,101]. The fit of our experimental data with Eq. (4.23) and $p = 2$ is shown by the red line in Fig. 4.5(a). By plotting $\tau_1 / t_{\exp} - 1$ as a function of concentration N_d in double logarithmic scale, a linear dependence is expected, with the slope equal to $p = 2$ [red line Fig. 4.5(b)]. In contrast, our experimental data are best reproduced with a slope of $p = 3.17$ [blue line in Fig. 4.5(b)]. The corresponding fit of the experimental lifetime data [blue line in Fig. 4.5(a)], extrapolated to zero concentration, results in an intrinsic lifetime of the first excited level of $\tau_1 = 7.55$ ms. According to Ref. [97], the deviation from $p = 2$ can be explained by the presence of electric dipole-quadrupole and quadrupole-quadrupole interactions or, alternatively, energy-transfer processes involving more than two particles [88]. However, our attempts to fit the luminescence decay curves of Figs. 4.3 and 4.4 with the modified Eq. (4.21) from Zubenko's model for $m = 8$ or 10 or starting from Eq. (4.20) with $N_1^3(t)$ did not provide meaningful results. Therefore, in the remainder of this work we will focus on electric dipole-dipole interactions involving 2 ions.

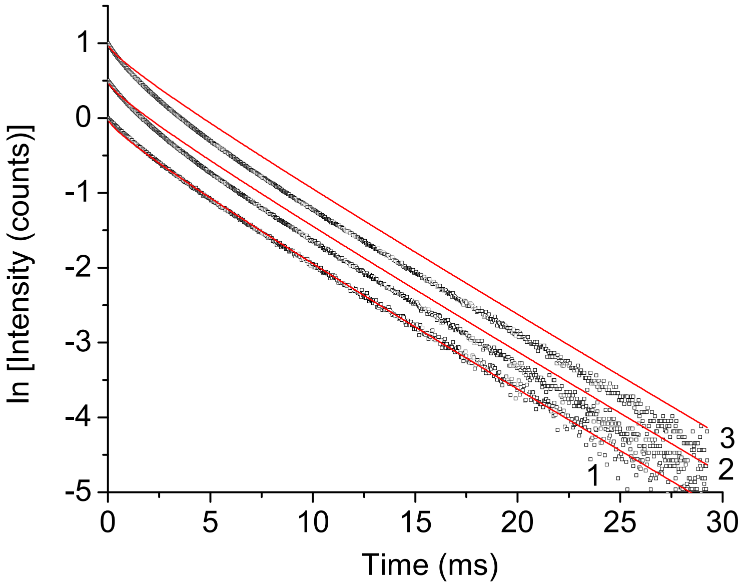
1
0
-1
-2
-3
-4
-5
ln [Intensity (counts)]
0
5
10
15
20
25
30
Time (ms)
3
2
1

(a)

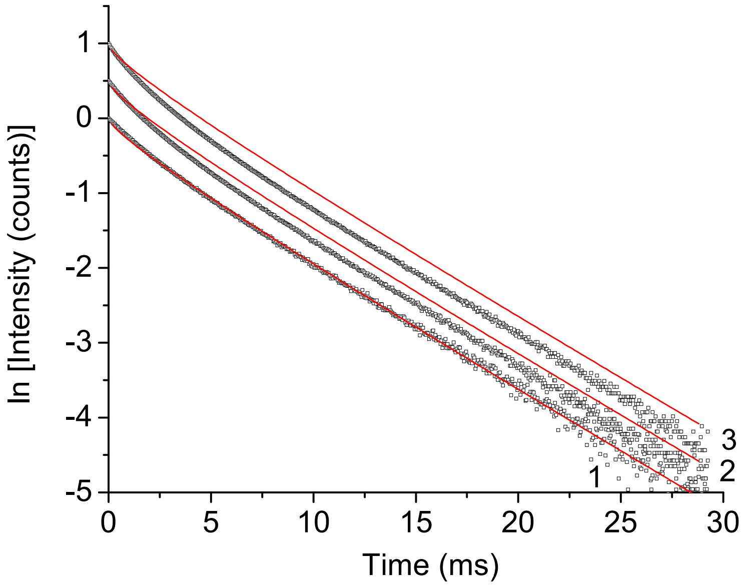
1
0
-1
-2
-3
-4
-5
ln [Intensity (counts)]
0
5
10
15
20
25
30
Time (ms)
3
2
1

(b)

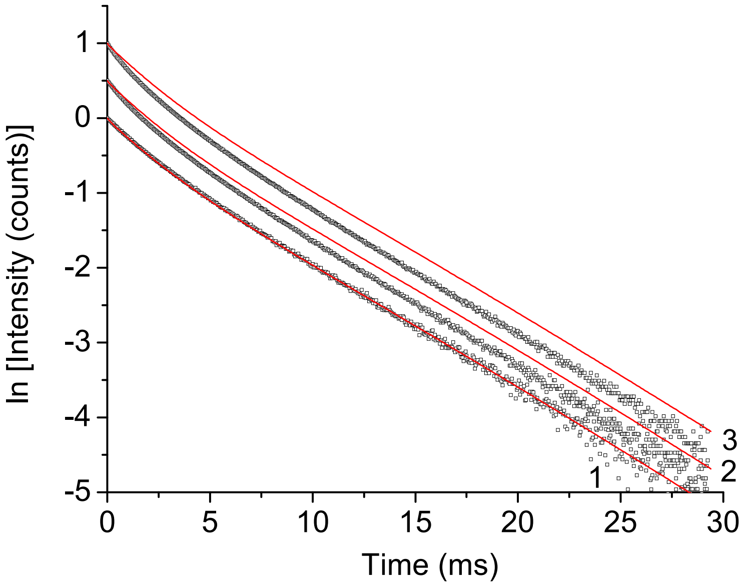
ln [Intensity (counts)]
Time (ms)
1
0
-1
-2
-3
-4
-5
0
5
10
15
20
25
30
1
2
3

(c)

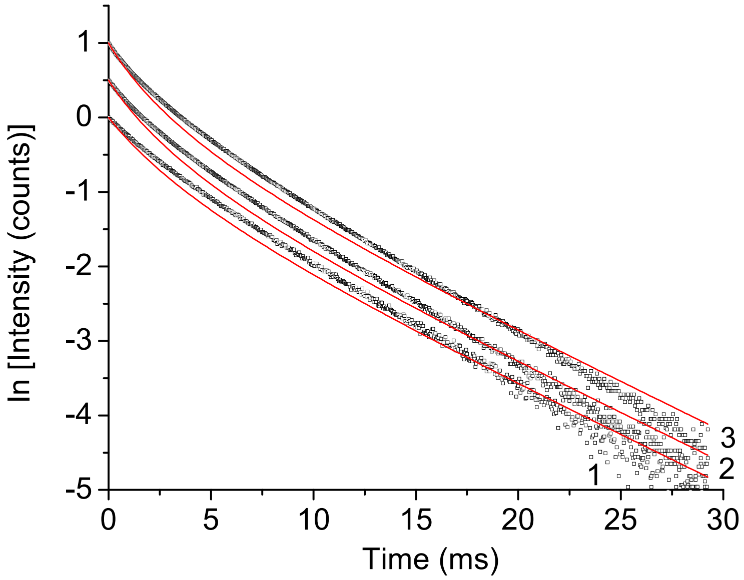
ln [Intensity (counts)]
Time (ms)
1
0
-1
-2
-3
-4
-5
0
5
10
15
20
25
30
1
2
3

(d)

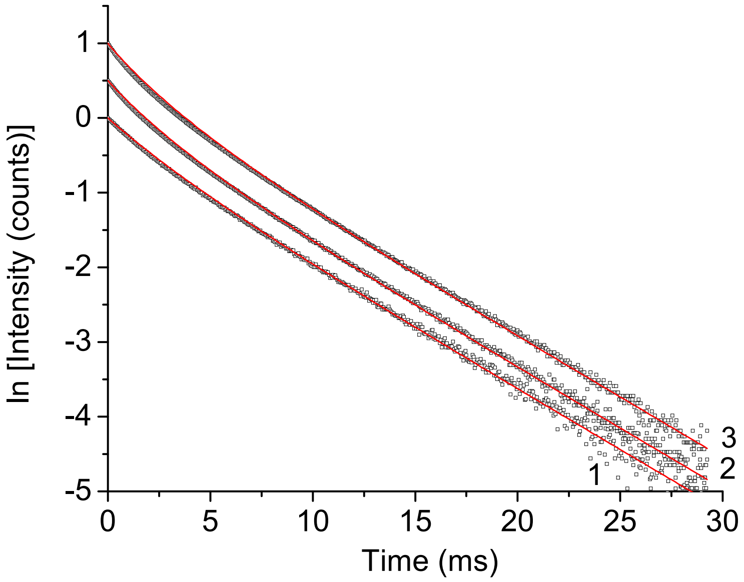

(e)

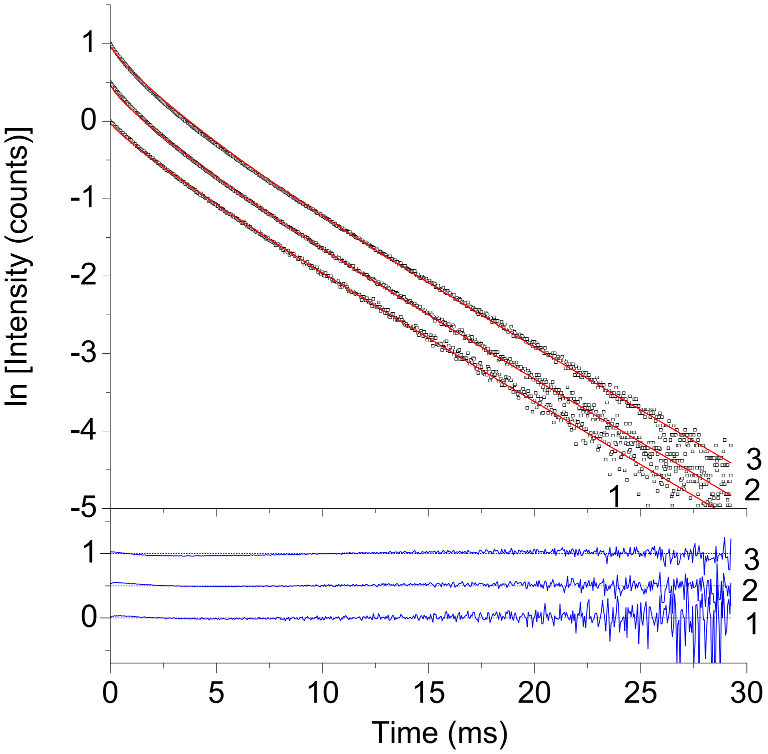

(f)

Fig. 4.3. Normalized luminescence decay curves from the $^4I_{13/2}$ level at a wavelength of 1530 nm for three different launched pump powers, for the example of an Er^{3+} concentration of 3.66 x 10^{20} cm^{-3}. For clarity, the curves are offset with respect to each other. The numbers 1 to 3 refer to launched pump powers of 3, 15 and 30 mW, respectively. In (a), (b), and (c) Burshteĭn's Eq. (4.10) is applied to the lower curve (corresponding to the lowest pump power) under the assumptions (a) $N_A = N_D = N_d$, (b) $N_D = N_d$, $N_A = N_1(t = 0)$, and (c) $N_D = N_d$, $N_A = N_1(t)$, respectively. In (d) and (e) Bernoulli's Eq. (4.22) is applied under the assumptions that (d) the upconversion coefficient W_{ETU} is the only free parameter, while τ_1 assumes the intrinsic lifetime value of 7.55 ms, and (e) both W_{ETU} and τ_1 as free parameters. In (f) Zubenko's Eq. (4.21) can fit the three curves simultaneously with free parameters C_{DA} and τ_0, while τ_1 correctly assumes the intrinsic lifetime value of 7.55 ms. The residual of this last fit are shown at the bottom of the graph. The R^2 values of all the fits are reported in the text.

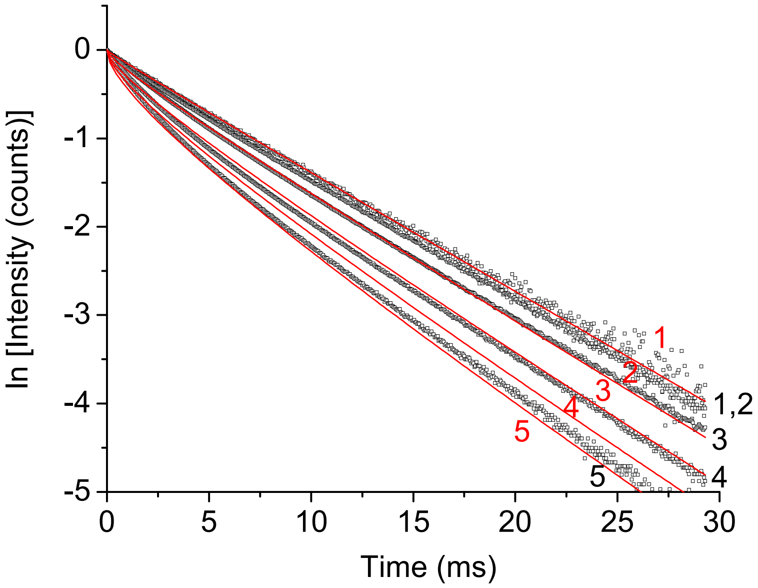
ln [Intensity (counts)]
0
-1
-2
-3
-4
-5
0
5
10
15
20
25
30
Time (ms)
1
2
3
4
5
1,2
3
4
5

(a)

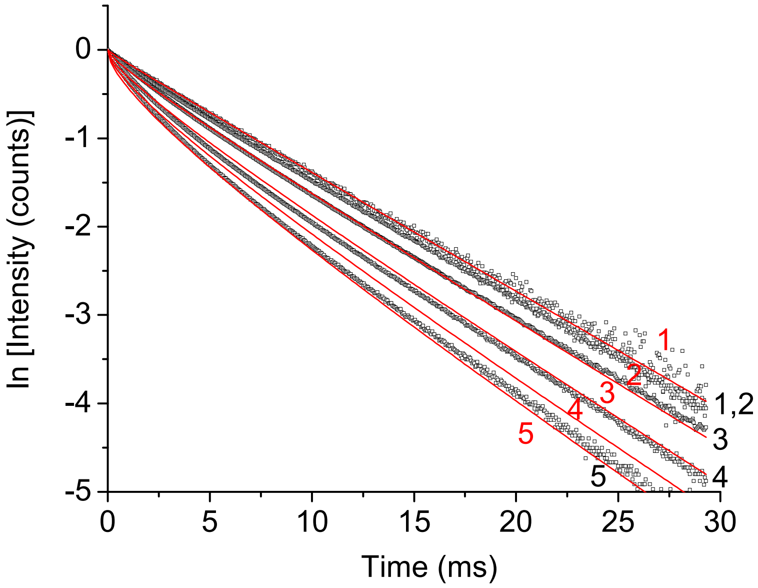
ln [Intensity (counts)]
0
-1
-2
-3
-4
-5
0
5
10
15
20
25
30
Time (ms)
1
2
3
4
5
1,2
3
4
5

(b)

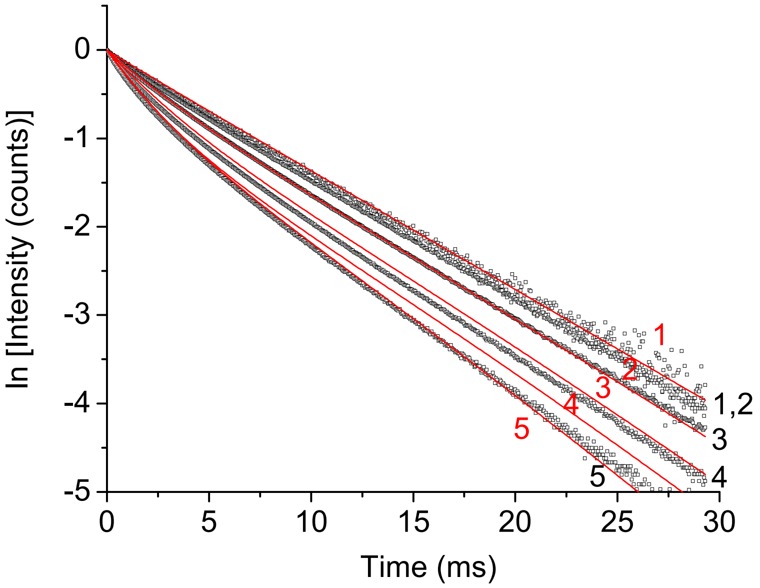
0
-1
-2
-3
-4
-5
ln [Intensity (counts)]
0
5
10
15
20
25
30
Time (ms)
1
2
3
4
5
1,2
3
4
5

(c)

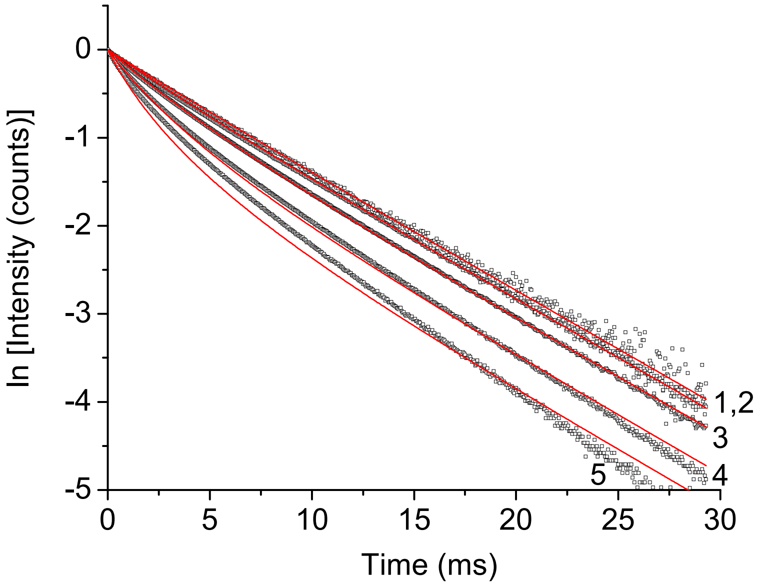
0
-1
-2
-3
-4
-5
ln [Intensity (counts)]
0
5
10
15
20
25
30
Time (ms)
1,2
3
4
5

(d)

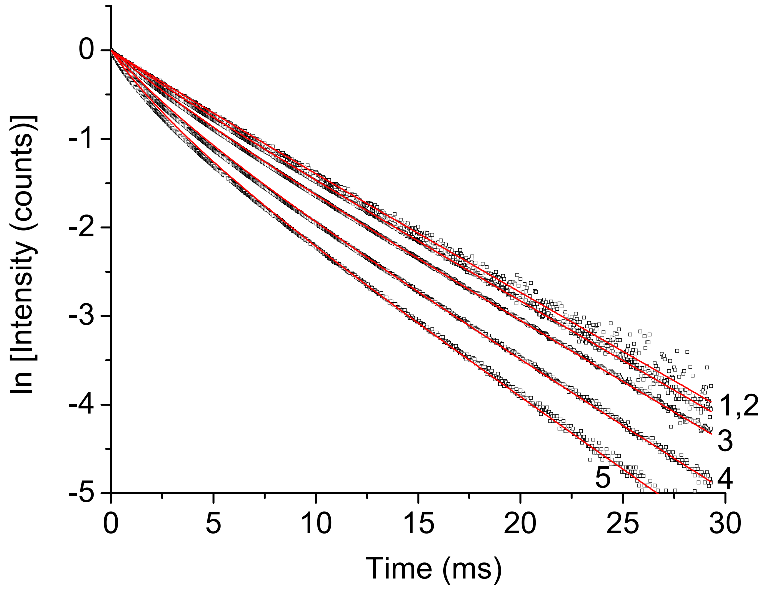
ln [Intensity (counts)]
0
-1
-2
-3
-4
-5
0
5
10
15
20
25
30
Time (ms)
1,2
3
4
5

(e)

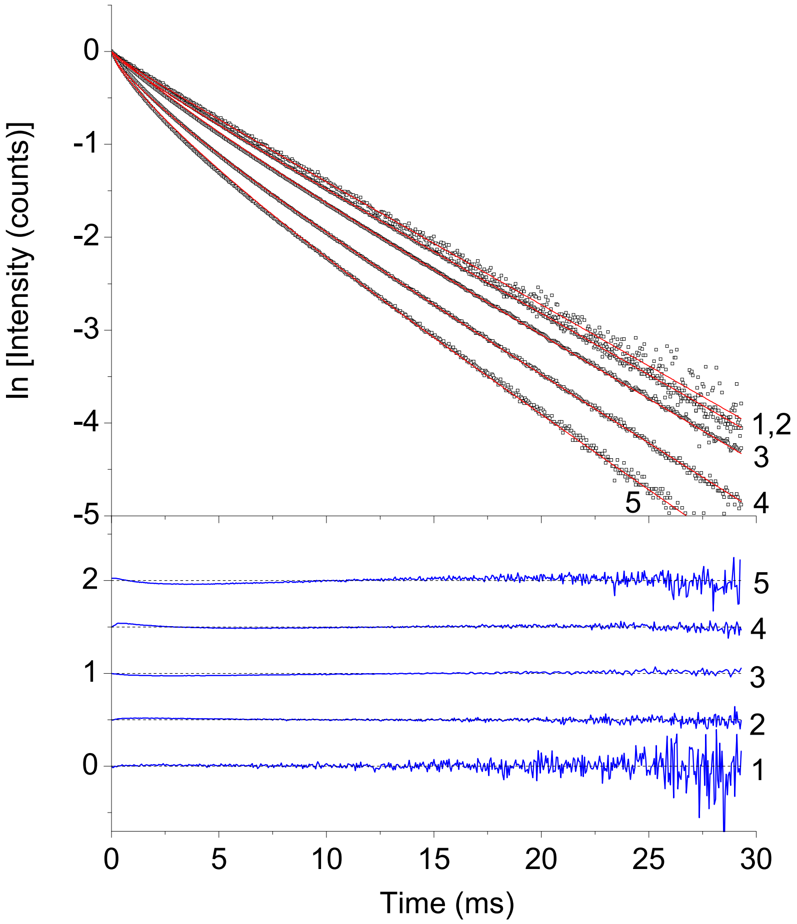
ln [Intensity (counts)]
0
-1
-2
-3
-4
-5
1,2
3
4
5
2
1
0
5
4
3
2
1
0
5
10
15
20
25
30
Time (ms)

(f)

Fig. 4.4. Normalized luminescence decay curves from the $^4I_{13/2}$ level at a wavelength of 1530 nm for five different Er^{3+} concentrations. The black numbers 1 to 5 refer to Er^{3+} concentrations of N_d = 0.27, 1.17, 2.12, 2.91, and 3.66 × 10^{20} cm^{-3}, resulting in decay times for the asymptotic exponential tail of t_{exp} = 7.55, 7.5, 7.3, 6.7, and 6.0 ms (± 0.15 ms), respectively. In (a), (b), and (c) Burshteîn's Eq. (4.10) is applied under the assumptions (a) $N_A = N_D = N_d$, (b) $N_D = N_d$, $N_A = N_1(t = 0)$, and (c) $N_D = N_d$, $N_A = N_1(t)$, respectively, and red numbers 1 to 5 have been added to clarify the assignment of each fit. In (d) and (e) Bernoulli's Eq. (4.22) is applied under the assumptions that (d) the upconversion coefficient W_{ETU} is the only free parameter, while τ_1 assumes the intrinsic lifetime value of 7.55 ms, and (e) both W_{ETU} and τ_1 as free parameters. In (f) the fit from Zubenko's Eq. (4.21) is shown, where C_{DA} and τ_0 are the free parameters, while τ_1 correctly assumes the intrinsic lifetime value of 7.55 ms. The residual of this last fit are shown at the bottom of the graph. The R^2 values of all the fits are reported in the text.

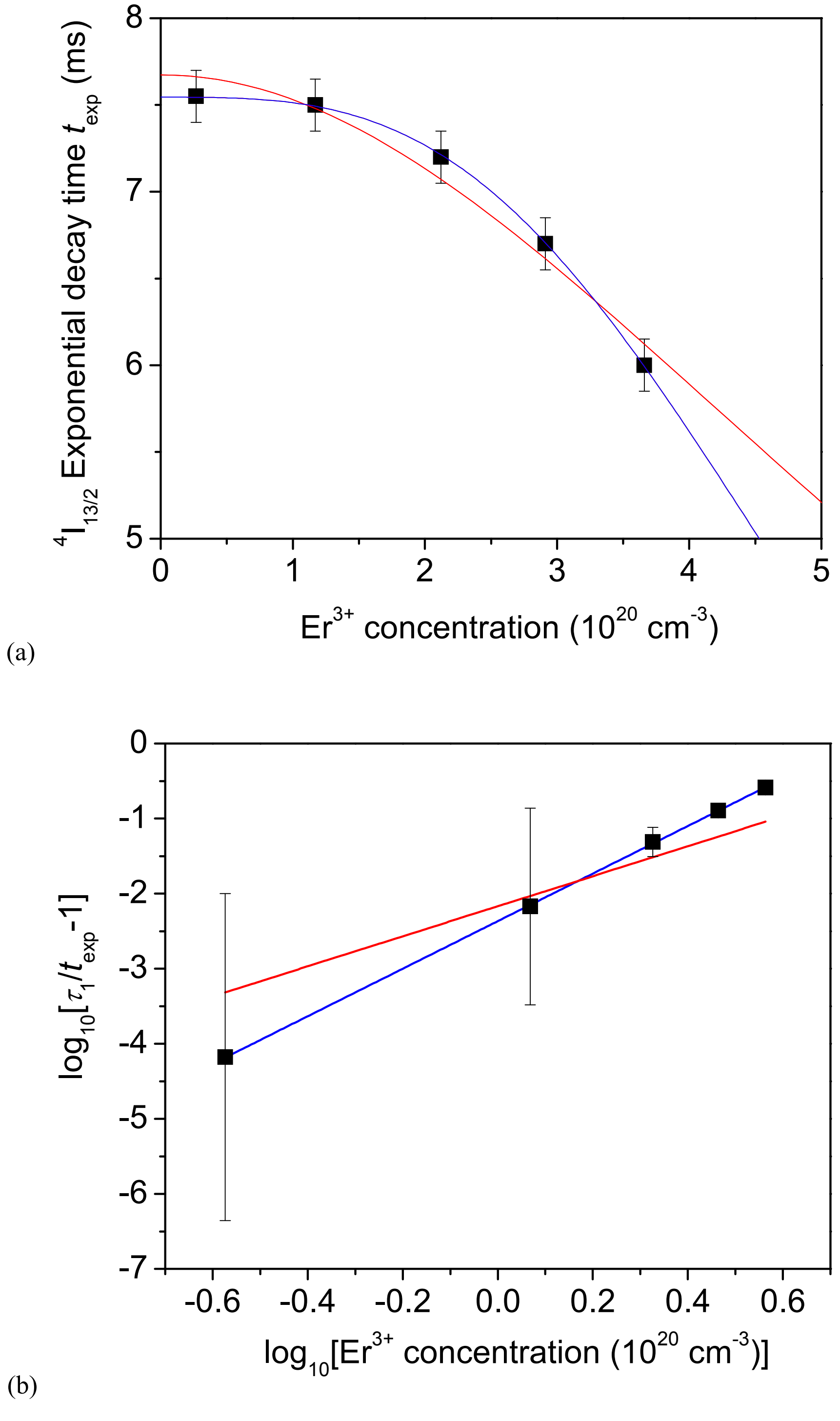

Fig. 4.5. (a) $^4I_{13/2}$ exponential decay time t_{exp} (squares), extracted from the asymptotic exponential tails, and (b) τ_1 / t_{exp} – 1 as a function of Er^{3+} concentration in double-logarithmic representation. The blue and red curves are the best least-square fits with Eq. (4.23) for p = 3.17 and p = 2, respectively.

4.2.2 Pump-Power Dependence

The comparison of luminescence decay curves for different pump powers is shown in Fig. 4.3(a-f) for the example of an Er^{3+} concentration of 3.66 × 10^{20} cm^{-3}. The asymptotic decay time for this specific Er^{3+} concentration is $t_{\mathrm{exp}} = 6$ ms. First we apply Burshteĭn's Eq. (4.10) to the measured decay curves. The donor concentration N_D seems to naturally equal the dopant concentration N_d and, according to the theory, excitation of a donor ion initializes its decay by either intrinsic relaxation or energy transfer to another ion. Although this approach neglects the additional decay channel in which this excited ion can act as an acceptor ion of an ETU process, one may argue that in the specific case investigated here the upconverted ion returns rapidly, via multiphonon relaxation, back to the first excited state, thereby leaving the situation unchanged. However, this interpretation is not correct, as the relaxation into the first excited state sets the time for its intrinsic decay back to zero. Furthermore, it is not *a priori* clear how to handle the acceptor concentration N_A in a donor-acceptor model in the specific case of ETU, because the acceptor ions are of the same species as the donor ions (in this specific case Er^{3+} ions) and, moreover, can act as acceptors only when being in their excited state, thereby complicating the situation. In previous investigations [94,102-104], it has been assumed that $N_A = N_D = N_d$, where N_d is the total ion concentration. As a consequence, γ and $\overline{W}$ (together with τ_D) are pump-power-independent parameters, hence Burshteĭn's Eq. (4.10) is invariant to pump power. With this assumption, in Fig. 4.3(a) Burshteĭn's Eq. (4.10) is initially applied to the lower decay curve, corresponding to the lowest pump power, thereby deriving C_{DA} and C_{DD}, which are then applied to the decay curves measured under higher pump power. Not surprisingly, because of the pump-power invariance of the equation, this approach fails to reproduce the increasingly non-exponential shape of the experimental decay curves with increasing pump power (medium and upper curve).The R^2 of the fits decreases from 0.9889 (lower curve) to 0.9821 (medium curve) and 0.9676 (upper curve).

One can try to adapt Burshteĭn's Eq. (4.10) to the case of ETU by assuming an acceptor density N_A of excited Er^{3+} ions that depends on pump excitation and/or time. In a simple approach, one can set N_A equal to the pump-power-dependent excitation density N_1 at $t = 0$. The underlying assumption is that a neighboring donor ion in its excited state will at all times find the acceptor ion available and acting as such, i.e., still in its excited state, which means that the ETU process must have a rate constant $W_{ETU} N_A$ that is much higher than the rate constant $1/\tau_D$ of the intrinsic decay, so that the probability that the ETU process takes place before the acceptor ion decays intrinsically is high. Again, we apply Burshteĭn's Eq. (4.10) to the lower decay curve and derive C_{DA} and C_{DD}, which are then applied to the higher decay curves. Although this approach introduces a pump-power dependence, because $N_A = N_1(t = 0)$ increases with pump power, it still does not fit the measured curves, see Fig. 4.3(b). The R^2 of the fits decreases from 0.9889 (lower curve) to 0.9824 (medium curve) and 0.9751 (upper curve).

Another possible approach is to assume a time-dependent $N_A = N_1(t)$. This causes an additional complication, as Burshteĭn's Eq. (4.10) becomes a transcendental equation, which we solve numerically. Again, a pump-power dependence is introduced, but also this approach is insufficient to fit the measured curves, see Fig. 4.3(c). The R^2 of the fits decreases from 0.9889 (lower curve) to 0.9855 (medium curve) and 0.9726 (upper curve).

A common approach to fitting the decay curves is to apply Bernoulli's Eq. (4.22), in conjunction with the expression for the initial condition $N_1(0)$. This value is calculated with Eq. (B5) in Appendix B (by setting the parameters $f_a = 1$ and $f_q = 0$; the meaning of these parameters will become obvious in the next Chapter). The parameters used in the calculation of $N_1(0)$ and their values are listed in the first three columns of Table 4.1. The upconversion coefficient W_{ETU} is the only free parameter, while the intrinsic lifetime τ_1 has the correct value of 7.55 ms. As becomes apparent from the results shown in Fig. 4.3(d), Eq. (4.22) is unsuccessful in fitting the measured decay curves, and the discrepancy increases slightly with higher pump power. The R^2 values of the fits are 0.9784 (lower curve), 0.9871 (medium curve), and 0.9894 (upper curve). Apparently, the assumption of infinitely fast migration and, hence, solely migration-accelerated ETU, as assumed in Grant's model, is insufficient to explain the luminescence decay curves. A better, albeit not perfect fit is obtained if we misinterpret τ_1 as a free parameter and set it equal to the value of t_{exp} = 6 ms for the Er^{3+} concentration of 3.66×10^{20} cm^{-3} [Fig. 4.3(e)]. The R^2 of the fits are 0.9889 (lower curve), 0.9979 (medium curve), and 0.9988 (upper curve).

In contrast, Zubenko's Eq. (4.21), which considers the nonlinear dependency of luminescence decay on the pump power in the initial excitation density $N_1(0)$, fits the same three curves extremely well [Fig. 4.3(f)] by use of a single set of parameters, which includes interpreting τ_1 correctly as the intrinsic luminescence decay time of 7.55 ms. The R^2 of the fits are 0.9981 (lower curve), 0.9979 (medium curve), and 0.9990 (upper curve).

Table 4.1. Parameter values used in luminescence-decay, pump-absorption, and gain calculations in $Al_2O_3:Er^{3+}$. Cross-sections and background loss values are taken from Ref. [32], except for $\sigma_{ESA}(\lambda_P)$, which is taken from [105].

Parameter	Symbol	Luminescence decay	Pump absorption	Gain	Unit
Pump wavelength	λ_P	1480	1480	976	[nm]
Luminescence/Signal wavelength	λ_S	1533	-	1533	[nm]
Launched pump power	$P_P(0)$	3, 15, 30 (pump-power dependence, Sect. 4.2.2); 30 (concentration dependence, Sect. 4.2.3)	60	100	[mW]
Launched signal power	$P_S(0)$			1	[μW]
Mode distributions pump/signal	$\psi_{P/S}(x,y)$	Imported from Phoenix software [106]	Imported from Phoenix software [106]	Imported from Phoenix software [106]	-
Pump absorption cross-section	$\sigma_{GSA}(\lambda_P)$	$(3.3 \pm 0.2) \times 10^{-21}$	$(3.3 \pm 0.2) \times 10^{-21}$	$(2.0 \pm 0.2) \times 10^{-21}$	[cm^2]
Pump emission cross-section	$\sigma_{em}(\lambda_P)$	$(1.1 \pm 0.2) \times 10^{-21}$	$(1.1 \pm 0.2) \times 10^{-21}$	$(2.0 \pm 0.2) \times 10^{-21}$	[cm^2]
Signal absorption cross-section	$\sigma_{GSA}(\lambda_S)$			$(5.65 \pm 0.24) \times 10^{-21}$	[cm^2]
Signal emission cross-section	$\sigma_{em}(\lambda_S)$			$(5.65 \pm 0.28) \times 10^{-21}$	[cm^2]
Excited-state absorption cross-section	$\sigma_{ESA}(\lambda_P)$			1.1×10^{-21}	[cm^2]
Luminescence lifetime	τ_1	7.55	7.55	7.55	[ms]
	τ_2	60	60	60	[μs]
Background loss pump	$\alpha_{bck}(\lambda_P)$	0.15 ± 0.10	0.15 ± 0.10	0.25 ± 0.10	[dB/cm]
Background loss signal	$\alpha_{bck}(\lambda_S)$	-	-	0.15 ± 0.10	[dB/cm]

4.2.3 Concentration Dependence

A comparison of measured luminescence decay curves for different Er^{3+} concentrations, for the same launched pump power of 30 mW, is shown in Fig. 4.4. Burshteîn's Eq. (4.10) is tested with the same three assumptions as above, $N_A = N_D = N_d$ [Fig. 4.4(a)], $N_D = N_d$ and $N_A = N_1(t = 0)$ [Fig. 4.4(b)], as well as $N_D = N_d$ and $N_A = N_1(t)$ [Fig. 4.4(c)]. Like for the pump-power dependence, Burshteîn's equation is unable to fit any of the decay curves in the concentration range investigated here. The R^2 values of the fits are in the range 0.9307–0.9967 [Fig. 4.4(a)], 0.9289–0.9977 [Fig. 4.4(b)], and 0.9309–0.9981 [Fig. 4.4(c)].

Also Bernoulli's Eq. (4.22) is applied in the same two ways as described for the pump-power dependence, in conjunction with the expression for the initial condition $N_1(0)$ as calculated with Eq. (B5) in Appendix B. The parameters used in the calculation of $N_1(0)$ are listed in the third column of Table 4.1. When assuming the upconversion coefficient W_{ETU1} as the only free parameter, while the intrinsic lifetime τ_1 has the correct value of 7.55 ms [Fig. 4.4(d)], Eq. (4.22) is unsuccessful in fitting the measured decay curves, especially at higher Er^{3+} concentrations, because its exponential tail, with the decay time representing the intrinsic lifetime τ_1, cannot reproduce the increasingly steeper exponential tail of the decay curves. The R^2 values of the fit are in the range 0.9894–0.9995. Misinterpreting τ_1 as the concentration-dependent values of t_{exp} [Fig. 4.4(e)] provides a better fit also for the concentration dependence. The R^2 values of the fit are in the range 0.9926–0.9995. This fit is performed in two different ways. In the first, Bernoulli's Eq. (4.22) is applied to each decay curve individually. In the second, the fit is performed on all eight decay curves simultaneously, assuming a linear increase of W_{ETU1} with dopant concentration. The results for W_{ETU1} obtained in these two ways are indicated by the open and solid circles in Fig. 4.6, respectively.

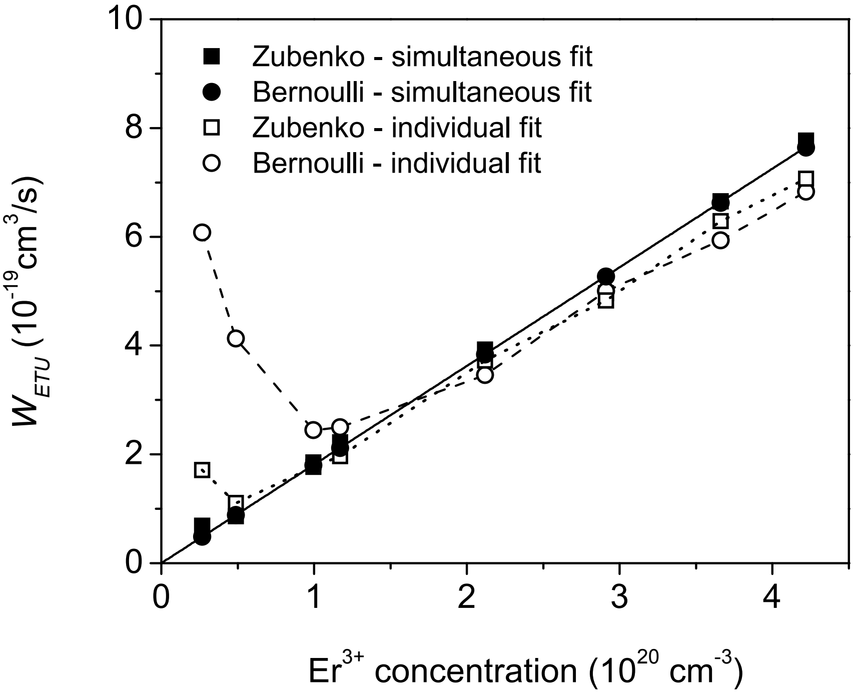

Fig. 4.6. Values of the ETU coefficient W_{ETU1} derived directly from the measured luminescence decay curves via Bernoulli's (circles) and Zubenko's (squares) models, with the equations performed on all eight decay curves simultaneously (solid symbols) and on the different decay curves individually (open symbols).

Finally, Eq. (4.21) of the more comprehensive Zubenko model, which takes into account energy migration and ETU, fits the luminescence decay curves with the intrinsic lifetime τ_1 = 7.55 ms for all dopant concentrations [Fig. 4.4(f)]. The R^2 values of the fit are in the range 0.9926–0.9998. A similar situation was found in Ref. [107], where the luminescence decay in different Nd^{3+}-doped crystals could not be reproduced with a rate-equation model, but only via Zubenko's treatment. In addition, this model provides more insight to the microscopic properties of the system, allowing us to extract information on the ETU microparameter C_{DA} and the most probable migration hopping time τ_0. Again, the fit is performed in two different ways. In the first, Zubenko's Eq. (4.21) is applied to each decay curve separately. In the second, the fit is performed on all eight decay curves simultaneously, assuming one common C_{DA} parameter. In the latter case, the fit with Zubenko's equation yields $C_{DA} = (6.1 \pm 0.6) \times 10^{-41}$ cm^6/s, while τ_0 exhibits a decrease from more than 100 ms down to 1 ms with increasing Er^{3+} concentration [Fig. 4.7(a)], because the decreasing distance among Er^{3+} ions enhances the probability of energy migration. Under the assumption $N_D = N_d$, Zusman's Eq. (4.14) becomes

$$\frac{1}{\tau_0} = C_{DD} N_d^{\,2}, \tag{4.24}$$

which is then fitted to the τ_0 data in the representation of Fig. 4.7(b), yielding $C_{DD} = (5.0 \pm 0.1) \times 10^{-39}$ cm^6/s. When substituting Eq. (4.24) into Eq. (4.18) we obtain

$$W_{ETU} = \frac{\pi^2}{3}\sqrt{C_{DA}C_{DD}}\, N_d\,, \tag{4.25}$$

and with C_{DA} and C_{DD} (or equivalently τ_0), the macroscopic ETU coefficient W_{ETU} can be obtained. The values of W_{ETU1} derived in this way, ranging from 0.7 to 7.8 × 10^{-19} cm^3/s, are indicated by the solid squares in Fig. 4.6 (and later in Fig. 5.8) and listed in the second column of Table 4.2. According to Eq. (4.25), W_{ETU} increases linearly with the Er^{3+} concentration, which is confirmed by our results. The W_{ETU1} values derived via the individual fits are indicated by the empty squares in Fig. 4.6.

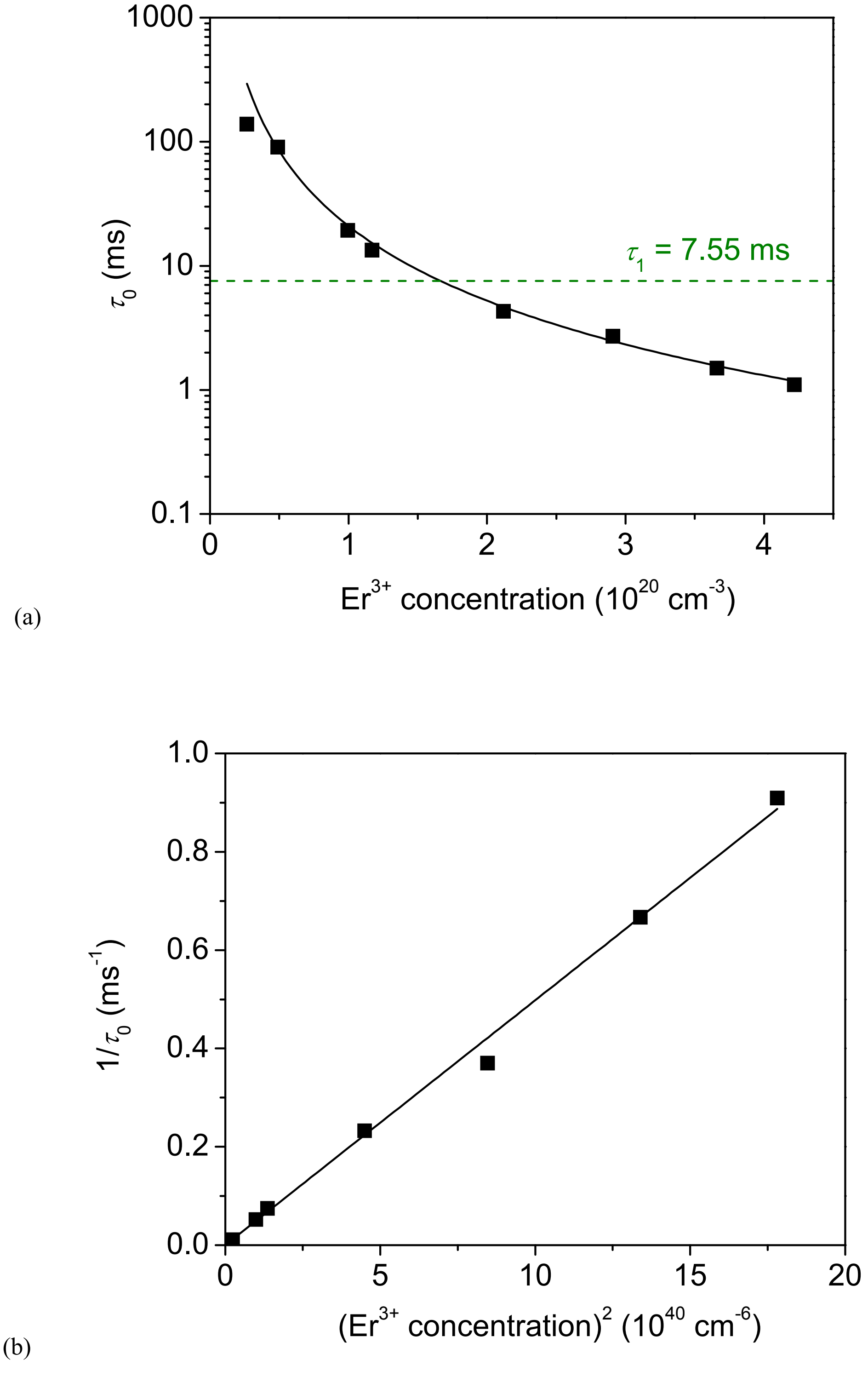

Fig. 4.7. (a) Most probable migration time τ_0 (squares) as a function of Er^{3+} concentration, along with the fit from Eq. (4.24). The intrinsic lifetime τ_1 = 7.55 ms (dashed line) is shown for comparison. (b) Inverse of τ_1 (squares) as a function of the square of Er^{3+} concentration, along with the linear fit from Eq. (4.24). In both graphs eight data points are present, but in the second graph the first two data points are so close to each other that they appear as one.

Table 4.2. Er^{3+} concentration N_d and upconversion coefficients W_{ETU1} extracted from, firstly, the analysis of luminescence decay curves with Zubenko's model in Sect. 4.2.3 (displayed as squares in Figs. 4.6 and later 5.8), secondly, the small-signal gain experiments of Ref. [32] after re-evaluation with an improved amplifier model explained in Sect. 5.1.3 (displayed as crosses in Fig. 5.8), and thirdly, the simultaneous fit of pump-absorption and luminescence-decay experiments with the quenched-ion rate-equation model in Sect. 5.1.1 (displayed as circles in Figs. 5.3(b) and 5.8). The latter are the values that correctly describe the luminescence-decay, pump-absorption, and gain experiments with a single set of parameters.

N_d [10^{20} cm^{-3}]	W_{ETU1} [10^{-19} cm^3/s]		
	Zubenko's model	**Simple amplifier model**	**Quenched-ion rate-equation model**
0.27	0.7		
0.49	0.9		
1.00	1.9		
1.17	2.2	25	2.9
2.12	3.9	50	4.7
2.91	5.0	85	7.5
3.66	6.7	89	9.2
4.22	7.8		

As can be seen from Fig. 4.6, the values of W_{ETU1}, extracted via Bernoulli's Eq. (4.22) when individual fits are performed, show a deviation at low Er^{3+} concentrations. The same occurs to the values of W_{ETU1}, extracted via the individual fits with Zubenko's Eq. (4.21), but to a lesser extent. One reason for this deviation is the smaller non-exponential part at the beginning of the luminescence decay at low concentrations, leading to a larger uncertainty in the estimation of the W_{ETU} coefficient. When Bernoulli's Eq. (4.22) and Zubenko's Eq. (4.21) are applied to each decay curve individually, this uncertainty reveals itself directly in the resultant value of W_{ETU}, whereas when the fits are performed on all eight decay curves simultaneously, the error decreases statistically. At low concentrations ETU is static, hence Grant's model breaks down [108], which explains the even larger deviation when Bernoulli's equation is applied. The linear dependence of W_{ETU} on dopant concentration is well reproduced at higher Er^{3+} concentrations, where ETU becomes migration-accelerated. In a number of publications, see, e.g., Refs. [81] and [108], a quadratic or even higher-order dependence was proposed, but in the light of our findings this was probably due to the limited range of dopant concentrations which were investigated and the high uncertainty at low dopant concentrations described above.

As can be seen from the solid data points in Fig. 4.6, the values of W_{ETU1} extracted via Bernoulli's Eq. (4.22), under the incorrect assumption of a concentration-dependent intrinsic lifetime and with the simultaneous fit of all decay curves, agree remarkably well with the same parameter values calculated from Zubenko's Eq. (4.25). The reason is that W_{ETU} is derived from the fast non-exponential part at the beginning of the decay curve, while ignoring the exponential tail. Therefore, one may conclude from the agreement of W_{ETU} values derived from Grant's and Zubenko's models that misinterpreting the intrinsic lifetime τ_1 in Bernoulli's Eq. (4.22) as a concentration-dependent fit parameter $\tau_1(N_d) = t_{\exp}(N_d)$ provides enough freedom to Grant's theory to fit the measured decay curves and derive reasonably correct values of the ETU parameter. Nevertheless, in the remainder of the paper we will continue to apply Zubenko's model, as it provides more physical insight than Grant's model.

4.3 Summary

Burshteĭn's and Zubenko's microscopic treatments of ETU, as well as Grant's macroscopic rate-equation approach have been applied to fit pump-power- and concentration-dependent decay curves of quasi-CW-excited luminescence in amorphous $Al_2O_3:Er^{3+}$. Whereas the donor-acceptor treatment by Burshteĭn does not adequately reproduce the measured decay curves, Zubenko's model provides very good agreement. When misinterpreting the intrinsic lifetime as a free parameter, also the traditional rate-equation approach results in reasonable fits and even delivers values of the macroscopic ETU parameter that are very similar to those derived from Zubenko's model.

Chapter 5

Quenched Ions in Er^{3+}- and Yb^{3+}-doped Al_2O_3

In Chapter 4 it was mentioned that one of the shortcomings of Zubenko's microscopic model of energy-transfer upconversion [91] is the fact that it treats all ions equally, thereby neglecting the locally different active environment of individual ions. In this Chapter we show that in fact Zubenko's model breaks down in the presence of a second, spectroscopically distinct class of ions, which in our experimental example is established by a fast quenching process that arises owing to, e.g., ion pairs and clusters or the presence of impurities or defects within the host material and affects only a fraction of the ions.

In this Chapter, in Section 5.1 we attempt to interpret simple pump-absorption and small-signal-gain experiments [28,32] with the values of the ETU parameter obtained in Chapter 4 from the analysis, with Zubenko's model, of luminescence decay curves from the Er^{3+} $^4I_{13/2}$ level measured under quasi-CW excitation. However, our attempt remains unsuccessful. The pump-absorption measurements reveal the presence of a quenching process which occurs at very short time scales and, consequently, is not shown in the luminescence decay curves under quasi-CW excitation. Based on this consideration, we extend Zubenko's model to account for such a fast quenching process. We extract the fraction of quenched ions and quantify its effect on the Al_2O_3:Er^{3+} amplifier performance. This approach allows us to describe the results of the luminescence-decay, pump-absorption, and small-signal-gain experiments over a large range of dopant concentrations with a single set of parameters. In Section 5.2 we prove that, regardless of the excitation conditions, Zubenko's model always breaks down when quenched ions are present. Under quasi-CW excitation it can fit the measured luminescence decay curves but provides incorrect values of the ETU parameter, because the quenching process remains undetected in the luminescence decay curves, whereas under short-pulse excitation, where the signature of the quenching process − a fast component at the beginning of luminescence decay − becomes evident, the model cannot fit the luminescence decay curves at all.

Finally, in Section 5.3 we further investigate the effect of the fast quenching on the small-signal gain in Al_2O_3:Er^{3+} waveguide amplifiers and on the laser performance of an Al_2O_3:Yb^{3+} distributed-feedback (DFB) laser. For the latter, we focus on the measurement of the laser relaxation-oscillation frequency as a function of pump rate, which are usually performed in order to determine parameters of the laser medium or cavity. We show that the fast quenching of a fraction of dopants affects the relaxation oscillations, resulting in incorrect values for the parameter deduced from this measurement. In the equations describing the relaxation oscillations, we replace the lifetime of the upper laser level by an effective lifetime that takes the quenching into account. In our Al_2O_3:Yb^{3+} DFB laser we observe significant quenching, with the effective lifetime being ≈ 18 times shorter than the intrinsic upper-laser-level lifetime.

5.1 Active and Quenched Ions

In this section we report two simple investigations in our channel waveguides, pump-absorption and signal-gain measurements, and try to fit their results with the macroscopic ETU parameter W_{ETU1} obtained from Zubenko's model in Chapter 4 in order to tests its validity. Both tests dramatically fail. From these investigations we understand that a significant fraction of doped ions is subject to a fast quenching process. An interpretation which includes this fast quenching process simultaneously explains both, the measured pump-absorption and signal-gain performance, with good quantitative agreement.

5.1.1 Pump-Absorption Measurements in Al_2O_3:Er^{3+}

In pump-absorption experiments, CW pump light is launched into the channel waveguide and the fraction of absorbed pump power as a function of launched pump power is deduced from the measured amount of transmitted pump light. For low pump power, a majority of ions is in the ground state and contributes to the pump absorption. At higher pump power, an increasing fraction of ions is excited to the $^4I_{13/2}$ level, thus pump absorption decreases and ultimately saturates.

Pump-absorption experiments were performed on four of the eight samples investigated in the previous Chapter. 1480-nm light from a diode laser was coupled into the waveguides through a single-mode fiber, and the transmitted pump light was coupled into a second fiber and sent to a detector. The fiber-to-chip coupling efficiency, necessary to estimate the launched and transmitted pump power [$P_P(0)$ and $P_P(L)$, respectively], was determined separately via insertion-loss measurements, by launching a small amount of pump light into the waveguides, measuring the transmitted light at the detector, and subtracting the known waveguide loss at 1480 nm. These were calculated with Eqs. (3.3) and (3.4) using the known waveguide confinement factors, Er^{3+} concentrations, cross-sections, and background propagation losses of Ref. [28]. A small length of $L \approx 1$ cm of each waveguide was used in order to ensure enough transmitted pump light could reach the detector [see "Length B" in Table 3.1(a) of Chapter 3].

As an example, the squares in Fig. 5.1 show the pump absorption versus launched pump power of the waveguide with an Er^{3+} concentration of 3.66×10^{20} cm^{-3}. These data were then simulated with the rate equations (B4-B5) and propagation Eq. (B9) in Appendix B (with $f_a = 1$ and $f_q = 0$), using the parameters listed in the fourth column of Table 4.1 of Chapter 4 and the values of W_{ETU1} (= 6.7×10^{-19} cm^3/s in the example of Fig. 5.1) obtained from Zubenko's model (solid squares in Fig. 4.6). The result of the simulation, represented by the black dashed line (1) in Fig. 5.1 strongly underestimates the amount of pump light absorbed in the waveguide. Apparently, a significant amount of absorption is nonsaturable at the applied pump powers.

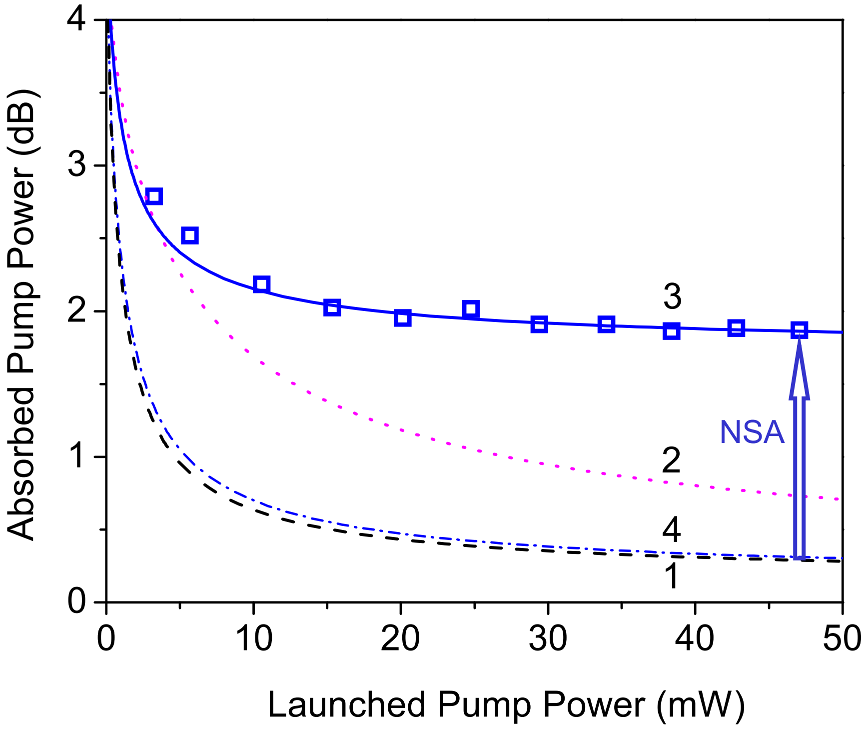

Fig. 5.1. Absorbed pump power, equal to -10·log[$P_P(L)$ / $P_P(0)$], versus launched pump power for a waveguide with an Er^{3+} concentration of 3.66 × 10^{20} cm^{-3} and 1 cm length. The squares are the experimental data. Calculated with the equations presented in Appendix B, Part 1, for $f_q = 0$ (no quenched ions), the black-dashed line (1) represents the simulation with $W_{ETU1} = 6.7 \times 10^{-19}$ cm^3/s from Zubenko's model and the magenta-dotted line (2) represents the simulation with $W_{ETU1} = 89 \times 10^{-19}$ cm^3/s, as obtained from fitting the measured internal net gain as a function of launched pump power with the simple amplifier model. Calculated with the quenched-ion rate-equation model, the blue solid line (3) is the fit of the experimental data with the correct parameters $W_{ETU1} = 9.2 \times 10^{-19}$ cm^3/s and $f_q = 32.5\%$ and the blue dashed-dotted line (4) is the simulation with the same model for $f_q = 0\%$ (no quenched ions). The arrow indicates the nonsaturable absorption (NSA) contribution. Only the quenched-ion rate-equation model resulting in curve 3 correctly fits the experimental results (for all investigated Er^{3+} concentrations).

A number of authors [109-113] have attributed a similar behavior observed in other host materials to a fast quenching process. In our samples, such a process can be induced by, e.g., fast static ETU due to active ion pairs or clusters, energy transfer to undesired impurities, or trapping of excitation energy by host material defects, such as voids. The presence of Er^{2+} ions as possible source of impurities was also considered initially, but this oxidation state does not absorb light at 1480 nm [114]. Besides, Er^{2+} absorption bands, which occur in the ranges 300-1100 nm and 1900-2400 nm, have never been detected in our absorption measurements. Host material defects are inherent to amorphous materials such as Al_2O_3, but can be diminished by increasing the deposition temperature, see Fig. 3.10. Fast static ETU requires a close proximity of active ions, i.e., pairs or clusters, the likeliness of which to occur also decreases with increasing deposition temperature. Accordingly, during the process of optimization of the Al_2O_3 deposition procedure [115] we have observed an increase in luminescence lifetime of the $^4I_{13/2}$ level with increasing deposition temperature, see Fig. 5.2. The incorporation of undesired impurities is largely determined by the purity of materials from which the active layer is fabricated. Since an Er metallic target of higher purity than 99.95% could not be purchased, the Er target included a number of other rare-earths, transition-metals, and other elements [116], see Table 5.1, which makes the occurrence of fast energy-transfer processes to those elements and according lifetime quenching of the excited states of Er^{3+} rather likely. Since with higher Er^{3+} concentration also larger concentrations of impurities from the same target were incorporated in the film, the fraction of Er^{3+} ions affected by this type of quenching increases with Er^{3+} concentration.

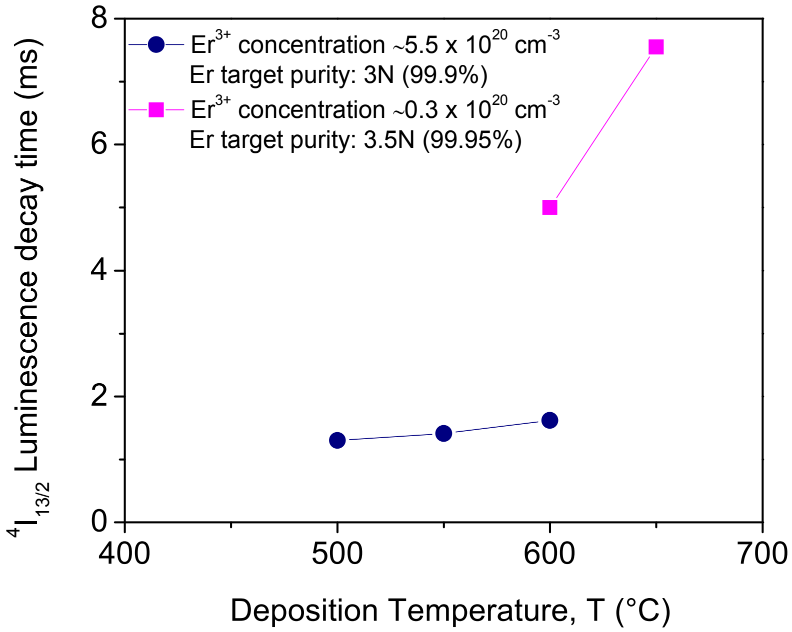

Fig. 5.2. $^4I_{13/2}$ lifetime as a function of deposition temperature for samples with an Er^{3+} concentration of ≈ 5.5×10^{20} cm^{-3}, deposited using an Er sputtering target with purity of 3N (99.9%) (blue dots) and for samples with an Er^{3+} concentration of ≈ 0.3×10^{20} cm^{-3}, deposited using an Er sputtering target with purity of 3.5N (99.95%) (magenta squares) [115].

Table 5.1. List of rare-earth and non-rare-earth impurities present in the Er sputtering target with a purity of 3.5N (99.95%) used in the deposition of the Er samples investigated in this thesis [116].The given purity refers to the purity among the rare-earths; non-rare-earth impurities may occur up to 1% (weight) in the starting material. TREM: Total Rare-Earth Metal.

TREM	**Er/TREM**	**Rare-Earth Impurities**	**Non-Rare-Earth Impurities**										
min %	**min %**	**max %**	**max %**										
		Dy+Ho+Tm+Yb+Y	**Fe**	**Mg**	**Ca**	**Si**	**Al**	**W**	**Mo**	**Ti**	**C**	**O**	**S**
99	99.95	0.05	0.01	0.05	0.01	0.01	0.03	0.03	0.03	0.01	0.02	0.03	0.01

The quenched ions absorb pump light and are excited to the first excited state, but are then rapidly deactivated by the quenching process and return to the ground state, thus contributing to absorption again. As a consequence, an increased fraction of ions resides in the ground state, adding a nonsaturable component to the 1480-nm pump-light absorption, and absorption saturates at a higher level.

This phenomenon of fast quenching of only a fraction of ions is in contradiction with the fundamental assumption of Zubenko’s model that all ions are identical, in the sense that they have identical environments and, hence, identical probabilities to decay via luminescence, energy transfer, or ETU. In order to determine the fraction of quenched ions, we introduce a simple quenched-ion rate-equation model (see Appendix B, Part 1) that generalizes the ion-pair scheme presented in Ref. [109] to all the potential quenching mechanisms mentioned above. The quenched ions still absorb pump light, like the active ions do, but their luminescence is strongly quenched with a characteristic decay time τ_{1q}. This quenched decay time has been the subject of several investigations in other host materials, resulting in values either on the order of a few μs [110] or as short as 50 ns [113], in both cases orders of magnitude shorter than the lifetime τ_1 of the $^4I_{13/2}$ metastable level.

The pump-absorption measurements presented in this section and the luminescence decay curves from the previous section are analyzed with the quenched-ion rate-equation model to extract the fractions f_a of active and f_q of quenched ions and the correct values of W_{ETU1}. Since the quenching effect was not taken into account in the analysis of luminescence decay curves in Chapter 4, $N_1(0)$ was overestimated, leading to an underestimation of W_{ETU1} via Zubenko's model.

The value of f_q is varied and the pump-absorption and luminescence-decay curves are fitted simultaneously until the same value of W_{ETU1} is obtained. The fractions of active and quenched ions as a function of Er^{3+} concentration are displayed in Fig. 5.3(a). The correct values of W_{ETU1} resulting from this procedure are given in the last column of Table 4.2 and shown in Fig. 5.3(b), together with a linear fit of the former W_{ETU1} values from Zubenko's model (taken from Fig. 4.6). The correct values of W_{ETU1} are found to be independent of the specific value chosen for τ_{1q}, for values up to $\tau_{1q} \approx \tau_2 = 60$ μs, the lifetime of the second excited state. This range of τ_{1q} includes both, the values of 50 ns [113] and few μs [110] found in the literature. f_q increases with increasing Er^{3+} concentration, reaching a value of 32.5% for the Er^{3+} concentration of 3.66×10^{20} cm^{-3}, potentially due to the increasing probability of Er^{3+}-pair/cluster formation, the larger number of luminescence-quenching defects, and/or the increasing concentration of impurities (if introduced to the samples as part of the Er^{3+}-containing raw material) and closer proximity of Er^{3+} ions to them with increasing dopant concentration.

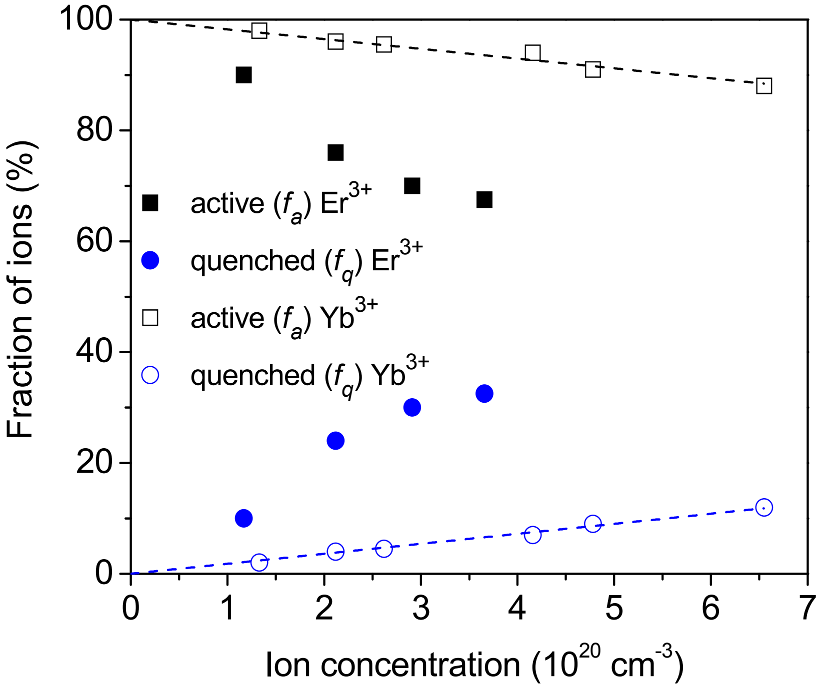

(a)

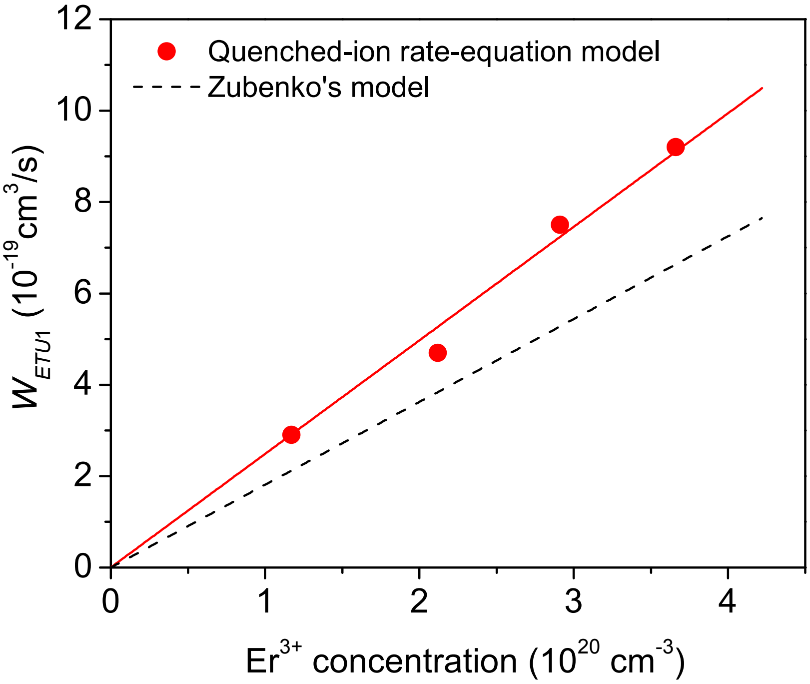

(b)

Fig. 5.3. (a) Fractions f_a of active and f_q of quenched ions (solid symbols) and (b) values for the ETU coefficient W_{ETU1} (circles) as a function of Er^{3+} concentration, derived by the simultaneous fit of pump-absorption and luminescence-decay measurements with the quenched-ion rate-equation model, along with a linear fit. In (a) the f_a and f_q values for Yb^{3+}-doped Al_2O_3 (open symbols) and in (b) the linear fit of W_{ETU1} from Zubenko's model (dashed line), taken from Fig. 4.6, are also shown for comparison.

From Table 4.2 it becomes evident that the correct ETU coefficients W_{ETU1} are different from those previously determined when solely fitting the luminescence-decay curves in Chapter 4, with an average increase of roughly 40%, resulting in a corresponding increase by 90% of C_{DA} to $(11.6 \pm 1.1) \times 10^{-41}$ cm^6/s, while τ_0 is not affected. Figure 5.1 shows the fit of the experimental pump-absorption data (squares) with the quenched-ion rate-equation model, represented by the blue solid line (3), yielding $f_q = 32.5\%$ and $W_{ETU1} = 9.2 \times 10^{-19}$ cm^3/s for the specific Er^{3+} concentration of 3.66×10^{20} cm^{-3}, as well as the calculated absorption curve for the same W_{ETU1} coefficient but $f_q = 0\%$ as comparison, represented by the blue dashed-dotted line (4). The nonsaturable component of the 1480-nm pump-light absorption, resulting in the gap between the two curves and indicated by the arrow, grows with sample length, fraction of quenched ions, and, thus, with Er^{3+} concentration. Figure 5.4 presents the proof that the luminescence decay curves can be fitted using the new and correct C_{DA} microparameter, in conjunction with considering the fraction of quenched ions. Equation (4.21) is again used to fit the curves, but $N_1(0)$ is replaced by $N_{1a}(0)$ calculated in Appendix B, Part 1. The R^2 values of the fit are in the range 0.9926–0.9998.

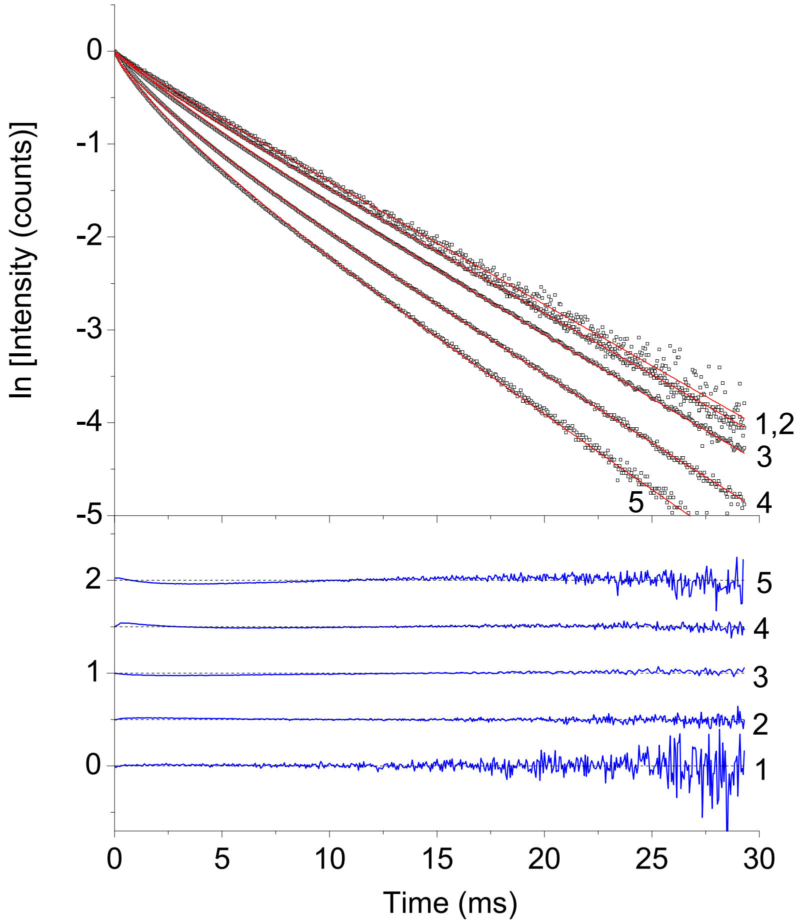

Fig. 5.4. The same normalized luminescence decay curves as in Fig. 4.4, this time fitted using Zubenko's model with the microscopic ETU parameter $C_{DA} = (11.6 \pm 1.1) \times 10^{-41}$ cm^6/s, derived under consideration of a concentration-dependent fraction of quenched ions. The residuals are shown at the bottom of the graph. There is no noticeable difference with Fig. 4.4(f).

5.1.2 Pump-Absorption Measurements in $Al_2O_3:Yb^{3+}$

In order to understand which mechanism is most likely responsible for the quenching in $Al_2O_3:Er^{3+}$, we performed luminescence-decay and pump-power experiments also on $Al_2O_3:Yb^{3+}$ waveguides which were fabricated in the same way as the Er^{3+}-doped samples. Yb^{3+} ions, unlike Er^{3+} ions, have only one excited state, hence they do not undergo ETU. Therefore, the quenching in $Al_2O_3:Yb^{3+}$ is due mostly to impurities and/or defects. In general, additional cooperative upconversion via exchange interaction between two Yb^{3+} ions may occur, but this process was discarded in Chapter 2 for the $Al_2O_3:Yb^{3+}$ case.

Pump-absorption experiments were performed on the six $Al_2O_3:Yb^{3+}$ samples listed in Table 3.1(b) in Chapter 3, with the same procedure used on $Al_2O_3:Er^{3+}$, but in this case 976-nm light was employed and the waveguide had a smaller length of $L \approx 0.5$ cm. As an example, the squares in Fig. 5.5 show the pump absorption versus launched pump power of the waveguide with an Yb^{3+} concentration of 4.16×10^{20} cm^{-3}.

Before the data could be simulated with the quenched-ion rate-equation model, the value of the luminescence lifetime of Yb^{3+} in Al_2O_3 needed to be determined. Therefore luminescence-decay measurements were performed on the six samples with the technique described in Sect. 3.2.4 of Chapter 3, and the results as a function of Yb^{3+} concentration are shown in Fig. 5.6. The $^2F_{5/2}$ luminescence decay time decreases from 708 µs down to 311 µs (± 18 µs) when the Yb^{3+} concentration increases from 1.33 to 6.55×10^{20} cm^{-3}. The empirical law of Eq. (4.23), with $p = 2$, provided a good fit to the data (red line). The extrapolation to zero concentration results in an intrinsic lifetime of the Yb^{3+}-excited level of $\tau_1 = 740$ µs.

These pump-absorption data were then simulated with the rate equations (C1-C2) and propagation Eq. (C4) in Appendix C, using the parameters listed in the Table 5.2. The simulation gives as result the fraction of active/quenched ions $f_{a/q}$, shown in Fig. 5.3(a). The $f_{a/q}$ values are found to be independent of the specific value chosen for τ_{1q}, as long as $\tau_{1q} << \tau_1$. The exact value of τ_{1q} is not known at this stage, but later we find in Sect. 5.3.2 that $\tau_{1q} = 4.7$ µs in an $Al_2O_3:Yb^{3+}$ laser with an Yb^{3+} concentration of 5.8×10^{20} cm^{-3}, which is comparable with a quenched lifetime of a few µs reported in an Yb^{3+}-doped silica fiber [112].

From the results presented in Fig. 5.3(a) we see that f_q reaches only 12% for the very high Yb^{3+} concentration of 6.55×10^{20} cm^{-3}, a value that is much lower than in the case of Er^{3+}, indicating that in our Er^{3+}-doped samples the pair/cluster formation, resulting in static ETU among nearest-neighbor Er^{3+} ions, might be the major cause of fast quenching. In the Yb^{3+} case f_q shows a rather linear dependence on dopant concentration, indicated by a qualitative linear fit, whereas in the Er^{3+} case the dependence is more complex. Although we cannot entirely exclude that experimental errors have led to the particular concentration dependence, it could arise due to the addition of several effects: the potentially dominant ETU between nearest-neighbor Er^{3+} ions, linear quenching owing to impurities and/or defects, and a saturation effect that seems to appear at high Er^{3+} concentrations.

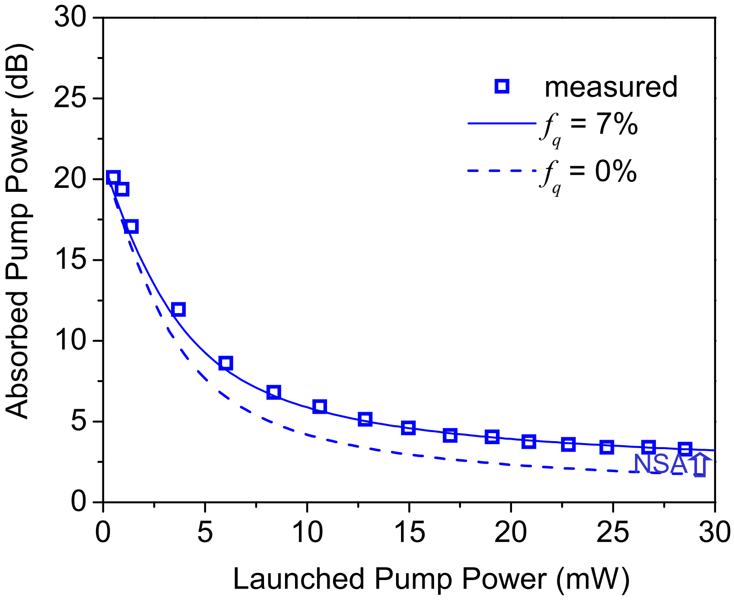

Fig. 5.5. Absorbed versus launched pump power for a waveguide with an Yb^{3+} concentration of 4.16 × 10^{20} cm^{-3} and 0.5 cm length. The squares are the experimental data, the blue solid line is the fit of the experimental data with the quenched-ion rate-equation model, yielding f_q = 7%, and the blue dashed-dotted line is the simulation with the same model for f_q = 0% (no quenched ions). The arrow indicates the nonsaturable absorption (NSA) contribution.

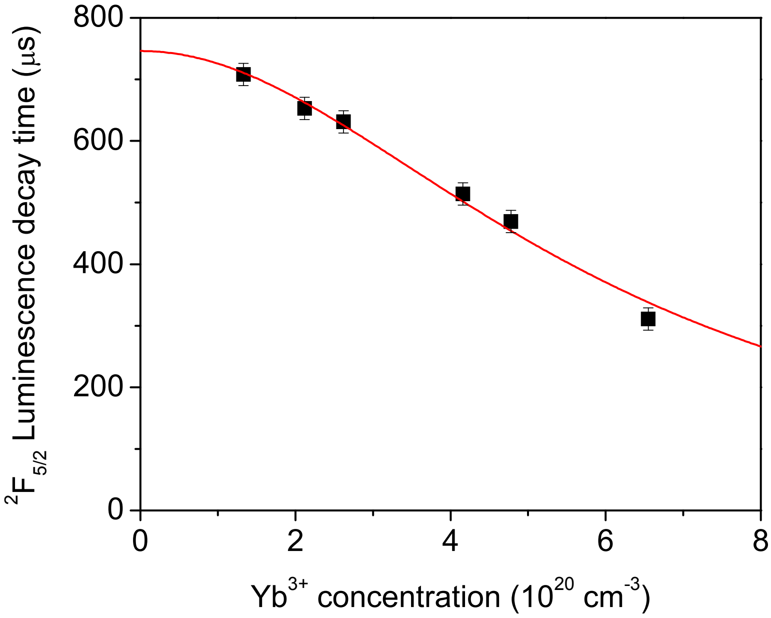

Fig. 5.6. $^2F_{5/2}$ luminescence decay time as a function of Yb^{3+} concentration. The red curve is the best least-square fit with Eq. (4.23) for $p = 2$.

Table 5.2. Parameter values used in pump-absorption calculations in Al_2O_3:Yb^{3+}. Unless otherwise specified, the parameter values are from this work.

Parameter	Symbol	Value	Units
Pump wavelength	λ_P	976	[nm]
Pump absorption cross-section	$\sigma_{GSA}(\lambda_P)$	12.70×10^{-21}	[cm^2]
Pump emission cross-section	$\sigma_{em}(\lambda_P)$	12.70×10^{-21}	[cm^2]
Luminescence lifetime	τ_1	740	[µs]
Fast quenched decay time	τ_{1q}	4.7	[µs]
Background loss pump	$\alpha_{bck}(\lambda_P)$	0.25 [28]	[dB/cm]

5.1.3 Signal-Gain Measurements in Al_2O_3:Er^{3+}

After the lesson we have learned from the pump-absorption measurements, it does not come as a surprise that also independent small-signal gain measurements in Al_2O_3:Er^{3+} exhibit a dramatic deviation from simple model predictions using the data obtained solely from Zubenko's model in Chapter 4. Since the quenched ions exhibit a fast decay-rate constant, not only the pump-rate constant is too small to evoke a significant excitation density among this fraction of ions (Sect. 5.1.1), but also the weak signal intensity in typical small-signal-gain experiments is insufficient to allow the stimulated-emission rate at the signal wavelength to compete with the fast quenching process. As a result, the fraction of quenched ions is not accessible by the signal light, but solely induces a loss of pump intensity. In contrast, as discussed later in Sect. 5.3.2, in an Al_2O_3:Yb^{3+} distributed-feedback laser [31] quenched ions introduced a saturable loss which increased the threshold pump rate, but otherwise did not affect the laser performance, because the enormous intra-cavity laser intensity enforced stimulated emission at a faster time scale than the value of τ_{1q} of a few µs.

In Refs. [28] and [32] small-signal gain experiments in Al_2O_3:Er^{3+} under 976-nm pumping were reported on the same samples investigated in the present paper, together with a simple amplifier model, and in Fig. 5.7 we reproduce one of the results (circles) reported therein, namely the measured internal net gain as a function of pump power for an Er^{3+} concentration of 2.12×10^{20} cm^{-3}. As shown in Fig. 5.7, the W_{ETU1} coefficient obtained with Zubenko's model in Chapter 4 (squares in Fig. 4.6), combined with the assumption of $f_q = 0\%$, represented by the black dashed curve (1), leads to a significant overestimation of the attainable small-signal gain (circles).

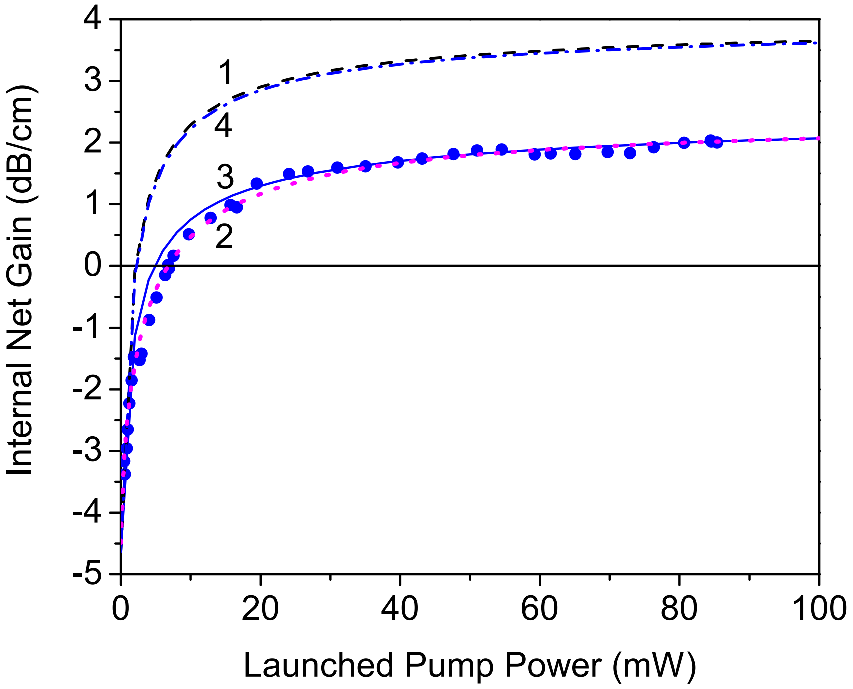

Fig. 5.7. Internal net gain as a function of launched pump power for a channel-waveguide amplifier with an Er^{3+} concentration of 2.12×10^{20} cm^{-3}. The dots are experimental data (from Ref. [28]). Calculated with the simple amplifier model, i.e., for $f_q = 0$ (no quenched ions), the black-dashed line (1) represents the simulation with $W_{ETU1} = 3.9 \times 10^{-19}$ cm^3/s from Zubenko's model and the magenta-dotted line (2) is the fit of the experimental data, resulting in $W_{ETU1} = 50 \times 10^{-19}$ cm^3/s. Calculated with the quenched-ion rate-equation model, the blue solid line (3) is the simulation with the correct parameters $W_{ETU1} = 4.7 \times 10^{-19}$ cm^3/s and $f_q = 24\%$ and the blue dashed-dotted line (4) is the simulation with the same model for $f_q = 0\%$ (no quenched ions). These curves have the same color and pattern as the corresponding curves in Fig. 5.1. Only the quenched-ion rate-equation model resulting in curve 3 simultaneously fits the experimental results of Figs. 5.1 and 5.7 (for all investigated Er^{3+} concentrations).

Compared to the correct W_{ETU1} coefficients obtained with the quenched-ion rate-equation model, the W_{ETU1} coefficients reported in Refs. [28,32], which were obtained by fitting the results of small-signal gain experiments with the simple amplifier model, represented by the magenta dotted line (2) in Fig. 5.7, are approximately one order of magnitude too high. Even when taking into account the real waveguide and optical mode geometries determined using the PhoeniX FieldDesigner software package [106] and a better estimate of 60 µs (instead of 100 µs [28,32]) for the lifetime τ_2 of the second excited state (the parameters of this calculation are listed in the fifth column of Table 4.1), the W_{ETU1} coefficients from the amplifier model (third column of Table 4.2) exhibit a one-order-of-magnitude difference with the correct W_{ETU1} coefficients obtained from the quenched-ion rate-equation model (Fig. 5.8). Since the fast quenching mechanism was not considered in the simple amplifier model nor in the model with improved consideration of the waveguide and optical mode geometries, the quenching was automatically attributed to stronger ETU, which was the only free parameter in the simple amplifier model [28,32], thereby significantly overestimating the W_{ETU1} coefficients. Moreover, the pump absorption predicted with the W_{ETU1} coefficients from the simple amplifier model ($W_{ETU1} = 89 \times 10^{-19}$ cm^3/s in the example of Fig. 5.1), represented by the magenta dotted line (2) in Fig. 5.1, underestimates the measured data (squares in Fig. 5.1). The formerly published [28] and also the revised (third column of Table 4.2) W_{ETU1} coefficients from the simple amplifier model are, therefore, incorrect.

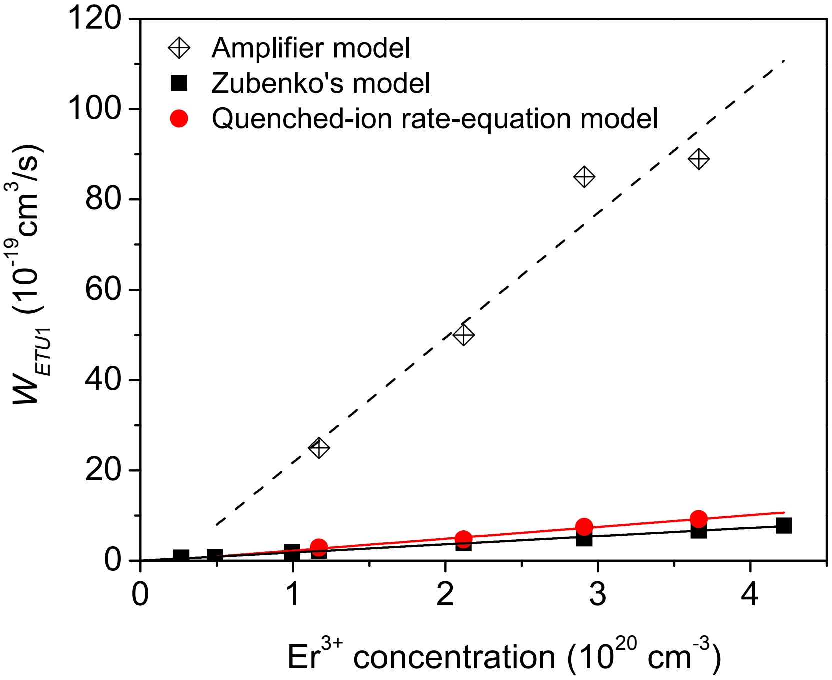

Fig. 5.8. Values of the ETU coefficient W_{ETU1} derived from the amplifier model of Refs. [28] and [32] (open diamonds), from Zubenko's model (squares), and from the quenched-ion rate-equation model (red dots). The latter are the values that correctly describe the luminescence-decay, pump-absorption, and gain experiments with a single set of parameters.

To account for the fast quenching process in the simple, 976-nm-pumped amplifier model, we introduce $f_{a/q}$ and τ_{1q} in Eqs. (10-12) of Ref. [28] in the same way as proposed by the equations in the Appendix B, Part 1 of this work. In the specific example of Fig. 5.8, i.e., for the Er^{3+} concentration of 2.12×10^{20} cm^{-3}, the values $W_{ETU1} = 4.7 \times 10^{-19}$ cm^3/s [Table 4.2 and Fig. 5.3(b)] and $f_q = 24\%$ [Fig. 5.3(a)] were used to calculate the blue solid curve (3), which agrees well with the measured data (circles). For comparison, we also show the calculated gain curve for the same W_{ETU1} coefficient, but $f_q = 0\%$, represented by the blue dashed-dotted line (4), which would result in a gain of ≈ 3.6 dB/cm, almost double the maximum value of 2 dB/cm which was experimentally achieved with the Er^{3+} concentration of 2.12×10^{20} cm^{-3}, indicating that the fast quenching process strongly affects the amplifier performance. With the f_q and correct W_{ETU1} values determined by the quenched-ion rate-equation model, the small-signal gain curves for the same four Er^{3+} concentrations investigated in the pump-absorption measurements are correctly reproduced.

This final proof completes the picture. With a single microscopic energy-migration parameter $C_{DD} = (5.0 \pm 0.1) \times 10^{-39}$ cm^6/s, resulting in the concentration dependence of the most probable migration hopping time τ_0 as displayed in Fig. 4.7 (a), and a single microscopic ETU parameter $C_{DA} = (11.6 \pm 1.1) \times 10^{-41}$ cm^6/s, derived under consideration of a concentration-dependent fraction of quenched ions [Fig. 5.3(a)] and resulting in a macroscopic W_{ETU1} coefficient [last column of Table 4.2 and circles in

Fig. 5.3(b)] which is proportional to the Er^{3+} concentration [solid line in Fig. 5.3(b)], Zubenko's microscopic model correctly predicts the 1533-nm luminescence-decay curves pumped at 1480 nm (Fig. 5.4), the macroscopic quenched-ion rate-equation model correctly predicts the pump-absorption measurements at 1480 nm (Fig. 5.1), and the macroscopic quenched-ion amplifier model correctly predicts the 1533-nm small-signal gain experiments pumped at 977 nm (Fig. 5.7), for the investigated Er^{3+} concentrations.

5.2 Fast Spectroscopic Processes as an Example of Distinct Ion Classes and the Breakdown of Upconversion Models

The finding of the previous section that only under the assumption of a fast quenching process with a decay time similar to or faster than a few μs one can verify theoretically the measured luminescence-decay, pump-absorption, and gain experiments, raises the question why the probably most comprehensive microscopic ETU model by Zubenko is unable to predict the correct microscopic parameters C_{DD} of energy migration and C_{DA} of ETU directly. In this section we show that the fast quenching process leads to a negligible emission of photons in steady-state conditions, i.e., luminescence decay curves after quasi-CW excitation do not deliver a complete picture of the population dynamics of the system. A short-pulse excitation is ideal to reveal the presence of quenched ions. Nevertheless, we show that Zubenko's model fails in both cases: in the first case it provides incorrect results, because an important deactivation mechanism is not revealed in the luminescence decay curves, whereas in the second case it is not even possible to fit the luminescence decay curves, because the upconversion model does *a priori* not distinguish between different ion classes.

5.2.1 Quenched Ions Undetected in Luminescence-Decay Measurements under Quasi-CW Excitation

Although the quenching process has been verified by pump-absorption and independently by signal-gain experiments, it is not revealed by any particular signature in luminescence decay curves under quasi-CW excitation. While the temporal resolution of the experimental setup (a few μs in our case) can influence the measurement, we proof that curves under quasi-CW excitation the relative luminescence intensity produced by the quenched ions is negligible to that arising from active ions even at the beginning of the decay ($t = 0$). Since the relative intensities depend on the value of τ_{1q}, we test both, the 50 ns reported in Ref. [113] and the value on the order of 1 μs found in Refs. [109-112]. Under quasi-CW excitation, the ratio $I_{1q}(0) / I_{1a}(0)$ of the luminescence intensities of quenched and active ions, respectively, at $t = 0$ is calculated as

$$\frac{I_{1q}(0)}{I_{1a}(0)} = \frac{N_{1q}(0)}{N_{1a}(0)}, \tag{5.1}$$

where $N_{1a}(0)$ and $N_{1q}(0)$ are the corresponding population densities calculated via Eq. (B5) and the $f_{a/q}$ values determined in the previous Section and shown in Fig. 5.3(a). Owing to their short lifetime, the relative excitation density and resulting luminescence intensity from quenched ions (second and third column of Table 5.3) is on the order of ≈ 10^{-3} in the best case and decreases further as τ_{1q} decreases. Such low intensities frequently vanish in the noise of the strong luminescence from the active ions. The implication is that luminescence decay experiments under quasi-CW excitation provide an incomplete picture of the dynamic response of the system, leaving quenched ions undetected. Other investigation tools, such as pump-absorption experiments, are indispensable to complete the picture.

Fast quenching processes are probably present in many optical materials, in crystals [117] as well as in glass hosts like ours. Applying an upconversion model that treats all ions equally to the incomplete picture provided by luminescence decay experiments under quasi-CW excitation necessarily leads to incorrect results. This type of experiments is a wide-spread investigation tool [118-120], and many spectroscopic studies are based exclusively on them. The parameter values derived from such studies may be inaccurate, resulting in incorrect predictions of device performance. Also the physical processes involved may be misinterpreted, as in Ref. [118] where the authors proposed a non-existing excited-state-absorption process at the 1480-nm pump wavelength and attributed it to the $^4I_{13/2} \rightarrow {}^4I_{9/2}$ transition which occurs only at longer wavelengths, in order to simulate the luminescence decay and luminescence vs. pump power curves measured in Al_2O_3:Er^{3+} samples. It was likely a fast quenching process, which did not reveal itself in the former but affected the latter measurement, that affected their analysis.

Table 5.3. Er^{3+} concentration N_d and calculated intensity ratio $I_{1q}(0)/I_{1a}(0)$ of luminescence from quenched and unquenched ions after quasi-CW and short-pulse excitation, for τ_{1q} assuming the value of 50 ns and 1 μs.

N_d [10^{20} cm^{-3}]	**$I_{1q}(0)/I_{1a}(0)$**			
	Quasi-CW excitation		**Short-pulse excitation**	
	τ_{1q} = 50 ns	**τ_{1q} = 1 μs**	**τ_{1q} = 50 ns**	**τ_{1q} = 1 μs**
1.17	1.57×10^{-5}	3.13×10^{-4}	1.11×10^{-1}	1.11×10^{-1}
2.12	1.13×10^{-4}	2.23×10^{-3}	3.16×10^{-1}	3.16×10^{-1}
2.91	2.37×10^{-4}	4.69×10^{-3}	4.29×10^{-1}	4.29×10^{-1}
3.66	3.07×10^{-4}	6.09×10^{-3}	4.81×10^{-1}	4.81×10^{-1}

5.2.2 Quenched Ions in Luminescence-Decay Curves under Pulsed Excitation and the Breakdown of Zubenko's Model

In order to boost the luminescent response of quenched ions, one can excite the system with a pulse of a duration short compared to τ_{1q}. In this case, all the ions are excited with equal probability at $t = 0$. The intensity ratio is then simply computed as

$$\frac{I_{1q}(0)}{I_{1a}(0)} = \frac{N_{1q}(0)}{N_{1a}(0)} = \frac{f_q}{f_a}, \tag{5.2}$$

and from the last two columns of Table 5.3 we see that in this case the luminescence intensity of quenched ions is noticeable, being on the order of 10^{-1}.

Consequently, luminescence decay curves after short-pulse and quasi-CW excitation look qualitatively very different. As an example, the black line in Fig. 5.9 represents the simulation of a luminescence decay curve after short-pulse excitation, for an Er^{3+} concentration of 2.12×10^{-20} cm^{-3}. For this calculation we chose τ_{1q} = 1 μs, but results are qualitatively similar for different (shorter) values. The fast decay of quenched ions at the beginning of the curve is evident.

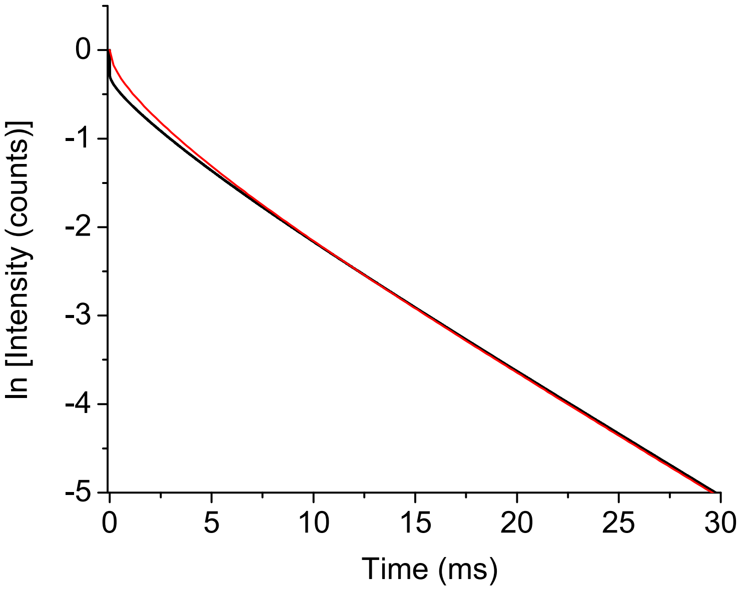

Fig. 5.9. Simulation of a luminescence decay curve (normalized) after short-pulse excitation (black line) for an Er^{3+} concentration of 2.12×10^{20} cm^{-3}. The red line is the tentative fit with Zubenko's model.

However, Zukenko's Eq. (4.21) fails to adapt to this fast decay, as proven by a tentative fit (red line). Under quasi-CW excitation Zubenko's model fits the luminescence decay curves properly, but it predicts incorrect values of the ETU parameter W_{ETU1}, because information about the quenched ions is missing in those luminescence decay curves. When information about the fast quenching process is included in the luminescence decay curves, because the measurement is performed under short-pulse excitation, Zubenko's model breaks down. The origin of this breakdown is of fundamental nature: Zubenko's theory and all the theories his model builds upon are based on the assumption of a homogeneous distribution of ions, i.e., all ions are assumed to have the same local environment, hence the same probabilities of intrinsic decay and interaction with neighboring ions. Consequently, the model treats all ions equally. This assumption is already violated in the case of a statistical distribution of ions in the host material, because statistically evoked pairs or clusters form localized aggregates in discrete regions, thus disrupting the homogeneity, hence one of the fundamental requirements of the theory is jeopardized. Ion clustering in glass matrices or two non-equal lattice sites for rare-earth-ion incorporation in specific crystalline hosts can even lead to a non-statistical, systematic violation of the model assumptions. Generally, the presence of spectroscopically distinct ion classes in a host material, whether resulting in fast luminescence quenching or otherwise influencing the temporal population dynamics, may lead to a breakdown of upconversion models that treat all ions equally.

Although our quenched-ion rate-equation model is successful in addressing the observed fast quenching process via only one phenomenological parameter τ_{1q}, it would be desirable to have a model available that takes into account such a quenching process or, more generally, different classes of ions with different transition probabilities *ab initio*. One step on the route toward such a more comprehensive model could be to include the non-uniformity in the ion distribution by looking directly at the local structure in the series of coordination spheres around the rare-earth ions [121]. This may be a practical approach in the case of crystalline host materials with well-defined lattice sites for the rare-earth ions and a statistical ion distribution, i.e., without chemically induced clustering effects, but for glass materials with pronounced clustering effects, such as silica, this approach will probably not suffice.

5.3 Impact of Fast Quenching on Amplifiers and Lasers

5.3.1 Effect on Small-Signal Gain in Al_2O_3:Er^{3+} Waveguide Amplifiers

In this Section, we investigate the quantitative influence of migration-accelerated ETU, determined by the concentration-dependent W_{ETU1} coefficient, and fast luminescence quenching, determined by the fraction of quenched ions f_q, on the performance of Al_2O_3:Er^{3+} waveguide amplifiers.

The dots in Fig. 5.10 indicate the experimental internal net gain per unit length for varying Er^{3+} concentration [28], for a launched pump power of 100 mW at 976 nm and signal power of 1 μW at 1533 nm, measured in the same samples investigated in this work. The simulations, whose results are given by the lines, were performed with the macroscopic quenched-ion amplifier model for the same parameters.

The upper solid line represents the gain in the absence of both, migration-accelerated ETU and fast quenching, i.e., W_{ETU1} and f_q were set to zero; only a weak saturation of internal net gain versus Er^{3+} concentration is visible, which results from an increasing fraction of the experimentally available pump power of 100 mW being absorbed at higher dopant concentrations, thus slowly approaching the maximum gain that can be obtained with the available pump power in this material. The dashed line represents a simulation where only migration-accelerated ETU is considered, under the assumption that the linear dependence of W_{ETU1} on Er^{3+} concentration in Fig. 5.3(b) persists at Er^{3+} concentrations higher than those measured (which according to the theory should indeed be the case), whereas $f_q = 0$ for all Er^{3+} concentrations; while the adverse effect of ETU is clearly visible, nevertheless a maximum gain of more than 7 dB/cm would be attainable for Er^{3+} concentrations around 8×10^{20} cm^{-3}. Finally, the lower solid lines represent the simulated gain versus Er^{3+} concentration when taking into account both, migration-accelerated ETU and fast quenching, under the assumption that also the dependence of f_q on Er^{3+} concentration in Fig. 5.3(a) is linear and persists at higher Er^{3+} concentrations (an assumption of rather speculative nature). Since the exact decay time τ_{1q} of the quenched ions is not known, we performed simulations for two different τ_{1q} values, the 50 ns reported in Ref. [113] and the value on the order of 1 μs found in Refs. [109-112]. The gain initially grows with Er^{3+} concentration, reaches a maximum value of 2 dB/cm at a concentration of $\approx 2\times10^{20}$ cm^{-3}, but then rapidly decreases. We observe no substantial difference between the simulations with the two different τ_{1q} values. Both curves coincide well with the experimental data.

A comparison of the different simulations demonstrates that the fast quenching process is a highly detrimental mechanism for the amplifier, degrading its performance already at low concentrations, while the migration-accelerated ETU significantly affects the gain only at rather high Er^{3+} concentrations.

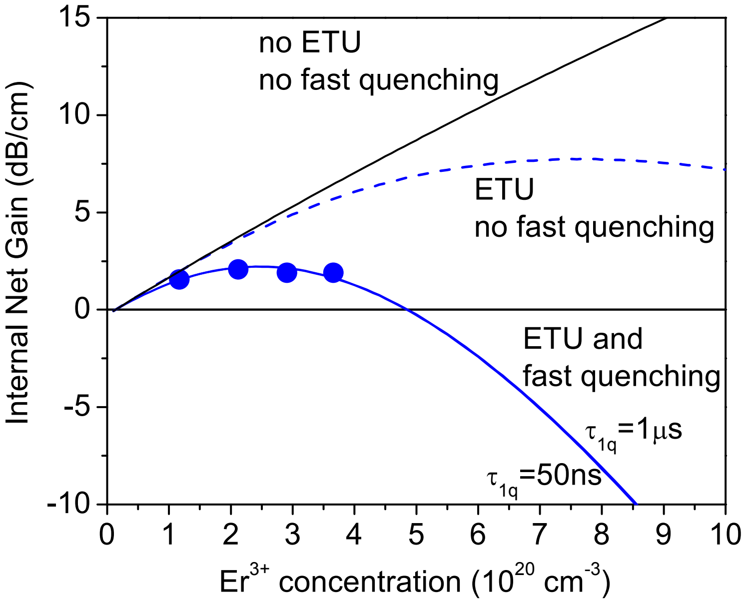

Fig. 5.10. Measured [28] (dots) and calculated (lines) internal net gain per unit length at 1533 nm versus Er^{3+} concentration, for a launched pump power of 100 mW at 976 nm and signal power of 1 μW at 1533 nm. The upper solid line represents a gain simulation where both, migration-accelerated ETU and fast quenching, are absent. The dashed line represents a simulation where only migration-accelerated ETU is considered. The lower solid lines represent simulations where both quenching processes are present; two different values τ_{1q} = 50 ns and 1 μs of the quenching process are tested; the two resulting curves are almost identical.

5.3.2 Impact on Relaxation-Oscillation Frequency in an Al_2O_3:Yb^{3+} DFB Waveguide Laser

Relaxation oscillations are a characteristic phenomenon in most solid-state lasers, which occur due to the coupled interaction between excess population inversion and laser radiation within the resonator. They are induced by small fluctuations in the pump power, cavity losses, or other laser parameters and generally take the form of damped sinusoidal fluctuations in the population inversion and laser output. The transient oscillatory behavior of the photon density ϕ with initial amplitude A' and phase θ is described by the equation

$$\partial\varphi(t) = A' e^{-\gamma_{ro} t} \cos\left(\omega_{ro} t + \theta\right). \qquad (5.3)$$

The laser eigenfrequency ω_L, relaxation-oscillation frequency ω_{ro}, and damping constant γ_{ro} are related to the pump rate R_P by the expressions [122]

$$\omega_L^2 = c'\left(\sigma_{GSA}\left(\lambda_L\right)+\sigma_{em}\left(\lambda_L\right)\right)\left(R_P - R_{P,thr}\right) = \omega_{ro}^2 + \gamma_{ro}^2 \approx \omega_{ro}^2 , \tag{5.4}$$

$$\gamma_{ro} = \frac{1}{2}\left[\frac{1}{\tau} + c'\tau_c\left(\sigma_{GSA}\left(\lambda_L\right)+\sigma_{em}\left(\lambda_L\right)\right)\left(R_P - R_{P,thr}\right)\right]. \tag{5.5}$$

$c' = c / n$ is the speed of light in the host material and λ_L is the laser wavelength. $R_{P,thr}$ is the threshold pump rate, given by

$$R_{P,thr} = \frac{1}{\tau}N_{1,cw} = \frac{1}{\tau}\frac{1}{c'\tau_c}\frac{1}{\left(\sigma_{GSA}\left(\lambda_L\right)+\sigma_{em}\left(\lambda_L\right)\right)}\left(1 + c'\sigma_{GSA}\left(\lambda_L\right)N_d\tau_c\right). \tag{5.6}$$

τ is usually the intrinsic lifetime τ_1 of the upper laser level, $N_{1,cw}$ is the population density in the upper laser level during steady-state laser operation, and τ_c is the cavity lifetime. In case of weakly damped relaxation oscillations, i.e., $\omega_{ro} >> \gamma_{ro}$, strong spiking occurs and the relaxation-oscillation frequency becomes $\omega_{ro}^2 \approx \omega_L^2$. Taking into account Eq. (5.6), Eqs. (5.4) and (5.5) can alternatively be written as [122]

$$\omega_L^2 = \frac{1}{\tau_c}\frac{1}{\tau}\left(1 + c'\sigma_{GSA}\left(\lambda_L\right)N_d\tau_c\right)\left(\frac{R_P}{R_{P,thr}} - 1\right) = \omega_{ro}^2 + \gamma_{ro}^2 \approx \omega_{ro}^2 , \tag{5.7}$$

$$\gamma_{ro} = \frac{1}{2\tau}\left[1 + \left(1 + c'\sigma_{GSA}\left(\lambda_L\right)N_d\tau_c\right)\left(\frac{R_P}{R_{P,thr}} - 1\right)\right]. \tag{5.8}$$

For an ideal four-level laser, $\sigma_{GSA}(\lambda_L) = 0$, which simplifies the results [34].

The simple expressions of Eqs. (5.3)-(5.8) are applicable to a large range of lasers. Plotting ω_{ro}^2 as a function of either R_P or $R_P / R_{P,thr}$ yields a straight line, whose intercept with the ω_{ro}^2-axis is, in both cases, equal to

$$-\frac{1}{\tau_c}\frac{1}{\tau}\left(1 + c'\sigma_{GSA}\left(\lambda_L\right)N_d\tau_c\right). \qquad . \tag{5.9}$$

From this expression the cavity lifetime τ_c can be determined in case the lifetime τ_1 of the upper laser level is known, or vice versa. For instance, Hanna *et al.* used relaxation-oscillation measurements to determine cavity losses in a fiber laser [123], and Weingarten *et al.* to calculate small-signal gain in a $YLiF_4:Nd^{3+}$ laser [124].

Here we apply expression (5.9) to relaxation-oscillation measurements in an $Al_2O_3:Yb^{3+}$ DFB channel waveguide laser, for which $\omega_{ro}^2 \approx \omega_L^2$ is a valid approximation. However, the calculation of the ω_{ro}^2-ordinate intercept for known values of τ_1 and τ_c results in a significant deviation from the measured value. The reason is the presence of the fast luminescence-quenching process in $Al_2O_3:Yb^{3+}$, discussed in Sect. 5.1.2, which influences the laser properties. We extend the theory to include the fast luminescence quenching in the calculation of the relaxation-oscillation frequency.

Our investigations were performed on an $Al_2O_3:Yb^{3+}$ DFB laser with Yb^{3+} concentration $N_d = 5.8 \times 10^{20}$ cm^{-3}. The sample was prepared by reactive co-sputtering of an amorphous $Al_2O_3:Yb^{3+}$ layer on a thermally oxidized silicon wafer (Sect. 3.1.1), microstructuring of a ridge channel waveguide with a $\pi/2$ phase shift by reactive ion etching (Sect. 3.1.2), and Bragg grating inscription in the SiO_2 top cladding by laser interference lithography and reactive ion etching [22]. The laser commenced oscillating above a threshold of 5 mW of absorbed pump power and delivered up to 55 mW of output power with a slope efficiency of 67% versus launched pump power [31].

The intrinsic lifetime of the Yb^{3+} upper laser level of $\tau_1 = 740$ µs in Al_2O_3 was determined in Section 5.2.1. The cavity lifetime was calculated as

$$\tau_c = -\frac{2\ell}{c'}\frac{1}{\ln\left[\left(1-L_{rt}\right)R_{out}\right]}, \tag{5.10}$$

where $\ell = 1.54$ mm is the path length of laser light inside the resonator, $L_{rt} = 0.022$ is the loss per roundtrip, and $R_{out} = 0.977$ is the reflectivity of the DFB resonator as calculated with coupled-mode theory [125], to yield a value of $\tau_c = 0.35$ ns. Other relevant parameters at the laser wavelength of 1022 nm are $\sigma_{GSA}(\lambda_L) = 0.29 \times 10^{-21}$ cm^2, $\sigma_{em}(\lambda_L) = 2.68 \times 10^{-21}$ cm^2, and $n = 1.6$ (effective refractive index of the channel waveguide).

The relaxation-oscillation frequency was experimentally determined by monitoring the laser noise spectrum with a 40 GHz photodiode which was connected to a RF spectrum analyzer. Figure 5.11 displays a typical RF spectrum used to determine the noise peak of ω_{ro}, measured in this example for a pump ratio of $R_P / R_{P,thr} = 6.1$.

The squares in Fig. 5.12 represent the square of the measured relaxation-oscillation frequency as a function of (a) pump rate R_P and (b) pump ratio $R_P / R_{P,thr}$. As expected from Eqs. (5.4) and (5.7), ω_{ro}^2 increases linearly with increasing pump rate or pump ratio. As expected from expression (5.9), the two ω_{ro}^2-ordinate intercepts coincide, being equal to -1.48×10^{14} rad^2 s^{-2}. In contrast, when substituting the known laser parameters into expression (5.9), the ω_{ro}^2-ordinate intercept equals -8.12×10^{12} rad^2 s^{-2}. Furthermore, the relaxation-oscillation frequency as a function of pump rate or pump ratio [dashed lines in Figs. 5.12(a) and 5.12(b)], as calculated from Eqs. (5.4) and (5.7), respectively, does not only fail to reproduce the experimental data, but even delivers two different, incompatible results. Alternatively, using expression (5.9) to determine the cavity lifetime would result in $\tau_c = 0.02$ ns, corresponding to a background propagation loss in our Al_2O_3 channel waveguide of more than 10 dB/cm, which is ≈ 40 times larger than the measured propagation loss of ≈ 0.25 dB/cm (Sect. 3.2.2).

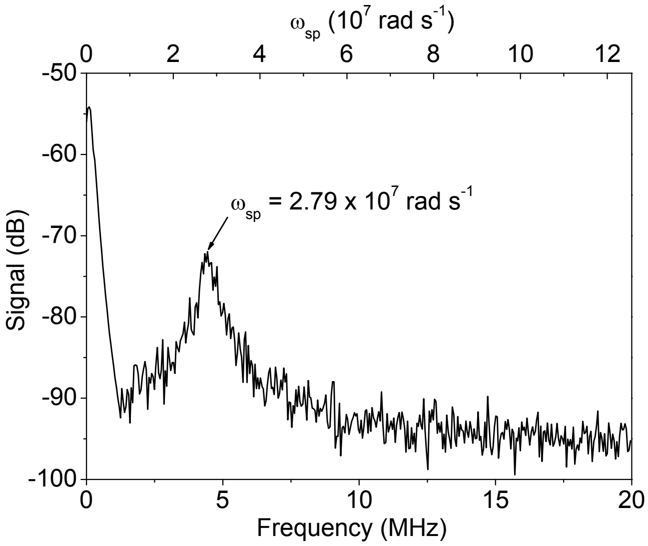

Fig. 5.11. RF spectrum indicating the relaxation-oscillation peak for a pump ratio of R_P / $R_{P,thr}$ = 6.1. The lower and upper abscissae show normal and angular frequencies, respectively.

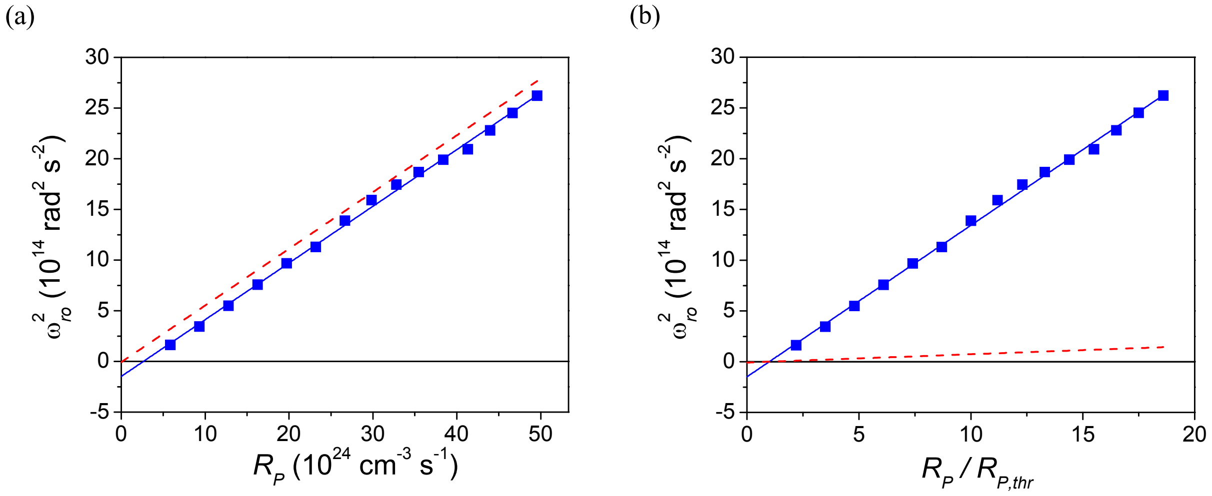

Fig. 5.12. Relaxation-oscillation frequency squared as a function of (a) pump rate and (b) pump ratio, for an Al_2O_3 DFB laser. The squares are measured values, and the solid lines are a linear fit through the data, yielding the same intercept with the ω_{ro}^2 ordinate in both cases. The dashed lines represent the calculation using Eqs. (5.4) and (5.7), respectively, for $\tau = \tau_1 = 740$ µs, while the same fits for $\tau = \tau_w = 40.5$ µs from Eq. (5.12) coincide with the solid lines.

Of all parameters that influence ω_{ro}, the lifetime τ_1 of the upper laser level is the most controversial. As explained in Sect. 5.2.1, our infrared luminescence decay experiments carried out under quasi-CW excitation provide information only on the lifetime of those ions that have a reasonable chance to luminesce. Ions that are subject to luminescence quenching exhibit a much faster decay time τ_{1q}, which can be on the order of a few µs for Yb^{3+} [112]. Luminescence quenching affects the laser performance of rare-earth-ion-doped materials by depleting the population of the upper level of the gain transition. Quenched ions are not revealed in a luminescence-decay experiment under quasi-CW excitation, because under such conditions these ions emit a negligible number of photons; nevertheless, they affect the laser performance and, thus, the relaxation oscillations.

We introduce luminescence quenching to the treatment of relaxation oscillations in order to determine its influence on ω_{ro}. In Al_2O_3:Yb^{3+} laser operation occurs between the excited state with population density N_1, pumped at a rate R_P, and the ground state with population density N_0. If the stimulated-emission rate is much higher than the luminescence and quenching-induced decay, the fraction f_q^* of quenched ions among all ions in the excited state approaches the fraction f_q of quenched ions among all ions: $f_q^* \rightarrow f_q$. This condition is approximately fulfilled in our Al_2O_3:Yb^{3+} DFB laser already just above threshold, thanks to the enormous intra-cavity laser intensity in the phase-shifted region, where the laser radiation is generated [126]. Therefore, we can describe the transient behavior of Yb^{3+} ions by a single rate equation,

$$\frac{dN_1}{dt} = R_P - c'\left(\sigma_{em}\left(\lambda_L\right)N_1 - \sigma_{GSA}\left(\lambda_L\right)N_0\right)\phi - \left[\frac{f_q^*}{\tau_{1q}} + \frac{1-f_q^*}{\tau_1}\right]N_1, \qquad (5.11)$$

combining the contributions of unquenched and quenched ions, which allows for a direct comparison of our solution with Eqs. (5.4)-(5.9). In the same way as in Ref. [122], we derive the solutions for ω_L, ω_{ro}, and γ_{ro}, which take the same form as Eqs. (5.4) and (5.5) or, alternatively, (5.7) and (5.8). However, the lifetime τ, instead of being represented by τ_1, assumes the value of an effective lifetime τ_w, obtained by weighting the lifetimes of quenched and unquenched ions,

$$\tau_w = \left(\frac{f_q}{\tau_{1q}} + \frac{1-f_q}{\tau_1}\right)^{-1}. \qquad (5.12)$$

By fitting expression (5.9), under consideration of Eq. (5.12), to the experimental ω_{ro}^2-ordinate intercept, we obtain τ_w = 40.5 μs. This result is applied to Eqs. (5.4) and (5.7) and the results in Figs. 5.12(a) and (b) coincide with the solid lines that correctly fit the data. The effective lifetime τ_w is a factor of 18 shorter than the intrinsic lifetime of the upper laser level of τ_1 = 740 μs, highlighting the dramatic effect of the quenching process on the Yb^{3+}-ion system and the laser behavior. Via non-saturable pump-absorption measurements (Fig. 5.13), similar to those described in Sect. 5.1.2 for Al_2O_3:Yb^{3+}, we estimate f_q to be 11%, and from Eq. (5.12) we then derive τ_{1q} = 4.7 μs, in reasonable agreement with a quenched lifetime of a few μs reported in an Yb^{3+}-doped silica fiber [112].

A clarification is required: the active ions exhibit an additional decay channel which reduces their lifetime from 740 μs down to ≈ 300 μs with increasing Yb^{3+} concentration (see Fig. 5.6). Such decay channel can be taken into account by inserting the luminescence decay time measured at the specific concentration of 5.8×10^{20} cm^{-3} (resulting in a value of 400 μs) in Eqs. (5.11) and (5.12) in place of τ_1 = 740 μs. However, this has negligible effects on the final result, the effective lifetime τ_w, indicating that the fast quenching is the predominant effect on the relaxation oscillations.

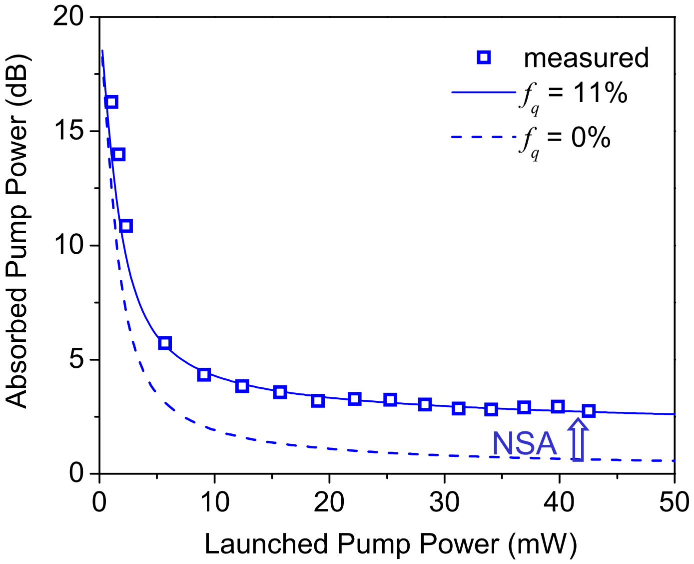

Fig. 5.13. Absorbed versus launched pump power for an Al_2O_3 channel waveguide with an Yb^{3+} concentration of 5.8×10^{20} cm^{-3} and a length of 0.7 cm. The squares are the measured data, the blue solid line is a fit based on the quenched-ion rate-equation model, yielding $f_q = 11\%$, and the blue dashed line is a calculation assuming the absence of quenched ions ($f_q = 0\%$). The arrow indicates the non-saturable absorption (NSA) induced by the quenched ions.

By comparing Eq. (5.6) in the unquenched and quenched case, i.e., τ assuming the value of τ_1 and τ_w, respectively, we understand the physical mechanism affecting the relaxation oscillations. The quenched ions introduce a saturable loss which increases the threshold pump rate by a factor of $\tau_1 / \tau_w \approx 18$; therefore, one has to invest accordingly more pump power to obtain the same value of relaxation-oscillation frequency. This is depicted in Fig. 5.12(a), where the horizontal gap between dashed line and measured data quantifies the increase in threshold due to quenching. In contrast, Fig. 5.12(b) is misleading, because it appears as if the quenching accelerated the relaxation oscillations, as a result of the abscissa being normalized with respect to the measured threshold. Consequently, Eq. (5.4) must be applied instead of Eq. (5.7) to represent correctly the underlying physics.

5.4 Summary

In this Chapter we have discussed the presence of fast luminescence quenching of a concentration-dependent fraction of dopant ions in $Al_2O_3:Er^{3+}$ and $Al_2O_3:Yb^{3+}$. Such quenching is undetected in the luminescence decay measurements under quasi-CW excitation, but can be revealed by pump-absorption measurements. The quenching can be induced in both materials by undesired impurities or host material defects, but in $Al_2O_3:Er^{3+}$ the major cause of fast quenching seems to be ion pair/cluster formation.

In a more general respect, we have also discussed the breakdown of Zubenko's model in the presence of distinct spectroscopic classes of ions such as the quenched ions. We have shown that an extended model that takes in consideration these ion classes can be successful. In the $Al_2O_3:Er^{3+}$ case, with a single microscopic energy-migration parameter C_{DD} = (5.0 ± 0.1) × 10^{-39} cm^6/s and a single microscopic ETU parameter C_{DA} = (11.6 ± 1.1) × 10^{-41} cm^6/s, derived under consideration of a concentration-dependent fraction of quenched ions and resulting in a macroscopic W_{ETU1} coefficient which is proportional to the Er^{3+} concentration, the extended model (named "quenched-ion rate-equation model") can correctly predict the luminescence-decay curves, the pump-absorption measurements, and the small-signal gain experiments, for the whole range of Er^{3+} concentrations investigated.

Moreover, we have investigated the impact of fast luminescence quenching on the small-signal internal net gain of Al_2O_3:Er^{3+} waveguide amplifiers, and observed that the fast quenching strongly degrades the amplifier performance already at low Er^{3+} concentrations.

Finally, we have shown that the common approach in solid-state lasers of measuring the relaxation-oscillation frequency versus pump rate to determine the cavity lifetime τ_c and, consequently, the cavity losses, has to be modified when investigating optical materials that suffer from luminescence quenching – such as in the example of our Al_2O_3:Yb^{3+} DFB waveguide laser – by replacing the intrinsic luminescence lifetime τ_1 of the upper laser level with an effective lifetime τ_w which takes the quenching effect into account. Alternatively, in case the cavity lifetime is known, a potential luminescence quenching effect and the resulting effective lifetime τ_w can be determined with this method.

Chapter 6

Spectroscopy of the Upper Energy Levels of $Al_2O_3:Er^{3+}$

In Fig. 2.4 of Chapter 2, a partial energy-level diagram of Er^{3+} up to the $^4F_{3/2}$ level was displayed. From the diagram, it appears that the specific energy-level structure of Er^{3+} with several almost equidistant crystal-field manifolds within the Er^{3+} 4*f* subshell can give rise to a number of processes and transitions, including ground-state absorption (GSA), excited-state absorption (ESA) [127], and various radiative and non-radiative relaxation processes. At the high Er^{3+} concentrations on the order of 10^{20} cm^{-3} – necessary to compensate for the weak oscillator strengths of these parity-forbidden 4*f*-4*f* transitions and ensure sufficient pump absorption and signal gain – energy-transfer processes, such as energy-transfer upconversion (ETU) and cross relaxation (CR), between neighboring Er^{3+} ions can take place [83]. In addition, the fast quenching process discussed in the previous Chapter further complicates the picture.

Due to its complexity, understanding the Er^{3+} system is challenging and the spectroscopic processes involved in the operation of Er^{3+}-doped devices can easily be misinterpreted. An example investigated in this Chapter is the $^4I_{13/2} \rightarrow {}^4I_{9/2}$ transition, which (as already mentioned in Chapter 5) allegedly is responsible for ESA at the common 1480-nm pump wavelength in Er^{3+}-doped Al_2O_3 and other hosts [118,128]. From GSA and ESA spectra in $Al_2O_3:Er^{3+}$ we show that, similar to the situation in other materials [129,130], this transition does not affect pump absorption at 1480 nm and overlaps with the $^4I_{13/2} \rightarrow {}^4I_{15/2}$ emission only at wavelengths longer than 1630 nm. Consequently, also the direct-overlap integral of the ETU process ($^4I_{13/2}$, $^4I_{13/2}$) → ($^4I_{15/2}$, $^4I_{9/2}$), which determines the probability of an energy-transfer process [94] in the absence of phonon assistance, delivers a very small microparameter for this ETU process. Nevertheless, this ETU process strongly depletes the metastable $^4I_{13/2}$ level of Er^{3+}, thereby diminishing the optical gain [131], and can also be exploited in upconversion-pumping schemes to realize a 3-μm laser on the $^4I_{11/2} \rightarrow {}^4I_{13/2}$ transition [80]. Several energy-transfer processes between other rare-earth ions have been found to exhibit weak or no spectral overlap at all, yet demonstrate significant transition rates and strong impact on practical device performance, e.g. the energy transfer from ytterbium to holmium [87], suggesting that these processes are phonon-assisted.

This raises the question which other energy-transfer processes, potentially without spectral overlap, can occur among Er^{3+} ions. By taking into account both, spectral overlap and phonon energy of the host material, we evaluate their efficiency.

Besides investigating the ETU process ($^4I_{11/2}$, $^4I_{11/2}$) → ($^4I_{15/2}$, $^4F_{7/2}$), we prove the presence of yet another ETU process, ($^4I_{13/2}$, $^4I_{11/2}$) → ($^4I_{15/2}$, $^4F_{9/2}$) or alternatively ($^4I_{11/2}$, $^4I_{13/2}$) → ($^4I_{15/2}$, $^4F_{9/2}$), whose existence has previously been proposed [85,132], and quantify its macroscopic ETU coefficient. Because of the rather high phonon energies in oxide host materials, such as Al_2O_3, the lifetimes of higher-lying Er^{3+} levels are quenched by multiphonon relaxation, thereby diminishing the influence of processes originating in those levels on practical device performance. Nonetheless, our approach can be generally applied to other rare-earth-ion-doped optical materials, for instance low-phonon-energy glasses such as fluorides, characterized by high population densities in higher-lying levels that allow lasers emitting in the visible spectral range.

After reporting in Section 6.1 on luminescence lifetime measurements from the $^4I_{11/2}$ and $^4S_{3/2}$ levels, in Section 6.2 we perform a Judd-Ofelt (J-O) analysis to determine optical intensity parameters, radiative transition probabilities, decay-rate constants, radiative lifetimes, and branching ratios of Er^{3+} manifold-to-manifold transitions. With the knowledge of these parameters and the measured luminescence lifetimes, we estimate the luminescence lifetimes of the $^4I_{9/2}$ and $^4F_{9/2}$ excited states that are too short to be directly measured with our experimental setup. ESA measurements performed in collaboration with the University of Hamburg, Germany are presented in Section 6.3 to determine the cross-sections of ESA transitions from the $^4I_{13/2}$ and $^4I_{11/2}$ levels, for which only a few reports related to erbium glass hosts exist in the literature. In Section 6.4 the results of these ESA measurements are used to estimate energy-transfer microparameters and evaluate the efficiency of resonant and phonon-assisted energy-transfer mechanisms among Er^{3+} ions. Finally, in Section 6.5 we study the $^4S_{3/2}$ vs. $^4F_{9/2}$ luminescence intensity as a function of Er^{3+} concentration and perform a quantitative analysis of the ETU process ($^4I_{13/2}$, $^4I_{11/2}$) → ($^4I_{15/2}$, $^4F_{9/2}$).

6.1 Luminescence Decay from $^4I_{11/2}$ and $^4S_{3/2}$ Levels

Four Al_2O_3 channel waveguide samples with Er^{3+} concentrations of 1.17, 2.12, 2.91, and 3.66 × 10^{20} cm^{-3} [listed in Table 3.1(a)] were investigated in this spectroscopic study. The setup and technique for luminescence decay measurements from the second excited state $^4I_{11/2}$ and the $^4S_{3/2}$ level were explained in Chapter 3, Section 3.2.4.

In both cases, after the pump is switched off at time $t = 0$, the initial population density N_i due to the quasi-CW excitation of level $i = 2$ or 5, respectively, decays with the intrinsic lifetime τ_i of this level mostly to the next lower-lying level. However, the ETU$_j$ process with its macroscopic ETU coefficient W_{ETUj} from the lower-lying metastable level $j = 1$ or 2, respectively (see Fig. 2.4), continues to populate level i due to the longer lifetime τ_j of the metastable level. This situation is described by the rate equations

$$\frac{dN_i}{dt} = -\frac{N_i}{\tau_i} + W_{ETU\,j} N_j^2 , \tag{6.1}$$

$$\frac{dN_j}{dt} = -\frac{N_j}{\tau_j} - 2W_{ETU\,j} N_j^2 + \frac{N_i}{\tau_i} . \tag{6.2}$$

At delay times *t* that are long compared to the intrinsic lifetime of level *i* the decay curves of luminescence from levels *i* and *j* take the forms

$$N_i(t) \approx \exp\left(-2t/\tau_j\right), \tag{6.3}$$

$$N_j(t) \approx \exp\left(-t/\tau_j\right), \tag{6.4}$$

with the decay time of level *i* equaling half the lifetime of level *j* [133].

As an example, Fig. 6.1(a) shows the measured luminescence decay curve from the $^4I_{11/2}$ level for an Er^{3+} concentration of 1.17×10^{20} cm^{-3}. The curve exhibits a fast exponential decay in the initial part with a decay time of $\tau_2 = 60 \pm 5$ μs, followed by a much slower decay with a decay time of ≈ 3.75 ms, which is about half the value of the lifetime $\tau_1 = 7.55$ ms of the $^4I_{13/2}$ first excited state (see Chapter 4). A similar situation occurs for the luminescence decay from the $^4S_{3/2}$ level. Figure 6.2(a) shows a measured luminescence decay curve for a waveguide with the same Er^{3+} concentration as above. Again, the curve is composed of two exponential decays, a fast one with a decay time of $\tau_5 = 12.6 \pm 1.0$ μs followed by a slow one with a decay time of ≈ 30.8 μs, roughly half the value of the lifetime τ_2 of the second excited state determined above. Equations (6.1)-(6.2) are solved numerically and the results are shown as red solid lines in Figs. 6.1(a) and 6.2(a), respectively. τ_2 and τ_5 are approximately constant throughout the concentration range investigated, see Figs. 6.1(b) and 6.2(b), respectively, indicating that the intrinsic multiphonon relaxations $^4I_{11/2} \rightarrow {}^4I_{13/2}$ and $^4S_{3/2} \rightarrow {}^4F_{9/2}$, which are independent of dopant concentration, are significantly faster than the competing depletion via the processes ETU_2 and CR_1 (Fig. 2.4).

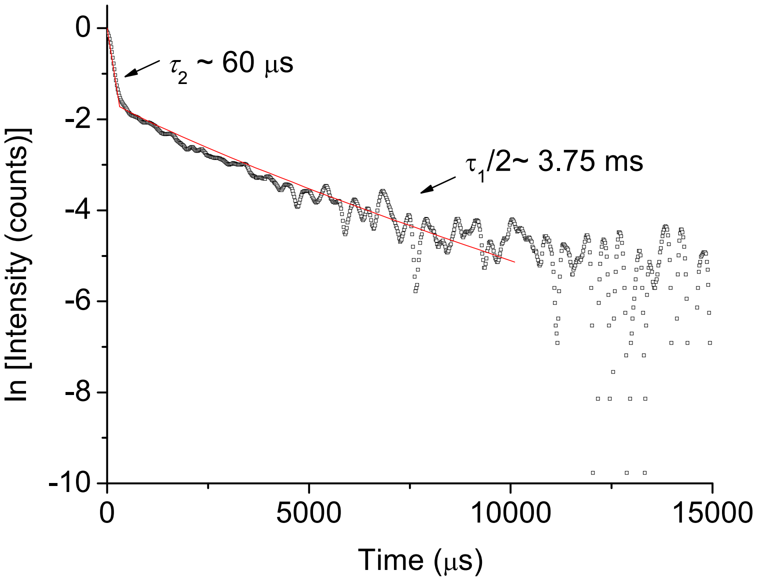

(a)

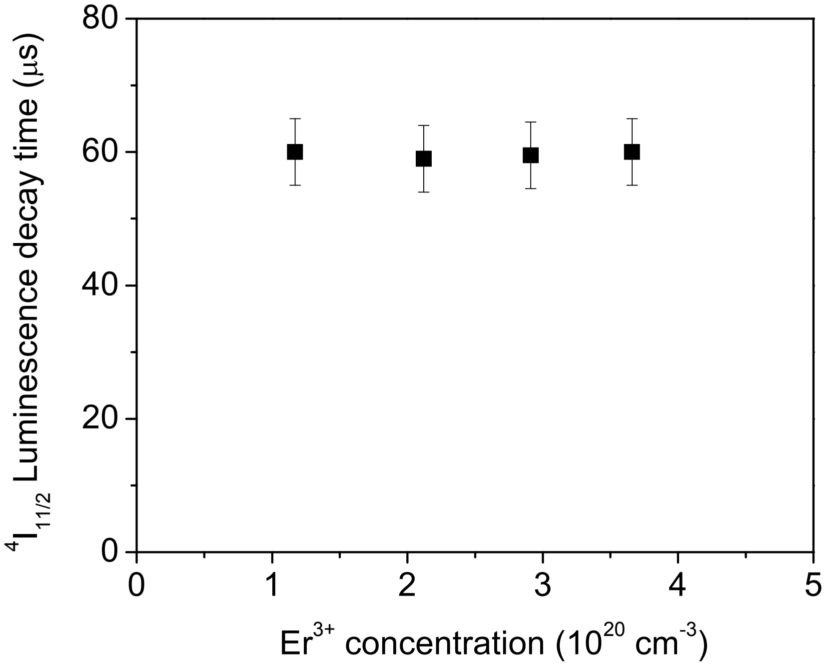

(b)

Fig. 6.1. (a) Normalized luminescence decay curve from the $^4I_{11/2}$ level at a wavelength of 980 nm for an Er^{3+} concentration of 1.17×10^{20} cm^{-3}. The solid line is a numerical fit to the data using Eqs. (6.1)-(6.2). (b) Concentration dependence of the $^4I_{11/2}$ luminescence decay time.

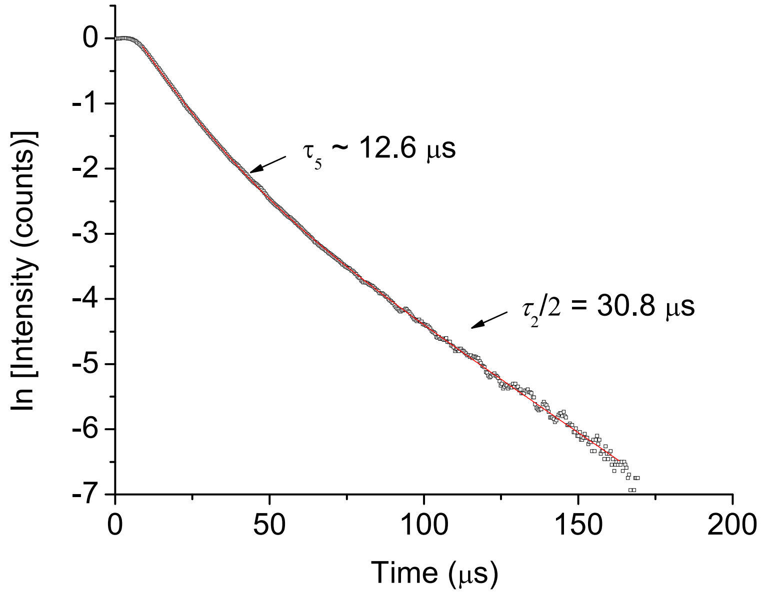

(a)

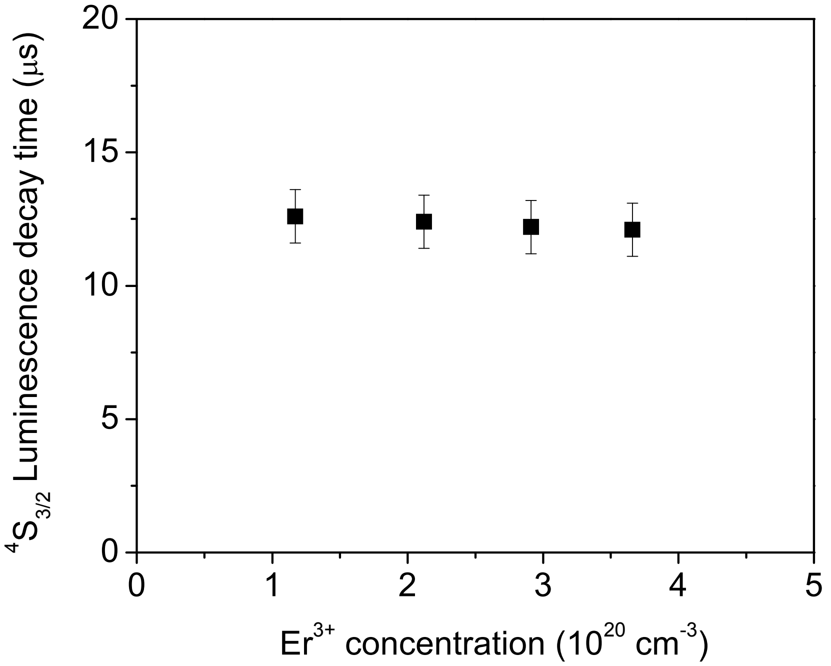

(b)

Fig. 6.2. (a) Normalized luminescence decay curve from the $^4S_{3/2}$ level at a wavelength of 550 nm for an Er^{3+} concentration of 1.17×10^{20} cm^{-3}. The solid line is a numerical fit to the data using Eqs. (6.1)-(6.2). (b) Concentration dependence of the $^4S_{3/2}$ luminescence decay time.

6.2 Judd-Ofelt Analysis

Figure 6.3 displays the room-temperature absorption spectrum of $Al_2O_3:Er^{3+}$ from 500 nm to 1700 nm. It consists of six absorption bands corresponding to the GSA transitions from $^4I_{15/2}$ to the excited states $^4I_{13/2}$, $^4I_{11/2}$, $^4I_{9/2}$, $^4F_{9/2}$, $^4S_{3/2}$, and $^2H_{11/2}$, respectively. The J-O theory (see Chapter 2) is applied to the GSA spectrum to calculate the manifold-to-manifold transition probabilities, from which the radiative lifetimes and branching ratios of emission are determined.

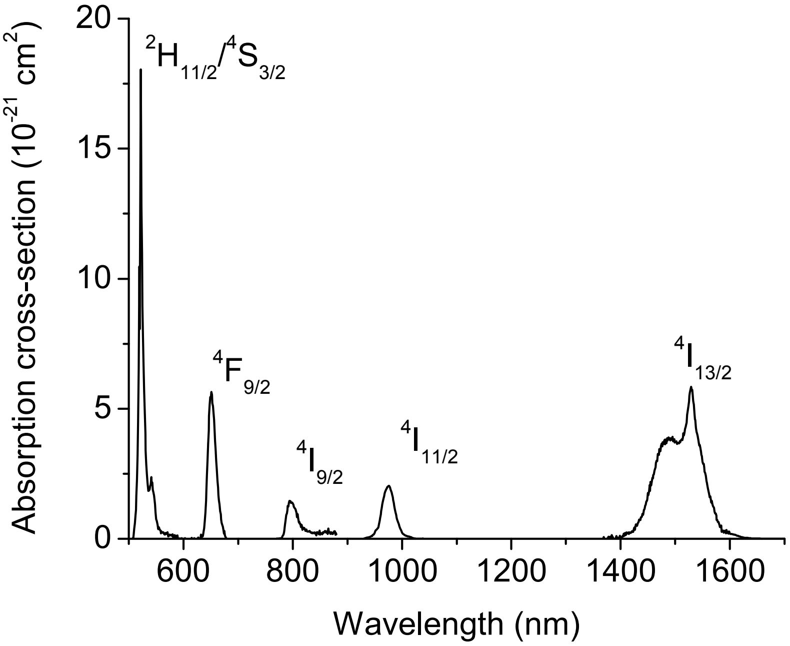

Fig. 6.3. Measured absorption cross-sections of $Al_2O_3:Er^{3+}$ over the wavelength range from 500 to 1700 nm.

The measured line strengths S_{meas} (Table 6.1) of each absorption band are determined using Eq. (2.28) and the mean wavelength $\bar{\lambda}$, the refractive indexes, and integrated absorption cross-sections also listed in Table 6.1. The values of the doubly reduced matrix elements $U^{(\tilde{t})}$ ($\tilde{t}$ = 2, 4, 6) [43,44] present in the expression (2.27) for the calculated line strengths S_{calc} are given in Table 6.1 as well. A least-squares fit of S_{meas} to S_{calc} provides the following values for the three J-O parameters of Er^{3+} in Al_2O_3: $\Omega_2 = (1.52 \pm 0.27) \times 10^{-20}$ cm^2, $\Omega_4 = (0.71 \pm 0.29) \times 10^{-20}$ cm^2, and $\Omega_6 = (1.10 \pm 0.11) \times 10^{-20}$ cm^2. The J-O parameters are then used to recalculate the transition line strengths of the absorption bands by Eq. (2.27) and the results are listed in the column S_{calc} of Table 6.1. With the J-O parameters parameters, the line strengths of emission transitions from the $^4I_{13/2}$, $^4I_{11/2}$, $^4I_{9/2}$, $^4F_{9/2}$, $^4S_{3/2}$, and $^2H_{11/2}$ manifolds to lower-lying manifolds can be calculated. The values are given in Table 6.2. Using these line strengths, the radiative decay-rate constants $A(J \rightarrow J')$ of electric dipole transitions between an excited state J and lower-lying manifolds J' (Table 6.2), the total radiative decay-rate constant A and radiative lifetime τ_{rad} of each excited state J (Table 6.3), and the radiative branching ratios $\beta(J\rightarrow J')$ (Table 6.2), respectively, are also calculated.

With A and the measured luminescence lifetime τ of level J, the decay-rate constant $A_{non\text{-}rad}$ of multiphonon relaxation from level J to level J–1 is determined with Eq. (2.32). The $^4I_{13/2}$, $^4I_{11/2}$, and $^4S_{3/2}$ luminescence lifetimes τ of 7.55 ms (see Chapter 4), 60 µs, and 12.6 µs, respectively, are used to calculate the corresponding values of $A_{non\text{-}rad}$. The results are presented in Table 6.3 and indicated by the superscript (*calc.*).

The non-radiative decay-rate constant is related to the energy gap ΔE between one energy level and the next lower level by Eq. (2.36). The energy gaps are listed in Table 6.3. In Fig. 6.4 the calculated non-radiative decay-rate constants for the $^4I_{13/2}$, $^4I_{11/2}$, and $^4S_{3/2}$ levels are plotted as a function of energy gap (solid squares) in semi-logarithmic scale. An exponential dependence of the decay-rate constant on the gap according to Eq. (2.36) is observed. From the exponential fit (black line), the values of C = 4.09 × 10^7 s^{-1} and α = 2.32 × 10^{-3} cm are determined. Subsequently, the non-radiative decay-rate constants of the $^4I_{9/2}$ and $^4F_{9/2}$ levels, whose lifetimes are too short to measure under quasi-CW excitation, are determined (open dots in Fig. 6.4) from the known energy gaps to the next lower-lying levels. By adding the total radiative decay-rate constants calculated via the J-O theory, the luminescence lifetimes of these two levels are determined from Eq. (2.32). In Table 6.3 the non-radiative decay-rate constants and luminescence lifetimes estimated with this method are listed and indicated by the superscript (*est.*). The luminescence lifetimes of the higher-lying $^4F_{7/2}$ and thermally coupled $^4F_{5/2}$ and $^4F_{3/2}$ levels could also be estimated with this method, assuming a predominance of non-radiative decay and with help of the energy gaps taken from [48] (as they are unknown in Al_2O_3:Er^{3+}). They are shown in Fig. 2.4.

When comparing the decay-rate constants A and $A_{non\text{-}rad}$ of the Er^{3+} levels in Al_2O_3, we observe that the non-radiative decay-rate constants are predominant in all levels, except for $^4I_{13/2}$. The reason is the high maximum phonon energy of ≈ 870 cm^{-1} assumed in Sect. 2.2.5 for Al_2O_3, which makes multiphonon relaxation highly probable. Only the energy gap between the first excited state $^4I_{13/2}$ and the ground state $^4I_{15/2}$ of ≈ 6500 cm^{-1} is too large to favor multiphonon relaxation, hence radiative decay in this case prevails over non-radiative decay.

Table 6.1. Mean wavelengths, values of reduced matrix elements [43,44], refractive indexes, integrated absorption cross-sections, and measured and calculated absorption line strengths for the absorption transitions of Er^{3+} in Al_2O_3.

Transition from $^4I_{15/2}$	$\bar{\lambda}$ **[nm]**	$[U^{(2)}]^2$	$[U^{(4)}]^2$	$[U^{(6)}]^2$	n	$\int\alpha(\lambda)d\lambda$ **[10^{-20} cm^2 nm]**	S_{meas} **[10^{-20} cm^2]**	S_{calc} **[10^{-20} cm^2]**
$^4I_{13/2}$	1512.5	0.0195	0.1173	1.4316	1.651	45.570	1.6700	1.6821
$^4I_{11/2}$	976.0	0.0282	0.0003	0.3953	1.659	7.8623	0.4437	0.4784
$^4I_{9/2}$	800.0	0	0.1733	0.0099	1.664	3.9168	0.2686	0.1340
$^4F_{9/2}$	657.8	0	0.5354	0.4618	1.669	10.169	0.8447	0.8868
$^4S_{3/2}$	545.2	0	0	0.2211	1.679	4.6332	0.4607	0.2423
$^2H_{11/2}$	523.2	0.7125	0.4125	0.0925	1.682	14.287	1.4768	1.4752

Table 6.2. Reduced matrix elements [43,44], predicted fluorescence line strengths, radiative decay-rate constants, and radiative branching ratios of Er^{3+} in Al_2O_3.

Transition		**State energy [cm^{-1}]**	**[$U^{(2)}$]^2**	**[$U^{(4)}$]^2**	**[$U^{(4)}$]^2**	**S_{calc} [10^{-20} cm^2]**	**$A(J \rightarrow J')$ [s^{-1}]**	**$\beta(J \rightarrow J')$**
$^4I_{13/2}$ →	$^4I_{15/2}$	6500	0.0195	0.1173	1.4316	1.682	97.81	1.000
$^4I_{11/2}$ →	$^4I_{13/2}$	3600	0.0331	0.1708	1.0864	1.362	15.96	0.115
	$^4I_{15/2}$	10100	0.0282	0.0003	0.3953	4.763	123.17	0.885
$^4I_{9/2}$ →	$^4I_{11/2}$	2150	0.0030	0.0674	0.1271	0.192	0.58	0.005
	$^4I_{13/2}$	5750	0.0004	0.0106	0.7162	0.793	45.88	0.378
	$^4I_{15/2}$	12250	0.0000	0.1732	0.0099	0.134	74.94	0.617
$^4F_{9/2}$ →	$^4I_{9/2}$	2900	0.1279	0.0059	0.0281	0.290	1.72	0.002
	$^4I_{11/2}$	5050	0.0704	0.0112	1.2839	1.522	60.23	0.057
	$^4I_{13/2}$	8650	0.0101	0.1533	0.0714	0.203	40.29	0.038
	$^4I_{15/2}$	15150	0.0000	0.5354	0.4619	0.887	947.72	0.902
$^4S_{3/2}$ →	$^4F_{9/2}$	3200	<0.001	<0.001	<0.001	<0.001	<0.001	<0.001
	$^4I_{9/2}$	6100	0.0000	0.0788	0.2542	0.335	59.53	0.034
	$^4I_{11/2}$	8250	0.0000	0.0042	0.0739	0.084	36.96	0.021
	$^4I_{13/2}$	11850	0.0000	0.0000	0.3462	0.379	494.85	0.280
	$^4I_{15/2}$	18350	0.0000	0.0000	0.2211	0.242	1173.52	0.665
$^2H_{11/2}$ →	$^4F_{9/2}$	4000	0.3629	0.0224	0.0022	0.569	9.56	0.003
	$^4I_{9/2}$	6900	0.2077	0.0662	0.2858	0.675	58.30	0.020
	$^4I_{11/2}$	9050	0.0357	0.1382	0.0371	0.193	37.60	0.013
	$^4I_{13/2}$	12650	0.0230	0.0611	0.0527	0.136	72.39	0.025
	$^4I_{15/2}$	19150	0.7125	0.4123	0.0925	1.475	2722.24	0.939

Table 6.3. Energy gaps to the next lower levels, total radiative decay-rate constants, radiative and luminescence lifetimes, and non-radiative decay-rate constants of the lowest five excited states of Er^{3+} in Al_2O_3. The $^4S_{3/2}$ and $^2H_{11/2}$ levels are treated as a single, thermally coupled level. The index (*calc.*) indicates that the non-radiative decay-rate constants are calculated via Eq. (2.32) with known radiative and luminescence lifetimes; the index (*est.*) indicates that the non-radiative decay-rate constants and luminescence lifetimes are estimated via the energy-gap analysis in Fig. 6.4 and the subsequent use of Eq. (2.32), respectively.

Excited state	**ΔE** [cm^{-1}]	**$\sum_{J'} A(J\rightarrow J')$** [s^{-1}]	**τ_{rad}** [ms]	**τ_{lum}** [ms]	**$A_{non\text{-}rad} = 1/\tau_{lum} - \sum_{J'} A(J\rightarrow J')$** [s^{-1}]
$^4I_{13/2}$	6061	97.815	10.22	7.55	34.603 $^{(calc.)}$
$^4I_{11/2}$	3263	139.129	7.19	0.060	1.653×10^4 $^{(calc.)}$
$^4I_{9/2}$	1911	121.392	8.24	0.0016 $^{(est.)}$	4.859×10^5 $^{(est.)}$
$^4F_{9/2}$	2377	1049.955	0.95	0.006 $^{(est.)}$	1.648×10^5 $^{(est.)}$
$^4S_{3/2}$ $^2H_{11/2}$	2810	1764.863	0.57	0.0126	7.575×10^4 $^{(calc.)}$

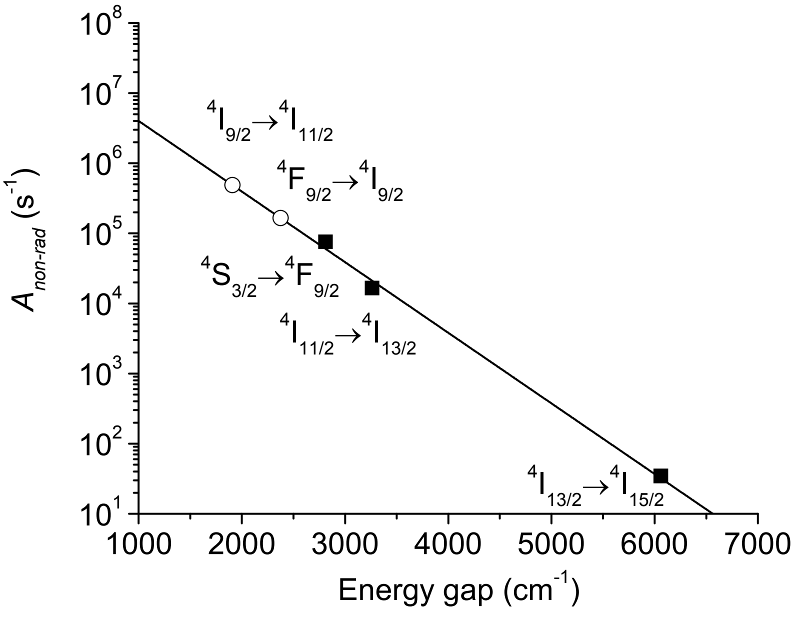

Fig. 6.4. Energy-gap dependence of the non-radiative decay-rate constants in Al_2O_3:Er^{3+} in semi-logarithmic scale. Solid squares are the non-radiative decay-rate constants determined from Eq. (2.32) with the measured luminescence lifetimes and the calculated radiative decay-rate constants. The line is the fit through these data with Eq. (2.36). The open dots are estimated non-radiative decay-rate constants based on this fit.

6.3 Excited-State-Absorption Measurements

The experimental setup at the University of Hamburg, Germany that was used for ESA measurements, based on the continuous-wave pump-probe technique [134], is shown in

Fig. 6.5. ESA is an intrinsic process of a single ion, the probability of which is naturally independent of dopant concentration. The doping level influences the host structure and modifies the local crystal field, hence it changes the level energies, transition peak cross-sections and linewidths. However, for the dopant concentrations under investigation here these changes are smaller than the typical experimental errors of ESA measurements and cannot be determined. Therefore, we investigated ESA in a single Al_2O_3:Er^{3+} sample with an Er^{3+} concentration of 1.17×10^{20} cm^{-3} and a length of 5.4 cm. The ions were excited by a Ti:Sapphire laser operating at 800 nm, with the pump power stabilized around 1 W and modulated at $\approx$ 10 Hz. About 100 mW of pump power were effectively launched into the waveguide. A white-light source modulated at $\approx$ 1 kHz was used as the probe beam. Its 5 mW/nm of spectral density, in total 8 W of output power, was reduced by density filters to about 1 μW/nm, such that the pump-induced populations of the Er^{3+} levels were unperturbed by the probe beam. The collinear and counterpropagating pump and probe beams were coupled to and from the waveguide via objective lenses. The probe light transmitted by the sample was then selected in wavelength through a monochromator with a resolution of 3 nm and detected by a Ge photodiode.

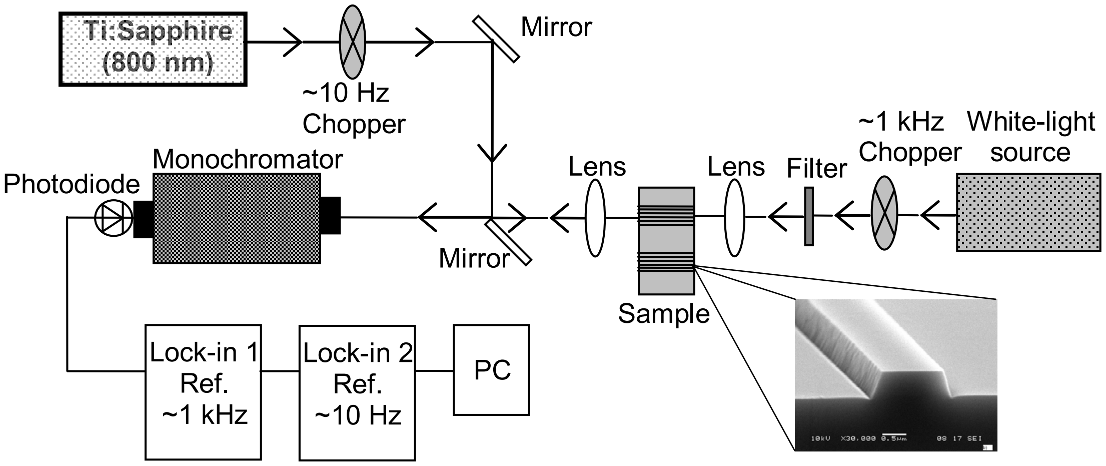

Fig. 6.5. Experimental setup of the ESA measurement based on the pump-and-probe technique described in Ref. [134].

Because of the tight confinement, the intensity of light propagating in a waveguide can be orders of magnitude higher than in bulk materials. Therefore, some of the assumptions made in the usual analysis of ESA experiments [134] may not be valid anymore. Moreover, the overlap of the probe beam with the active region of the waveguide needs to be taken into account. When the probe beam of intensity I_0 propagates through the sample of length L, the transmitted intensities I_u and I_p in the unpumped and pumped case, respectively, are given by

$$I_u = I_0 \exp\left[-\alpha_{Loss} L + \int_0^L dz \iint_{A_r} dxdy \left(-\sigma_{GSA} N_d \psi_S \right) \right], \tag{6.5a}$$

$$I_p = I_0 \exp\left[-\alpha_{bck} L + \int_0^L dz \iint_{A_r} dxdy \left(-\sigma_{GSA} \left(N_d - N_e \right) \psi_S - \sum_i \left(\sigma_{ESA,i} - \sigma_{SE,i} \right) N_i \psi_S \right) \right], \tag{6.5b}$$

$$\Rightarrow \ln\left(\frac{I_p}{I_u} \right) = \int_0^L dz \iint_{A_r} dxdy \left(\sigma_{GSA} N_e \psi_S - \sum_i \left(\sigma_{ESA,i} - \sigma_{SE,i} \right) N_i \psi_S \right). \tag{6.5c}$$

Here α_{bck} is the background propagation loss at the probe wavelength, σ_{SE} is the stimulated emission (SE) cross-section, $N_e = \sum_i N_i$ is the total excitation density summed over the population densities N_i of the substantially populated excited states, and ψ_S is the probe-power distribution normalized over the active area A_r. In the above equations, for simplicity, the *xyz* discretization is taken into account implicitly.

A double-modulation scheme with two lock-in amplifiers was employed for the measurement. The first lock-in amplifier, set at the modulation frequency of the probe beam (≈ 1 kHz), measured the transmitted light signal I_u or I_p directly from the photodiode. The second lock-in amplifier was set at the modulation frequency of the pump beam (≈ 10 Hz) and received the output signal of the first lock-in amplifier as its input signal. Therefore, it amplified the difference in probe-beam transmission through the sample between the pumped and unpumped case,

$$\Delta I = I_p - I_u = I_u \exp\left[\int_0^L dz \iint_{A_r} dxdy \left(\sigma_{GSA} N_e \psi_S + \sum_i \left(\sigma_{SE,i} - \sigma_{ESA,i} \right) N_i \psi_S \right) \right] - I_u . \tag{6.6}$$

The output of the second lock-in amplifier is $\Delta I' = A^* \Delta I$, where A^* is the amplification factor of the amplifier. The output signals of the two lock-in amplifiers are then divided and the final result is $\Delta I'/I_u$.

In the measurement analysis, usually it is assumed that the variation ΔI in transmitted probe-beam intensity induced by the pump beam is weak compared to the probe-light intensity transmitted by the sample, i.e., $I_u \approx I_p$ [134]. However, this is not always the case in waveguides. As an example, we evaluate the situation at the probe wavelength of 1533 nm, corresponding to the zero-phonon line of the $^4I_{15/2} \leftrightarrow {}^4I_{13/2}$ transition. At this wavelength σ_{GSA} ($^4I_{15/2} \rightarrow {}^4I_{13/2}$) = σ_{SE} ($^4I_{13/2} \rightarrow {}^4I_{15/2}$) (Fig. 3.15), and from ESA investigations in phosphate glass we can expect σ_{ESA} ($^4I_{13/2} \rightarrow {}^4I_{9/2}$) ≈ 0 [129], while potential SE and ESA from the weakly populated $^4S_{3/2}$ level at this wavelength has only a small influence. Because of the strong excitation density N_e induced by the high pump intensity in the waveguides, the ground-state population density is bleached under pumping: $N_0 = N_d - N_e << N_d$. In addition, from the rate-equation simulations explained later on we find that most of the excitation resides in the $^4I_{13/2}$ manifold, $N_1 \approx N_e$. When comparing Eqs. (6.5a) and (6.5b), it becomes evident that I_p can then be much higher than I_u. Hence the approximation

$$\ln\left(\frac{I_p}{I_u} \right) = \ln\left(1 + \frac{I_p - I_u}{I_u} \right) = \ln\left(1 + \frac{\Delta I}{I_u} \right) \approx \frac{\Delta I}{I_u}, \tag{6.7}$$

which is applied in Ref. [134] to connect Eqs. (6.5c) and (6.6) with each other, becomes invalid at such wavelengths. The ratio between the output signals of the second and first detector is

$$\frac{\Delta I'}{I_u} = A^* \left\{ \exp\left[\int_0^L dz \iint_{A_r} dxdy \left(\sigma_{GSA} N_e \psi_S + \sum_i \left(\sigma_{SE,i} - \sigma_{ESA,i} \right) N_i \psi_S \right) \right] - 1 \right\}, \qquad (6.8)$$

whereas, had the approximation of Eq. (6.7) been valid, the following would have derived:

$$\frac{\Delta I'}{I_u} = A^* \int_0^L dz \iint_{A_r} dxdy \left(\sigma_{GSA} N_e \psi_S + \sum_i \left(\sigma_{SE,i} - \sigma_{ESA,i} \right) N_i \psi_S \right). \qquad (6.9)$$

Therefore, our measurement analysis proceeds as follows. The measured spectra $\Delta I'/I_u$ are calibrated for absolute cross-sections in those spectral regions in which σ_{ESA} and σ_{SE} are negligible, by exploiting the independently measured cross-sections σ_{GSA} (Fig. 3.15). We chose to calibrate the spectra in the wavelength range 1400-1430 nm, where basically only GSA occurs, i.e., the bleaching of GSA in the signal $\Delta I'/I_u$. Figure 6.6, from top to bottom, displays a series of three consecutive graphs. The black solid lines in the graphs are spectra extracted from Eq. (6.8), whereas the red dashed lines derive from Eq. (6.9). The spectra in Fig. 6.6(a) represent the signal

$$-\sigma_{GSA} + \sum_i \left(\sigma_{ESA,i} - \sigma_{SE,i} \right) \frac{N_i^{eff}}{N_e^{eff}}, \qquad (6.10)$$

where we have chosen to display the ESA contribution on the positive branch of the ordinate. N_i^{eff} and N_e^{eff} represent the integrals of the population densities averaged over the waveguide volume and probe-beam distribution deriving from Eqs. (6.8) and (6.9) and are defined as follows:

$$N_i^{eff} = \frac{1}{L} \int_0^L dz \iint_{A_r} dxdy \; N_i \psi_S , \qquad (6.11a)$$

$$N_e^{eff} = \frac{1}{L} \int_0^L dz \iint_{A_r} dxdy \; N_e \psi_S = \frac{1}{L} \int_0^L dz \iint_{A_r} dxdy \sum\nolimits_i N_i \psi_S = \sum\nolimits_i N_i^{eff} . \qquad (6.11b)$$

N_i^{eff} and N_e^{eff}, which we refer to as the effective population densities, take into account the variation of the excited population density inside the waveguide and are simple expressions that allow us to relate Eq. (6.10) (and following) in our waveguide case to the corresponding equations in bulk materials, e.g. in Ref. [134].

Subsequently, the measured bleaching of GSA in the spectra was eliminated by adding the cross-sections σ_{GSA} of the $^4I_{15/2} \rightarrow {}^4I_{13/2}$ and $^4I_{15/2} \rightarrow {}^4I_{11/2}$ transitions. The resulting spectra, shown in Fig. 6.6(b), represent the signal

$$\sum_i \left(\sigma_{ESA,i} - \sigma_{SE,i}\right) \frac{N_i^{eff}}{N_e^{eff}} . \tag{6.12}$$

This term is the spectral difference of ESA and SE cross-sections, summed over all substantially populated excited states and weighted with the factors N_i^{eff} / N_e^{eff}, hereafter referred to as relative excited population densities, which need to be evaluated in order to obtain the pure ESA spectra. This evaluation is performed in Appendix B, Part 2 with an analytical rate-equation model that stems from the quenched-ion rate-equation system delineated in Chapter 5 and accounts for the presence of a fraction of quenched ions in $Al_2O_3:Er^{3+}$. These calculations, which depend slightly on the lateral overlap of the probe wavelength with the active region, result in N_1^{eff} / N_e^{eff} = 0.712–0.732, N_2^{eff} / N_e^{eff} = 0.217–0.232, and N_5^{eff} / N_e^{eff} = 0.051–0.056. N_1^{eff} / N_e^{eff} determines the strength of the SE transition $^4I_{13/2} \rightarrow {}^4I_{15/2}$ in the wavelength range 1450–1650 nm, the ESA transition $^4I_{13/2} \rightarrow {}^4I_{9/2}$ in the wavelength range 1630–1750 nm, and the ESA transition $^4I_{13/2} \rightarrow {}^4F_{9/2}$ between 1100 and 1210 nm, see Fig. 6.6(b) and Eq. (6.12). N_2^{eff} / N_e^{eff} determines the strength of the SE transition $^4I_{11/2} \rightarrow {}^4I_{15/2}$ and ESA transition $^4I_{11/2} \rightarrow {}^4F_{7/2}$ in the range 960-1000 nm. Knowledge of these values allowed us to eliminate the SE contributions $^4I_{13/2} \rightarrow {}^4I_{15/2}$ and $^4I_{11/2} \rightarrow {}^4I_{15/2}$ from Fig. 6.6(b) and obtain the ESA spectra displayed in Fig. 6.6(c). N_5^{eff} / N_e^{eff} determines the strength of the SE transition $^4S_{3/2} \rightarrow {}^4I_{9/2}$ and ESA transition $^4S_{3/2} \rightarrow {}^2H_{9/2}$ in the spectral region ≈ 1450-1750 nm. However, the $^4S_{3/2}$ level is weakly populated, therefore the rates of these transitions are rather small. Furthermore, the $^4S_{3/2} \rightarrow {}^4I_{9/2}$ luminescence spectrum overlaps with that of the luminescence $^4I_{13/2} \rightarrow {}^4I_{15/2}$, and in the ESA measurements the $^4S_{3/2} \rightarrow {}^4I_{9/2}$ SE and $^4S_{3/2} \rightarrow {}^2H_{9/2}$ ESA spectra overlap with the strong $^4I_{15/2} \rightarrow {}^4I_{13/2}$ GSA bleaching, $^4I_{13/2} \rightarrow {}^4I_{15/2}$ SE, and $^4I_{13/2} \rightarrow {}^4I_{9/2}$ ESA, hence the transitions from the $^4S_{3/2}$ level are difficult to record separately. Consequently, we could not calculate the $^4S_{3/2} \rightarrow {}^4I_{9/2}$ SE out of the spectrum of Fig. 6.6(b).

Three ESA transitions are visible in Fig. 6.6(c), namely the $^4I_{13/2} \rightarrow {}^4I_{9/2}$ transition between 1630-1750 nm, the $^4I_{13/2} \rightarrow {}^4F_{9/2}$ transition between 1100-1210 nm, and the $^4I_{11/2} \rightarrow {}^4F_{7/2}$ transition between 960-1000 nm. The absolute peak cross-sections of these ESA transitions are listed in Table 6.4. Only a handful of ESA investigations on other erbium-doped glass hosts are found in the literature, some of which have been performed with other techniques than the pump-probe technique applied here. Our $^4I_{13/2} \rightarrow {}^4I_{9/2}$ ESA spectrum is qualitatively comparable to that of phosphate glass [129]. In both cases there is negligible overlap between this ESA and the $^4I_{15/2} \leftrightarrow {}^4I_{13/2}$ GSA and SE. This ESA transition may affect laser operation at wavelengths longer than 1630 nm, but it does not evoke ESA at the common Er^{3+} 1480-nm pump wavelength, as was previously assumed by other authors [118,128]. The small features that occur in the spectrum of Fig. 6.6(c) in the wavelength range from 1450 nm to slightly beyond 1600 nm are partly artefacts resulting from the fact that the strong GSA $^4I_{15/2} \rightarrow {}^4I_{13/2}$ leads to a very weak probe-signal intensity I_u in the unpumped case, hence a non-perfect cancellation of the $^4I_{15/2} \leftrightarrow {}^4I_{13/2}$ GSA and SE. In addition, the signal is slightly negative in the wavelength range 1500-1630 nm, which is most probably due to the above-mentioned SE transition from the weakly populated $^4S_{3/2}$ level to the short-lived, practically unpopulated $^4I_{9/2}$ level, which could not be eliminated from the spectrum of Fig. 6.6(b) in order to arrive at a spectrum in Fig. 6.6(c) that contains only ESA transitions.

Deriving the ESA spectrum of Fig. 6.6(c) from the approximation of Eq. (6.9) (red dashed lines) instead of the correct Eq. (6.8) (black solid lines) further pronounces the non-perfect cancellation of the $^4I_{15/2} \leftrightarrow {}^4I_{13/2}$ GSA and SE. In all the other regions the difference between the derivations of Eqs. (6.8) and (6.9) is minimal, because the approximation of Eq. (6.7) is still reasonably good.

The $^4I_{11/2} \rightarrow {}^4F_{7/2}$ ESA spectrum needs to be treated carefully. The original spectrum appeared to be very noisy, with various spikes and dips instead of well-defined and smooth lines. The low signal-to-noise ratio in this wavelength range is due to, firstly, the short $^4I_{11/2}$ luminescence lifetime of 60 μs and accordingly low relative population density N_2^{eff} / N_e^{eff} and, secondly, the overlap of ESA with GSA in this region, which significantly decreases the signal intensity I_u. Although the measured spectrum was carefully smoothened, evaluation of the ESA cross-section in this spectral region is subject to a large error. Quimby *et al.* investigated this ESA transition in fluorophosphate and ZBLAN glass [105], in which the $^4I_{11/2}$ level exhibits a significantly longer lifetime, and their results differ from ours: their peak cross-sections are higher and shifted toward shorter wavelengths.

We compare the integrated ESA cross-sections, calculated as the areas underneath the experimental curve in Fig. 6.6(c), with the corresponding values obtained semi-theoretically with the aid of the J-O formalism, calculated using Eq. (2.28) for S_{meas} and the reduced matrix elements listed in Table 6.2. Considering the approximations made by the J-O formalism and well-known, rather large error margins of the resulting transition probabilities, as well as the quality of the measured ESA spectra, the data provided in Table 6.4 show a reasonably good agreement within a factor of two.

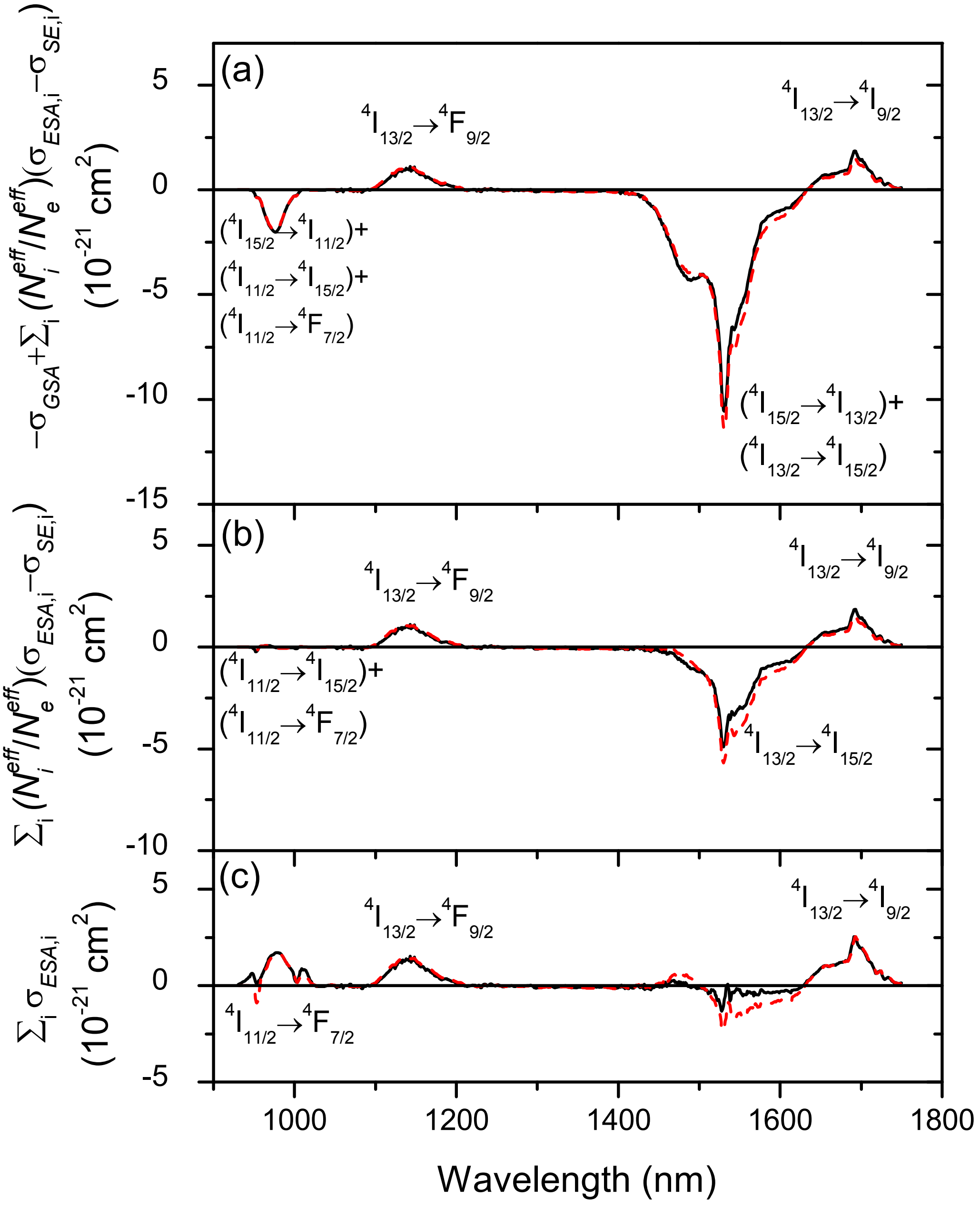

Fig. 6.6. Spectra representing (a) $-\sigma_{GSA}+\sum_i N_i^{eff}/N_e^{eff}\left(\sigma_{ESA,i}-\sigma_{SE,i}\right)$, (b) $\sum_i N_i^{eff}/N_e^{eff}\left(\sigma_{ESA,i}-\sigma_{SE,i}\right)$, and (c) $\sum_i \sigma_{ESA,i}$. The black solid lines in the graphs are spectra obtained from Eq. (6.8), whereas the red dashed lines derive from Eq. (6.9).

Table 6.4. ESA transitions, corresponding peak wavelengths, peak cross-sections, and comparison between the measured integrated ESA cross-sections and those calculated by the J-O formalism.

ESA transition	**Peak wavelength [nm]**	**Peak ESA cross-section $[10^{-21}\ cm^2]$**	$\int \sigma_{ESA}^{meas}(\lambda)d\lambda$ **$[10^{-20}\ cm^2\ nm]$**	$\int \sigma_{ESA}^{J-O}(\lambda)d\lambda$ **$[10^{-20}\ cm^2\ nm]$**
${}^4I_{13/2} \rightarrow {}^4I_{9/2}$	1692	2.53	11.653	13.150
${}^4I_{13/2} \rightarrow {}^4F_{9/2}$	1143	1.51	7.648	4.075
${}^4I_{11/2} \rightarrow {}^4F_{7/2}$	979	1.71	7.171	4.219

6.4 Energy-Transfer Parameters

With the knowledge obtained in the previous sections about the absorption, emission, and ESA cross-sections, it is possible to evaluate the probabilities of the energy-transfer processes indicated in Fig. 2.4 by calculating the energy-transfer microparameters introduced by the Förster-Dexter theory, assuming dipole-dipole interionic interactions [92,93]. We recall from Chapter 2, Section 2.2.3 and Chapter 4, Section 4.1.1 that the donor-donor microparameter C_{DD} is related to migration-type energy transfer between Er^{3+} ions, in which one excited donor ion transfers its energy to a neighboring ion initially in its ground state, which can then act as new donor; the donor-acceptor microparameter C_{DA} is related to ETU, i.e., energy transfer from an excited donor ion to a neighboring acceptor ion already in its excited state, which is then upconverted to a higher excited state. The two microparameters can be calculated through the cross-section overlap function (4.3) [94]. These microparameters were calculated by use of our measured cross-section spectra for the relevant energy-transfer processes and are gathered in Table 6.5.

6.4.1 Energy-Transfer Processes from the First Excited State

The donor-donor microparameter C_{DD} of the $({}^4I_{13/2}, {}^4I_{15/2}) \rightarrow ({}^4I_{15/2}, {}^4I_{13/2})$ energy-migration process is derived by calculating the overlap integral of the ${}^4I_{15/2} \leftrightarrow {}^4I_{13/2}$ GSA and emission cross-section spectra with Eq. (4.3). The spectra which are taken from Ref [28] and were shown in Fig. 3.15 overlap rather well, indicating that this energy migration is a resonant process. The calculation results in a value of $C_{DD} = 4.27 \times 10^{-39}\ cm^6/s$, which compares rather well with the value of $5.00 \times 10^{-39}\ cm^6/s$ determined in Chapter 4 from the analysis of luminescence decay curves.

The donor-acceptor microparameter C_{DA} of the upconversion process ETU_1 is calculated with the ${}^4I_{13/2} \rightarrow {}^4I_{15/2}$ emission cross-section taken from Ref [28] and shown in Fig. 3.15, and the ${}^4I_{13/2} \rightarrow {}^4I_{9/2}$ ESA cross-section determined in Sect. 6.3. Both cross-section spectra which are shown in Fig. 6.7 barely overlap, hence the calculation yields a low value of $C_{DA} = 4.23 \times 10^{-42}\ cm^6/s$, which is much smaller than the value of $1.16 \times 10^{-40}\ cm^6/s$ derived in Chapter 5 from the analysis of luminescence decay curves and pump-absorption measurements. ETU_1 is an almost non-resonant process, consequently its C_{DA} parameter cannot be determined directly via the overlap integral of the Förster-Dexter theory. This energy-transfer mechanism is phonon-assisted, i.e., the surplus of energy generated by the decay process ${}^4I_{13/2} \rightarrow {}^4I_{15/2}$ that is not used for the excitation process $^4I_{13/2} \rightarrow {}^4I_{9/2}$ is dissipated by the emission of a phonon. Multiphonon-induced sidebands in the emission and ESA spectra were calculated according to the theory of Auzel [135] to test if they could explain the difference between the calculated C_{DA} value and the value determined from luminescence decay measurements, but their influence is negligible. Therefore, we explain the situation with the following argument. Coupling of a phonon bridges the energy gap between the decay and excitation processes that contribute to this ETU process. Consequently, in Fig. 6.7 the ESA spectrum is shifted until the C_{DA} value calculated with the overlap integral of Eq. (4.3) is equal to 1.16×10^{-40} cm^6/s, as determined in Chapter 5. The required shift amounts to an energy of 195 cm^{-1}, equivalent to 50 nm. With a maximum phonon energy in Al_2O_3 of 870 cm^{-1} (assumed in Sect. 2.2.5), such phonon-assisted processes are possible. However, their probability is significantly lower than for resonant transitions, resulting in an effective shift that is significantly smaller than 870 cm^{-1}, which is equivalent to a real shift of 870 cm^{-1} combined with a probability of less than unity that the process takes place.

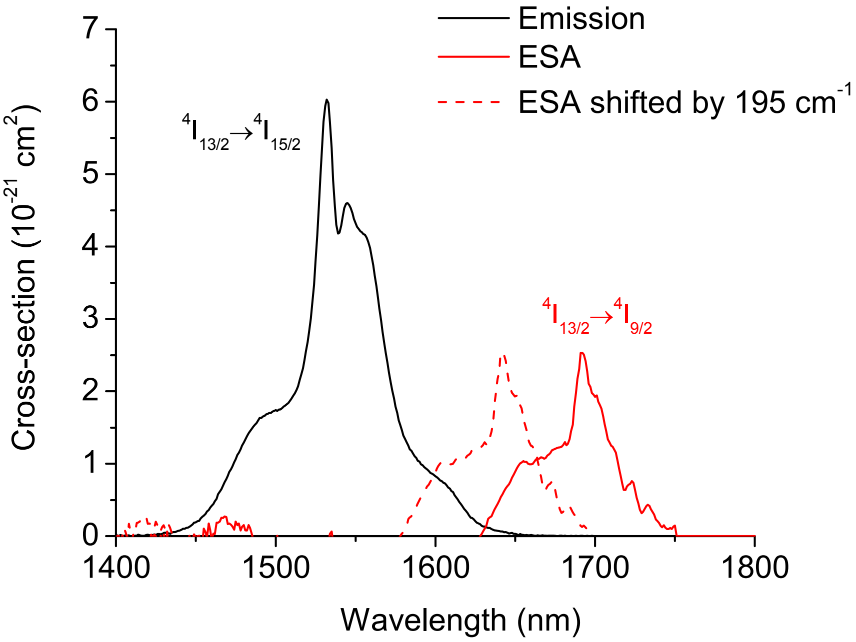

Fig. 6.7. $^4I_{13/2} \rightarrow {}^4I_{15/2}$ emission cross-section, taken from Ref [28] and shown in Fig. 3.15, and $^4I_{13/2} \rightarrow {}^4I_{9/2}$ ESA cross-section derived in Sect. 6.3 and then shifted by 195 cm^{-1}, as explained in Sect. 6.4.1.

6.4.2 Energy-Transfer Processes from the Second Excited State

The donor-donor microparameter C_{DD} of the ($^4I_{11/2}$, $^4I_{15/2}$) → ($^4I_{15/2}$, $^4I_{11/2}$) energy migration is calculated with the overlap integral of the $^4I_{15/2} \leftrightarrow {}^4I_{11/2}$ GSA and emission cross-section spectra and Eq. (4.3). The absorption cross-section was taken from Ref. [28], while the emission cross-section was determined from the absorption spectrum using the McCumber relation explained in Sect. 2.1.4. Both spectra are shown in Fig. 6.8, and similarly to the $^4I_{15/2} \leftrightarrow {}^4I_{13/2}$ cross-sections they exhibit a very good overlap, indicating that also this energy migration is a resonant process. The calculation results in a value of $C_{DD} = 2.94 \times 10^{-40}$ cm^6/s, which is more than one order of magnitude smaller than the C_{DD} value of the energy migration involving the first excited state, because the $^4I_{15/2} \leftrightarrow {}^4I_{11/2}$ cross-sections are smaller and narrower than the $^4I_{15/2} \leftrightarrow {}^4I_{13/2}$ cross-sections.

The donor-acceptor microparameter C_{DA} of the upconversion process ETU_2 is calculated from the $^4I_{11/2} \rightarrow {}^4I_{15/2}$ emission spectrum in Fig. 6.8 mentioned above and the $^4I_{11/2} \rightarrow {}^4F_{7/2}$ ESA cross-section determined in Sect. 6.3. Both cross-section spectra are shown in Fig. 6.9. The calculation yields $C_{DA} = 3.13 \times 10^{-40}$ cm^6/s, which is almost three times the value of $C_{DA} = 1.16 \times 10^{-40}$ cm^6/s of the ETU_1 process, because in this case emission and ESA cross-sections overlap well, hence the process is resonant.

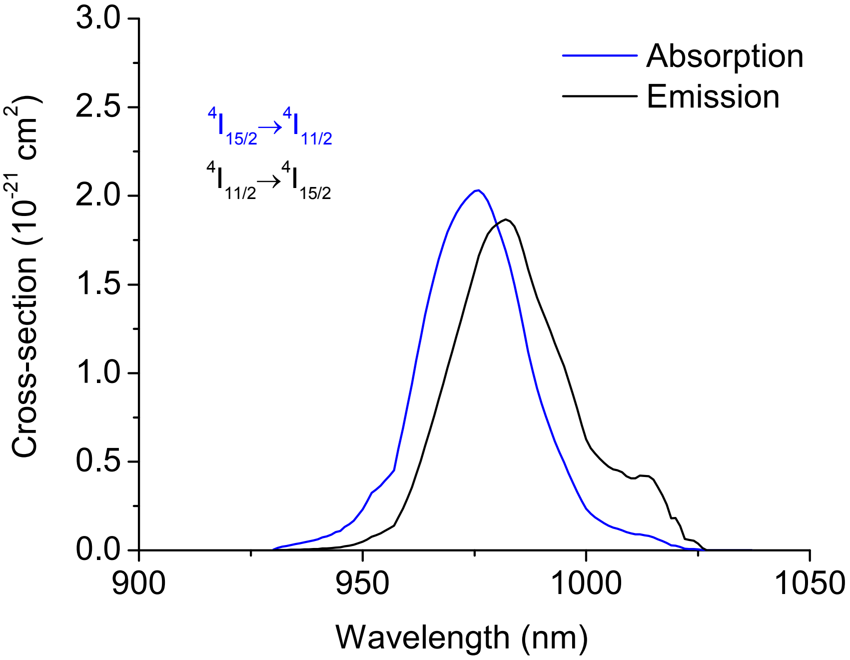

Fig. 6.8. $^4I_{15/2} \leftrightarrow {}^4I_{11/2}$ absorption and emission cross-sections. The former is taken from Ref. [28], the latter is calculated with the McCumber relation explained in Sect. 2.1.4.

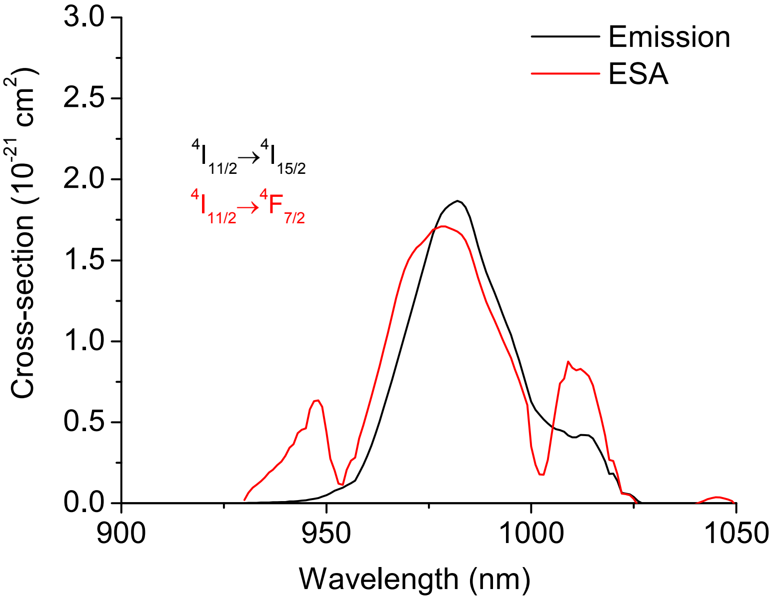

Fig. 6.9. $^4I_{11/2}$ → $^4I_{15/2}$ emission cross-section from Fig. 6.8 and $^4I_{11/2}$ → $^4F_{7/2}$ ESA cross-section derived in Sect. 6.3.

6.4.3 Upconversion Coefficients

Now that the microparameters of energy-transfer processes from the first and second excited state have been determined, we can calculate the corresponding ETU macroparameters W_{ETU} from Eq. (4.25) in Chapter 4.

The W_{ETU} macroparameters of the ETU$_1$ and ETU$_2$ processes as a function of Er^{3+} concentration, calculated with the C_{DD} and C_{DA} parameters and the resulting $(\pi^2/3)\sqrt{C_{DA}C_{DD}}$ values of Table 6.5, are displayed in Fig. 6.10 as a solid black and dashed red line, respectively, and listed in Table 6.6 for the four Er^{3+} concentrations considered in this study. For calculation of the W_{ETU1} coefficient we used the microparameter $C_{DA} = 1.16 \times 10^{-40}$ cm^6/s derived in Chapter 5, to which the C_{DA} value obtained with the shifted ESA spectrum in Sect. 6.4.1 is equivalent. For comparison, the values of the W_{ETU1} coefficient derived individually from luminescence decay curves and pump-absorption measurements in Chapter 5 for the four Er^{3+} concentrations considered in this study are shown as squares in Fig. 6.10 and listed in Table 6.6. We observe that W_{ETU2} is a factor of approximately 2.3 smaller than W_{ETU1}, because energy migration with its corresponding C_{DD} parameter is significantly slower in the second compared to the first excited state. A similar quantitative behavior was observed also in ZBLAN glass [99].

Table 6.5. Microparameters of energy migration within, and ETU from, the first and second excited states, calculated with Eq. (4.3) and the measured donor emission and either donor GSA or acceptor ESA spectra. The fourth column refers to the overlap integral mentioned in Sect. 6.4.1, as calculated with the ESA spectrum shifted by 195 cm^{-1} toward the emission spectrum, and the last column lists the $\left(\pi^2/3\right)\sqrt{C_{DA}C_{DD}}$ values appearing in Eq. (4.25), where for the first excited state the C_{DA} value obtained with the shifted ESA spectrum is used. The second row refers to microparameters of energy migration and ETU from the $^4I_{13/2}$ level obtained from the evaluation of luminescence decay curves and pump-absorption measurements in Chapter 5.

Excited state	**C_{DD} from overlap absorption-emission** **[10^{-40} cm^6/s]**	**C_{DA} from overlap emission-ESA** **[10^{-40} cm^6/s]**	**C_{DA} from overlap emission-shifted ESA** **[10^{-40} cm^6/s]**	**$\frac{\pi^2}{3}\sqrt{C_{DA}C_{DD}}$** **[$10^{-40}$ cm^6/s]**
$^4I_{13/2}$	42.67	0.04	1.16	23.15
luminesc. decay	50.0 [Chapter 4]		1.16 [Chapter 5]	
$^4I_{11/2}$	2.94	3.13	-	9.98

Table 6.6. Values of the macroscopic ETU coefficients W_{ETU1} taken from Chapter 5, along with the calculations of W_{ETU1} and W_{ETU2} with Eq. (4.25), and W_{ETU3} derived from the analysis of the I_{green}/I_{red} ratio under 1480-nm pumping, for the four Er^{3+} concentrations considered in this study.

N_d **[10^{20} cm^{-3}]**	**W_{ETU1}** [Chapter 5] **[10^{-19} cm^3/s]**	**W_{ETU1}** **[10^{-19} cm^3/s]**	**W_{ETU2}** **[10^{-19} cm^3/s]**	**W_{ETU3}** **[10^{-19} cm^3/s]**
1.17	2.9	2.7	1.3	0.03
2.12	4.7	4.9	2.3	0.09
2.91	7.5	6.7	3.1	0.24
3.66	9.2	8.6	4.0	0.39

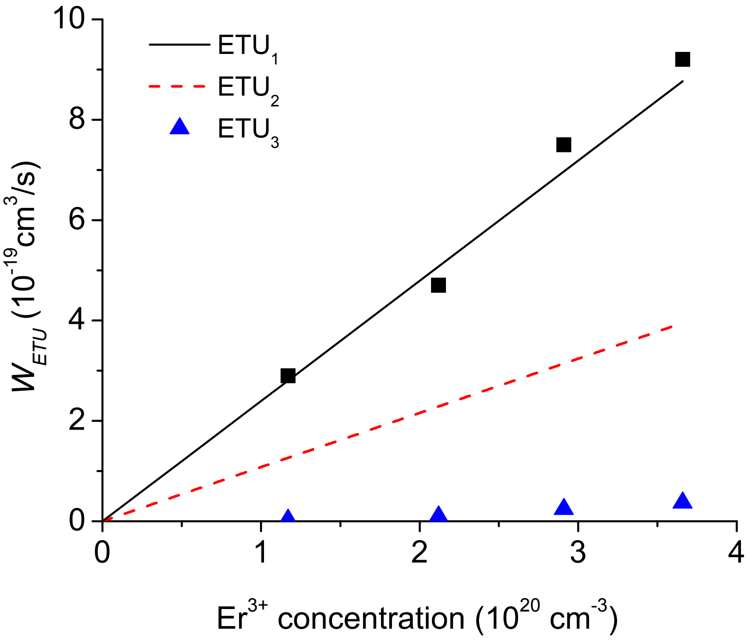

Fig. 6.10. Values of the macroscopic ETU coefficients W_{ETU1} taken from Chapter 5 (squares) for the four Er^{3+} concentrations considered in this study, along with the calculations of W_{ETU1} and W_{ETU2} with Eq. (4.25) (solid and dashed line, respectively), and W_{ETU3} derived from the analysis of the I_{green}/I_{red} ratio under 1480-nm pumping (triangles), as a function of Er^{3+} concentration.

6.5 Green versus Red Luminescence Intensities

In a number of publications [47,85,132,136-138], the presence of the additional upconversion process ($^4I_{13/2}$, $^4I_{11/2}$) → ($^4I_{15/2}$, $^4F_{9/2}$) or, alternatively, ($^4I_{11/2}$, $^4I_{13/2}$) → ($^4I_{15/2}$, $^4F_{9/2}$), labeled as ETU$_{3a/b}$ in Fig. 2.4 of Chapter 2, was suggested. However, in most cases its existence was only assumed (and not thoroughly investigated) or the presented proof was quantitatively not entirely convincing. To the best of our knowledge, only Balda *et al.* [132] provide persuasive evidence with a quantitative analysis of luminescence decay curves from the $^4F_{9/2}$ and $^4S_{3/2}$ levels.

A possible approach to investigate this process is by studying the integrated upconversion luminescence intensities in the red and green spectral region. Figure 6.11 shows the upconversion luminescence spectra in the 500-750 nm region under 976-nm (dashed magenta line) and 1480-nm (solid blue line) pump excitation for a sample with an Er^{3+} concentration of 1.17×10^{20} cm^{-3}. The spectra were measured by launching 30 mW of pump light at either 976 nm or 1480 nm into a channel waveguide and collecting the emission perpendicular to the waveguide with a liquid-core fiber. The spectra were then recorded using a Horiba Jobin Yvon iHR550 spectrometer with a resolution of < 1 nm. Emission bands around 525 nm, 550 nm, and 660 nm were observed and assigned to radiative transitions from the $^2H_{11/2}$, $^4S_{3/2}$, and $^4F_{9/2}$ level to the ground state, respectively.

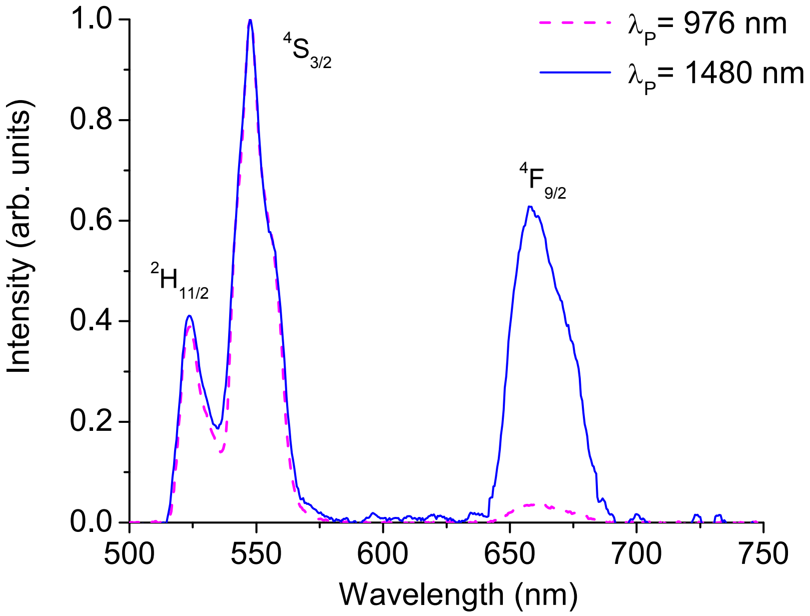

Fig. 6.11. Upconversion emission spectra in the 500–750 nm spectral region, after excitation with 1480-nm pump light (solid blue line) and 976-nm pump light (dashed magenta line). Both spectra are normalized with respect to the $^4S_{3/2}$ peak.

In case of 976-nm pumping, the green emission at 525 nm and 550 nm from the thermally coupled $^2H_{11/2}$ and $^4S_{3/2}$ levels is much stronger than the red emission at 660 nm from the $^4F_{9/2}$ level, whereas in case of 1480-nm pumping, the former is comparable to the latter. Figure 6.12 shows the dependence of the ratio I_{green}/I_{red} of 525-550-nm to 660-nm integrated emission intensities on Er^{3+} concentration, for both pump wavelengths. The ratio does not show any dependence on Er^{3+} concentration under 976-nm pumping, whereas it increases with Er^{3+} concentration under 1480-nm pumping.

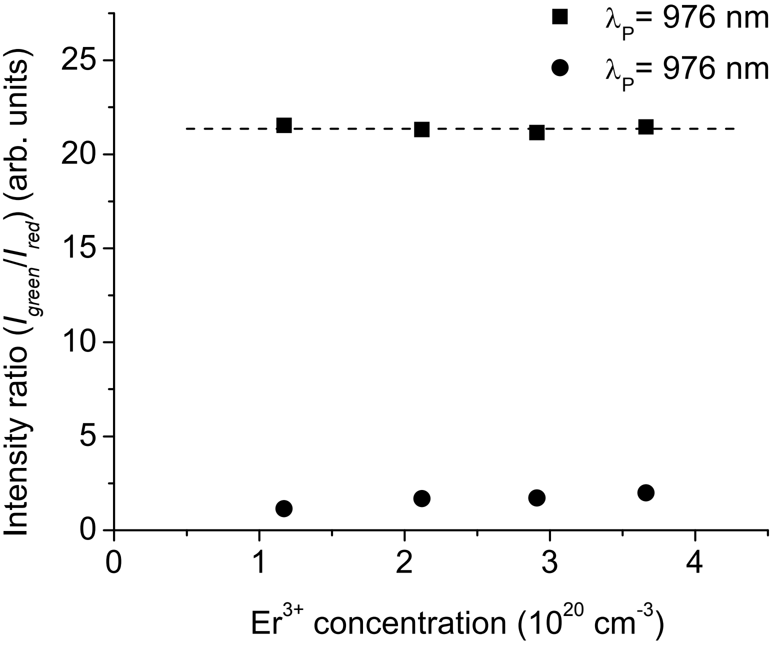

Fig. 6.12. Ratio of 525-550 nm vs. 660 nm intensity (I_{green}/I_{red}) as a function of Er^{3+} concentration.

In order to understand the situation a rate-equation analysis is performed, again in the framework of the quenched-ion rate-equation model delineated in Chapter 5 which takes into account the presence of quenched ions in $Al_2O_3:Er^{3+}$. First we analyze the situation in the absence of the ETU_3 process, where the $^4F_{9/2}$ level is populated only via multiphonon relaxation from the $^4S_{3/2}$ level (see Fig. 2.4). Then

$$\frac{dN_{4a/q}}{dt} = \frac{1}{\tau_5} N_{5a/q} - \frac{1}{\tau_4} N_{4a/q} = 0, \tag{6.13a}$$

$$\Rightarrow N_{4a/q} = \frac{\tau_4}{\tau_5} N_{5a/q}, \tag{6.13b}$$

where N_4 and N_5, τ_4 and τ_5 are the population densities and luminescence lifetimes of the $^4F_{9/2}$ and $^2H_{11/2}$ + $^4S_{3/2}$ levels, respectively. The emission intensities are proportional to the populations in each level, therefore the intensity ratio can be written as

$$\frac{I_{green}}{I_{red}} \propto \left(\frac{N_{5a} + N_{5q}}{N_{4a} + N_{4q}} \right) = \frac{\tau_5}{\tau_4}. \tag{6.14}$$

Under these excitation conditions, the I_{green}/I_{red} intensity ratio depends only on the luminescence lifetimes, but is independent of Er^{3+} concentration and choice of pump level, $^4I_{13/2}$ or $^4I_{11/2}$, in contrast with what is observed in the measurements. A note: in Eq. (6.13a) [but previously also in other rate-equations, and later in Eq. (6.15b)] we assume that all the decay from one level populates the next lower level. The radiative decays from one level to the remaining lower ones, with the corresponding branching ratios and radiative lifetimes, are neglected, because of the predominance of non-radiative decay over radiative decay for all the levels above $^4I_{13/2}$, see Sect. 6.2.

The upconversion process ETU$_3$ ($^4I_{13/2}$, $^4I_{11/2}$) → ($^4I_{15/2}$, $^4F_{9/2}$) or ($^4I_{11/2}$, $^4I_{13/2}$) → ($^4I_{15/2}$, $^4F_{9/2}$) constitutes an alternative, interionic channel for populating the $^4F_{9/2}$ level, which introduces a concentration and pump-level dependence to the I_{green}/I_{red} intensity ratio. With reference to Fig. 2.4, we first analyze the situation in case of 976-nm pumping. The $^2H_{11/2}$ + $^4S_{3/2}$ levels are populated by pump excitation to the $^4I_{11/2}$ level, followed by ETU$_2$ ($^4I_{11/2}$, $^4I_{11/2}$) → ($^4I_{15/2}$, $^4F_{7/2}$) and ESA$_2$ to the $^4F_{7/2}$ level and subsequent multiphonon relaxation. The $^4F_{9/2}$ level is assumed to be populated by non-radiative relaxation from the $^4S_{3/2}$ level and ETU$_3$. The corresponding rate equations are

$$\frac{dN_{5a/q}}{dt} = \varphi_P \sigma_{ESA2}\left(\lambda_P\right) N_{2a/q} + W_{ETU2} N_{2a/q}^2 - \frac{1}{\tau_5} N_{5a/q} = 0\,, \tag{6.15a}$$

$$\frac{dN_{4a/q}}{dt} = \frac{1}{\tau_5} N_{5a/q} - \frac{1}{\tau_4} N_{4a/q} + W_{ETU3} N_{1a/q} N_{2a/q} = 0\,, \tag{6.15b}$$

where φ_P is the pump photon flux per unit area launched into the detected small volume, which results in an intensity ratio of

$$\frac{I_{green}}{I_{red}} \propto \left(\frac{N_{5a}+N_{5q}}{N_{4a}+N_{4q}}\right) = \left(\frac{\varphi_P\sigma_{ESA2}\left(\lambda_P\right)\left(N_{2,a}+N_{2,q}\right)+W_{ETU2}N_{2a}^2}{\varphi_P\sigma_{ESA2}\left(\lambda_P\right)\left(N_{2,a}+N_{2,q}\right)+W_{ETU2}N_{2a}^2+W_{ETU3}N_{1a}N_{2a}}\right)\frac{\tau_5}{\tau_4}\,. \tag{6.16}$$

Here the terms including N_{2q}^2 and $N_{1q}N_{2q}$ have been ignored because their influence is negligible. The process ETU$_3$ is quantified in the intensity ratio via the macroscopic upconversion coefficient W_{ETU3}, which is a combination of both ETU$_{3a}$ and ETU$_{3b}$. In our specific case of a channel waveguide with small geometrical cross-section and moderate dopant concentrations, hence large pump intensities and excitation densities, the ESA$_2$ process exhibits a strong excitation rate and turns out to be the dominating upconversion mechanism, therefore ETU$_3$ has a negligible effect on the I_{green}/I_{red} intensity ratio – the same holds for ETU$_2$ and the corresponding W_{ETU2}. The value of W_{ETU3} is not yet known at this stage, but assuming it is on the same order of magnitude as W_{ETU1} and W_{ETU2} (we will show later that it is actually even lower), the ratio $\left(W_{ETU2}N_{2a}^2+W_{ETU3}N_{1a}N_{2a}\right)/\left[\varphi_P\sigma_{ESA2}\left(\lambda_P\right)\left(N_{2,a}+N_{2,q}\right)\right]$ would assume values between 10^{-3} and 10^{-2} (depending on the Er^{3+} concentration). Therefore, in our experimental situation Eq. (6.16) approximately reduces to Eq. (6.14) for the case without the ETU$_3$ process. Consequently, the measured intensity ratio under 976-nm pumping does not show any detectable dependence on Er^{3+} concentration (horizontal line in Fig. 6.12).

Again with reference to Fig. 2.4, the situation under 1480-nm pumping is as follows. Absorption of 1480-nm pump photons excites the Er^{3+} ions to the $^4I_{13/2}$ level, then ETU$_1$ ($^4I_{13/2}$, $^4I_{13/2}$) → ($^4I_{15/2}$, $^4I_{9/2}$) and subsequent multiphonon relaxation populate the $^4I_{11/2}$ level, followed by ETU$_2$ ($^4I_{11/2}$, $^4I_{11/2}$) → ($^4I_{15/2}$, $^4F_{7/2}$) to the $^4F_{7/2}$ level and subsequent multiphonon relaxation to the $^2H_{11/2}$ + $^4S_{3/2}$ levels. The $^4F_{9/2}$ level is again assumed to be populated by multiphonon relaxation from the $^4S_{3/2}$ level and ETU$_3$. The corresponding rate equations are

$$\frac{dN_{5a/q}}{dt} = W_{ETU2}N_{2a/q}^2 - \frac{1}{\tau_5}N_{5a/q} = 0\,, \tag{6.17a}$$

$$\frac{dN_{4a/q}}{dt} = \frac{1}{\tau_5}N_{5a/q} - \frac{1}{\tau_4}N_{4a/q} + W_{ETU3}N_{1a/q}N_{2a/q} = 0\,, \tag{6.17b}$$

which result in an intensity ratio of

$$\frac{I_{green}}{I_{red}} \propto \left(\frac{N_{5a}+N_{5q}}{N_{4a}+N_{4q}}\right) = \left(\frac{W_{ETU2}N_{2a}^2}{W_{ETU2}N_{2a}^2 + W_{ETU3}N_{1a}N_{2a}}\right)\frac{\tau_5}{\tau_4}\,. \tag{6.18}$$

Again, the terms including N_{2q}^2 and $N_{1q}N_{2q}$ have been ignored because their influence is negligible. In this case, the I_{green}/I_{red} intensity ratio depends on the interplay between ETU$_2$ and ETU$_3$. With knowledge of the population density distributions N_{1a} and N_{2a}, as calculated with the rate-equation system in Appendix B, Part 1 and displayed in Fig. 6.13, and by fitting the I_{green}/I_{red} ratio for the 1480-nm pump case in Fig. 6.12 with Eq. (6.18), we derive the macroscopic upconversion parameter W_{ETU3}, which is displayed in Fig. 6.10 and listed in Table 6.6 as a function of Er^{3+} concentration. Unlike W_{ETU1} and W_{ETU2}, W_{ETU3} appears to increase more than linearly with Er^{3+} concentration. Such non-linearity might simply be the result of the error propagation within our derivation, leading to a significantly larger uncertainty in the estimation of W_{ETU3}; another reason might have to do with the nature of this upconversion process: unlike ETU$_1$ and ETU$_2$, which involve energy migration in only one excited state, either the first or second excited state, respectively, ETU$_3$ involves energy migration in both excited states. Therefore, it is possible that W_{ETU3} requires a more complex and possibly non-linear description than that given by Eq. (4.25), which considers only one migration process.

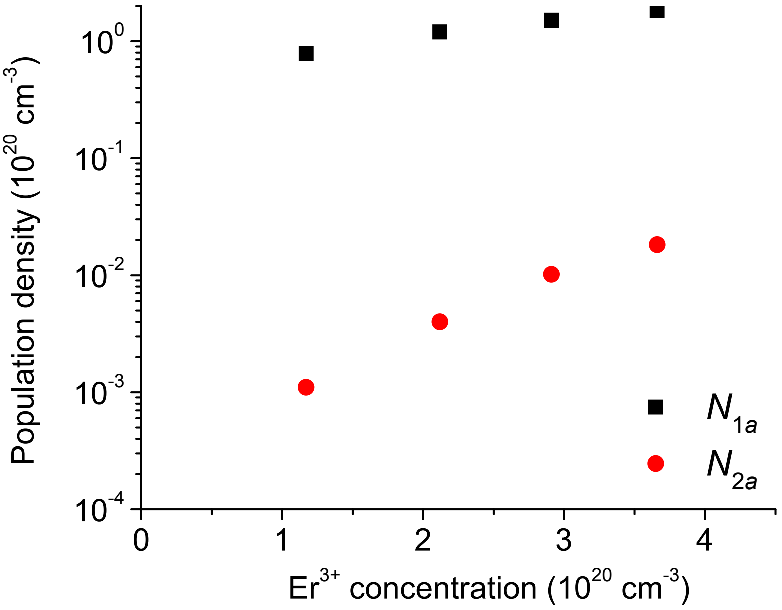

Fig. 6.13. Population densities N_{1a} and N_{2a} under 1480-nm pumping calculated with the rate-equation system of Appendix B, Part 1.

We observe from the values in Table 6.6 that, depending on the Er^{3+} concentration, W_{ETU3} is a factor of approximately 25 to 100 times smaller than W_{ETU1} and 10 to 40 times smaller than W_{ETU2}. Nevertheless, ETU_3 affects the I_{green}/I_{red} ratio under 1480-nm pumping, because the rate $R_{ETU} = W_{ETU}\ N_i\ N_j$ of this upconversion process depends on the population density N_{1a}, whereas the rate of ETU_2 depends entirely on the population density N_{2a}, see the denominator of Eq. (6.18). According to Fig. 6.13, under our experimental conditions N_{1a} is much larger than N_{2a}. The small magnitude of the W_{ETU3} coefficient can be partially understood by inspecting the $^4I_{11/2} \rightarrow {}^4I_{15/2}$ emission cross-section spectrum derived in Sect. 6.4.2 and $^4I_{13/2} \rightarrow {}^4F_{9/2}$ ESA cross-section spectrum evaluated in Sect. 6.3, which are both shown in Fig. 6.14, although the overlap integral of these two transitions clarifies only the strength of the ETU_{3a} upconversion (whereas we do not have the spectra necessary to examine the process ETU_{3b}). There is no overlap between the two cross-section spectra, hence ETU_{3a} is a non-resonant, phonon-assisted process. Even shifting the ESA spectrum by 84 nm (dashed line in Fig. 6.14), corresponding to the maximum phonon energy of 870 cm^{-1}, does not produce a spectral overlap. Therefore, ETU_{3a} can energetically occur only if more than one phonon is emitted, which further decreases the probability compared to one-phonon-assisted processes.

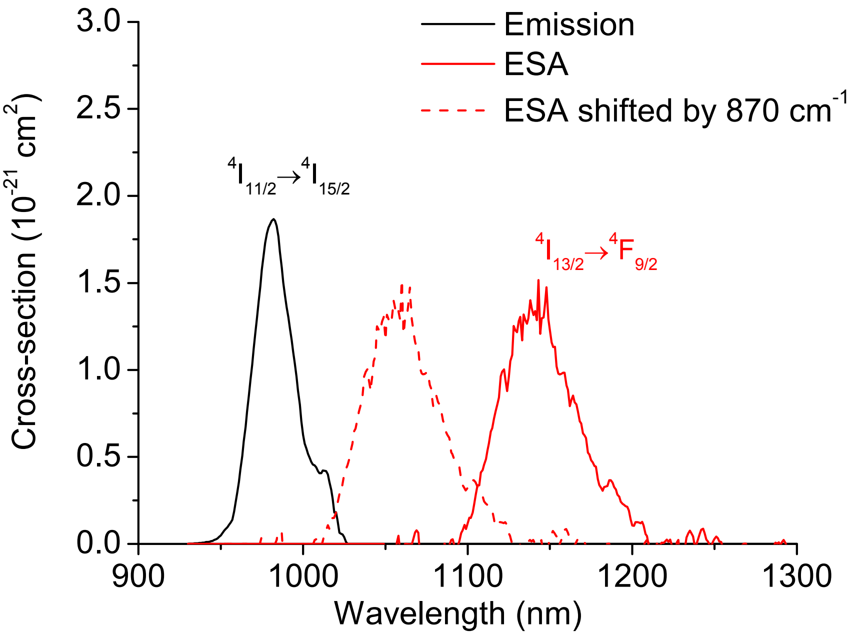

Fig. 6.14. $^4I_{11/2} \rightarrow {}^4I_{15/2}$ emission cross-section and $^4I_{13/2} \rightarrow {}^4F_{9/2}$ ESA cross-section derived in Sect. 6.3 and then shifted by 870 cm^{-1}, as explained in Sect. 6.5.

6.6 Summary

In this Chapter, a comprehensive investigation of the upper energy levels of Al_2O_3:Er^{3+}, up to the $^2H_{11/2}/^4S_{3/2}$ levels, has been presented. The J-O intensity parameters, radiative decay-rate constants, and radiative lifetimes have been calculated, and the luminescence lifetimes have been directly measured or estimated. The cross-sections of ESA transitions from the $^4I_{13/2}$ and $^4I_{11/2}$ levels have been determined; specifically, it has been shown that the $^4I_{13/2} \rightarrow {}^4I_{9/2}$ ESA transition, which in the past was incorrectly assumed to overlap with the 1480-nm pump wavelength in Er^{3+}-doped Al_2O_3 and other hosts [118,128], occurs at wavelengths longer than 1630 nm. The ESA cross-sections have been used to calculate the microparameters C_{DA} and C_{DD} of the energy-transfer processes occurring from the first and second excited states. The C_{DA} microparameter related to the ETU process ($^4I_{13/2}$, $^4I_{13/2}$) → ($^4I_{15/2}$, $^4I_{9/2}$) is significantly smaller than the one derived from the analysis of luminescence decay curves and pump-absorption measurements in Chapter 5, suggesting that this ETU processes is assisted by a phonon with an effective energy of 195 cm^{-1}. No phonons are involved in the energy migration and ETU process ($^4I_{11/2}$, $^4I_{11/2}$) → ($^4I_{15/2}$, $^4F_{7/2}$) originating from the second excited state. The presence of yet another phonon-assisted process, ($^4I_{13/2}$, $^4I_{11/2}$) → ($^4I_{15/2}$, $^4F_{9/2}$) or alternatively ($^4I_{11/2}$, $^4I_{13/2}$) → ($^4I_{15/2}$, $^4F_{9/2}$) has been proved and its macroscopic ETU coefficient has been determined thanks to the investigation of the $^4S_{3/2}$ vs. $^4F_{9/2}$ luminescence intensity as a function of Er^{3+} concentration.

Chapter 7

Conclusions

In this thesis, in-depth spectroscopic investigations of the optical properties of $Al_2O_3:Er^{3+}$ and $Al_2O_3:Yb^{3+}$ have been presented. The aim has been to provide important spectroscopic parameters for the design and optimization of integrated active devices based on these materials. Nevertheless, some of the spectroscopic investigations presented in this thesis are relevant from a fundamental point of view as well.

Er^{3+}- and Yb^{3+}-doped slab and channel waveguides were fabricated in Al_2O_3, largely thanks to the work of K. Wörhoff and J. D. B. Bradley. Thin films were deposited on thermally oxidized silicon wafers by reactive co-sputtering and channel waveguides were patterned by reactive ion etching. Monolithic integration of $Al_2O_3:Er^{3+}$ gain structures with passive silicon-on-insulator (SOI) waveguides was demonstrated in this thesis. A signal enhancement of 7.2 dB at 1533 nm was shown in an $Al_2O_3:Er^{3+}$-Si-$Al_2O_3:Er^{3+}$ structure. To our knowledge, this is the first time that monolithic integration of active rare-earth-ion-doped waveguides with passive SOI waveguides is achieved and signal enhancement is measured. In the future, these fundamental results will allow us to make use of potential Er-doped gain devices – such as high-speed amplifiers and arrays of narrow-linewidth DFB lasers – in passive Si photonic circuits.

Basic optical and spectroscopic properties, including propagation losses, absorption and emission cross-sections, and lifetimes were determined. The results for $Al_2O_3:Er^{3+}$ had already been reported in the PhD thesis of J. D. B. Bradley, whereas the $Al_2O_3:Yb^{3+}$ results were presented in this thesis.

We investigated the ion-ion process of energy-transfer upconversion (ETU) in $Al_2O_3:Er^{3+}$, which generally, in combination with energy migration, can be detrimental for the amplifier or laser performance of a number of rare-earth-ion-doped compounds by depleting the population of the long-lived upper state of the corresponding luminescence transition, thereby diminishing the available optical gain. The most important energy-transfer models found in the literature from the last sixty years – Burshteîn's and Zubenko's microscopic treatments of ETU, as well as Grant's macroscopic rate-equation approach – were applied to fit luminescence decay measurements under quasi-CW excitation performed on $Al_2O_3:Er^{3+}$. Zubenko's model, which combines a microscopic and macroscopic approach, provided the best agreement with the measured decay curves, although also the traditional rate-equation approach, under certain conditions, resulted in reasonable fits. From this investigation, values of the microparameters C_{DA} and C_{DD} of energy migration and ETU, respectively, and of the macroscopic ETU parameter W_{ETU} were obtained. However, fast luminescence quenching of a concentration-dependent fraction of Er^{3+} ions remained undetected in the luminescence decay measurements under quasi-CW excitation, hence Zubenko's model was applied to incomplete experimental information and, consequently, the obtained values of the macroscopic ETU parameter did not allow us to fit pump-absorption and small-signal gain measurements in the same samples.

Analysis of the quenching process by simple pump-absorption measurements provided essential quantitative information and allowed us to extend the theoretical models by considering the quenched ions. The quenching was investigated in both $Al_2O_3:Er^{3+}$ and $Al_2O_3:Yb^{3+}$ and results were compared. In $Al_2O_3:Yb^{3+}$ the quenching is most likely due to undesired impurities and/or host material defects; in $Al_2O_3:Er^{3+}$ there is an additional, major source of fast quenching which can probably be attributed to ion pair/cluster formation. In $Al_2O_3:Er^{3+}$ the microscopic energy-transfer parameters were derived, resulting in a macroscopic W_{ETU} coefficient that, together with the derived concentration-dependent fraction of quenched ions, allowed us to correctly describe luminescence-decay, pump-absorption and gain experiments for the whole range of Er^{3+} concentrations investigated. Since many rare-earth-ion-doped devices have doping levels comparable to those investigated in this thesis and the measurement of luminescence decay curves under quasi-CW excitation is a commonly applied experimental method, it is likely that fast quenching processes have remained undetected in a significant number of published works. In certain cases, this may have led to incorrect values of ETU parameters and could explain various discrepancies between theoretical and experimental results encountered in the literature. The model that has been proposed in this thesis can be helpful in predicting and optimizing the performance of rare-earth-ion-doped devices.

In a more general respect, Zubenko's model fails. This and most of the other available models treat all ions equally, thus neglecting the different local environment of individual ions. We observed that Zubenko's equation cannot fit the corresponding luminescence decay curves under short-pulse excitation, which include the information about quenching of a fraction of Er^{3+} ions as a fast component at the beginning of the luminescence decay. This failure exemplifies the fundamental breakdown of Zubenko's model in the presence of distinct spectroscopic classes of ions. In this thesis it has been shown that the separate consideration of these ion classes can be successful.

The impact of quenching on $Al_2O_3:Er^{3+}$ waveguide amplifiers and $Al_2O_3:Yb^{3+}$ integrated DFB lasers was discussed. In the former, it was observed that the fast quenching strongly degrades the amplifier performance already at low concentrations. In the latter, we focused on the measurement of the laser relaxation-oscillation frequency as a function of pump rate, usually performed in order to determine parameters of the laser medium or cavity. We showed that the fast quenching of a fraction of dopants affects the relaxation oscillations, resulting in incorrect values for the parameter deduced from this measurement. In the equations describing the relaxation oscillations, we replaced the lifetime of the upper laser level by an effective lifetime that takes the quenching into account.

Finally, a comprehensive investigation of the upper energy levels of $Al_2O_3:Er^{3+}$, up to the $^2H_{11/2}/^4S_{3/2}$ levels, was presented. A Judd-Ofelt analysis was performed, and luminescence lifetimes were measured or estimated. The cross-sections of ESA transitions from the $^4I_{13/2}$ and $^4I_{11/2}$ levels were determined; specifically, it was shown that the $^4I_{13/2} \rightarrow {}^4I_{9/2}$ ESA transition, which in the past was incorrectly assumed to overlap with the 1480-nm pump wavelength in Er^{3+}-doped Al_2O_3 and other hosts [118,128], occurs at wavelengths longer than 1630 nm. The ESA cross-sections were used to calculate the microparameters C_{DA} and C_{DD} of the energy-transfer processes occurring from the first and second excited states. Results suggest that the ETU process $(^4I_{13/2}, {}^4I_{13/2}) \rightarrow (^4I_{15/2}, {}^4I_{9/2})$ is assisted by a phonon, whereas no phonons are involved in the energy migration and ETU originating from the second excited state. The presence of yet another phonon-assisted process, $(^4I_{13/2}, {}^4I_{11/2}) \rightarrow (^4I_{15/2}, {}^4F_{9/2})$ or alternatively $(^4I_{13/2}, {}^4I_{11/2}) \rightarrow (^4F_{9/2}, {}^4I_{15/2})$ was proved and its macroscopic ETU coefficient was determined.

To summarize, a number of spectroscopic parameters have been determined in $Al_2O_3:Er^{3+}$ and $Al_2O_3:Yb^{3+}$, and fundamental investigations that help understanding the behavior of rare-earth ions in dielectric materials have been presented in this thesis.

There are a number of different areas where further work could be carried out to extend this research. For example, with reference to Fig. 5.10, the internal net gain per unit length at 1533 nm could be measured for Er^{3+} concentrations higher than those investigated so far, to help validate or even improve the quenched-ion rate-equation model.

With reference to Sect. 5.3.2, where the impact of the quenching on $Al_2O_3:Yb^{3+}$ integrated DFB lasers is investigated, the simple rate equation (5.12) that describes the transient behavior of the Yb^{3+} ions could be modified to represent also those lasers in which the condition $f_q^* \rightarrow f_q$ is not always fulfilled. A study of this kind was carried out in Refs. [139] and [140], and it was predicted that under certain pump-power, cavity and doping conditions, rare-earth-ion pairs and clusters can be exploited to achieve Q-switching operation. Following these investigations, we could possibly demonstrate Q-switching in $Al_2O_3:Er^{3+}$ and $Al_2O_3:Yb^{3+}$ lasers.

Certainly it would be desirable to understand and differentiate between the different mechanisms that cause the fast quenching, of which at the moment we have only a basic understanding. Knowledge of the local environment of rare-earth ions in the Al_2O_3 matrix could help. Local structures around the rare-earth ions can be investigated using extended X-ray absorption fine structure (EXAFS) [141], X-ray or neutron scattering [142], or nuclear-magnetic resonance (NMR) [143], just to name a few techniques. Ultimately is would be desirable to control – and for some applications even to eliminate – the cause of quenching.

Appendix A

Derivation of Zubenko's Equation

In Ref. [91] Zubenko's equation [Eq. (4.17) in Chapter 4] is presented as the solution of a system of equations [Eqs. (4.11a), (4.12), and (4.16)]. However, the detailed mathematical derivation of Zubenko's equation, which is quite lengthy and complicated, is not provided. We present it in this appendix, with all the relevant steps and intermediate equations.

First, Eq. (4.11a) needs to be solved:

$$\frac{\partial f(r,t)}{\partial t} = -W_{DA}(r) f(r,t) - \frac{1}{\tau_0} f(r,t) + \frac{1}{\tau_0}, \tag{A1}$$

which can be written and solved as

$$f' = -af + b \Rightarrow \int_{f_0}^{f} \frac{df}{af - b} = -\int_{0}^{t} dt \Rightarrow \ln\left(\frac{af - b}{af_0 - b}\right) = -af\,,$$

$$\Rightarrow f = f_0 \exp(-at) + \frac{b}{a}\left[1 - \exp(-at)\right] \tag{A2}$$

where $a = W_{DA}(r) + \frac{1}{\tau_0}$ and $b = \frac{1}{\tau_0}$. The initial condition is $f_0 = f(r,0) = 1$, consequently the solution of Eq. (4.11a) is

$$f(r,t) = \exp\left[-\left(W_{DA}(r) + \frac{1}{\tau_0}\right)t\right] + \frac{1}{W_{DA}(r)\tau_0 + 1}\left\{1 - \exp\left[-\left(W_{DA}(r) + \frac{1}{\tau_0}\right)t\right]\right\}, \tag{A3}$$

which corresponds to Eq. (4.11b).

Second, the nonlinear quenching rate *F*(*t*) (Eq. 4.12) is calculated:

$$
\begin{aligned}
F(t) &= \int_0^\infty W_{DA}(r) f(r,t) 4\pi r^2 dr \\
&= \int_0^\infty \frac{C_{DA}}{r^6}\left(\exp\left[-\left(\frac{C_{DA}}{r^6}+\frac{1}{\tau_0}\right)t\right] + \frac{1}{\frac{C_{DA}}{r^6}\tau_0+1}\left\{1-\exp\left[-\left(\frac{C_{DA}}{r^6}+\frac{1}{\tau_0}\right)t\right]\right\}\right) 4\pi r^2 dr \\
&= \underbrace{4\pi C_{DA}\int_0^\infty \frac{1}{r^4}\exp\left[-\left(\frac{C_{DA}}{r^6}+\frac{1}{\tau_0}\right)t\right]dr}_{\text{(a)}} + \underbrace{4\pi C_{DA}\int_0^\infty \frac{1}{r^4}\frac{1}{\frac{C_{DA}}{r^6}\tau_0+1}dr}_{\text{(b)}} \\
&\quad \underbrace{-4\pi C_{DA}\int_0^\infty \frac{1}{r^4}\frac{1}{\frac{C_{DA}}{r^6}\tau_0+1}\exp\left[-\left(\frac{C_{DA}}{r^6}+\frac{1}{\tau_0}\right)t\right]dr}_{\text{(c)}} .
\end{aligned}
\tag{A4}
$$

(a) $4\pi C_{DA}\int_0^\infty \frac{1}{r^4}\exp\left[-\left(\frac{C_{DA}}{r^6}+\frac{1}{\tau_0}\right)t\right]dr = \frac{2}{3}\pi^{3/2}\sqrt{C_{DA}}\,\frac{\exp(-t/\tau_0)}{\sqrt{t}}$,

(b) $4\pi C_{DA}\int_0^\infty \frac{1}{r^4}\frac{1}{\frac{C_{DA}}{r^6}\tau_0+1}dr = \frac{2}{3}\pi^2\sqrt{\frac{C_{DA}}{\tau_0}}$,

(c) $-4\pi C_{DA}\int_0^\infty \frac{1}{r^4}\frac{1}{\frac{C_{DA}}{r^6}\tau_0+1}\exp\left\{-\left(\frac{C_{DA}}{r^6}+\frac{1}{\tau_0}\right)t\right\}dr = -\frac{2}{3}\pi^2\sqrt{\frac{C_{DA}}{\tau_0}}\left[1-\operatorname{erf}\left(\sqrt{t/\tau_0}\right)\right]$.

To solve the integral in (c), see the section “Error Functions, Dawson’s and Fresnel Integrals” in Ref. [144]. Adding (a), (b), and (c) provides the solution

$$
F(t) = \frac{2\pi^2}{3}\sqrt{\frac{C_{DA}}{\tau_0}}\left[\sqrt{\frac{\tau_0}{\pi\, t}}\exp\left(-\frac{t}{\tau_0}\right)+\operatorname{erf}\left(\sqrt{\frac{t}{\tau_0}}\right)\right],
\tag{A5}
$$

which corresponds to Eq. (4.12).

Third, Eq. (4.16) needs to be solved:

$$
\frac{dN_1(t)}{dt} = -\frac{N_1(t)}{\tau_D} - F(t)N_1^2(t).
\tag{A6}
$$

With the substitution $z(t) = N_1^{-1}(t)$, Eq. (A6) can be rewritten as

$$
\frac{dz(t)}{dt} = \frac{z}{\tau_D} + F(t).
\tag{A7}
$$

The general solution of Eq. (A7) is

$$z\left(t\right)=C^{*}e^{G}+e^{G}\int e^{-G}F(t)dt\,, \tag{A8}$$

where $G=\int\frac{1}{\tau_D}dt=\frac{t}{\tau_D}$ and C^{*} is an arbitrary constant. It follows:

$$\begin{aligned}
z\left(t\right)&=C^{*}e^{\frac{t}{\tau_D}}+e^{\frac{t}{\tau_D}}\int e^{-\frac{t}{\tau_D}}\left\{\frac{2\pi^2}{3}\sqrt{\frac{C_{DA}}{\tau_0}}\left[\sqrt{\frac{\tau_0}{\pi\,t}}\exp\left(-\frac{t}{\tau_0}\right)+\operatorname{erf}\left(\sqrt{\frac{t}{\tau_0}}\right)\right]\right\}dt\\
&=C^{*}e^{\frac{t}{\tau_D}}+e^{\frac{t}{\tau_D}}\int\frac{2\pi^2}{3}\sqrt{\frac{C_{DA}}{\pi t}}\exp\left[-\left(\frac{1}{\tau_0}+\frac{1}{\tau_D}\right)t\right]dt\\
&\quad+e^{\frac{t}{\tau_D}}\int\frac{2\pi^2}{3}\sqrt{\frac{C_{DA}}{\tau_0}}e^{-\frac{t}{\tau_D}}\operatorname{erf}\left(\sqrt{\frac{t}{\tau_0}}\right)dt\\
&=e^{\frac{t}{\tau_D}}\left(C^{*}+\frac{2\pi^2}{3}\sqrt{C_{DA}}\,\frac{\operatorname{erf}\left[\sqrt{\left(\frac{1}{\tau_0}+\frac{1}{\tau_D}\right)t}\right]}{\sqrt{\frac{1}{\tau_0}+\frac{1}{\tau_D}}}\right)\\
&\quad+e^{\frac{t}{\tau_D}}\left(\frac{2\pi^2}{3}\sqrt{\frac{C_{DA}}{\tau_0}}\left\{\sqrt{\frac{1}{\tau_0}}\,\frac{\operatorname{erf}\left[\sqrt{t\left(\frac{1}{\tau_0}+\frac{1}{\tau_D}\right)}\right]}{\sqrt{\frac{1}{\tau_0}+\frac{1}{\tau_D}}}-\frac{e^{-\frac{t}{\tau_D}}\operatorname{erf}\left(\sqrt{\frac{t}{\tau_0}}\right)}{\frac{1}{\tau_D}}\right\}\right)\\
&=e^{\frac{t}{\tau_D}}\left\{C^{*}+\frac{2\pi^2}{3}\sqrt{C_{DA}}\left(1+\frac{\tau_D}{\tau_0}\right)\frac{\operatorname{erf}\left[\sqrt{\left(\frac{1}{\tau_0}+\frac{1}{\tau_D}\right)t}\right]}{\sqrt{\frac{1}{\tau_0}+\frac{1}{\tau_D}}}\right\}\\
&\quad-e^{\frac{t}{\tau_D}}\left\{\frac{2\pi^2}{3}\tau_D\sqrt{\frac{C_{DA}}{\tau_0}}e^{-\frac{t}{\tau_D}}\operatorname{erf}\left(\sqrt{\frac{t}{\tau_0}}\right)\right\}.
\end{aligned} \tag{A9}$$

The initial condition is $z(t=0)=N_1^{-1}\left(t=0\right)=N_1^{-1}\left(0\right)=C^{*}$. Consequently:

$$N_1(t) = z^{-1}(t) = \frac{N_1(0)\exp(-t/\tau_D)}{1 + N_1(0)\frac{2\pi^2}{3}\sqrt{C_{DA}}\left(1+\frac{\tau_D}{\tau_0}\right)\tau_D \frac{\mathrm{erf}\left(\sqrt{\left(\frac{1}{\tau_0}+\frac{1}{\tau_D}\right)t}\right)}{\sqrt{\frac{1}{\tau_0}+\frac{1}{\tau_D}}} - N_1(0)\frac{2\pi^2}{3}\sqrt{\frac{C_{DA}}{\tau_0}}\,\tau_D\mathrm{erf}\left(\sqrt{\frac{t}{\tau_0}}\right)}$$

$$= \frac{N_1(0)\exp(-t/\tau_D)}{1+N_1(0)\frac{2\pi^2}{3}\sqrt{\frac{C_{DA}}{\tau_0}}\,\tau_D\left[\sqrt{1+\frac{\tau_0}{\tau_D}}\,\mathrm{erf}\left(\sqrt{t\left(\frac{1}{\tau_0}+\frac{1}{\tau_D}\right)}\right)-\exp(-t/\tau_D)\,\mathrm{erf}\left(\sqrt{\frac{t}{\tau_0}}\right)\right]}, \tag{A10}$$

which corresponds to Zubenko’s Equation (4.17).

Appendix B

Er^{3+} Rate Equations under 1480-nm and 800-nm Pumping

Part 1. Rate Equations under 1480-nm Pumping

Part 1 of this appendix explains the parameters and equations applied to calculate the population densities in Al_2O_3:Er^{3+} under CW pumping at 1480 nm. We show that under steady-state conditions the time-dependent nonlinear quenching rate $F(t)$ in Zubenko's treatment reaches a time-independent value, reducing the microscopic approach to simple, standard rate equations. From these equations we extract the population density of the $^4I_{13/2}$ level under steady-state excitation, which equals the parameter $N_1(t = 0) = N_1(0)$ at starting time $t = 0$ in Eqs. (4.21) and (4.22), that is used for the analysis of luminescence decay curves in Chapters 4 and 5, as well as the transmitted pump power $P_P(L)$ in the analysis of pump-absorption experiments in Sect. 5.1.1.

We use a simplified three-level model which includes the $^4I_{15/2}$ ground state (level 0) as well as the excited states $^4I_{13/2}$ (level 1) and $^4I_{11/2}$ (level 2) of Fig. 2.4 in Chapter 2; we assume that all higher excited states have a short lifetime and are practically unpopulated. The relevant processes and parameters for the calculations are shown in Fig. 4.2 and listed in Table 4.1. Following Zubenko's treatment and the assumptions made in Sect. 4.1.5, the rate equations for the population densities N_i can be written as

$$\frac{dN_{2a/q}}{dt} = \frac{F_1(t)}{2} N_{1a/q}^2 - \frac{1}{\tau_2} N_{2a/q}, \tag{B1}$$

$$\frac{dN_{1a/q}}{dt} = R_{Pa/q} + \frac{1}{\tau_2} N_{2a/q} - \frac{1}{\tau_{1/1q}} N_{1a/q} - F_1(t) N_{1a/q}^2 . \tag{B2}$$

These equations account for the presence of quenched ions, which is described from Sect. 5.1 onward; the subscripts a/q indicate active and quenched ions, respectively. In Eq. (B2) $R_{Pa/q}$ indicate the pump rates for active and quenched ions,

$$R_{Pa/q} = \frac{\lambda_P}{hc} I_P \left[\sigma_{GSA1}(\lambda_P) N_{0a/q} - \sigma_{em}(\lambda_P) N_{1a/q} \right]$$

$$= \varphi_P \left[\sigma_{GSA1}\left(\lambda_P\right) N_{0a/q} - \sigma_{em}\left(\lambda_P\right) N_{1a/q} \right]. \tag{B3}$$

Here, λ_P is the pump wavelength and I_P is the pump intensity and φ_P is the pump photon flux per unit area. In Eq. (B3) the first term in the parenthesis represents GSA_1, while the second term is the stimulated emission at the pump wavelength, which is important in the presented case of channel waveguides with their accordingly high pump intensities and excitation densities.

Equation (B2) requires some clarification. As explained in Chapter 5, the quenched ions decay with a fast quenched decay time τ_{1q}, which comprises the effects of fast ETU in ion pairs and clusters, as well as quenching to due impurities and defects. Nevertheless, an excited quenched ion can also undergo "normal" ETU with other excited ions outside the pair or cluster. Therefore, we include separately the $-F_1\left(t\right)N_{1q}^2$ term, which assumes ETU of the quenched ions with the same parameter as for the unquenched ions. The upconverted quenched ion quickly relaxes back to the metastable state with decay time τ_2, hence the term N_{1q}/τ_2.

Under steady-state conditions, $\mathrm{d}N_{1a/q}/\mathrm{d}t = \mathrm{d}N_{2a/q}/\mathrm{d}t = 0$, while $F_1(t)$ reaches the time-independent value of $\frac{2\pi^2}{3}\sqrt{\frac{C_{DA}}{\tau_0}} \equiv 2W_{ETU1}$ (this was explained in Sect. 4.1.4). Equations (B1)-(B2) are then equivalent to standard rate equations and, together with the boundary conditions $N_{0a/q} + N_{1a/q} + N_{2a/q} = f_{a/q}N_d$ and $f_a + f_q = 1$ (where $f_{a/q}$ are the fractions of active and quenched ions, respectively), can be solved analytically, yielding the following expressions for the population densities:

$$N_{2a/q} = W_{ETU1} N_{1a/q}^2 \tau_2 , \tag{B4}$$

$$N_{1a/q} = \frac{-B_{a/q} + \sqrt{B_{a/q}^2 - 4AC_{a/q}}}{2A}, \tag{B5}$$

where A, $B_{a/q}$, and $C_{a/q}$ are given by

$$A = W_{ETU1}\left[1 + \varphi_P \sigma_{em}\left(\lambda_P\right)\tau_2\right], \tag{B6}$$

$$B_{a/q} = \varphi_P\left[\sigma_{em}\left(\lambda_P\right) + \sigma_{GSA1}\left(\lambda_P\right)\right] + \frac{1}{\tau_{1/1q}}, \tag{B7}$$

$$C_{a/q} = -f_{a/q} N_d \sigma_{GSA1}\left(\lambda_P\right)\varphi_P . \tag{B8}$$

In the above equations, for simplicity, the *xyz* discretization is taken into account implicitly. Equation (B5), evaluated at $z = 0$, corresponds to the initial condition $N_1(t = 0) = N_1(0)$ of the luminescence decay.

The longitudinal evolution of the pump power along the active waveguide is described by the propagation equation

$$\frac{dP_P(z)}{dz} = -P_P(z)\iint_{A_r} \psi_P\left[\sigma_{GSA1}(\lambda_P)\left(N_{0a}+N_{0q}\right)-\sigma_{em}(\lambda_P)\left(N_{1a}+N_{1q}\right)\right]dxdy$$
$$-P_P(z)\alpha_{bck}(\lambda_P), \qquad \text{(B9)}$$

where ψ_P is the normalized pump power distribution determined using the PhoeniX FieldDesigner software package [106]. The percentage of pump power which is outside the active region does not contribute to the population dynamics and simply decreases according to the wavelength-dependent background losses. The transmitted pump power $P_P(L)$, which is important for the pump-absorption calculations in Sect. 5.1.1, is determined by numerical integration of Eq. (B9).

Part 2. Rate Equations under 800-nm Pumping

1. Rate Equations

Part 2 of this appendix explains the parameters and equations from which the population densities in $Al_2O_3:Er^{3+}$ under CW pumping at 800 nm were calculated in order to extract the ESA cross-sections in Chapter 6. The rate equations involve the $^4I_{15/2}$ ground state (level 0) and the excited states $^4I_{13/2}$ (level 1), $^4I_{11/2}$ (level 2), and $^4S_{3/2}$ (level 5) of Fig. 2.4 in Chapter 2. In Part 1 of this Appendix we were allowed to neglect the $^4S_{3/2}$ level, as the relevant processes described there (see Fig. 4.2) create a substantial population density only in the levels up to $^4I_{11/2}$. Instead the processes taken into account in this Part (discussed shortly) can create a significant population density in the $^4S_{3/2}$ level.

The lifetimes of the other levels are rather short and the excitation densities of these levels are negligible. For the same reason no ESA from those levels was observed in Fig. 6.6. Also in this case, the applied rate-equation system originates from the quenched-ion rate-equation system delineated in Chapter 5 and accounts for the presence of a fraction of quenched ions. Like in Chapter 5, it is assumed here that the quenching mechanism affects only the first excited state, and for consistency with the calculations performed there, the decay time τ_{1q} of the quenched ions is set to the upper limit of 1 μs, but results are quantitatively similar for shorter values.

The relevant processes and parameters for the calculations are shown in Fig. 2.4 and listed in the next Subsection. With reference to Fig. 2.4, after the Er^{3+} ions are excited by pump light at 800 nm via GSA_3 to the short-lived $^4I_{9/2}$ level, a fast multiphonon relaxation populates the $^4I_{11/2}$ level and subsequent multiphonon relaxation and luminescent decay populate the $^4I_{13/2}$ level. Because of its relatively long lifetime, the $^4I_{13/2}$ level exhibits the largest excited population density, followed by the $^4I_{11/2}$ and $^4S_{3/2}$ levels. Pump light is additionally absorbed by the excited-state transitions $^4I_{13/2} \rightarrow {}^2H_{11/2}$ (ESA_3) and $^4I_{11/2} \rightarrow {}^4F_{3/2}$ (ESA_4) [127,145]. This excitation quickly relaxes to the $^4S_{3/2}$ level and from there decays via three sequential multiphonon-relaxation processes to the $^4I_{11/2}$ level. We take into account the ETU_1 process, while owing to the much shorter lifetime and accordingly lower population density of the $^4I_{11/2}$ level, in combination with moderate doping concentrations, the processes ETU_2 and ETU_3 produce negligible variations of the simulation results, therefore they have been discarded.

With the above considerations, the rate equations for the population densities N_i of the important levels read:

$$\frac{dN_{5a/q}}{dt} = R_{ESA3a/q} + R_{ESA4a/q} - \frac{1}{\tau_5} N_{5a/q}, \tag{B11}$$

$$\frac{dN_{2a/q}}{dt} = R_{GSA3a/q} - R_{ESA4a/q} + \frac{1}{\tau_5} N_{5a/q} - \frac{1}{\tau_2} N_{2a/q} + W_{ETU1} N_{1a/q}^2, \tag{B12}$$

$$\frac{dN_{1a/q}}{dt} = -R_{ESA3a/q} + \frac{1}{\tau_2} N_{2a/q} - \frac{1}{\tau_{1/1q}} N_{1a/q} - 2W_{ETU1} N_{1a/q}^2. \tag{B13}$$

The GSA$_3$, ESA$_3$, and ESA$_4$ rates for active and quenched ions are given by

$$R_{GSA3,a/q} = \frac{\lambda_P}{hc} I_P \sigma_{GSA3}\left(\lambda_P\right) N_{0a/q} = \varphi_P \sigma_{GSA3}\left(\lambda_P\right) N_{0a/q}, \tag{B14}$$

$$R_{ESA3,a/q} = \frac{\lambda_P}{hc} I_P \sigma_{ESA3}\left(\lambda_P\right) N_{1a/q} = \varphi_P \sigma_{ESA3}\left(\lambda_P\right) N_{1a/q}, \tag{B15}$$

$$R_{ESA4,a/q} = \frac{\lambda_P}{hc} I_P \sigma_{ESA4}\left(\lambda_P\right) N_{2a/q} = \varphi_P \sigma_{ESA4}\left(\lambda_P\right) N_{2a/q}. \tag{B16}$$

Under steady-state conditions, $dN_{1a/q}/dt = dN_{2a/q}/dt = dN_{5a/q}/dt = 0$, and equations (B11)-(B13), together with the boundary conditions $N_{0a/q} + N_{1a/q} + N_{2a/q} + N_{5a/q} = f_{a/q} N_d$ and $f_a + f_q = 1$, can be solved analytically, yielding the following expressions for the population densities in each level:

$$N_{5a/q} = \tau_5 \varphi_P \left(\sigma_{ESA3}\left(\lambda_P\right) N_{1a/q} + \sigma_{ESA4}\left(\lambda_P\right) N_{2a/q} \right), \tag{B17}$$

$$N_{2a/q} = \tau_2 \left[N_{1a/q} \left(\varphi_P \sigma_{ESA3}\left(\lambda_P\right) + \frac{1}{\tau_{1/1q}} \right) + 2W_{ETU1} N_{1a/q}^2 \right], \tag{B18}$$

$$N_{1a/q} = \frac{-B_{a/q} + \sqrt{B_{a/q}^2 - 4AC_{a/q}}}{2A}, \tag{B19}$$

where A, $B_{a/q}$, and $C_{a/q}$ are given by

$$A = W_{ETU1} \left[2\varphi_P \tau_2 \left(\sigma_{GSA3}\left(\lambda_P\right) + \varphi_P \sigma_{GSA3}\left(\lambda_P\right) \sigma_{ESA4}\left(\lambda_P\right) \tau_5 \right) + 1 \right], \tag{B20}$$

$$\begin{aligned} B_{a/q} = {} & \varphi_P \sigma_{GSA3}\left(\lambda_P\right) \left[1 + \left(\frac{1}{\tau_{1/1q}} + \varphi_P \sigma_{ESA3}\left(\lambda_P\right) \right) \tau_2 \right] \\ & + \varphi_P^2 \sigma_{GSA3}\left(\lambda_P\right) \tau_5 \left(\sigma_{ESA3}\left(\lambda_P\right) + \sigma_{ESA4}\left(\lambda_P\right) \frac{\tau_2}{\tau_{1/1q}} + \varphi_P \sigma_{ESA3}\left(\lambda_P\right) \sigma_{ESA4}\left(\lambda_P\right) \tau_2 \right) \end{aligned}$$

$$+\frac{1}{\tau_{1/1q}}, \tag{B21}$$

$$C_{a/q} = -f_{a/q}\, N_d \varphi_P \sigma_{GSA3}\left(\lambda_P\right). \tag{B22}$$

Also in these equations, for simplicity, the *xyz* discretization is taken into account implicitly. The longitudinal evolution of the pump power along the active waveguide is described by the propagation equation

$$\begin{aligned}\frac{dP_P(z)}{dz} &= -P_P(z)\iint_{A_r}\psi_P\left[\sigma_{GSA3}(\lambda_P)\left(N_{0a}+N_{0q}\right)\right]dxdy\\ &\quad -P_P(z)\iint_{A_r}\psi_P\left[\sigma_{ESA3}(\lambda_P)\left(N_{1a}+N_{1q}\right)+\sigma_{ESA4}(\lambda_P)\left(N_{2a}+N_{2q}\right)\right]dxdy\\ &\quad -P_P(z)\alpha_{bck}(\lambda_P).\end{aligned} \tag{B23}$$

2. Results

The sample investigated in the present ESA measurements had an Er^{3+} concentration of 1.17×10^{20} cm^{-3} and, according to Chapter 5, a fraction f_q of quenched ions equal to 10%. The W_{ETU1} value of 2.7×10^{-19} cm^{3}s^{-1} (third column of Table 6.6) was used. The background propagation loss α_{bck} at the 800-nm pump wavelength amounted to 0.4 dB/cm and the GSA$_3$ cross-section at 800 nm was $\sigma_{GSA3}(\lambda_P) = 1.24 \times 10^{-21}$ cm^2 [14]. The ESA$_3$ and ESA$_4$ cross-sections at this wavelength were both not contained in the measured ESA spectra of Fig. 6.6 but, based on experimental results obtained for ZBLAN [145], chosen to be $\sigma_{ESA3}(\lambda_P) = \sigma_{ESA4}(\lambda_P) = 0.7 \times 10^{-21}$ cm^2. Given $N_i = N_{ia} + N_{iq}$, Eqs. (6. 11a) and (6. 11b) can be rewritten as

$$\begin{aligned}N_i^{eff} &= \frac{1}{L}\int_0^L dz\iint_{A_r} dxdy\; N_i\psi_S = \frac{1}{L}\int_0^L dz\iint_{A_r} dxdy\left(N_{ia}+N_{iq}\right)\psi_S\\ &= \frac{1}{L}\int_0^L dz\iint_{A_r} dxdy\; N_{ia}\psi_S + \frac{1}{L}\int_0^L dz\iint_{A_r} dxdy\; N_{iq}\psi_S = N_{ia}^{eff} + N_{iq}^{eff}\end{aligned} \tag{B24}$$

$$N_e^{eff} = \sum\nolimits_i N_i^{eff} = \sum\nolimits_i N_{ia}^{eff} + N_{iq}^{eff} \tag{B25}$$

where $N_{i,a/q}^{eff}$ are the effective population densities of active and quenched ions, respectively. By inserting the solutions (B17)-(B19) into (B24)-(B25), it is possible to calculate N_i^{eff} for the substantially populated first, second and fifth excited states, then $N_e^{eff} = N_1^{eff} + N_2^{eff} + N_5^{eff}$, and finally the relative excited population densities N_i^{eff} / N_e^{eff}. From the above integrals it appears that the effective population densities depend on the probe wavelength and normalized probe-power distribution ψ_S. However, when evaluating the effective population densities, we found only minimal differences throughout the whole probe-wavelength range of 900-1800 nm. Calculations result in $N_1^{eff} / N_e^{eff} = 0.712–0.732$, $N_2^{eff} / N_e^{eff} = 0.217–0.232$, and $N_5^{eff} / N_e^{eff} = 0.051–0.056$. As an example, Table B1 illustrates the calculations for the case $\lambda_S = 980$ nm.

Alternatively, one could argue that in ZBLAN GSA$_3$, ESA$_3$, and ESA$_4$ have almost the same cross-section at 800 nm [145]. Accordingly, simulations with the ESA$_3$ and ESA$_4$ cross-sections set equal to the GSA$_3$ cross-section, i.e., $\sigma_{GSA3}(\lambda_P) = \sigma_{ESA3}(\lambda_P) = \sigma_{ESA4}(\lambda_P) = 1.24 \times 10^{-21}$ cm^2 were performed, resulting in N_1^{eff} / N_e^{eff} = 0.614–0.639, N_2^{eff} / N_e^{eff} = 0.280–0.298, and N_5^{eff} / N_e^{eff} = 0.081–0.088. However, this leads to a quite large negative signal in the ESA spectrum from 1450 nm to slightly beyond 1600 nm, too large to be explained by a non-perfect cancellation of the $^4I_{15/2} \leftrightarrow {}^4I_{13/2}$ GSA and SE and non-addressed $^4S_{3/2} \rightarrow {}^4I_{9/2}$ SE. Therefore, these results were discarded.

Table B1. Effective population densities and relative excited population densities under the experimental conditions of the ESA measurements of Sect. 6.3, for the example of λ_S = 980 nm.

Level	**Active ions (N_{ia}^{eff}) [cm^{-3}]**	**Quenched ions (N_{iq}^{eff}) [cm^{-3}]**	**Total (N_i^{eff}) [cm^{-3}]**	N_i^{eff} / N_e^{eff}
$^4I_{13/2}$ (1)	5.87×10^{19}	4.63×10^{16}	5.88×10^{19}	0.712
$^4I_{11/2}$ (2)	1.64×10^{19}	2.79×10^{18}	1.92×10^{19}	0.232
$^4S_{3/2}$ (5)	4.43×10^{18}	1.92×10^{17}	4.62×10^{18}	0.056
			$N_e^{eff} = N_1^{eff} + N_2^{eff} + N_5^{eff}$ $= 8.26 \times 10^{19}$ cm^{-3}	

Appendix C

Yb^{3+} Rate Equations under 976-nm Pumping

This appendix explains the parameters and equations applied to calculate the population densities in Al$_2$O$_3$:Yb^{3+} under CW pumping at 976 nm, which are used for the analysis of the transmitted pump power $P_P(L)$ in pump-absorption experiments explained in Sect. 5.1.2.

Al$_2$O$_3$:Yb^{3+} constitutes a two-multiplet-level system, see Fig. 2.5 in Chapter 2. The relevant processes and parameters for the calculations are listed in Table 5.2. The rate equation for the population density N_1 in the ^{2}F$_{5/2}$ excited state can be written as

$$\frac{dN_{1a/q}}{dt} = R_{Pa/q} - \frac{N_{1a/q}}{\tau_{1/1q}} . \tag{C1}$$

This equation accounts for the presence of quenched ions. In Eq. (C1) $R_{Pa/q}$ are the pump rates for active and quenched ions,

$$\begin{aligned} R_{Pa/q} &= \frac{\lambda_P}{hc} I_P \left[\sigma_{GSA}(\lambda_P) N_{0a/q} - \sigma_{em}(\lambda_P) N_{1a/q}\right] \\ &= \varphi_P \left[\sigma_{GSA}(\lambda_P) N_{0a/q} - \sigma_{em}(\lambda_P) N_{1a/q}\right]. \end{aligned} \tag{C2}$$

Here, N_0 is the population density in the ^{2}F$_{7/2}$ ground state. In Eq. (C2) the first term in the parenthesis represents the GSA, while the second term is the stimulated emission at the pump wavelength, which is important in the presented case of channel waveguides with their accordingly high pump intensities and excitation densities.

Under steady-state conditions, $dN_{1a/q}/dt = 0$, and, together with the boundary conditions $N_{0a/q} + N_{1a/q} = f_{a/q} N_d$ and $f_a + f_q = 1$ (where $f_{a/q}$ are the fractions of active and quenched ions, respectively), Eq. (C1) can be solved analytically

$$N_{1a/q} = \frac{\varphi_P \sigma_{GSA}(\lambda_P)}{\varphi_P \left[\sigma_{GSA}(\lambda_P) + \sigma_{em}(\lambda_P)\right] + \dfrac{1}{\tau_{1/1q}}} f_{a/q} N_d . \tag{C3}$$

In the above equations, for simplicity, the *xyz* discretization is taken into account implicitly.

The longitudinal evolution of the pump power along the active waveguide is described by the propagation equation

$$\begin{aligned}\frac{dP_P(z)}{dz} = &-P_P(z)\iint_{A_r}\psi_P\left[\sigma_{GSA}(\lambda_P)\left(N_{0a}+N_{0q}\right)-\sigma_{em}(\lambda_P)\left(N_{1a}+N_{1q}\right)\right]dxdy \\ &-P_P(z)\alpha_{bck}(\lambda_P)\,.\end{aligned} \tag{C4}$$

The transmitted pump power $P_P(L)$, which is important for the pump-absorption calculations of Sects. 5.1.2 and 5.3.2, is determined by numerical integration of Eq. (C4).

References

1. R. C. Alfreness, "Optical guided-wave devices," Science **234**, 825-829 (1986).
2. C. R. Pollock and M. Lipson, *Integrated Photonics* (Kluwer Academic Publisher, Boston, 2003).
3. R. G. Hunsperger, *Integrated Optics*, 5th edn. (Springer, Berlin, 2002)
4. L. Eldada, "Advances in telecom and datacom optical components," Opt. Eng. **40**, 1165-1178 (2001).
5. Y. Vlasov, W. M. J. Green, and F. Xia, "High-throughput silicon nanophotonic wavelength-insensitive switch for on-chip optical networks," Nat. Photonics **2**, 242-246 (2008).
6. A. N. Sloper, J. K. Deacon, and M. T. Falnagan, "A planar indium phosphate monomode waveguide evanescent field immunosensor," Sens. Actuators B **1**, 589-591 (1990).
7. R. Horváth, H. C. Pedersen, N. Skivesen, D. Selmeczi, and N. B. Larsen, "Optical waveguide sensor for on-line monitoring of bacteria," Opt. Lett. **28**, 1233-1235 (2003).
8. P. J. Caspers, G. W. Lucassen, and G. J. Puppels, "Combined in vivo confocal Raman spectroscopy and confocal microscopy of human skin," Biophys. J. **85**, 572-580 (2003).
9. M. Lipson, "Guiding, modulating, and emitting light on silicon – challenges and opportunities," J. Lightwave Technol. **23**, 4222-4238 (2005).
10. Q. Xu, B. Schmidt, S. Pradhan, and M. Lipson, "Micrometre-scale silicon electro-optic modulator," Nature **435**, 325-327 (2005).
11. G. Masini, L. Colace, G. Assanto, H. C. Luan, K. Wada, and L. C. Kimerling, "High responsitivity near infrared Ge photodetectors integrated on Si," Electron. Lett. **35**, 1467-1468 (1999).
12. A. W. Fang, H. Park, Y. H. Kuo, R. Jones, O. Cohen, D. Liang, O. Raday, M. N. Sysak, M. J. Paniccia, and J. E Bowers, "Hybrid silicon evanescent devices," Mater. Today **10**, 28-35 (2007).
13. G. Roelkens, J. Van Campenhout, J. Brouckaert, D. Van Thourhout, R. Baets, P. Rojo Romeo, P. Regreny, A. Kazmierczak, C. Seassal, X. Letartre, G. Hollinger, J. M. Fedeli, L. Di Cioccio, and C. Lagehe-Blanchard, "III-V/Si photonics by die-to-wafer bonding," Mater. Today **10**, 36-43 (2007).
14. K. Wörhoff, J. D. B. Bradley, F. Ay, D. Geskus, T. P. Blauwendraat, and M. Pollnau, "Reliable low-cost fabrication of low-loss $Al_2O_3:Er^{3+}$ waveguides with 5.4-dB optical gain," IEEE J. Quantum Electron. **45**, 454-461 (2009).
15. C. A. Barrios and M. Lipson, "Electrically driven silicon resonant light emitting device based on slot-waveguide," Opt. Express **13**, 10092-10101 (2005).
16. D. R. Zimmerman and L. H. Spiekman, "Amplifiers for the masses: EDFA, EDWA, and SOA amplets for metro and access applications," J. Lightwave Technol. **22**, 63-70 (2004).
17. D. Geskus, S. Aravazhi, S. García Blanco, and M. Pollnau, "Giant optical gain in a rare-earth-ion-doped microstructure," Adv. Mater. **24**, OP19-OP22 (2011).

18. J. D. B. Bradley, M. Costa e Silva, M. Gay, L. Bramerie, A. Driessen, K. Wörhoff, J. C. Simon, and M. Pollnau, "170 GBit/s transmission in an erbium-doped waveguide amplifier on silicon," Opt. Express **17**, 22201-22208 (2009).
19. M. Nakazawa, T. Yamamoto, and K. R. Tamura, "1.28 Tbit/s-70 km OTDM transmission using third- and fourth-order simultaneous dispersion compensation with a phase modulation," Electron. Lett. **36**, 2027-2029 (2000).
20. L. H. Spiekman, "Semiconductor optical amplifiers," in *Optical Fiber Telecommunications Volume IV-A*, I. P. Kaminow and T. Li, eds. (Academic Press, San Diego, California, 2002).
21. S. Blaize, L. Bastard, C. Cassagnètes, and J. E. Broquin, "Multiwavelengths DFB waveguide laser arrays in Yb-Er codoped phosphate glass substrate," IEEE Photon. Technol. Lett. **15**, 516-518 (2003).
22. E. H. Bernhardi, H. A. G. M. van Wolferen, L. Agazzi, M. R. H. Khan, C. G. H. Roeloffzen, K. Wörhoff, M. Pollnau, and R. M. de Ridder, "Ultra-narrow-linewidth, single-frequency distributed-feedback waveguide laser in Al_2O_3:Er^{3+} on silicon," Opt. Lett. **35**, 2394-2396 (2010).
23. *Frankfurt Laser Company*. http://www.frlaserco.com/
24. J. Seufert, M. Fischer, M. Legge, J. Koeth, R. Werner, M. Kamp, and A. Forchel, "DFB laser diodes in the wavelength range from 760 nm to 2.5 μm," Spectrochemica Acta Part A **60**, 3243-3247 (2004).
25. J. D. B. Bradley, F. Ay, K. Wörhoff, and M. Pollnau, "Fabrication of low-loss channel waveguides in Al_2O_3 and Y_2O_3 layers by inductively coupled plasma reactive ion etching," Appl. Phys. B **89**, 311-318 (2007).
26. G. N. van den Hoven, R. J. I. M. Koper, A. Polman, C. van Dam, K. W. M. van Uffelen, and M. K. Smit, "Net optical gain at 1.53 μm in Er-doped Al_2O_3 waveguides on silicon," Appl. Phys. Lett. **68**, 1886-1888 (1996).
27. J. Yang, "Neodymium-doped waveguide amplifiers and lasers for integrated optical applications," Ph.D. Thesis, University of Twente, The Netherlands, 2010.
28. J. D. B. Bradley, L. Agazzi, D. Geskus, F. Ay, K. Wörhoff, and M. Pollnau, "Gain bandwidth of 80 nm and 2 dB/cm peak gain in Al_2O_3:Er^{3+} optical amplifiers on silicon," J. Opt. Soc. Am. B **27**, 187-196 (2010).
29. J. D. B. Bradley, R. Stoffer, A. Bakker, L. Agazzi, F. Ay, K. Wörhoff, and M. Pollnau, "Integrated Al_2O_3:Er^{3+} zero-loss optical amplifier and power splitter with 40 nm bandwidth," IEEE Photon. Technol. Lett. **22**, 278-280 (2010).
30. J. D. B. Bradley, R. Stoffer, L. Agazzi, F. Ay, K. Wörhoff, and M. Pollnau, "Integrated Al_2O_3:Er^{3+} ring laser on silicon with wide wavelength selectivity," Opt. Lett. **35**, 73-75 (2010).
31. E. H. Bernhardi, K. Wörhoff, R. M. de Ridder, and M. Pollnau, "Highly Efficient Distributed Feedback Waveguide Laser in Al_2O_3:Yb^{3+} on Silicon," in *Advanced Solid-State Photonics Conference, Istanbul, Turkey, 2011* (Optical Society of America, Washington DC, 2011), paper ATuD7.
32. J. D. B. Bradley, "Al_2O_3:Er^{3+} as gain platform for integrated optics," Ph.D. Thesis, University of Twente, The Netherlands, 2009.
33. W. Koechner, *Solid-State Laser Engineering*, 5th edn. (Springer, Berlin, 1999).
34. A. E. Siegman, *Lasers* (University Science Books, Mill Valley, California, 1986).
35. C. Füchtbauer, G. Joos, and O. Dinkelacker, "Über intensität, verbreiterung und druckverschiebung vor spectrallinen, insbesondere der absorptionslinie 2537 des quecksilbers," Ann. Phys.-Leipzig **71**, 204-226 (1923).

36. R. Ladenburg, “Die quantentheoretische deutung der zahl der dispersionelektronen,” Zeitschr. Phys. **4**, 451-471 (1921).
37. W. B. Fowler and D. L. Dexter, “Relation between absorption and emission probabilities in luminescent centers in ionic solids,” Phys. Rev. **128**, 2154-2165 (1962).
38. B. F. Aull and H. P. Jenssen, “Vibronic interaction in Nd:YAG resulting in nonreciprocity of absorption and stimulated emission cross sections,” IEEE J. Quantum Electron. **QE-18**, 925-930 (1982).
39. D. E. McCumber, “Einstein relations connecting broadband emission and absorption spectra,” Phys. Rev. **136**, 954-957 (1964).
40. W. J. Miniscalco and R. S. Quimby, “General procedure for the analysis of Er^{3+} cross-sections,” Opt. Lett. **16**, 258-260 (1991).
41. B. R. Judd, “Optical absorption intensities of rare-earth ions,” Phys. Rev. **127**, 750-761 (1962).
42. G. S. Ofelt, “Intensities of crystal spectra of rare-earth ions,” J. Chem. Phys. **37**, 511-520 (1962).
43. A. A. Kaminskii, *Crystalline Lasers: Physical Processes and Operating Schemes* (CRC Press, New York, 1996).
44. W. T. Carnall, P. R. Fields, and R. Rajnak, “Electronic energy levels in the trivalent lanthanide aquo ions,” J. Chem. Phys. **49**, 4424-4442 (1968).
45. W. J. Miniscalco, “Optical and electronic properties of rare earth ions in glasses,” in *Rare Earth Doped Fibre Lasers and Amplifiers*, edited by M. J. F. Digonnet (Marcel Dekker, New York, 1993).
46. E. Desurvire, “Erbium doped fiber amplifiers: principles and applications,” John Wiley and Sons, New York, 1994.
47. X. Zou and T. Izumitani, “Spectroscopic properties and mechanisms of excited state absorption and energy transfer upconversion for Er^{3+}-doped glasses,” J. Non-Cryst. Solids **162**, 68-80 (1993).
48. D. K. Sardar, J. B. Gruber, B. Zandi, J. A. Hutchinson, and C. W. Trussell, “Judd–Ofelt analysis of the $Er^{3+}(4f^{11})$ absorption intensities in phosphate glass: Er^{3+}, Yb^{3+},” J. Appl. Phys. **93**, 2041-2046 (2003).
49. S. Magne, Y. Ouerdane, M. Druetta, J.P. Goure, P. Ferdinand, and G. Monnom, “Cooperative luminescence in an ytterbium-doped silica fibre,” Opt. Comm. **111**, 310-316 (1994).
50. Ph. Goldner, F. Pellé, D. Meichenin, and F. Auzel, “Cooperative luminescence in ytterbium-doped $CsCdBr_3$,” J. Lumin. **71**, 137-150 (1997).
51. E. Montoya, O. Espeso, and L. E. Bausá, “Cooperative upconversion in Yb^{3+}:$LiNbO_3$,” J. Lumin. **87-89**, 1036-1038 (2000).
52. H. Schober, D. Strauch, and B. Dorner, “Lattice dynamics of sapphire (Al_2O_3),” Z. Phys. B **92**, 273-283 (1993).
53. J. C. Mackechnie, W. L. Barnes, D. C. Hanna, and J. E. Townsend, “High power ytterbium (Yb^{3+})-doped fiber laser operating in the 1.12 μm region,” Electron. Lett. **29**, 52-53 (1993).
54. J. Y. Allain, M. Monerie, H. Poignant, and T. Georges, “High-efficiency ytterbium-doped fluoride fiber laser,” J. Non-Cryst. Solids **161**, 270 -273 (1993).
55. H. M. Pask, R. J. Carman, D. C. Hanna, A. C. Tropper, C. J. Mackechnie, P. R. Barber, and J. M. Dawes, “Ytterbium-doped silica fiber lasers: versatile sources for the 1-1.2 μm region,” IEEE J. Select. Topics Quantum Electron. **1**, 2-13 (1995).

56. R. Paschotta, J. Nilsson, A. C. Tropper, and D. C. Hanna, “Ytterbium-doped fiber amplifiers,” IEEE J. Quantum Electron. **33**, 1049-1056 (1997).
57. A. J. Kenyon, “Recent developments in rare-earth doped materials for optoelectronics,” Prog. Quantum Electron. **26**, 225-284 (2002).
58. Polman, “Erbium implanted thin film photonic materials,” J. Appl. Phys. **82**, 1-39 (1997).
59. D. C. Hanna, J. K. Jones, A. C. Large, D. P. Shepherd, A. C. Tropper, P. J. Chandler, M. J. Rodman, P. D. Townsend, and L. Zhang, “Quasi-3 level 1.03 μm laser operation of a planar ion-implanted Yb:YAG waveguide,” Opt. Commun. **99**, 211-215 (1993).
60. U. Griebner and H. Schonnagel, “Laser operation with nearly diffraction-limited output from a Yb:YAG multimode channel waveguide,” Opt. Lett. **24**, 750-752 (1999).
61. M. Fujimura, H. Tsuchimoto, and T. Suhara, “Yb-diffused $LiNbO_3$ annealed/proton exchanged waveguide lasers,” IEEE Photon. Technol. Lett. **17**, 130-132 (2005).
62. Y. E. Romanyuk, C. N. Borca, M. Pollnau, S. Rivier, V. Petrov, and U. Griebner, “Yb-doped $KY(WO_4)_2$ planar waveguide laser,” Opt. Lett. **31**, 53-55 (2006).
63. D. Geskus, S. Aravazhi, K. Wörhoff, and M. Pollnau, “High-power, broadly tunable, and low-quantum-defect $KGd_{1-x}Lu_x(WO_4)_2:Yb^{3+}$ channel waveguide lasers,” Opt. Express **18**, 26107-26112 (2010).
64. L. Agazzi, J. D. B. Bradley, M. Dijkstra, F. Ay, G. Roelkens, R. Baets, K. Wörhoff, and M. Pollnau, “Monolithic integration of erbium-doped amplifiers with silicon-on-insulator waveguides,” Opt. Express **18**, 27703-27711 (2010).
65. P. K. Tien and R. Ulrich, “Theory of prism-film coupler and thin-film light guides,” J. Opt. Soc. Am. **60**, 1325-1337 (1970).
66. H. P. Weber, F. A. Dunn, and W. N. Leibolt, “Loss measurements in thin-film optical waveguides,” Appl. Opt. **12**, 755-757 (1973).
67. M Hoekman, “A characterization technique for loss in arbitrarily shaped IO waveguiding structures using camera imaging,” internal communication, 2009.
68. C. Strohhöfer and A. Polman, “Absorption and emission spectroscopy in Er^{3+}-Yb^{3+} doped aluminum oxide waveguides,” Opt. Mater. **21**, 705-712 (2003).
69. B. J. Ainslie, S. P. Craig-Ryan, S. T. Davey, J. R. Armitage, C. G. Atkins, J. F. Massicott, and R. Wyatt, “Erbium doped fibers for efficient optical amplifiers,” Proc. Inst. Elect. Eng. **137**, 205-208 (1990).
70. P. Blixt, J. Nilsson, T. Carlnas, and B. Jaskorzynska, “Concentration-dependent upconversion in Er^{3+}-doped fiber amplifiers: experiments and modeling,” IEEE Photon. Technol. Lett. **3**, 996-998 (1991).
71. E. Snoeks, G. N. van den Hoven, A. Polman, B. Hendriksen, M. B. J. Diemeer, and F. Priolo, “Cooperative upconversion in erbium-implanted soda-lime silicate glass optical waveguides,” J. Opt. Soc. Am. B **12**, 1468-1474 (1995).
72. S. Guy, C. L. Bonner, D. P. Shepherd, D. C. Hanna, A. C. Tropper, and B. Ferrand, “High-inversion densities in Nd:YAG: upconversion and bleaching,” IEEE J. Quantum Electron. **34**, 900-909 (1998).
73. T. Chuang and H. R. Verdun, “Energy transfer upconversion and excited state absorption of laser radiation in Nd:YLF laser crystals,” IEEE J. Quantum Electron. **32**, 79-91 (1996).

74. M. Pollnau, P. J. Hardman, M. A. Kern, W. A. Clarkson, and D. C. Hanna, “Upconversion-induced heat generation and thermal lensing in Nd:YLF and Nd:YAG,” Phys. Rev. B **58**, 16076-16092 (1998).
75. J. Yang, M. B. J. Diemeer, G. Sengo, M. Pollnau, and A. Driessen, “Nd-doped polymer waveguide amplifiers,” IEEE J. Quantum Electron. **46**, 1043-1050 (2010).
76. J. Yang, K. van Dalfsen, K. Wörhoff, F. Ay, and M. Pollnau, “High-gain $Al_2O_3:Nd^{3+}$ channel waveguide amplifiers at 880 nm, 1060 nm and 1330 nm,” Appl. Phys. B **101**, 119-127 (2010).
77. V. Ostroumov, T. Jensen, J. P. Meyn, G. Huber, and M. A. Noginov, “Study of luminescence concentration quenching and energy transfer upconversion in Nd-doped $LaSc_3(BO_3)_4$ and $GdVO_4$ laser crystals,” J. Opt. Soc. Am. B **15**, 1052-1060 (1998).
78. Y. Guyot, H. Manaa, J. Y. Rivoire, R. Moncorgé, N. Garnier, E. Descroix, M. Bon, and P. Laporte, “Excited-state-absorption and up-conversion studies of Nd^{3+}-doped single crystals $Y_3Al_5O_{12}$, $YLiF_4$, and $LaMgAl_{11}O_{19}$,” Phys. Rev. B **51**, 784-799 (1995).
79. V. I. Zhekov, V. A. Lobachev, T. M. Murina, and A. M. Prokhorov, “Efficient cross-relaxation laser emitting at $\lambda = 2.94$ µm,” Kvantovaya Elektron. **10**, 1871-1873 (1983).
80. M. Pollnau, T. Graf, J. E. Balmer, W. Lüthy, and H. P. Weber, “Explanation of the cw operation of the Er^{3+} 3-µm crystal laser,” Phys. Rev. A **49**, 3990-3996 (1994).
81. M. Pollnau and S. D. Jackson, “Energy recycling versus lifetime quenching in erbium-doped 3-µm fiber lasers,” IEEE J. Quantum Electron. **38**, 162-169 (2002).
82. D. Faucher, M. Bernier, G. Androz, N. Caron, and R. Vallee, “10 W passively cooled single-mode all-fiber laser at 2.8 µm,” Opt. Lett. **36**, 1104-1106 (2011).
83. F. Auzel, “Upconversion and anti-stokes processes with f and d ions in solids,” Chem. Rev. **104**, 139-173 (2004).
84. N. J. Cockroft, G. D. Jones, and D. C. Nguyen, “Dynamics and spectroscopy of infrared-to-visible up-conversion in erbium-doped cesium cadmium bromide ($CsCdBr_3:Er^{3+}$),” Phys. Rev. B **45**, 5187-5198 (1992).
85. S. R. Lüthi, M. Pollnau, H. U. Güdel, and M. P. Hehlen, “Near-infrared to visible upconversion in Er^{3+} doped $Cs_3Lu_2Cl_9$, $Cs_3Lu_2Br_9$, and $Cs_3Y_2I_9$ excited at 1.54 µm,” Phys. Rev. B **60**, 162-178 (1999).
86. H. U. Güdel and M. Pollnau, “Near-infrared to visible photon upconversion processes in lanthanide doped chloride, bromide and iodide lattices,” J. Alloys Compd. **303-304**, 307-315 (2000).
87. P. E. A. Möbert, A. Diening, E. Heumann, G. Huber, and B. H. T. Chai, “Room-temperature continuous-wave upconversion-pumped laser emission in Ho, $Yb:KYF_4$ at 756, 1070, and 1390 nm,” Laser Phys. **8**, 210-213 (1998).
88. W. J. C. Grant, “Role of rate equations in the theory of luminescent energy transfer,” Phys. Rev. B **4**, 648-663 (1971).
89. A. I. Burshteîn, “Concentration quenching of noncoherent excitation in solutions,” Sov. Phys. Usp. **143**, 553-606 (1984).
90. L. D. Zusman, “Kinetics of luminescence damping in the hopping mechanism of quenching,” Sov. Phys. JETP **46**, 347-351 (1977).
91. D. A. Zubenko, M. A. Noginov, V. A. Smirnov, and I. A. Shcherbakov, “Different mechanisms of nonlinear quenching of luminescence,” Phys. Rev. B **55**, 8881-8886 (1997).

92. T. Förster, “Zwischenmolekulare Energiewanderung und Fluoreszenz,” Ann. Phys. (Leipzig) **2**, 55-75 (1948).
93. D. L. Dexter, “A theory of sensitized luminescence in solids,” J. Chem. Phys. **21**, 836-850 (1953).
94. J. A. Caird, A. J. Ramponi, and P. R. Staver, “Quantum efficiency and excited-state relaxation dynamics in neodymium-doped phosphate laser glasses,” J. Opt. Soc. Am. B **8**, 1391-1403 (1991).
95. F. Auzel, “Material and devices using double-pumped phosphors with energy transfer,” Proc. IEEE **61**, 758-786 (1973).
96. M. Inokuti and F. Hirayama, “Influence of energy transfer by the exchange mechanism on donor luminescence,” J. Chem. Phys. **43**, 1978-1989 (1965).
97. T. Kushida, “Energy transfer and cooperative optical transitions in rare-earth doped inorganic materials. III. Dominant transfer mechanism,” J. Phys. Soc. Jpn. **34**, 1334-1337 (1973).
98. H. Dornauf and J. Heber, “Concentration-dependent fluorescence-quenching in $La_{1-x}Pr_xP_5O_{14}$,” J. Lumin. **22**, 1-16 (1980).
99. P. S. Golding, S. D. Jackson, T. A. King, and M. Pollnau, “Energy-transfer processes in Er^{3+}-doped and Er^{3+}, Pr^{3+}-codoped ZBLAN glasses,” Phys. Rev. B **62**, 856-864 (2000).
100. W. J. Miniscalco, “Erbium-doped glasses for fiber amplifiers at 1500 nm,” IEEE J. Lightwave Technol. **9**, 234-250 (1991).
101. F. Auzel, F. Bonfiglia, S. Gagliaria, and G. Baldacchini, “The interplay of self-trapping and self-quenching for resonant transitions in solids; role of a cavity,” J. Lumin. **94-95**, 293-297 (2001).
102. B. Viana, A.M. Lejus, D. Saber, N. Duxin, and D. Vivien, “Optical properties and energy transfer among Nd^{3+} in $Nd:Ca_2Al_2SiO_7$ crystals for diode pumped lasers,” Opt. Mater. **3**, 307-316 (1994).
103. A. S. S. Camargo, C. Jacinto, L. A. O. Nunes, T. Catunda, D. Garcia, E. R. Botero, and J. A. Eiras, “Effect of Nd^{3+} concentration quenching in highly doped lead lanthanum zirconate titanate transparent ferroelectric ceramics,” J. Appl. Phys. **101**, 0531111 (2007).
104. G. C. Jones and S. N. Houde-Walter, “Erbium partitioning in a heavily doped transparent glass ceramic,” Opt. Lett. **30**, 2122-2124 (2005).
105. R. S. Quimby, W. J. Miniscalco, and B. Thompson, “Excited state absorption at 980 nm in erbium doped glass,” in Fiber Laser Sources and Amplifiers III, Proc. SPIE 1581, 72-79 (1991).
106. *PhoeniX.* http://www.phoenixbv.com
107. L. Palatella, F. Cornacchia, A. Toncelli, and M. Tonelli, “Microscopic treatment of upconversion in Nd^{3+}-doped samples,” J. Opt. Soc. Am. B **20**, 1708-1714 (2003).
108. T. Jensen, “Upconversion-Prozesse und Wirkungsquerschnitte in Er^{3+}-dotierten 3 µm Fluorid- und Granat-Lasern, gepumpt mit cw und quasicw Dioden-Arrays,” Ph.D. Thesis, Institute of Laser-Physics, University of Hamburg, 1996.
109. E. Delevaque, T. Georges, M. Monerie, P. Lamouler, and J.-F. Bayon, “Modeling of pair-induced quenching in erbium-doped silicate fibers,” IEEE Photon. Technol. Lett. **5**, 73-75 (1993).
110. R. Wyatt, “Spectroscopy of rare earth doped fibers,” Proc. Soc. Photo-Opt. Instrum. Eng. **1171**, 54-64 (1990).

111. E. Maurice, G. Monnom, B. Dussardier, and D. B. Ostrowsky, “Clustering-induced nonsaturable absorption phenomenon in heavily erbium-doped silica fibers,” Opt. Lett. **20**, 2487-2489 (1995).
112. R. Paschotta, J. Nilsson, P. R. Barber, J. E. Caplen, A. C. Tropper, and D. C. Hanna, “Lifetime quenching in Yb-doped fibres,” Opt. Commun. **136**, 375-378 (1997).
113. P. Myslinski, J. Fraser, and J. Chrostowski, “Nanosecond kinetics of upconversion process in EDF and its effect on EDFA performance,” in *Optical Amplifiers and Their Applications, Proc. OAA’95, 1995* (Optical Society of America, Washington DC, 1995), paper ThE3, pp. 100-103.
114. Y. E. Kariss and P. P. Feofilov, “The absorption and emission of holmium and erbium,” Opt. Spektrosk. **15**, 572-574 (1963).
115. K. Wörhoff, “Results of the lifetime measurements results in Hamburg,” internal communication, 2007.
116. Sichuan Lanthanum Rare Materials Limited. http://www.chemical-plant.com/sichuan-lanthanum-rare-materials-limited.html
117. D. Fagundes-Peters, N. Martynyuk, K. Lünstedt, V. Peters, K. Petermann, G. Huber, S. Basun, V. Laguta, and A. Hofstaetter, “High quantum efficiency YbAG-crystals,” J. Lumin. **125**, 238-247 (2007).
118. G. N. van den Hoven, E. Snoeks, A. Polman, C. van Dam, J. W. M. van Uffelen, and M. K. Smit, “Upconversion in Er-implanted Al_2O_3 waveguides,” J. Appl. Phys. **79**, 1258-1266 (1996).
119. B. Hwang, S. Jiang, T. Luo, J. Watson, G. Sorbello, and N. Peyghambarian, “Cooperative upconversion and energy transfer of new high Er^{3+}- and Yb^{3+}–Er^{3+}-doped phosphate glasses,” J. Opt. Soc. Am. B **17**, 833-839 (2000).
120. V. Lopez, G. Paez, and M. Strojnik, “Characterization of upconversion coefficient in erbium-doped materials,” Opt. Lett. **31**, 1660-1662 (2006).
121. S. O. Vasquez and C. D. Flint, “A shell model for cross relaxation in elpasolite crystals: application to the $^3P_0$ and $^1G_4$ states of $Cs_2NaY_{1-x}Pr_xCl_6$,” Chem. Phys. Lett. **238**, 378-386 (1995).
122. J. R. Salcedo, J. M. Sousa, and V. V. Kuzmin, “Theoretical treatment of relaxation oscillations in quasi-three-level systems,” Appl. Phys. B **62**, 83-85 (1996).
123. D. C. Hanna, R. G. Smart, P. J. Suni, A. I. Ferguson, and M. W. Phillips, “Measurements of fiber laser losses via relaxation oscillations,” Opt. Commun. **68**, 128-132 (1988).
124. K. J. Weingarten, B. Braun, and U. Keller, “In situ small-signal gain of solid-state lasers determined from relaxation oscillation frequency measurements,” Opt. Lett. **19**, 1140-1142 (1994).
125. A. Yariv and M. Nakamura, “Periodic structures for integrated optics,” IEEE J. Quantum Electron. **QE-13**, 233-253 (1977).
126. G. Chen, S. R. Seshadri, and F. Cerrina, “Distributed feedback lasers with distributed phase-shift structure,” Appl. Phys. Lett. **60**, 2586-2588 (1992).
127. M. Pollnau, E. Heumann, and G. Huber, “Time-resolved spectra of excited-state absorption in Er^{3+} doped $YAlO_3$,” Appl. Phys. A **54**, 404-410 (1992).
128. F. Qian, Q. Song, E.-K. Tien, S. K. Kalyoncu, Y. Huang, and O. Boyraz, “Effects of design geometries and nonlinear losses on gain in silicon waveguides with erbium-doped regions,” IEEE J. Quantum Electron. **47**, 327-334 (2011).

129. P. Le Boulanger, J.-L. Doualan, S. Girard, J. Margerie, and R. Moncorgé, "Excited-state absorption spectroscopy of Er^{3+}-doped $Y_3Al_5O_{12}$, YVO_4, and phosphate glass," Phys. Rev. B **60**, 11380-11390 (1999).
130. L. Fornasiero, K. Petermann, E. Heumann, and G. Huber, "Spectroscopic properties and laser emission of Er^{3+} in scandium silicates near 1.5 µm," Opt. Mater. **10**, 9-17 (1998).
131. M. Pollnau, D. R. Gamelin, S. R. Lüthi, H. U. Gudel, and M. P. Hehlen, "Power dependence of upconversion luminescence in lanthanide and transition-metal-ion systems," Phys. Rev. B **61**, 3337-3346 (2000).
132. R. Balda, A. J. Garcia-Adeva, J. Fernández, and J. M. Fdez-Navarro, "Infrared-to-visible upconversion of Er^{3+} ions in GeO_2–PbO–Nb_2O_5 glasses," J. Opt. Soc. Am. B **21**, 744-752 (2004).
133. J. Rubin, A. Brenier, R. Moncorgé, and C. Pedrini, "Excited-state absorption and energy-transfer in Er^{3+} doped $LiYF_4$," J. Lumin. **36**, 39-47 (1986).
134. J. Koetke and G. Huber, "Infrared excited-state absorption and stimulated-emission cross sections of Er^{3+}-doped crystals," Appl. Phys. B **61**, 151-158 (1995).
135. F. Auzel, "Multiphonon-assisted anti-Stokes and Stokes fluorescence of triply ionized rare-earth ions," Phys. Rev. B **13**, 2809-2817 (1976).
136. H. T. Amorim, M. T. de Araujo, E. A. Gouveia, A. S. Gouveia-Neto, J. A. Medeiros Neto, and A. S. B. Sombra, "Infrared to visible frequency up-conversion fluorescence spectroscopy in Er^{3+}-doped chalcogenide glass," J. Lumin. **78**, 271-275 (1998).
137. I. R. Martın, P. Velez, V. D. Rodrıguez, U. R. Rodrıguez-Mendoza, and V. Lavın, "Upconversion dynamics in Er^{3+}-doped fluoroindate glasses," Spectrochim. Acta Part A **55**, 935-940 (1999).
138. G. Qin, J. Lu, J. F. Bisson, Y. Feng, and K. Ueda, "Upconversion luminescence of Er^{3+} in highly transparent YAG ceramics," Solid State Commun. **132**, 103-106 (2004).
139. F. Sanchez, P. L. François, G. Stephan, and P. Le Boudec, "Effects of ion pairs on the dynamics of erbium-doped fiber lasers," Phys. Rev. A **48**, 2220-2229 (1993).
140. H. L. An, E. Y. B. Pun, H. D. Liu, and X. Z. Lin, "Effects of ion clusters on the performance of a heavily doped erbium-doped fiber laser," Opt. Lett. **23**, 1197-1199 (1998).
141. G. E. Brown Jr., G. A. Waychunas, C. W. Ponader, W. E. Jackson, and D. A. McKeown, "EXAFS and NEXAFS studies of cations environements in oxide glasses, " J. Phys. Colloques **47**, C-8-661- C-8-668 (1986).
142. A. C. Wright, G. Etherington, J. A. Erwin-Desa, and R. N. Sinclair, "Neutron diffraction studies of rare-earth ions in glasses," J. Phys. Colloques **43**, C-9-31- C-9-34 (1982).
143. S. Sen and J. F. Stebbins, "Structural role of Nd^{3+} and Al^{3+} cations in SiO_2 glass: a ^{29}Si MAS-NMR spin-lattice relaxation, ^{27}Al NMR and EPR study," J. Non-Cryst. Solids **188**, 54-62 (1995).
144. Digital Library of Mathematical Functions. http://dlmf.nist.gov
145. M. Pollnau, C. Ghisler, W. Lüthy, and H. P. Weber, "Cross sections of excited-state absorption at 800 nm in erbium-doped ZBLAN fiber," Appl. Phys. B **67**, 23-28 (1998).

Acknowledgments

At last, it is finally time to write the acknowledgment section of the thesis. This will probably be the most read section of the entire thesis, therefore it is important to write something interesting! I'll try to follow a sort of chronological order, and I hope I won't forget anybody…

In the summer of 2007 I came for the first time to Twente for an on-site interview. Kerstin Wörhoff and René de Ridder welcomed me and introduced me to the IOMS world. Once I was hired Kerstin became my daily supervisor, providing me with many beautiful Al_2O_3 layers to characterize… but most important, showing me how to plan and carry on my measurements in a systematic way and how to improve the logical structure of my papers. I thank Kerstin and René for their guidance, helpful discussions and support during the good and especially bad times.

I met my supervisor Markus Pollnau as soon as I stepped in for the first day of work. His enthusiastic attitude toward science in general and spectroscopy of rare-earths in particular is contagious. I am very grateful for the countless discussions which guided me in the right direction, his insights and encouraging words, and for patiently revising (many times…) my manuscripts. I thank him for allowing me to pursue my interest in spectroscopy (when I should have done more integrated optics) and for letting me stay a little bit longer in the group.

After the first days Feridun Ay came and dragged me to the lab. I'll never forget the first time I managed, with his guidance, to couple some red light into an Al_2O_3 layer with the prism-coupling setup. He was always there to assist with the first loss and lifetime measurements, to answer my sometimes silly questions, and to calm me down when I felt overwhelmed by the amount of work awaiting me.

During my first two years Jonathan Bradley and I spent a lot of time working together. Thank you for your psychological support during the loss measurements, for your strong work ethic, your Phoenix scripts and for inviting me to give a seminar at your new group at Harvard, that was awesome!

Anton Hollink and Henk van Wolferen were always there to help me build and optimize with my setups. Anton, thank you for your patience when I broke all those expensive prisms and I burned one fiber after the other… I enjoyed our conversations about running and Dutch football. Meindert Dijkstra, thank you for your prompt help whenever I needed some etching or dicing done in the cleanroom.

In the first years I shared the office in the Hogekamp building with the following colleagues: Dimitri Geskus, the lab guru, initiator of many fun PIOMS activities, and our Dutch guide; Edward Bernhardi, the Matlab expert (I don't know what I would have done without your scripts… thank you!!!), initiator of many challenging but interesting conversations about laser physics, and the guy who introduced me to rock-climbing; Chaitanya Dongre, the tireless traveler, who never failed to amaze me with his knowledge of languages and Italian culture.

Afterwards we moved to Carrè where I got to share a bigger room which included also the following colleagues: Marko van Dalfsen, Fehmi Civitci, and Lantian Chang. Thank you guys for making the atmosphere enjoyable.

Other fellow PhD students: Jing Yang (thank you for the discussions about being a PhD student during my first months at work), Marcel Hoekman (your loss-measurement software saved me so much time!), Lasse Kauppinen (Finnish mosquitoes and vodka), Imran Akca (delicious Turkish food and conversations about how difficult it is to be a girl in science), and So Van Pham (the power of meditation). Nur Ismail, thank you for reminding me to speak Italian once in a while… I forgot so many words during these years! The new guys: Mustafa Sefünç, and Sergio Vázquez-Córdova and Yean-Sheng Yong, who will continue the Al_2O_3 work: good luck!

Of course our secretaries: Rita ter Weele-Stokkers (thank you for arranging my first accommodation in the Netherlands and for never giving up on my Dutch), Annitta David, and Birgit Binkhorst-Reinshagen (thank you for handling the last-minute madness with my promotion papers)

The rest of the IOMS staff (old and new): Gabriël Sengo, Hugo Hoekstra, Alfred Driessen, Manfred Hammer (thanks for your help with some crazy integrals), Sonia García Blanco, Shanmugam Aravazhi (thank you Sonia and Abu for your suggestions on job hunting), Henri Uranus, and Fei Sun.

To my one and only student, Francois Parcy: thank you for helping me develop the streak-of-luminescence loss measurements. You did a much work and showed a lot of initiative, whilst maintaining a laid-back attitude. I'm sure your PhD will be a success!

Christos Grivas: although we didn't directly collaborate, I benefited a lot from you expertise on lasers and I enjoyed our conversations about moving from one country to another.

During my third year I had the opportunity to go to Hamburg to do some ESA experiments there: I had a great time in Günther Huber's group, and I'd like to thank him and Klaus Petermann for making my stay possible. Andreas Kahn and Matthias Fechner helped me with the measurements and together with Francesca Moglia, Ulrike Wolters, Fabian Reichert, Thomas Calmano and Henning Kühn created a very welcoming environment.

I'd like to thank Günther Roelkens and Roel Baets from Ghent University for our collaboration on the Al_2O_3-Si integration. In particular Günther, who had to answer to my many (annoying) e-mails.

The people of the Telecommunication group: Chris Roeloffzen and Reza Kahn, who were involved in the Memphis Project, and Maurizio Burla, you're a great guy!

I greatly thank the committee members, Willem Vos, Jan Eijkel, Pieter Dorenbos, Alessandra Toncelli, Kerstin Wörhoff, and Markus Pollnau for their valuable input, time and efforts in reviewing my thesis.

Of course we worked hard, but we made sure we took some time off to relax and do some fun activities. Here I'll thank again some people who were already mentioned, but what can I do, you guys are just too great. ☺ Dimitri Geskus, you don't know how much it meant to me when you handed me a bike on my first week in the Netherlands… and for free! It made me realize that yes, maybe I could make it in this new, foreign

country. I'll never forget that. You and Saara-Maarit are a great couple. Edward and Michelle Bernhardi, Imran Akca, and Akin Avci, I enjoyed so much living with you guys in the Waarbekenweg. All the "braai", the cakes, the movies and the girls' nights… too many tales to mention. Michelle, thank you for getting me back into running during a time in which I lacked motivation. How to forget the "Huttenkloasloop half-marathon" in Oldenzaal? More running was done with Sonia García Blanco, Fraser Williamson, and Liesbeth Hartsuiker. Sadjad Khan, Saskia Kulinga, Thomas Denis, and Sergio Vázquez-Córdova, thanks for being my climbing partners in these years.

I'd like to acknowledge my M. Sc. Supervisor Giorgio Samoggia and the late Emanuele Reguzzoni at the University of Pavia in Italy for encouraging me to do a Ph. D. I dedicate this thesis to my family: my parents, Flavio and Giovanna, and my siblings, Andrea, Francesco and Silvia, with her husband Gianfranco and their three wonderful kids Gabriele, Paolo and Damiano. They have always encouraged and supported me, even when this meant sending me abroad… My Dutch adoptive family: Jan, Marianne, Suzanne and Bert with little Gijs. Thank you for making me feel welcome in this country. And last but not least… Vincent, thank you for your love, patience and support. And sorry if I often misuse the expression "tjonge-jonge"…

Thank you all,

Laura

List of Publications

Peer-reviewed Journal Articles

1. L. Agazzi, K. Wörhoff, A. Kahn, M. Fechner, K. Petermann, G. Huber, and M. Pollnau, "Spectroscopy of upper energy levels in an Er^{3+}-doped oxide," submitted (2012).

2. L. Agazzi, K. Wörhoff, and M. Pollnau, "Energy-transfer-upconversion models, their applicability and breakdown in the presence of spectroscopically distinct ion classes: Investigations on the example of amorphous $Al_2O_3:Er^{3+}$," submitted (2012).

3. L. Agazzi, E. H. Bernhardi, K. Wörhoff, and M. Pollnau, "Impact of luminescence quenching on relaxation-oscillation frequency in solid-state lasers," Appl. Phys. Lett. **100**, 011109 (2012).

4. L. Agazzi, J. D. B. Bradley, M. Dijkstra, F. Ay, G. Roelkens, R. Baets, K. Wörhoff, and M. Pollnau, "Monolithic integration of erbium-doped amplifiers with silicon-on-insulator waveguides," Opt. Express **18,** 27703-27711 (2010).

5. E. H. Bernhardi, H. A. G. M. van Wolferen, L. Agazzi, M. R. H. Khan, C. G. H. Roeloffzen, K. Wörhoff, M. Pollnau, and R. M. de Ridder, "Ultra-narrow-linewidth, single-frequency distributed feedback waveguide laser in $Al_2O_3:Er^{3+}$ on silicon," Opt. Lett. **35**, 2394-2396 (2010).

6. J. D. B. Bradley, R. Stoffer, A. Bakker, L. Agazzi, F. Ay, K. Wörhoff, and M. Pollnau, "Integrated $Al_2O_3:Er^{3+}$ zero-loss optical amplifier and power splitter with 40 nm bandwidth," IEEE Photon. Technol. Lett. **22**, 278-280 (2010).

7. J. D. B. Bradley, L. Agazzi, D. Geskus, F. Ay, K. Wörhoff, and M. Pollnau, "Gain bandwidth of 80 nm and 2 dB/cm peak gain in $Al_2O_3:Er^{3+}$ optical amplifiers on silicon," J. Opt. Soc. Am. B **27**, 187-196 (2010).

8. J. D. B. Bradley, R. Stoffer, L. Agazzi, F. Ay, K. Wörhoff, and M. Pollnau, "Integrated $Al_2O_3:Er^{3+}$ ring laser on silicon with wide wavelength selectivity," Opt. Lett. **35**, 73-75, (2010).

Proceedings

9. K. Wörhoff, E.H. Bernhardi, J.D.B. Bradley, J. Yang, L. Agazzi, F. Ay, R.M. de Ridder, and M. Pollnau, “Rare-earth-ion doped amplifiers and lasers integrated on silicon”, International Conference on Transparent Optical Networks, Stockholm, Sweden, Tu.C1.1 (2011).
   DOI: 10.1109/ICTON.2011.5970947.

10. K. Wörhoff, J.D.B. Bradley, L. Agazzi, and M. Pollnau, “Rare-earth-ion-doped Al_2O_3 for integrated optical amplification”, Integrated Optics: Devices, Materials, and technologies XIV, edited by J.E. Broquin and C.M. Greiner, Proceedings of the SPIE, paper 760408 (2010).

Contributions to International Conferences

11. L. Agazzi, K. Wörhoff, and M. Pollnau, “Upconversion spectroscopy of erbium in amorphous aluminum oxide microstructures,” MRS Fall Meeting, Boston, Massachusetts (2012). Submitted.

12. M. Pollnau, J. D. B. Bradley, E. H. Bernhardi, L. Agazzi, D. Geskus, K. van Dalfsen, J. Yang, A. Driessen, S. M. García-Blanco, K. Wörhoff, and R. M. de Ridder, “On-chip integrated amplifiers and lasers utilizing rare-earth-ion activation,” Nanoscience and Nanotechnology Congress, Ankara, Turkey (2012). Plenary Lecture.

13. L. Agazzi, E. H. Bernhardi, K. Wörhoff, and M. Pollnau, “The impact of lifetime quenching on relaxation oscillations in solid-state lasers,” Conference on Lasers and Electro-Optics, Technical Digest, San José, California (Optical Society of America, Washington, DC 2012), paper CTu1D.6 (2012).

14. L. Agazzi, K. Wörhoff, and M. Pollnau, “Energy-transfer processes in Al_2O_3:Er^{3+} waveguide amplifiers,” Conference on Lasers and Electro-Optics, Technical Digest, San José, California (Optical Society of America, Washington, DC 2012), paper CF3A.3 (2012).

15. D. Geskus, S. Aravazhi, E. H. Bernhardi, L. Agazzi, S. M. García Blanco, and M. Pollnau, “150 dB/cm over 55 nm wavelength range near 1 μm in an Yb^{3+} waveguide amplifier,” Conference on Lasers and Electro-Optics, Technical Digest, San José, California (Optical Society of America, Washington, DC 2012), paper CM1A.6 (2012).

16. L. Agazzi, K. Wörhoff, and M. Pollnau, "Fast quenching processes and their impact on 1.5-μm amplifier performance in Al_2O_3:Er^{3+}," European Conference on Integrated Optics, Barcelona, Spain, paper 84 (2012).

17. D. Geskus, S. Aravazhi, E. H. Bernhardi, L. Agazzi, S. M. García Blanco, and M. Pollnau, "Ultra-high, broadband gain in a lattice-engineered, Yb-doped double tungstate channel waveguide," European Conference on Integrated Optics, Barcelona, Spain, paper 109 (2012).

18. L. Agazzi, E. H. Bernhardi, K. Wörhoff, and M. Pollnau, "Luminescence quenching in rare-earth-ion-doped Al_2O_3 lasers and its influence on relaxation oscillation frequency," Advanced Solid-State Photonics Conference, San Diego, California (Optical Society of America, Washington, DC 2012), paper AT4A.18 (2012).

19. L. Agazzi, J. D. B. Bradley, K. Wörhoff, and M. Pollnau, "Al_2O_3:Er^{3+} amplifiers: The impact of fast spectroscopic quenching processes," International Quantum Electronics Conference and Conference on Lasers and Electro-Optics Pacific Rim, Conference Handbook, Sydney, Australia, paper 5420-CT-5 (2011).

20. L. Agazzi, J. D. B. Bradley, J. Yang, F. Ay, K. Wörhoff, and M. Pollnau, "Er^{3+}- and Nd^{3+}-doped Al_2O_3 amplifiers on a silicon chip," International Laser Physics Workshop, Program, Sarajevo, Bosnia and Herzegovina, paper 4.2.5 (2011).

21. L. Agazzi, J. D. B. Bradley, F. Ay, K. Wörhoff, and M. Pollnau, "Presence of fast quenching mechanisms in Al_2O_3:Er^{3+}," International Conference on Luminescence, Ann Arbor, Michigan, paper MH6 (2011).

22. K. Wörhoff, E. H. Bernhardi, J. D. B. Bradley, J. Yang, L. Agazzi, F. Ay, R. M. de Ridder, and M. Pollnau, "Rare-earth-ion doped amplifiers and lasers integrated on silicon," International Conference on Transparent Optical Networks, Conference Program, Stockholm, Sweden, paper Tu.C1.1 (2011). Invited Paper.

23. L. Agazzi, K. Wörhoff, and M. Pollnau, "Excitation quenching in Er^{3+}-doped Al_2O_3 amplifiers," Conference on Lasers and Electro-Optics Europe, Munich, Germany, paper CE3.4 (2011).

24. L. Agazzi, K. Wörhoff, and M. Pollnau, "Non-saturable absorption and its impact on amplifier performance in Al_2O_3:Er^{3+}," Conference on Lasers and Electro-Optics, Technical Digest, Baltimore, Maryland (Optical Society of America, Washington, DC 2011), paper JWA59 (2011).

25. L. Agazzi, K. Wörhoff, M. Pollnau, A. Kahn, M. Fechner, K. Petermann, and G. Huber, "Upconversion spectroscopy of Al_2O_3:Er^{3+}," IV International Workshop on Photonic and Electronic Materials, Scientific Program and Workshop Abstracts, San Sebastian, Spain, p. 49 (2010).

26. L. Agazzi, J. D. B. Bradley, G. Roelkens, R. Baets, F. Ay, K. Wörhoff, and M. Pollnau, “Wafer-scale monolithic integration of Al_2O_3:Er amplifiers with Si waveguides,” Conference on Lasers and Electro-Optics, Technical Digest, San José, California (Optical Society of America, Washington, DC 2010), paper JWA92 (2010).

27. E. H. Bernhardi, H. A. G. M. van Wolferen, L. Agazzi, M. R. H. Khan, C. G. H. Roeloffzen, K. Wörhoff, M. Pollnau, and R. M. de Ridder, “Low-threshold, single-frequency distributed-feedback waveguide laser in Al_2O_3:Er^{3+} on silicon,” Conference on Lasers and Electro-Optics, Technical Digest, San José, California (Optical Society of America, Washington, DC 2010), paper CTuU4 (2010).

28. F. Ay, E. H. Bernhardi, L. Agazzi, J. D. B. Bradley, K. Wörhoff, M. Pollnau, and R. M. de Ridder, “Characterization of Bragg gratings in Al_2O_3 waveguides fabricated by focused ion beam milling and laser interference lithography,” Conference on Lasers and Electro-Optics, Technical Digest, San José, California (Optical Society of America, Washington, DC 2010), paper CMQ4 (2010).

29. J. D. B. Bradley, R. Stoffer, L. Agazzi, F. Ay, K. Wörhoff, and M. Pollnau, “Widely wavelength-selective integrated ring laser in Al_2O_3:Er,” Conference on Lasers and Electro-Optics, Technical Digest, San José, California (Optical Society of America, Washington, DC 2010), paper CMQ2 (2010).

30. J. D. B. Bradley, L. Agazzi, F. Ay, K. Wörhoff, M. Pollnau, and R. Stoffer, “Widely wavelength-selective Al_2O_3:Er^{3+} ring laser,” European Conference on Integrated Optics, Cambridge, United Kingdom, paper ThE3 (2010).

31. L. Agazzi, J. D. B. Bradley, F. Ay, K. Wörhoff, and M. Pollnau, “Al_2O_3:Er^{3+} waveguide amplifiers at 1.5 μm,” European Conference on Integrated Optics, Cambridge, United Kingdom, paper ThE2 (2010).

32. E. H. Bernhardi, H. A. G. M. van Wolferen, L. Agazzi, M. R. H. Khan, C. G. H. Roeloffzen, K. Wörhoff, M. Pollnau, and R. M. de Ridder, “Single-frequency, narrow-linewidth distributed feedback waveguide laser in Al_2O_3:Er^{3+} on silicon,” European Conference on Integrated Optics, Cambridge, United Kingdom, paper ThE1 (2010).

33. K. Wörhoff, J. D. B. Bradley, L. Agazzi, and M. Pollnau, “Rare-earth-ion-doped Al_2O_3 for integrated optical amplification and lasing,” OPTO, Photonics West, Technical Abstract Summaries, Conference “Integrated Optics: Devices, Materials, and Technologies XIV”, San Francisco, California, paper 7604-07 (2010). Invited Paper.

34. J. D. B. Bradley, L. Agazzi, F. Ay, K. Wörhoff, and M. Pollnau, “High-performance Al_2O_3:Er^{3+} integrated optical amplifiers,” International Laser Physics Workshop, Book of Abstracts, Barcelona, Spain, paper 8.3.5 (2009).

35. M. Pollnau, J. D. B. Bradley, L. Agazzi, E. H. Bernhardi, F. Ay, K. Wörhoff, and R. M. de Ridder, “Al_2O_3:Er^{3+} as a new platform for active integrated

optics," International Conference on Transparent Optical Networks, São Miguel, Azores, Portugal, paper We.D2.1 (2009). Invited Paper.

36. J. D. B. Bradley, L. Agazzi, D. Geskus, F. Ay, K. Wörhoff, and M. Pollnau, "Higher gain in 977-nm-pumped Al_2O_3:Er^{3+} integrated optical amplifiers," Conference on Lasers and Electro-Optics Europe, Conference Digest, Munich, Germany, paper CE1.4 MON (2009).

37. L. Agazzi, J. D. B. Bradley, F. Ay, A. Kahn, H. Scheife, G. Huber, R. M. de Ridder, K. Wörhoff, and M. Pollnau, "Energy migration governs upconversion losses in Er^{3+}-doped integrated amplifiers," Conference on Lasers and Electro-Optics Europe, Conference Digest, Munich, Germany, paper CE1.3 MON (2009).

38. J. D. B. Bradley, L. Agazzi, D. Geskus, F. Ay, K. Wörhoff, and M. Pollnau, "2.0 dB/cm gain in an Al_2O_3:Er^{3+} waveguide on silicon," Conference on Lasers and Electro-Optics, Technical Digest, Baltimore, Maryland (Optical Society of America, Washington, DC 2009), paper CThCC2 (2009).

39. K. Wörhoff, J. D. B. Bradley, L. Agazzi, D. Geskus, F. Ay, A. Kahn, H. Scheife, K. Petermann, G. Huber, and M. Pollnau, "Energy-transfer upconversion in Al_2O_3:Er^{3+} thin layers," International Workshop on Advanced Spectroscopy and Optical Materials, Book of Abstracts, Gdansk, Poland, paper 6-O-3 (2008).

40. L. Agazzi, J. D. B. Bradley, F. Ay, K. Wörhoff, and M. Pollnau, "Spectroscopy and gain in Al_2O_3:Er waveguides," International Conference on Luminescence and Optical Spectroscopy of Condensed Matter, Book of Abstracts, Lyon, France, paper TuA2-O2 (2008).

41. L. Agazzi, J. D. B. Bradley, F. Ay, K. Wörhoff, and M. Pollnau, "Al_2O_3:Er waveguide amplifiers for Si-technology compatible integrated optical applications," ePIXnet Spring School on Technology for Photonics Integration, Book of Abstracts, Portoferraio/Elba, Italy, p. 66 (2008).

42. J. D. B. Bradley, L. Agazzi, D. Geskus, T. Blauwendraat, F. Ay, K. Wörhoff, and M. Pollnau, "Investigation of optical gain in Al_2O_3:Er channel waveguide amplifiers," Conference on Lasers and Electro-Optics, Technical Digest, San José, California (Optical Society of America, Washington, DC 2008), paper JTuA30 (2008).

Contributions to National Conferences

43. E. H. Bernhardi, L. Agazzi, H. A. G. M. van Wolferen, K. Wörhoff, R. M. de Ridder, and M. Pollnau, "Monolithic channel waveguide lasers in rare-earth-ion-doped alumina," Fotonica Evenement, Nieuwegein, The Netherlands, (2011).

44. E. H. Bernhardi, L. Agazzi, K. Wörhoff, R. M. de Ridder, and M. Pollnau, "Narrow-linewidth distributed feedback channel waveguide laser in Al_2O_3:Er^{3+}," Proceedings of the 2010 Annual Symposium of the IEEE Photonics Benelux Chapter, Delft, The Netherlands, pp. 85-88 (2010).

45. L. Agazzi, J. D. B. Bradley, F. Ay, K. Wörhoff, and M. Pollnau, "Understanding Al_2O_3:Er^{3+} device performance," Proceedings of the 2010 Annual Symposium of the IEEE Photonics Benelux Chapter, Delft, The Netherlands, pp. 261-264 (2010).

46. E. H. Bernhardi, H. A. G. M. van Wolferen, L. Agazzi, M. R. H. Khan, C. G. H. Roeloffzen, K. Wörhoff, M. Pollnau, and R. M. de Ridder, "Ultra-narrow-linewidth, single-frequency distributed feedback waveguide laser in Al_2O_3:Er^{3+} on silicon," Fotonica Evenement, Nieuwegein, The Netherlands, (2010).

47. E. H. Bernhardi, H. A. G. M. van Wolferen, M. Dijkstra, L. Agazzi, K. Wörhoff, M. Pollnau, and R. M. de Ridder, "Designing an integrated Al_2O_3:Er^{3+} distributed feedback laser," Proceedings of the 2009 Annual Symposium of the IEEE Photonics Benelux Chapter, Brussels, Belgium, pp. 197-200 (2009).

48. J. D. B. Bradley, L. Agazzi, F. Ay, K. Wörhoff, and M. Pollnau, "Al_2O_3:Er^{3+} as a broad gain medium for 1.53-μm integrated optical applications," Proceedings of the 2009 Annual Symposium of the IEEE Photonics Benelux Chapter, Brussels, Belgium, pp. 13-16 (2009).

49. J. D. B. Bradley, L. Agazzi, D. Geskus, F. Ay, K. Wörhoff, M. Pollnau, and W. M. Arnoldbik, "Enhanced gain in Er-doped Al_2O_3 channel waveguide amplifiers," Proceedings of the Twelfth Annual Symposium of the IEEE/LEOS Benelux Chapter, Enschede, The Netherlands, pp. 131-134 (2008).

50. L. Agazzi, J. D. B. Bradley, F. Ay, A. Kahn, H. Scheife, K. Petermann, G. Huber, R. M. de Ridder, K. Wörhoff, and M. Pollnau, "Upconversion spectroscopy of Al_2O_3:Er^{3+}," Proceedings of the Twelfth Annual Symposium of the IEEE/LEOS Benelux Chapter, Enschede, The Netherlands, pp. 51-53 (2008).

51. J. D. B. Bradley, L. Agazzi, D. Geskus, F. Ay, K. Wörhoff, and M. Pollnau, "Reactively co-sputtered Al_2O_3:Er^{3+} for active photonic devices," Proceedings of the Annual Workshop of the IEEE/LEOS Benelux Chapter, Brussels, Belgium, pp. 9-10 (2008).